Excitation dynamics of strongly dissipative quantum systems

Jacob Christan Iles-Smith

September 2015

Department of Physics

Imperial College London

Supervised by Ahsan Nazir and Brendon Lovett

Submitted in part fulfilment of the requirements for the degree of Doctor of Philosophy in Physics of Imperial College London

ABSTRACT

Strong coupling between a quantum system and its many-body environment is becoming an increasingly important topic for many branches of physics. Numerous systems of experimental and technological relevance demonstrate strong system-environment coupling, leading to complex dynamical behaviour. This thesis is concerned with two particular examples of such systems, namely quantum dots (QDs) and excitonic energy transfer (EET) in molecular systems.

Traditional quantum optics treatments are often insufficient to describe the transient, steady state, and optical properties of QDs due to system-environment correlations. In contrast, we present a modified theory of quantum optics capable of capturing the influence of a thermal environment on the behaviour of QDs. Using this framework we demonstrate a striking departure of the emission spectra and photon measurement statistics of a classically driven QD when compared to an analogous atomic system. Furthermore, in contradiction to accepted notions of decoherence and dissipation, we show that the interaction between a QD and its thermal environment induces non-classical light-matter correlations in an otherwise semi-classical regime of cavity quantum electrodynamics.

Away from QDs, we develop the reaction coordinate (RC) formalism to describe the dynamics of a system coupled to a low frequency environment — a regime important to EET systems. We do so by identifying and incorporating important environmental degrees of freedom into an enlarged system Hamiltonian. Uniquely, this approach gives insight directly into the dynamical evolution of the environment and correlations accumulated between the system and environment. Furthermore, it is demonstrated that these correlations persist into the steady state, generating non-canonical equilibrium states of the system and environment.

We then apply the RC model to describe EET in a molecular dimer, highlighting the effect that under- and over-damped environments have on the excitation dynamics. In doing so, we show interactions between the dimer and a structured environment can significantly enhance the energy transfer rate.

ACKNOWLEDGEMENTS

There are many people I want to thank for making my PhD such a great experience. First and foremost I would like to thank Ahsan for his excellent supervision and tolerating my endless cynicism. I have learnt much from my time as his PhD student, not only in terms of physics, but also in 'effective methods of networking'. I'd also like to thank Brendon for his advice and guidance.

Throughout my PhD have been lucky enough to discuss and collaborate with many fantastic scientist. In particular I'd like to thank Neill Lambert who has diligently and patiently produced a vast amount of data for me. Thank you also to my fellow MaNQ, Zach Blunden-Codd, for your shining example of how to be a rigorous scientist – I hope time around my cowboy physics hasn't done too much damage. I would like to express my gratitude to Ollie Woolland, whose pathological selflessness and linux wizardry made many of the calculations in the final chapter of this thesis possible. I'd also like to thank everyone at the Imperial, in particular Howard Dale for patiently answering my many many stupid questions on the foundations of quantum mechanics, as well as my quantum optics comrade Kyle McEnery, and to the rest of Cohort 3 – we will always have San Antonio.

A big thanks to my parents who have been a great source of support and inspiration throughout my life. To my brother and sister – our bickering at the dinner table made me the argumentative bastard I am today, a skill set I use everyday. Thanks also to Alex Winter for your help battling seagulls, earning hangovers, and for so often tolerating my cowardice.

Finally, thank you Alice for always being there.

DECLARATION

The following thesis was written solely by me. It presents my own work, and work by others is appropriately referenced.

— Jake Iles-Smith

The copyright of this thesis rests with the author and is made available under a Creative Commons Attribution Non-Commercial No Derivatives licence. Researchers are free to copy, distribute or transmit the thesis on the condition that they attribute it, that they do not use it for commercial purposes and that they do not alter, transform or build upon it. For any reuse or redistribution, researchers must make clear to others the licence terms of this work.

"Nobody climbs mountains for scientific reasons.
Science is used to raise money for the expeditions,
but you really climb for the hell of it."

— Sir Edmund Hillary

CONTENTS

Abstract **2**

Acknowledgements **3**

1 Introduction and overview **12**

2 Basic concepts in open quantum systems **14**
2.1 The density matrix formalism 14
2.1.1 Introducing the density matrix 14
2.1.2 Properties of the density matrix 15
2.1.3 Time evolution of the density matrix 16
2.1.4 Composite systems 17
2.2 The master equation formalism 18
2.2.1 Projection operator techniques and the quantum master equation . . 19
2.2.2 The quantum regression theorem 24
2.2.3 The secular approximation 25
2.3 The spin-boson model 27
2.3.1 Weak-coupling master equation 27
2.3.2 System dynamics and the shortcomings of the weak coupling theory 29

3 Emission properties of optically driven quantum dots **31**
3.1 Introduction 31
3.2 The classically driven atom 32
3.2.1 The quantum optical master equation 34
3.2.2 Emission properties of a two-level atom 37
3.3 Phonon effects in quantum dots 41
3.3.1 The variational polaron formalism 41
3.3.2 The variational polaron master equation and exciton dynamics . . . 44
3.3.3 QD dynamics 49
3.4 Coherent and incoherent scattering from a QD 51
3.4.1 Enhanced coherent scattering 52
3.4.2 The balance of coherent and incoherent scattering in QDs 52
3.5 Phonon effects in higher order correlation functions 55
3.5.1 Hong-Ou-Mandel, Hanbury-Brown Twiss, and $G^{(2)}$ measurements . 55
3.5.2 Hong-Ou-Mandel experiments 56
3.5.3 Hanbury-Brown-Twiss experiments 64
3.6 Summary 67

4 Quantum correlations of light and matter through environmental transitions **69**
4.1 Introduction 69
4.2 Cavity QD systems 70

4.3 Dissipation in Cavity QED systems . . . 72
4.3.1 The phonon environment and polaron formalism . . . 72
4.3.2 Cavity loss and spontaneous emission . . . 74
4.3.3 Input-Output formalism . . . 75
4.4 Phonon Induced Asymmetries . . . 78
4.4.1 The semi-classical regime of cavity QED . . . 78
4.4.2 Phonon induced asymmetries . . . 79
4.4.3 Phonon induced light-matter correlations . . . 80
4.4.4 Cavity florescence spectra . . . 81
4.4.5 Beyond the Intermediate coupling regime . . . 82
4.5 Summary and Discussion . . . 84

5 The Reaction Coordinate Formalism 85
5.1 Introduction . . . 85
5.2 Reaction coordinate mapping and master equation . . . 86
5.2.1 The Reaction Coordinate Mapping . . . 86
5.2.2 Reaction coordinate master equation . . . 90
5.3 Time evolution of the RC model . . . 93
5.3.1 Benchmarking . . . 93
5.3.2 Environmental dynamics and correlations . . . 94
5.4 Noncanonical equilibrium states . . . 96
5.5 Summary . . . 98

6 Energy transfer in non-adiabatic regimes 100
6.1 Introduction . . . 100
6.2 System Hamiltonian and the reaction coordinate mapping . . . 101
6.2.1 Energy transport Hamiltonian . . . 101
6.2.2 Reaction coordinate mapping . . . 103
6.3 Time evolution in the RC model . . . 104
6.3.1 Reaction coordinate master equation . . . 104
6.3.2 Zusman equations . . . 104
6.4 System dynamics . . . 106
6.4.1 Overdamped spectral density . . . 107
6.4.2 Underdamped spectral density . . . 108
6.5 Structured environments . . . 112
6.5.1 Reaction coordinate model for structured environments . . . 113
6.5.2 Transition from coherent to incoherent energy transport . . . 113
6.6 Summary . . . 115

7 Conclusions and further work 116

A Correlation function for the variational theory 118

B The Zusman equations 122

Bibliography 135

LIST OF FIGURES

2.1 Pictorial representation of a quantum system coupled to an external environment. 18

2.2 Schematic of the spin-boson model 27

2.3 Dynamics predicted by the weak coupling master equation for various system-environment coupling strengths. 30

3.1 Dynamics of an driven atom as predicted by the quantum optical master equation. 36

3.2 Figure showing the driving dependence of the first-order correlation function, and incoherent emission spectra for a driven atom. 39

3.3 Schematic of the light-matter dressed states. 41

3.4 Schematic representation of the polaron transformation on a single mode of the environment. 46

3.5 Renormalisation of the Rabi frequency due to phonon processes. 49

3.6 The effect of phonons on the absorption spectrum of a quantum dot. 50

3.7 Schematic of phonon assisted photon absorption processes. 51

3.8 Enhanced coherent scattering in strongly driven quantum dots. 51

3.9 Balance of coherent to incoherent scattering for the phenomenological and full phonon theories 53

3.10 Fraction of coherent to incoherent scattering at strong driving and large detunings. 53

3.11 Schematic of experimental apparatus that can be used to measure second-order correlation functions. 55

3.12 Driving dependence of the Hong-Ou-Mandel correlation function for a driven atom. 60

3.13 Dephasing dependence of the Hong-Ou-Mandel correlation function for a driven atom. 62
3.14 Driving, temperature, and phonon coupling strength dependence of the Hong-Ou-Mandel correlation function for a quantum dot 63
3.15 Driving, temperature, and phonon coupling strength dependence of $g^{(2)}_{HOM}(0)$ for a quantum dot 64
3.16 The behaviour of the Hanbury-Brown-Twiss correlation function for a driven atom. 66
3.17 The effect of phonons on the Hanbury-Brown-Twiss correlation function. . . 67

4.1 Schematic of a cavity quantum dot system, and the eigenstates of the Jaynes-Cummings Hamiltonian. 71
4.2 Phonon asymmetries in the cavity reflectivity and occupation. 79
4.3 Measuring the light matter correlations induced by phonons. 81
4.4 Signatures of phonon interactions in the cavity fluorescence. 82
4.5 Asymmetries in the cavity reflectivity for the Fano and strong regimes. . . . 83

5.1 Schematic of the reaction coordinate mapping. 87
5.2 Benchmarking the RC master equation against the HEOM and Redfield theory. 93
5.3 The non-Gaussianity of the reaction corrdinate as well as the dynamical evolution of the correlations shared between the two level system and reaction coordinate 96
5.4 Steady state non-Gaussianity and mutual information as a function of the system-environment coupling strength. 97
5.5 Temperature and system-environment coupling strength dependence of the non-canonical steady state. 98

6.1 Comparison of the population dynamics predicted by the reaction coordinate master equation, the Zusman equations, and the hierarchical equations of motion for an overdamped spectral density. 106
6.2 Comparing the population dynamics for a dimer initiated in a canonical thermal state. 108

6.3 Comparison of the reaction coordinate and hierarchy for the underdamped spectral density, with Zusman equations inset. 109
6.4 Dynamics of the reaction coordinate position and momentum(inset). 110
6.5 Fourier transforms of the population dynamics. 110
6.6 Transition of the underdamped reaction coordinate to the overdamped case. 111
6.7 Schematic of the reaction coordinate mapping for a structured environment, and the associated spectral density. 112
6.8 Comparing the energy transfer rate predicted by the RC, Redfield, and hierarchy. 114
6.9 Energy transfer rate for a structured environment. 115

LIST OF PUBLICATIONS

Parts of this thesis is based on the following publications:

- J. Iles-Smith, N. Lambert, and A. Nazir, Phys. Rev. A 90, 032114 (2014).
- J. Iles-Smith and A. Nazir, arXiv:1412.6044 (2014)

CHAPTER 1

INTRODUCTION AND OVERVIEW

In the context of open quantum systems, the interaction between a system and its environment is often suggestive of a loss of quantum coherence, entanglement, and excitation, eventually leading to the emergence of classical behaviour. However, there are a number of situations where this notion is incomplete, and in some cases entirely incorrect. For example, when the memory time of an environment is of the same order as the dynamical timescales of the system, revivals of coherent dynamics may occur, effectively restoring quantum mechanical behaviour of the system.

This leads to a number of important considerations when studying open quantum systems. For instance, the correlations shared between a system and its external environment can have unexpected effects on the energy transfer dynamics in molecular systems – a topical example being the generation of long-lived excitonic coherence in photosynthetic systems. In the field of quantum computation, environmental influences beyond simple decoherence can have dramatic effects on the viability of quantum information processing schemes, as well as the functionality of components in larger devices.

The present thesis will investigate the role of quantum dissipation beyond simple open quantum systems techniques. By constructing formalism valid outside the weak system-environment coupling regime, insights into the dynamical effects of system-environment correlations are developed, and ultimately applied to a number of experimentally relevant systems. A persistent theme throughout this work is that for many cases of practical importance a detailed quantum mechanical description of the environment is essential to accurately describe the behaviour of the system under consideration. This often leads to counter-intuitive, and in some cases surprising, consequences of the interaction between a system and its environment.

In the first part of this thesis, the effect of phonons on the optical properties of quantum dots (QDs), and more generally solid-state photonic structures, is investigated. The solid-state nature of QDs inherently causes strong coupling between the excitonic degrees of freedom of the QD and the vibrational lattice of the host material. This has significant effects on both the excitation dynamics and resultant emission properties of the device. In particular, it is demonstrated that despite regular use in the literature the pure dephasing model is insufficient to describe the transient, steady state, and optical properties of driven solid-state photonic devices.

In contrast, through this investigation, a modified theory of quantum optics is pre-

sented, capable of capturing system-phonon interactions in a broad range of contexts and parameter regimes. This theory is used to analyse the emission spectra and corresponding photon statistics of a classically driven QD, demonstrating significant deviations from the analogous atomic case.

Subsequently, we generalise the above formalism to analyse the effect of phonons on the emission properties of a QD coupled to an optical cavity. Here it is shown that phonons induce quantum light-matter correlations in otherwise semi-classical regimes of cavity quantum electrodynamics (QED). This not only challenges the traditional notion that interactions between a system and its thermal environment manifest classical behaviour, but also further highlights the need for a full microscopic treatment of the phonon environment in these systems.

The second half of the thesis focuses on the development of a formalism to describe the dynamics of a quantum system interacting with an environment with a long memory time. This is an extremely computationally challenging regime with long environmental correlation times generating significant system-environment correlations. The so-called reaction coordinate formalism provides a powerful and intuitive formalism for describing such systems, and uniquely, gives a method to probe the dynamical evolution of the environment and the correlations generated between the system and environment, without incurring excessive computational overheads.

Though interesting in its own right, this regime is also of immense practical importance, specifically to the description of electron transfer in biological systems. There is a growing body of evidence to suggest that the interplay between the excitonic degrees of freedom and the vibrational modes of pigment-protein complexes of photosynthetic systems lead to long-lived vibronic coherences, and potentially the fast and efficient energy transfer observed in these systems. The reaction coordinate formalism offers a powerful and intuitive method for describing excitonic energy transfer, providing the opportunity to gain physical insight into the dynamical behaviour of such systems without resorting to hefty numerical simulations.

CHAPTER 2

BASIC CONCEPTS IN OPEN QUANTUM SYSTEMS

2.1 The density matrix formalism

In this chapter we shall lay down the mathematical foundations for the subsequent chapters. We shall start with the density matrix formulation of quantum mechanics, an essential component for the description of open quantum system.

2.1.1 Introducing the density matrix

According to the postulates of quantum mechanics, any state of an isolated physical system can be fully described by its state vector $|\psi\rangle$, with its time evolution governed by the Schrödinger equation [1]

$$i\frac{\partial|\psi\rangle}{\partial t} = H|\psi\rangle, \tag{2.1}$$

where H is the Hamiltonian of the system, and we have set $\hbar = 1$ for brevity throughout the thesis. This provides a full description of the dynamical evolution of *any closed quantum system*, that is, a quantum system isolated from its external environment. However, many systems of practical importance are inevitably influenced by an external environment, introducing classical uncertainty into the reduced state of the so-called *open quantum system* [2]. In this situation the state-vector formalism becomes insufficient to describe such systems.

To illustrate this, consider a situation in which an experimentalist is able to generate, with probability p, the state $|\psi_1\rangle$ and with $1-p$ the state $|\psi_2\rangle$, where these states may be non-orthogonal. Using these states, the experimentalist wishes to obtain the expectation value of the observable $\hat{O}$. After many measurements, the expectation value of $\hat{O}$ is given by the average of the two possible preparations,

$$\langle\hat{O}\rangle = p\langle\psi_1|\hat{O}|\psi_1\rangle + (1-p)\langle\psi_2|\hat{O}|\psi_2\rangle. \tag{2.2}$$

A natural question is then, can we construct a theoretical framework to capture the effects of classical uncertainty, and thus recover the measurement statistics described above?

Naively one might try to formulate the problem by way of the state vector formalism,

defining the state $|\Psi\rangle = \mathcal{N}^{-1}\left(p|\psi_1\rangle + (1-p)|\psi_2\rangle\right)$, where the state is normalised by $\mathcal{N}^2 = 1-2p(1-p)\left(1 - Re\left[\langle\psi_1|\psi_2\rangle\right]\right)$. It can be quickly seen that this approach does not produce the required measurement statistics, instead yielding

$$\langle\Psi|\hat{O}|\Psi\rangle = p^2\langle\psi_1|\hat{O}|\psi_1\rangle + (1-p)^2\langle\psi_2|\hat{O}|\psi_2\rangle + 2p(1-p)\left(\langle\psi_1|\hat{O}|\psi_2\rangle + \langle\psi_2|\hat{O}|\psi_1\rangle\right), \quad (2.3)$$

The discrepancies with Eq. 2.2 occur as the state $|\Psi\rangle$ does not describe a statistical mixture of the two states $|\psi_1\rangle$ and $|\psi_2\rangle$, but rather a quantum superposition between them.

In order to describe the effect of classical mixing, we make use of the fact that the *trace* of a number is still a number, and the cyclic invariance property of the trace, in Eq. 2.2:

$$\begin{aligned}\langle\hat{O}\rangle =& p\,\mathrm{tr}(\langle\psi_1|\hat{O}|\psi_1\rangle) + (1-p)\,\mathrm{tr}(\langle\psi_2|\hat{O}|\psi_2\rangle),\\ =& p\,\mathrm{tr}(\hat{O}|\psi_1\rangle\langle\psi_1|) + (1-p)\,\mathrm{tr}(\hat{O}|\psi_2\rangle\langle\psi_2|),\\ =& \,\mathrm{tr}\left(\hat{O}\rho\right),\end{aligned} \quad (2.4)$$

where we have defined a new quantum object, the so-called *density matrix*, $\rho = p|\psi_1\rangle\langle\psi_1| + (1-p)|\psi_2\rangle\langle\psi_2|$.

2.1.2 Properties of the density matrix

We can naturally generalise the density matrix, or equivalently the density operator, to describe any statistical ensemble of states. Consider the set of states $\{|\psi_i\rangle\}_{i=1}^n$, each of which occurs with probability p_i. The density matrix is thus

$$\rho = \sum_{i=1}^{n} p_i|\psi_i\rangle\langle\psi_i|, \quad (2.5)$$

if $p_1 = 1$ and $p_n = 0$ for all other n, then we call this state a pure state, otherwise a mixed state. From Eq. 2.5 we see that the density matrix has the general properties:

Properties of the density operator:

- The density matrix is a Hermitian operator: $\rho^\dagger = \rho$
- The density matrix is normalised: $\mathrm{tr}(\rho) = \sum_{i=1}^{n} p_i = 1$
- Positive: the eigenvalues of ρ are probabilities and therefore positive or null.

Other important properties of the density operator include:

- The expectation value of an observable $\hat{O}$ is given by $\mathrm{tr}(\hat{O}\rho) = \sum_{i=1}^{n} p_i\langle\psi_i|\hat{O}|\psi_i\rangle$
- The purity of a state is given by $P[\rho] = \mathrm{tr}(\rho^2)$.
  - *For a pure state:* $P[|\psi\rangle\langle\psi|] = \mathrm{tr}(|\psi\rangle\langle\psi|) = 1$

- *For a mixed state:* $P[\rho] < 1$
- *Maximally mixed state:* a state is said to be maximally mixed if $P[\rho] = \frac{1}{N}$ where N is the dimension of the system

2.1.3 Time evolution of the density matrix

Schrödinger picture

To describe the time evolution of the density matrix, consider the formal solution of the Schrödinger equation

$$|\psi(t)\rangle = \mathcal{U}(t, t_0)|\psi(t_0)\rangle, \tag{2.6}$$

where $\mathcal{U}(t, t_0) = \exp(-iH(t - t_0))$ for a time-independent Hamiltonian. Thus the time evolution of the density matrix for this state is given by $\rho(t) = \mathcal{U}(t, t_0)|\psi(t_0)\rangle\langle\psi(t_0)|\mathcal{U}^\dagger(t, t_0)$. Differentiating this yields the von Neumann equation

$$\frac{\partial \rho(t)}{\partial t} = -i\left[H, \rho(t)\right]. \tag{2.7}$$

This is often referred to as the Schrödinger picture, in which the time evolution of the system is encoded within the density matirx, while the operators of observable remain time-independent. Alternatively, we may also formulate quantum mechanics with the time-dependence in the system operators, as in the *Heisenberg picture*, or a combination of the two, as in the *Interaction picture*.

Heisenberg picture

To define the Heisenberg picture, consider the time evolution of the expectation value of an observable $\hat{O}$, that is,

$$\left\langle \hat{O}(t) \right\rangle = \mathrm{tr}\left\{\hat{O}\rho(t)\right\} = \mathrm{tr}\left\{\hat{O}\mathcal{U}(t, t_0)\rho(t_0)\mathcal{U}^\dagger(t, t_0)\right\} = \mathrm{tr}\left\{\hat{O}(t)\rho(t_0)\right\}, \tag{2.8}$$

where we have used the cyclic invariance of the trace, and defined the operator in the Heisenberg picture as $\hat{O}(t) = \mathcal{U}^\dagger(t, t_0)\hat{O}(t_0)\mathcal{U}(t, t_0)$. In this picture, the state $\rho(t_0)$ is time-independent and is specified by the initial condition in the Schrödinger picture, where the Heisenberg and Schrödinger pictures coincide, the time evolution is then transferred to the Heisenberg operator, $\hat{O}(t)$. We can obtain an equation of motion for this operator by differentiating with respect to time, giving the Heisenberg equation

$$\frac{\partial \hat{O}(t)}{\partial t} = i[H, \hat{O}(t)] + \mathcal{U}^\dagger(t)\left(\frac{\partial \hat{O}}{\partial t}\right)\mathcal{U}(t), \tag{2.9}$$

If the Schrödinger picture operator $\hat{O}$ has no explicit time-dependence, then the derivative on the right hand side of Eq. (2.9) is zero.

Interaction picture

In many scenarios, both the Schrödinger and Heisenberg equations are challenging to solve analytically, as such we are often required to resort to perturbative treatments to find the time evolution of the system. This is often most easily formulated in *the interaction picture*.

Here, the system Hamiltonian is split into two parts $H = H_0 + H_I$, where H_0 is often straightforward to solve either analytically or numerically, while H_I contains terms that make the solution non-trivial, such as an interaction between a system and its many-body environment. We then define the interaction picture density operator as

$$\tilde{\rho}(t) = \mathcal{U}_0^\dagger(t, t_0)\rho(t)\mathcal{U}_0(t, t_0), \tag{2.10}$$

where $\mathcal{U}_0(t, t_0) = \exp\left(-iH_0(t - t_0)\right)$. Differentiating this state then gives

$$\frac{\partial\tilde{\rho}(t)}{\partial t} = i\left[H_0, \tilde{\rho}(t)\right] - i\mathcal{U}_0^\dagger(t, t_0)\left[H, \rho(t)\right]\mathcal{U}_0(t, t_0). \tag{2.11}$$

Since $\mathcal{U}_0^\dagger(t, t_0)H_0\mathcal{U}_0(t, t_0) = H_0$, and defining $H_I(t) = \mathcal{U}_0^\dagger(t, t_0)H_I\mathcal{U}_0(t, t_0)$, we can write the von-Neumann equation in the interaction picture as

$$\frac{\partial\tilde{\rho}(t)}{\partial t} = -i\left[H_I(t), \tilde{\rho}(t)\right]. \tag{2.12}$$

2.1.4 Composite systems

Central to much of the work in this thesis is the behaviour of composite quantum systems, that is, the dynamics of two or more interacting quantum systems. This often leads to the generation of non-local correlations between the sub-systems that cannot be described classically, referred to as quantum entanglement [3]. In this section we outline how composite quantum systems may be described in quantum mechanics.

Consider two non-interacting quantum systems $\mathcal{A}$ and $\mathcal{B}$, each in the pure state $|\psi_A\rangle \in \mathcal{H}_A$ and $|\psi_B\rangle \in \mathcal{H}_B$. The composite system may then be written as

$$|\Psi\rangle = |\psi_A\rangle \otimes |\psi_B\rangle \in \mathcal{H}_A \otimes \mathcal{H}_B, \tag{2.13}$$

where $\otimes$ denotes the tensor product between the two spaces. Naturally, the density matrix may be written as $\rho_{AB} = |\Psi\rangle\langle\Psi| = |\psi_A\rangle\langle\psi_A| \otimes |\psi_B\rangle\langle\psi_B|$. This is often referred to as a product state, where both subsystems are unaffected by the other and the state may be separated into the appropriate subspaces.

Not every state may be written in this separable form, e.g when systems $\mathcal{A}$ and $\mathcal{B}$ interact. Instead we may decompose the state as

$$|\Psi\rangle = \sum_{i,j} a_{i,j}|i_A, j_B\rangle, \tag{2.14}$$

where $|i_A, j_B\rangle = |i_A\rangle \otimes |j_B\rangle$ and $|i_A\rangle$ ($|i_B\rangle$) is an orthonormal basis for system $\mathcal{A}$ ($\mathcal{B}$). In

the density matrix picture we may write $\rho_{AB} = \sum_{i,j}\sum_{kl}\rho_{ij;kl}|i_A, j_B\rangle\langle k_A, l_B|$, where $\rho_{ij;kl} = \langle i_A, j_B|\Psi\rangle\langle\Psi|k_A, l_B\rangle$. When the coefficients $a_{i,j}$ cannot be written as $a_i^{(A)}a_j^{(B)}$ the state is said to be inseparable, or entangled.

We can consider the state of only subsystems $\mathcal{A}$, that is *the reduced state*, by taking a partial trace over the subsystem $\mathcal{B}$, that is,

$$\rho_A = \mathrm{tr}_B\,\rho_{AB} = \sum_{i,k}\sum_{jl}\rho_{ij;kl}\langle l_B|j_B\rangle|i_A\rangle\langle k_A| = \sum_{i,k}\sum_{j}\rho_{ij;kj}|i_A\rangle\langle k_A|. \tag{2.15}$$

If systems $\mathcal{A}$ and $\mathcal{B}$ are entangled, then the reduced state ρ_A is now mixed. To demonstrate this, consider the Bell state $|\psi_+\rangle = \frac{1}{\sqrt{2}}(|01\rangle + |10\rangle) \in \mathcal{H}_A \otimes \mathcal{H}_B$ [1], whose density operator is given by

$$\rho = |\psi_+\rangle\langle\psi_+| = \frac{1}{2}\left(|01\rangle\langle 01| + |01\rangle\langle 10| + |10\rangle\langle 01| + |10\rangle\langle 10|\right). \tag{2.16}$$

Taking a partial trace over subsystem $\mathcal{B}$ then gives $\rho_A = \frac{1}{2}(|0\rangle\langle 0| + |1\rangle\langle 1|)$, which has purity $P[\rho_A] = 1/2$, and is therefore maximally mixed. We call any entangled pure state *maximally entangled* if the reduced state for the subsystem is maximally mixed.

Mixed states also exhibit entanglement and non-local correlations, with the density operator given by $\rho = \sum_i p_i|\varphi_i\rangle\langle\varphi_i|$, where $|\varphi_i\rangle \in \mathcal{H}_A \otimes \mathcal{H}_B$, and p_i is the probability of preparing the state $|\varphi_i\rangle$. A separable state then naturally generalises to mixed states as

$$\rho = \sum_i p_i|\psi_i^A\rangle\langle\psi_i^A| \otimes |\psi_i^B\rangle\langle\psi_i^B| = \sum_i p_i\rho_i^A \otimes \rho_i^B, \tag{2.17}$$

where $\rho_i^A \in \mathcal{H}_A$ and $\rho_i^B \in \mathcal{H}_B$.

2.2 The master equation formalism

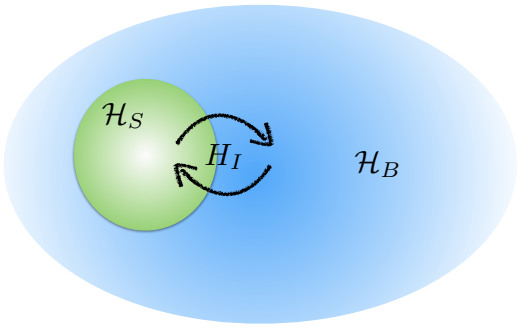


Figure 2.1: Pictorial representation of a quantum system coupled to an external environment.

Describing a quantum system interacting with a many-body environment is a challenging theoretical endeavour, with very few examples of exactly solvable systems [2, 4]. In the following we shall outline the master equation formalism, a powerful and intuitive technique for describing open quantum systems. Here, environmental degrees of freedom

are not tracked explicitly, but rather we consider only their influence on the behaviour of the system of interest.

To derive the master equation description for a given open system we consider a Hamiltonian H, which acts on the composite space $\mathcal{H}_S \otimes \mathcal{H}_B$, where $\mathcal{H}_S$ is the Hilbert space of the system and $\mathcal{H}_B$ its environment, as demonstrated pictorially in Fig 2.1. This Hamiltonian can then be decomposed as $H = H_S + H_B + H_I$, where the $H_S \in \mathcal{H}_S$ and $H_B \in \mathcal{H}_B$ are Hamiltonians describing the free evolution of the system and environment, respectively, and $H_I \in \mathcal{H}_S \otimes \mathcal{H}_B$ is the interaction Hamiltonian for the system and environment.

2.2.1 Projection operator techniques and the quantum master equation

To derive the master equation we shall make use of the projection operator method first outlined by Nakajima and Zwanzwig [2, 5–7]. Let $\chi(t) \in \mathcal{H}_S \otimes \mathcal{H}_B$ be the joint state of the system *and* environment. The time evolution of this state is generated by the Hamiltonian

$$H = H_0 + \alpha H_I, \tag{2.18}$$

where $H_0 = H_S + H_B$ is the free Hamiltonian of the system and environment, H_I is the interaction Hamiltonian, and α is a dimensionless coupling strength between the system and environment.

From the above Hamiltonian, we may write the time evolution of the state $\chi(t)$ in the interaction picture as

$$\frac{\partial \tilde{\chi}(t)}{\partial t} = -i\alpha \left[H_I(t), \tilde{\chi}(t)\right] \equiv \alpha \mathcal{L}(t)\tilde{\chi}(t), \tag{2.19}$$

where we have definied the Liouvillian super-operator $\mathcal{L}(t)$, and $\tilde{\chi}(t)$ is the interaction picture density operator. Rather than calculate the time evolution of the full state $\chi(t)$, which is often intractable for a system coupled to a many-body environment, we instead define a projection operator $\mathcal{P}$, such that

$$\mathcal{P}\chi(t) = \rho_s(t) \otimes \rho_B. \tag{2.20}$$

This operator projects the full density matrix onto a separable state of the reduced system $\rho_s(t) = \mathrm{tr}_B(\chi(t))$, and a reference state of the environment ρ_B, which we will define later. From the definition of $\mathcal{P}$ we may also define the projector $\mathcal{Q} = \mathbb{1} - \mathcal{P}$, which projects on to the irrelevant components of $\chi(t)$. These operators have the following general properties:

$$\mathcal{P}^2 = \mathcal{P}, \quad \mathcal{Q}^2 = \mathcal{Q}, \quad \text{and} \quad \mathcal{P}\mathcal{Q} = \mathcal{Q}\mathcal{P} = 0. \tag{2.21}$$

Applying these projectors to Eq. (2.19), we have

$$\frac{\partial}{\partial t}\mathcal{P}\tilde{\chi}(t) = \mathcal{P}\frac{\partial}{\partial t}\tilde{\chi}(t) = \alpha \mathcal{P}\mathcal{L}(t)\mathcal{P}\tilde{\chi}(t) + \alpha \mathcal{P}\mathcal{L}(t)\mathcal{Q}\tilde{\chi}(t), \tag{2.22}$$

and similarly for the non-separable components

$$\frac{\partial}{\partial t}\mathcal{Q}\tilde{\chi}(t) = \alpha\mathcal{Q}\mathcal{L}(t)\mathcal{P}\tilde{\chi}(t) + \alpha\mathcal{Q}\mathcal{L}(t)\mathcal{Q}\tilde{\chi}(t). \tag{2.23}$$

We can simplify this expression by considering an explicit form for the reference state of the environment, ρ_B. We shall take this state to be the Gibbs state, $\rho_B = \mathcal{Z}^{-1}\exp(-\beta H_B)$, where $\mathcal{Z} = \mathrm{tr}_B(\exp(-\beta H_B))$. This state has the useful property that odd moments with many interaction Hamiltonians are zero, that is,

$$\mathrm{tr}_B\left\{H_I(t_1)H_I(t_2)\ldots H_I(t_{2n+1})\rho_B\right\} = 0, \tag{2.24}$$

which leads to the relation

$$\mathcal{P}\mathcal{L}(t_1)\mathcal{L}(t_2)\ldots\mathcal{L}(t_{2n+1})\mathcal{P} = 0, \tag{2.25}$$

and will greatly simplify the form of the final master equation. The equation of motion for the separable components may thus be written as

$$\frac{\partial}{\partial t}\mathcal{P}\tilde{\chi}(t) = \alpha\mathcal{P}\mathcal{L}(t)\mathcal{Q}\tilde{\chi}(t). \tag{2.26}$$

To proceed, we start by finding the formal solution to Eq. (2.23):

$$\mathcal{Q}\tilde{\chi}(t) = G_{\mathcal{Q}}(t,t_0)\mathcal{Q}\tilde{\chi}(t_0) + \alpha\int_{t_0}^{t} ds G_{\mathcal{Q}}(t,s)\mathcal{Q}\mathcal{L}(s)\mathcal{P}\tilde{\chi}(s), \tag{2.27}$$

where we have defined the forward time propagator for the non-separable components as

$$G_{\mathcal{Q}}(t,s) = \overrightarrow{\mathcal{T}}\exp\left(\alpha\int_{s}^{t} ds'\mathcal{Q}\mathcal{L}(s')\right), \tag{2.28}$$

where $\overrightarrow{\mathcal{T}}$ is the forward propagating time-ordering operator. Substituting this into our expression for the separable components gives

$$\frac{\partial}{\partial t}\mathcal{P}\tilde{\chi}(t) = \alpha\mathcal{P}\mathcal{L}(t)G_{\mathcal{Q}}(t,t_0)\mathcal{Q}\tilde{\chi}(t_0) + \alpha^2\int_{t_0}^{t} ds\mathcal{P}\mathcal{L}(t)G_{\mathcal{Q}}(t,s)\mathcal{Q}\mathcal{L}(s)\mathcal{P}\tilde{\chi}(s). \tag{2.29}$$

This is the Nakajima-Zwanzwig equation [5–7] and describes the exact time evolution of the reduced system, thus it is as difficult to solve as the original von-Neumann equation. The first term in this equation is an inhomogeneous contribution caused by non-separable initial conditions [8], which vanishes for the factorising initial condition $\chi(t_0) = \rho_s(t_0)\otimes\rho_B$ since $\mathcal{Q}\chi(t_0) = 0$, leaving only the homogeneous term.

The right hand side of the Nakajima-Zwanzwig equation involves a convolution over all previous states of the density matrix. This often makes solving even approximations to Eq. (2.29) challenging. We can remove this explicit dependence on past states by defining

the backwards time propagator

$$\tilde{\chi}(s) = G(t,s)(\mathcal{P}+\mathcal{Q})\tilde{\chi}(t), \tag{2.30}$$

for $s < t$, where the propagator is defined as

$$G(t,s) = \overleftarrow{\mathcal{T}} \exp\left(-\alpha \int_s^t ds' \mathcal{L}(s')\right), \tag{2.31}$$

and $\overleftarrow{\mathcal{T}}$ is the backward propagating time-ordering operator. Substituting this expression into Eq. (2.32) gives

$$\mathcal{Q}\tilde{\chi}(t) = G_{\mathcal{Q}}(t,t_0)\mathcal{Q}\tilde{\chi}(t_0) + \alpha \int_{t_0}^t ds G_{\mathcal{Q}}(t,s)\mathcal{Q}\mathcal{L}(s)\mathcal{P}G(t,s)(\mathcal{P}+\mathcal{Q})\tilde{\chi}(s). \tag{2.32}$$

Now, defining the superoperator

$$\Sigma(t) = \alpha \int_{t_0}^t ds G_{\mathcal{Q}}(t,s)\mathcal{Q}\mathcal{L}(s)\mathcal{P}G(t,s), \tag{2.33}$$

we may write the non-separable components as

$$\mathcal{Q}\tilde{\chi}(t) = [1-\Sigma(t)]^{-1}\left(G_{\mathcal{Q}}(t,t_0)\mathcal{Q}\tilde{\chi}(t_0) + \Sigma(t)\mathcal{P}\tilde{\chi}(t)\right), \tag{2.34}$$

where the above solution requires the superoperator $\Sigma(t)$ to have a unique inverse. Substituting the above description into the master equation we obtain the time convolution-less (TCL) master equation

$$\frac{\partial}{\partial t}\mathcal{P}\tilde{\chi}(t) = \mathcal{K}(t)\mathcal{P}\tilde{\chi}(t) + \mathcal{I}(t)\mathcal{Q}\tilde{\chi}(t_0), \tag{2.35}$$

where we now have a time local generator,

$$\mathcal{K}(t) = \alpha\mathcal{P}\mathcal{L}(t)\left[1-\Sigma(t)\right]^{-1}\mathcal{P}, \tag{2.36}$$

and an inhomogeneous contribution,

$$\mathcal{I}(t) = \alpha\mathcal{P}\mathcal{L}(t)\left[1-\Sigma(t)\right]^{-1}G_{\mathcal{Q}}(t,t_0)\mathcal{Q}. \tag{2.37}$$

In deriving the TCL master equation we have made no approximation, thus Eq. (2.35) is just as difficult to solve as the original von-Neumann equation, with the influence of the environment (including both Markovian and non-Markovian dissipation) hidden in the generators $\mathcal{K}(t)$ and $\mathcal{I}(t)$. In the next subsection we shall expand these operators perturbatively, leading to a tractable master equation relevant to numerous physical systems.

Perturbation theory and the TCL master equation

To gain a tractable master equation we need to simplify the time dependent generators. To do this we shall expand the time convolution-less master equation with respect to the coupling parameter α. Both the inhomogeneous and homogeneous generators may be written as a power series in α such that

$$\mathcal{K}(t) = \sum_{n=1}^{\infty} \alpha^n \mathcal{K}_n(t) \qquad \text{and} \qquad \mathcal{I}(t) = \sum_{n=1}^{\infty} \alpha^n \mathcal{I}_n(t), \tag{2.38}$$

where $\mathcal{I}_n(t)$ and $\mathcal{K}_n(t)$ are the coefficients of the n^{th} power of α. Note that the summation starts at $n = 1$ as there is no zeroeth order contribution. Starting with the homogeneous generator, we first write $\Sigma(t)$ in terms of a geometric series

$$[1 - \Sigma(t)]^{-1} = \sum_{n=0}^{\infty} [\Sigma(t)]^n, \tag{2.39}$$

thus,

$$\mathcal{K}(t) = \alpha \sum_{n=0}^{\infty} \mathcal{P}\mathcal{L}(t)[\Sigma(t)]^n \mathcal{P}. \tag{2.40}$$

To find the forms of the coefficients $\mathcal{K}_n(t)$ we must also expand $\Sigma(t)$ as power series in α, that is $\Sigma(t) = \sum_{n=1}^{\infty} \alpha^n \Sigma_n(t)$. Thus, if we consider the first three terms in the power series for $\mathcal{K}(t)$, we have

$$\begin{aligned} \mathcal{K}_1(t) &= \mathcal{P}\mathcal{L}(t)\mathcal{P} = 0, \\ \mathcal{K}_2(t) &= \mathcal{P}\mathcal{L}(t)\Sigma_1(t)\mathcal{P}, \\ \mathcal{K}_3(t) &= \mathcal{P}\mathcal{L}(t)\left(\Sigma_1^2(t) + \Sigma_2(t)\right)\mathcal{P}. \end{aligned} \tag{2.41}$$

In order to then gain expressions for $\Sigma_n(t)$ we must expand both the forward, $G_{\mathcal{Q}}(t,s)$, and backwards, $G(t,s)$, propagators in terms of the coupling strength

$$\begin{aligned} G_{\mathcal{Q}}(t,s) &= \overrightarrow{\mathcal{T}} \exp\left(\alpha \int_s^t ds' \mathcal{Q}\mathcal{L}(s')\right), \\ &= \mathbb{1} + \alpha \int_s^t ds' \mathcal{Q}\mathcal{L}(s') + \alpha^2 \int_{s'}^t ds' \int_s^{s'} ds'' \mathcal{Q}\mathcal{L}(s')\mathcal{Q}\mathcal{L}(s'') + \ldots, \\ &= \mathbb{1} + \alpha G_{\mathcal{Q}}^{(1)}(t,s) + \alpha^2 G_{\mathcal{Q}}^{(2)}(t,s) + \ldots, \end{aligned}$$

$$\begin{aligned} G(t,s) &= \overleftarrow{\mathcal{T}} \exp\left(-\alpha \int_s^t ds' \mathcal{L}(s')\right), \\ &= \mathbb{1} - \alpha \int_s^t ds' \mathcal{L}(s') + \alpha^2 \int_{s'}^t ds' \int_s^{s'} ds'' \mathcal{L}(s'')\mathcal{L}(s') + \ldots, \\ &= \mathbb{1} + \alpha G^{(1)}(t,s) + \alpha^2 G^{(2)}(t,s) + \ldots, \end{aligned}$$

where the forward and reverse time-ordering operators have been incorporated in the choice of the limits of integration. This leads to the terms

$$\begin{aligned}\Sigma_1(t) &= \int_{t_0}^{t} ds \mathcal{Q}\mathcal{L}(s)\mathcal{P}, \\ \Sigma_2(t) &= \int_{t_0}^{t} ds \left(G_{\mathcal{Q}}^{(1)}(t,s)\mathcal{Q}\mathcal{L}(s)\mathcal{P} + \mathcal{Q}\mathcal{L}(s)\mathcal{P}G^{(1)}(t,s) \right).\end{aligned} \tag{2.42}$$

The TCL generators may therefore be written as

$$\mathcal{K}_2(t) = \int_{t_0}^{t} ds\ \mathcal{P}\mathcal{L}(t)\mathcal{L}(s)\mathcal{P} \qquad \text{and} \qquad \mathcal{K}_3(t) = 0, \tag{2.43}$$

where we have used the property that $\mathcal{Q} = 1 - \mathcal{P}$ and $\mathcal{P}\mathcal{Q} = 0$. Following this approach, we see that for the appropriate initial conditions all odd terms in the expansion are zero. A general form for higher order terms may be found using the cumulative expansion method [2], however, for most practical purposes the second order master equation is sufficient.

Using a similar method to the above, the inhomogeneous terms may also be written up to 2^{nd}-order as

$$\mathcal{I}_1(t) = \mathcal{P}\mathcal{L}(t)\mathcal{Q} \qquad \text{and} \qquad \mathcal{I}_2(t) = \int_{t_0}^{t} ds\ \mathcal{P}\mathcal{L}(t)\mathcal{L}(s)\mathcal{Q}. \tag{2.44}$$

Combining these terms, we obtain *the 2^{nd}-order inhomogeneous, time convolution-less master equation* in the interaction picture:

$$\frac{\partial}{\partial t}\mathcal{P}\tilde{\chi}(t) = \alpha\mathcal{P}\mathcal{L}(t)\mathcal{Q}\tilde{\chi}(t_0) + \alpha^2 \int_{t_0}^{t} ds\mathcal{P}\mathcal{L}(t)\mathcal{L}(s)\mathcal{Q}\tilde{\chi}(t_0) + \alpha^2 \int_{t_0}^{t} ds\ \mathcal{P}\mathcal{L}(t)\mathcal{L}(s)\mathcal{P}\tilde{\chi}(t). \tag{2.45}$$

Finally, by tracing over the environmental degrees of freedom, and recalling that $\mathcal{L}(t)\tilde{\chi}(t) = -i\left[H_I(t), \tilde{\chi}(t)\right]$, the master equation may then be written in the form:

$$\begin{aligned}\frac{\partial\tilde{\rho}_s(t)}{\partial t} =& -i\alpha\ \mathrm{tr}_B\left[H_I(t), \mathcal{Q}\tilde{\chi}(t_0)\right] - \alpha^2 \int_{t_0}^{t} ds\ \mathrm{tr}_B\left[H_I(t), \left[H_I(s), \mathcal{Q}\tilde{\chi}(t_0)\right]\right] \\ & - \alpha^2 \int_{t_0}^{t} ds\ \mathrm{tr}_B\left[H_I(t), \left[H_I(s), \tilde{\rho}_s(t)\otimes\rho_B\right]\right].\end{aligned} \tag{2.46}$$

Throughout this thesis we shall assume that the system and environment are initially uncorrelated such that the initial state is seperable, that is $\chi(t_0) = \rho_s(t_0)\otimes\rho_B(t_0)$, thus we have $\mathcal{Q}\chi(t_0) = \rho_s(t_0)\otimes(\rho_B(t_0) - \rho_{ref})$, where ρ_{ref} is the reference state of the environment. If we take both the reference and initial states to be the Gibbs state, then $\mathcal{Q}\chi(t_0) = 0$,

leaving the homogeneous second-order master equation:

$$\frac{\partial\tilde{\rho}_s(t)}{\partial t} = -\int_0^t ds\ \ \mathrm{tr}_B\left[H_I(t),[H_I(s),\tilde{\rho}_s(t)\otimes\rho_B]\right], \tag{2.47}$$

where we have set $t_0 = 0$, and absorbed the dimensionless coupling parameter α into the definition of the interaction Hamiltonian for convenience.

Strictly Markovian limit

In its current form the homogeneous master equation is an integro-differential equation referencing some initial state at $t = 0$. However, we can simplify Eq. (2.47) further by taking the full Markovian limit, which ensures that there are no explicit environmental memory effects, such that the future state of the system is affected only by its current state. We do this by making the substitution $s \to t - \tau$ in Eq. (2.47) and taking the limit of integration to infinity

$$\frac{\partial\tilde{\rho}_s(t)}{\partial t} = -\int_0^\infty d\tau\ \ \mathrm{tr}_B\left[H_I(t),[H_I(t-\tau),\tilde{\rho}_s(t)\otimes\rho_B]\right]. \tag{2.48}$$

This approximation is valid when the environment relaxes on a timescale much shorter than the system evolution.

Finally, we may write the master equation in the Schrödinger picture

$$\begin{aligned}\frac{\partial\rho_s(t)}{\partial t} =& \frac{\partial}{\partial t}\left\{\mathcal{U}_0(t,0)\tilde{\rho}_s(t)\mathcal{U}_0^\dagger(t,0)\right\} = -i\left[H_s,\rho_s(t)\right] + \mathcal{U}_0(t,0)\frac{\partial\tilde{\rho}_s(t)}{\partial t}\mathcal{U}_0^\dagger(t,0)\\ =& -i\left[H_s,\rho_s(t)\right] - \int_0^\infty d\tau\ \ \mathrm{tr}_B\left[H_I,[H_I(-\tau),\rho_s(t)\otimes\rho_B]\right] = \mathcal{L}_{ME}[\rho_s(t)],\end{aligned} \tag{2.49}$$

where $\mathcal{L}_{ME}$ is the super-operator representation of the master equation. This equation is often referred to as the Born-Markov master equation, describing the evolution of a system under the assumption of a static, memoryless environment.

2.2.2 The quantum regression theorem

Two-time correlation functions of the form $\langle A(t+\tau)B(t)\rangle$ are important in a range of situations in quantum mechanics. They can be used to find emission spectra from optically driven systems, extract counting statistics, as well as measure the indistinguishability of emitted photons. In this section we shall outline the quantum regression theorem, which allows one to draw a formal connection between the master equation and system two-time correlation functions [7, 9].

Consider the two-time correlation function

$$C(t,\tau) = \langle A(t+\tau)B(t)\rangle = \mathrm{tr}_{S+B}\left(A(t+\tau)B(t)\chi\right), \tag{2.50}$$

where A and B are operators acting on the Hilbert space of the system. We now define

the *reduced effective density operator*, $\Lambda(t,\tau)$, such that the two-time correlation function may be written as

$$C(t,\tau) = \mathrm{tr}_S\left(A\Lambda(t,\tau)\right), \tag{2.51}$$

where $\Lambda(t,\tau) = \mathrm{tr}_B(\mathcal{U}(\tau)B\chi(t)\mathcal{U}^\dagger(\tau))$, with $\mathcal{U}(t) = e^{-iHt}$ and H is the Hamiltonian of the system and environment.

From this expression we see that the calculation of the two-time correlation function amounts to finding the expectation value of A with respect to the effective density operator, $\Lambda(t,\tau)$. By differentiating $\Lambda(t,\tau)$ with respect to τ, we see that the effective density operator satisfies the same equation of motion as the reduced physical density operator. Thus we can apply the same prescription as outlined in Sec. 2.2.1 [7] to obtain the second order master equation

$$\frac{\partial\Lambda(t,\tau)}{\partial\tau} = \mathcal{L}_{ME}[\Lambda(t,\tau)], \tag{2.52}$$

with a form identical to that of the reduced physical density operator given in Eq. (2.49). The two-time correlation function $C(t,\tau)$ may then be found by solving this equation with the initial condition $\Lambda(t,0) = B\rho_S(t)$, and calculating the expectation value with respect to operator A.

2.2.3 The secular approximation

The master equation given in Eq. (2.49) describes (peturbatively) the evolution of a quantum system influenced by its environment. However, this master equation does not necessarily generate physical dynamics, that is, we have no guarantee that the reduced density operator of the system has unit trace or positive eigenvalues – a consequence of terminating the perturbative expansion of the master equation at second-order. In specific situations we can ensure the time evolution generated by a master equation remains physical for all time, by removing rapidly oscillating terms on the right hand side of Eq 2.49. This leads to a *completely positive, trace preserving* (CPTP) dynamical map, and thus a guaranteed physical evolution [2, 10].

Starting with the Born Markov master equation in the interaction picture we have:

$$\frac{\partial\tilde{\rho}_s(t)}{\partial t} = -\int_0^\infty d\tau\ \ \mathrm{tr}_B\left[H_I(t),\left[H_I(t-\tau),\tilde{\rho}_s(t)\otimes\rho_B\right]\right]. \tag{2.53}$$

We may now decompose the interaction Hamiltonian operators acting on the system and environment such that

$$H_I(t) = \sum_\alpha A_\alpha(t)\otimes B_\alpha(t),$$

where A_k is an operator acting on the system and B_k acts on the environment. Substituting this into Eq. (2.53) gives

$$\frac{\partial\tilde{\rho}_s(t)}{\partial t} = -\sum_{\alpha\beta}\int_0^\infty d\tau\left(\left[A_\alpha(t),A_\beta(t-\tau)\tilde{\rho}_s(t)\right]C_{\alpha\beta}(\tau) - \left[A_\alpha(t),\tilde{\rho}_s(t)A_\beta(t-\tau)\right]C_{\beta\alpha}(-\tau)\right), \tag{2.54}$$

where the bath correlation functions are defined such that $C_{\alpha\beta}(\tau) = \langle B_\alpha(\tau)B_\beta\rangle$, provided $[H_B, \rho_B] = 0$.

We can now formally move into the interaction picture by decomposing the system operators into eigenoperators, that is,

$$A_\alpha = \sum_\omega A_\alpha(\omega) = \sum_\omega A_\alpha^\dagger(\omega), \tag{2.55}$$

where the eigenoperators $A(\omega)$ and $A^\dagger(\omega)$ satisfy the commutation relations

$$[H_S, A_\alpha(\omega)] = -\omega A_\alpha(\omega) \quad \text{and} \quad [H_S, A_\alpha^\dagger(\omega)] = \omega A_\alpha^\dagger(\omega). \tag{2.56}$$

Substituting this into Eq. (2.54) we find

$$\begin{aligned}\frac{\partial\tilde{\rho}_S(t)}{\partial t} &= -\sum_{\omega\ \omega'}\sum_{\alpha\beta}\int_0^\infty d\tau\left(e^{i\omega' t}e^{-i\omega(t-\tau)}[A_\alpha^\dagger(\omega'), A_\beta(\omega)\tilde{\rho}_S(t)]C_{\alpha\beta}(\tau) + h.c.\right),\\ &= \sum_{\omega\ \omega'}\sum_{\alpha\beta}\left(e^{i(\omega'-\omega)t}\ \Gamma_{\alpha\beta}(\omega)(A_\beta(\omega)\tilde{\rho}_S(t)A_\alpha^\dagger(\omega') - A_\alpha^\dagger(\omega')A_\beta(\omega)\tilde{\rho}_S(t)) + h.c.\right),\end{aligned} \tag{2.57}$$

where $\Gamma_{\alpha\beta}(\omega) = \int_0^\infty d\tau e^{i\omega\tau}C_{\alpha\beta}(\tau)$, and *h.c.* denotes the hermitian conjugate. When the system evolves quickly compared to the relaxation time of the open system we are able to make the so-called *secular approximation* [2], where we discard terms where $\omega' \neq \omega$, since these terms lead to rapid oscillations that average out over the relaxation time of the system. Introducing $\gamma_{\alpha\beta}(\omega) = \Gamma_{\alpha\beta}(\omega) + \Gamma^*_{\beta\alpha}(\omega)$ and $S_{\alpha\beta}(\omega) = \frac{1}{2i}(\Gamma_{\alpha\beta}(\omega) - \Gamma^*_{\beta\alpha}(\omega))$ we obtain a master equation that guarantees physicality

$$\frac{\partial\tilde{\rho}_S(t)}{\partial t} = -i[H_{LS}, \rho_S(t)] + \mathcal{D}(\rho_S(t)), \tag{2.58}$$

where

$$H_{LS} = \sum_\omega\sum_{\alpha\beta} S_{\alpha\beta}(\omega)A_\alpha^\dagger(\omega)A_\beta(\omega), \tag{2.59}$$

and

$$\mathcal{D}(\rho_S(t)) = \sum_\omega\sum_{\alpha\beta}\gamma_{\alpha\beta}(\omega)\left(A_\beta(\omega)\rho_S(t)A_\alpha^\dagger(\omega) - \frac{1}{2}\{A_\alpha^\dagger(\omega)A_\beta(\omega), \rho_S(t)\}\right). \tag{2.60}$$

The term H_{LS} leads to an environmentally induced Lamb shift of the system's energy levels, while $\mathcal{D}(\rho_S(t))$ describes the dissipative dynamics of the system. We refer to this master equation as being in *Lindblad form*, and will be important in the discussion of the quantum optical master equation in Chapters 3 and 4. Eq. (2.58) can be trivially transformed into the Schrödinger picture to give:

$$\frac{\partial\rho_S(t)}{\partial t} = -i[H_S + H_{LS}, \rho_S(t)] + \mathcal{D}(\rho_S(t)). \tag{2.61}$$

The Lindblad master equation ensures that the system dynamics remain physical, however,

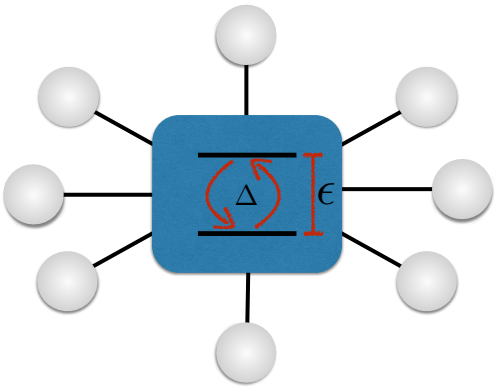


Figure 2.2: Graphical representation of the spin-boson model. A TLS with splitting ϵ and tunnelling rate Δ is coupled to a continuum of harmonic oscillators described by some spectral density $J(\omega)$.

there are many situations where the system relaxation does not occur on a time-scale short enough for the secular approximation to be valid, e.g. phonon processes in quantum dots. Although the dynamics predicted by the Lindblad master equation are completely positive in this regime, they are not necessarily an accurate representation of the system evolution. Therefore, in this situation we do not make a secular approximation, but instead keep all terms in the second-order master equation as given in Eq. (2.54).

2.3 The spin-boson model

Central to much of the work in this thesis is the canonical spin-boson model which describes a two-level system linearly coupled to a continuum of harmonic oscillators [4, 11]. This model is relevant to a variety of physical systems, including quantum dots (QDs), superconducting qubits, and molecular energy transport systems. As an example of the master equation approach, in the following section we shall outline the derivation of the weak coupling (Redfield) master equation for the spin-boson model, where the interaction between the system and environment is treated pertubatively.

2.3.1 Weak-coupling master equation

Consider a two level system (TLS) described by the orthonormal basis $\{|0\rangle, |1\rangle\}$, linearly coupled to a continuum of harmonic oscillators, a schematic is given in Fig. 2.2. The Hamiltonian for this system is given by $H = H_S + H_I + H_B$, where

$$H_S = \frac{\epsilon}{2}\sigma_z + \frac{\Delta}{2}\sigma_x, \quad H_B = \sum_k \nu_k b_k^\dagger b_k, \quad \text{and} \quad H_I = \sigma_z \sum_k g_k (b_k^\dagger + b_k). \tag{2.62}$$

Here $\sigma_z = |0\rangle\langle 0| - |1\rangle\langle 1|$ and $\sigma_x = |0\rangle\langle 1| + |1\rangle\langle 0|$ are Pauli operators, and $b_k^\dagger$ (b_k) is the creation (annihilation) operator of the k^{th} mode of the environment. The TLS is characterised by the bias ϵ, and the tunnelling rate Δ, while the k^{th} mode of the environment has frequency ν_k, and couples to the TLS with magnitude g_k. The coupling between the

system and environment is fully specified by the spectral density [2, 4]:

$$J(\omega) = \sum_k |g_k|^2 \delta(\omega - \omega_k), \tag{2.63}$$

which is a measure of the coupling strength between the system and environment weighted by the environmental density of states [2].

Using Eq. (2.49) we can immediately write the equation of motion for the reduced state of the TLS as:

$$\frac{\partial \rho_s(t)}{\partial t} = -i\left[H_S, \rho_s(t)\right] - \int_0^\infty d\tau \left(\left[\sigma_z, \sigma_z(-\tau)\rho_s(t)\right] C(\tau) - \left[\sigma_z, \rho_s(t)\sigma_z(-\tau)\right] C(-\tau)\right), \tag{2.64}$$

where,

$$\begin{aligned} C(\tau) =& \sum_k |g_k|^2 \ \mathrm{tr}_B \left\{ (b_k^\dagger e^{i\nu_k \tau} + b_k e^{-i\nu_k \tau})(b_k^\dagger + b_k)\rho_B \right\}, \\ =& \sum_k |g_k|^2 \left((2\bar{n}_k + 1)\cos\nu_k\tau - i\sin\nu_k\tau \right). \end{aligned} \tag{2.65}$$

Here, $\rho_B = \exp\left(-\beta \sum_k \nu_k b_k^\dagger b_k\right)/\mathcal{Z}$ is the canonical thermal state of the environment, with $\mathcal{Z} = \mathrm{tr}_B \exp\left(-\beta \sum_k \nu_k b_k^\dagger b_k\right)$ the partition function, and $\bar{n}_k = \langle b_k^\dagger b_k \rangle = (e^{\beta\nu_k} - 1)^{-1}$ is the thermal occupation of mode k. We can write this correlation function in terms of the spectral density by taking the continuum limit:

$$C(\tau) = \int_0^\infty d\omega J(\omega) \left(\coth\left(\frac{\beta\omega}{2}\right)\cos\omega\tau - i\sin\omega\tau \right). \tag{2.66}$$

Now that we have the correlation function we need to transform the system operator σ_z to the interaction picture. We can do this straighfowardly by writing the operator in the eigenbasis of the system Hamiltonian, such that:

$$\sigma_z(t) = \frac{1}{\eta}\left\{ \epsilon(|\psi_-\rangle\langle\psi_-| + |\psi_+\rangle\langle\psi_+|) - \Delta(|\psi_+\rangle\langle\psi_-|e^{-i\eta t} + |\psi_-\rangle\langle\psi_+|e^{i\eta t}) \right\}, \tag{2.67}$$

where $|\psi_i\rangle$ are the eigenvectors associated with the system Hamiltonian H_S, which have the form: $|\psi_\pm\rangle = \frac{1}{\sqrt{2\eta}}\left(\sqrt{\eta \pm \epsilon}|0\rangle \pm \sqrt{\eta \mp \epsilon}|1\rangle\right)$, with the associated eigenvalues $H_S|\psi_\pm\rangle = \lambda_\pm|\psi_\pm\rangle$, where $\lambda_\pm = \pm\eta/2$, and $\eta = \sqrt{\epsilon^2 + \Delta^2}$. We can therefore write the weak-coupling master equation as

$$\frac{\partial \rho_s(t)}{\partial t} = -i\left[H_S, \rho_s(t)\right] - \left[\sigma_z, Z\rho_s(t)\right] + \left[\sigma_z, \rho_s(t), Z^\dagger\right], \tag{2.68}$$

where we have defined the rate operator

$$Z = \frac{1}{\eta}\left\{ \epsilon(|\psi_-\rangle\langle\psi_-| - |\psi_+\rangle\langle\psi_+|)\Gamma(0) - \Delta\left(|\psi_+\rangle\langle\psi_-|\Gamma(\eta) + |\psi_-\rangle\langle\psi_+|\Gamma(-\eta)\right)\right\},$$

with $\Gamma(\omega) = \int_0^\infty d\tau e^{i\omega\tau} C(\tau)$. The imaginary part of this rate operator leads to frequency shifts in the system energies, while the real part give rise to dissipation. The rates can be resolved analytically using the Sokhotski integral [2]:

$$\int_0^\infty d\omega f(\omega) \int_0^\infty d\tau e^{\pm i(\omega-\lambda)\tau} = \pi \int_0^\infty d\omega f(\omega)\delta(\omega-\lambda) \pm i\mathcal{P}\left(\int_0^\infty d\omega \frac{f(\omega)}{\omega-\lambda}\right), \tag{2.69}$$

where $f(\omega)$ is a function of ω, and $\mathcal{P}$ denotes the Cauchy principal value integral. Thus, the one-sided Fourier transform of the correlation functions becomes:

$$\begin{aligned}\Gamma(\lambda) =& \frac{\pi}{2}\int_0^\infty J(\omega)\left[\left(\coth\left(\frac{\beta\omega}{2}\right)-1\right)\delta(\omega-\lambda) + \left(\coth\left(\frac{\beta\omega}{2}\right)+1\right)\delta(\omega+\lambda)\right]d\omega \\ &+ \frac{i\mathcal{P}}{2}\left[\int_0^\infty J(\omega)\left(\frac{\coth\left(\frac{\beta\omega}{2}\right)-1}{\omega-\lambda} - \frac{\coth\left(\frac{\beta\omega}{2}\right)+1}{\omega+\lambda}\right)d\omega\right].\end{aligned} \tag{2.70}$$

Resolving the delta function integrals, we have:

$$\Gamma(\lambda) = \begin{cases} \frac{\pi}{2}J(\lambda)\left(\coth\left(\frac{\beta\omega}{2}\right)-1\right) + \frac{i\mathcal{P}}{2}\left[\int_0^\infty J(\omega)\left(\frac{\coth\left(\frac{\beta\omega}{2}\right)-1}{\omega-\lambda} - \frac{\coth\left(\frac{\beta\omega}{2}\right)+1}{\omega+\lambda}\right)d\omega\right] & \text{for } \lambda > 0, \\ \frac{\pi}{2}\lim_{x\to 0}\left(J(x)\coth\left(\frac{\beta x}{2}\right)\right) - i\mathcal{P}\left[\int_0^\infty \frac{J(\omega)}{\omega}d\omega\right] & \text{for } \lambda = 0, \\ \frac{\pi}{2}J(|\lambda|)\left(\coth\left(\frac{\beta\omega}{2}\right)+1\right) + \frac{i\mathcal{P}}{2}\left[\int_0^\infty J(\omega)\left(\frac{\coth\left(\frac{\beta\omega}{2}\right)-1}{\omega+|\lambda|} - \frac{\coth\left(\frac{\beta\omega}{2}\right)+1}{\omega-|\lambda|}\right)d\omega\right] & \text{for } \lambda < 0. \end{cases}$$

2.3.2 System dynamics and the shortcomings of the weak coupling theory

To find the system dynamics from the weak coupling master equation we first need to specify a spectral density. As an example relevant to later sections, we choose a super-ohmic spectral density often used to describe phonon coupling in QDs [12–14]:

$$J(\omega) = \alpha\omega^3 e^{-\omega^2/\omega_c^2}, \tag{2.71}$$

where α is the coupling strength and ω_c is the cut-off frequency which specifies the peak of the spectral density.

Fig. 2.3 (Top) and (Left) show the TLS dynamics in the $\{|0\rangle, |1\rangle\}$ basis given by the weak coupling theory for coupling strengths relevant to QD systems, $\alpha = 0.025$ and 0.05 ps^2 respectively. Here, we see damped coherent oscillations, which in this case decay to the canonical thermal state $\rho_{ss} = \exp(-\beta H_s)/\operatorname{tr}_S(\exp(-\beta H_s))$. The damping rate of the coherent oscillations is determined by the system-environment coupling strength; at large coupling strengths, the oscillations are quickly suppressed, and the system thermalises on a shorter timescale than the weaker coupling.

Fig. 2.3 (Right) gives an example of when the weak coupling theory goes unphysical, predicting negative populations at large driving and coupling strengths ($\Delta = 2\pi$ ps^{-1}

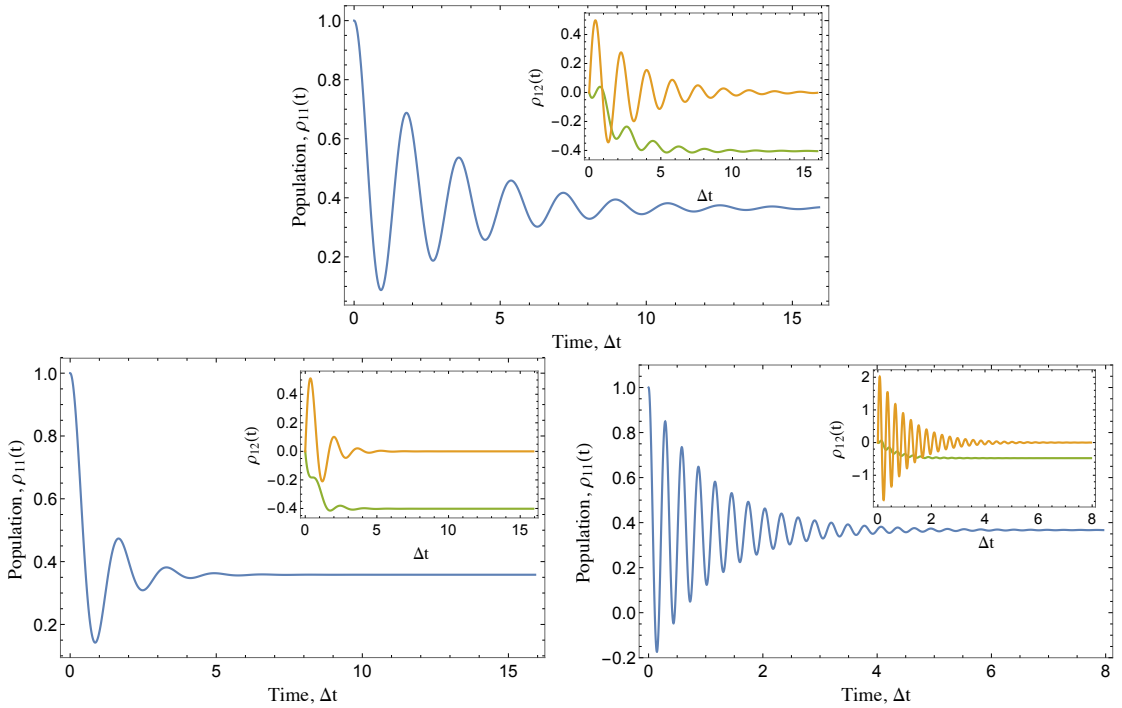


Figure 2.3: (Top, Left) Plots showing the dynamics of the population and the real and imaginary parts of the coherence (inset) of a TLS as predicted by the weak coupling theory for $\alpha = 0.025$ ps^2 and $\alpha = 0.05$ ps^2 respectively. The driving strength for these plots is $\Delta = \pi$ ps^{-1}. Right Plot showing the unphysical behaviour predicted by the weak coupling theory for $\Delta = 2\pi$ ps^{-1} and $\alpha = 5$ ps^2. Other parameters for these plots are $T = 10$ K, and $\omega_c = 2.2$ ps^{-1}.

and $\alpha = 5$ ps^{-1}). In this regime the master equation no longer preserves the positive definite nature of the density matrix leading to unphysical time evolution. By applying the secular approximation to the Refield master equation the possibility of negative probabilities would be removed, and the system dynamics would remain physical. However, in this situation the large system-environment coupling strength cannot be considered a perturbative parameter and the relaxation time of the system is of the same order as the environmental dynamics. This means that the secular master equation is not guaranteed to accurately capture the dynamical evolution of the system.

The situation described above is one of great importance for many examples of open quantum systems; a number of physical systems have been shown to couple strongly to their external environment, generating significant system-environment correlations that play a large role in both their transient dynamics, steady-states, and even optical properties. In these cases the Redfield (and secular Redfield) master equations are insufficient to describe the properties of the system. One of the primary goals of the present work is to develop master equation techniques capable of describing the dynamics of open quantum systems in just such regimes. In doing so we also highlight resultant phenomena that would not be present if a weak coupling treatment were to be used.

CHAPTER 3

EMISSION PROPERTIES OF OPTICALLY DRIVEN QUANTUM DOTS

3.1 Introduction

Semiconductor photonic devices have many potential application in both quantum and classical technologies. Several topical examples include on-demand single photon sources [15, 16], ultra-fast optical switching [17, 18], and optical schemes for quantum computation [19, 20]. Despite significant advances in the manufacturing of semiconductor nanostructures, there still remain several obstacles to overcome before scalable nano-photonic devices can be realised. Most significant for optical transitions are the dephasing and dissipation induced by strong interactions between the system and its host material, that is, the vibrational modes of the lattice.

One particularly prevalent example of semiconductor nanostructures are quantum dots (QDs). In their simplest form, these structures consist of two semiconductor materials with differing lattice constants, and consequently electronic band structures [21]. The lower band-gap material is grown epitaxially over the higher band gap material; the mismatch in lattice constants of the two materials then causes strain on the epitaxial layer, resulting in bunching of the growth substrate, which is then incased in another layer of the higher band-gap material [22]. The differing electrical properties of the two materials result in electrons within the QD becoming confined in all three spatial directions, resulting in a discrete energy spectrum in the dot region, much like those found in atoms [23, 24]. These energy levels may then be addressed optically, generating bound electron-hole pairs (known as excitons) within the QD.

The discrete energy structure combined with the solid-state nature of QDs make them a desirable system for quantum information applications. As such, a huge effort has been made to observe fundamental quantum optical phenomena in these systems, including photon anti-bunching [15, 23], the observation of Rabi oscillations [25–27] and the Mollow triplet [28, 29], and the measurement of two photon interference [30–32]. Despite the many similarities between QDs and atomic systems there remains an important distinction; the solid state nature of QDs leads to interactions between their excitonic degrees of freedom and the vibrational modes of the host material. Ramsay et al. [13, 14] demonstrated that longitudinal acoustic (LA) phonons are the principal source of decoherence in optically

active QDs under coherent control conditions. This has important implications for the nature of dissipation in QD systems; specifically, phonon-induced processes are sensitive to the energy scales over which the environmental spectral density is sampled, this leads to dissipation rates that are dependent on the underlying eigenstructure of the system. In particular, for classically driven QDs, the dephasing rates become sensitive to the driving strength. Thus, in order to accurately describe the excitation dynamics of a QD, the microscopic nature of the phonon environment must be accounted for [33].

In addition to the effects of phonons on the excitation dynamics of QDs, several theoretical studies have now shown that competition between the vibrational and electromagnetic environments can result in striking departures of the system emission properties in comparison to analogous atomic systems. Examples include asymmetric absorption spectrum [34], phonon induced population inversions [35, 36], and the revival of coherent scattering processes at strong driving [37]. In order to develop viable solid state photonic devices, it is thus essential to understand the effect environmental interactions have on the optical properties of such a system.

In this chapter we develop a generalised theory of quantum optics based on the variational polaron formalism [8, 38–40], to incorporate the effects of phonons on the optical properties of a classically driven QD. In particular, we demonstrate the qualitative differences caused by phonon processes in both the first and second-order correlation functions when compared to an analogous atomic system. These quantities have particular experimental importance, containing information on the spectral properties and photon measurement statistics used to characterise photonic systems.

Specifically, we will show that phonons have a significant effect on the balance of coherent and incoherent scattering from a QD. We highlight the sensitivity of phonon processes to the eigenstructure of the QD together with the failure of a phenomenological pure dephasing theory, demonstrating that in order to describe the emission properties of QDs accurately, one must account for the underlying microscopic behaviour of the phonon environment. Furthermore, we find that phonons can greatly alter photon measurement statistics from the QD, demonstrating that, in direct contrast to generally accepted notions of dissipation, increasing the system-environment coupling strength or temperature can in fact enhance the visibility of two photon interference in Hong-Ou-Mandel experiments [41] due to the renormalisation of system energy scales through phonon interactions.

3.2 The classically driven atom

In order to determine the effect phonon interactions have on the emission properties of a QD, we shall compare the full phonon theory (i.e. the variational polaron theory) with the canonical quantum optics example of a classically driven atom. We shall assume that the atom is driven by a continuous-wave (CW) source, and is subject to pure dephasing noise, which we shall include phenomenologically in our theoretical description.

Consider a two level atom with an excited state $|e\rangle$ of energy ω_e, and ground-state $|g\rangle$ with $\omega_g = 0$. The atom is driven by a CW classical light-source with frequency ω_l. Within

the dipole approximation, we may write the system Hamiltonian as [42]:

$$H_s(t) = \omega_e|e\rangle\langle e| - \hat{d}.\vec{E}(t). \tag{3.1}$$

Here $\hat{d}$ is the dipole operator of the atom and $\vec{E}(t) = |\vec{E}|\cos(\omega_l t)\,\hat{\boldsymbol{e}}$ is the time-dependent electric field strength of the driving field, where $|\vec{E}|$ is the electric field strength, and $\hat{\boldsymbol{e}}$ is its polarisation vector. By making use of dipole selection rules, we can decompose the dipole operator into the basis of the two level system as $\hat{d} = \langle e|\hat{d}|g\rangle(\sigma^\dagger + \sigma)$, with $\sigma = |g\rangle\langle e|$, the Hamiltonian may be written as:

$$H_s(t) = \omega_e\sigma^\dagger\sigma + \frac{\Omega}{2}(\sigma^\dagger + \sigma)\left(e^{i\omega_l t} + e^{-i\omega_l t}\right). \tag{3.2}$$

Here $\Omega = -2\langle e|\hat{d}.\hat{\boldsymbol{e}}|g\rangle|\vec{E}|$ is the Rabi frequency, which quantifies the coupling strength between the atom and the driving field.

In its current form, the time-dependence in the Hamiltonian makes theoretical treatments challenging, requiring sophisticated tools to accurately describe the resultant dynamics. We can, however, simplify the above Hamiltonian using the *rotating wave approximation* (RWA) [42]; this removes fast oscillating terms in the Hamiltonian that average to zero on timescales relevant to atomic systems. We start by transforming the driving term into the interaction picture with respect to the Hamiltonian $H_0 = \omega_e\sigma^\dagger\sigma$, such that:

$$\begin{aligned}\tilde{H}_I(t) &= e^{iH_0 t}\left[\frac{\Omega}{2}(\sigma^\dagger + \sigma)\left(e^{i\omega_l t} + e^{-i\omega_l t}\right)\right]e^{-iH_0 t} = \frac{\Omega}{2}(\sigma^\dagger e^{i\omega_e t} + \sigma e^{-i\omega_e t})\left(e^{i\omega_l t} + e^{-i\omega_l t}\right),\\ &= \frac{\Omega}{2}\left[\sigma^\dagger(e^{i(\omega_e-\omega_l)t} + e^{i(\omega_e+\omega_l)t}) + \sigma(e^{-i(\omega_e-\omega_l)t} + e^{-i(\omega_e+\omega_l)t})\right]).\end{aligned} \tag{3.3}$$

If we assume that the atom is driven close to resonance, then we may identify two distinct time-scales in this Hamiltonian – slow oscillating terms with frequencies $\pm(\omega_e - \omega_l)$ and rapidly oscillating terms with frequencies $\pm(\omega_e + \omega_l)$. Hence, in regimes that $(\omega_e + \omega_l) \gg (\omega_e - \omega_l)$, these rapidly oscillating terms average to zero over timescales important to atomic systems (and later quantum dots), allowing them to be neglected. After transforming back to the Schrödinger picture, this procedure yields the RWA Hamiltonian:

$$H_s(t) \approx \omega_e\sigma^\dagger\sigma + \frac{\Omega}{2}\left(\sigma e^{i\omega_l t} + \sigma^\dagger e^{-i\omega_l t}\right). \tag{3.4}$$

Finally, we can eliminate the time-dependence from the Hamiltonian completely by moving into a frame rotating with respect to the laser frequency. We do so using the unitary transformation $\mathcal{U}_{rot}(t) = e^{-i\omega_l\sigma^\dagger\sigma t}$, such that:

$$\begin{aligned}H_S &= \mathcal{U}^\dagger_{rot}(t)H_s\mathcal{U}_{rot}(t) - i\mathcal{U}^\dagger_{rot}(t)\frac{\partial\mathcal{U}_{rot}(t)}{\partial t},\\ &= \delta\sigma^\dagger\sigma + \frac{\Omega}{2}\sigma_x,\end{aligned} \tag{3.5}$$

where $\delta = \omega_e - \omega_l$ is the detuning between the atom and laser, and $\sigma_x = \sigma^\dagger + \sigma$. We

now have a time-independent Hamiltonian for an atom driven by a CW laser, written in a frame rotating with respect to the laser frequency.

3.2.1 The quantum optical master equation

In order to model the emission properties of an atom, we need to account for the interaction between the atom and an external quantised electromagnetic field, resulting in spontaneous emission processes. We shall do so by modelling the electromagnetic environment as a continuum of quantum harmonic oscillators and derive a second-order master equation in the light-matter coupling strength. The Hamiltonian for the light-matter interaction may be written as $H(t) = H_s(t) + H_I + H_B$, with $H_s(t) = \omega_e \sigma^\dagger \sigma + \frac{\Omega}{2}\left(\sigma e^{i\omega_l t} + \sigma^\dagger e^{-i\omega_l t}\right)$, and

$$H_I = \sum_k (f_k^* \sigma^\dagger a_k + f_k \sigma a_k^\dagger) \quad \text{and} \quad H_B = \sum_k \omega_k a_k^\dagger a_k, \tag{3.6}$$

where, by assuming that the atom couples to modes of the electromagnetic environment primarily about its resonance, we have made the RWA between the atom and field, which is a very good approximation for atomic systems typically discussed in the context of quantum optics. This assumption allows us to discard fast oscillating terms with frequency $\pm(\omega_e + \omega_k)$ in the interaction picture Hamiltonian. Writing the full Hamiltonian of the system and environment in a frame rotating with respect to the laser frequency we have:

$$\tilde{H} = \delta \sigma^\dagger \sigma + \frac{\Omega}{2}\sigma_x + \sum_k \left(f_k^* \sigma^\dagger a_k e^{-i\omega_l t} + f_k \sigma a_k^\dagger e^{i\omega_l t}\right) + \sum_k \omega_k a_k^\dagger a_k. \tag{3.7}$$

We now transform to the interaction picture:

$$\tilde{H}_I(t) = \mathcal{U}_0^\dagger(t) \left\{ \sum_k \left(f_k^* \sigma^\dagger a_k e^{-i\omega_l t} + f_k \sigma a_k^\dagger e^{i\omega_l t}\right) \right\} \mathcal{U}_0(t). \tag{3.8}$$

We may simplify this transformation by recognising that the spectral density of the electromagnetic field does not vary appreciably over the energy scales of the atom, therefore we can take the spectral density to be flat [9], i.e. $J(\omega) = \sum_k |f_k|^2 \delta(\omega - \omega_k) \approx \zeta$, where ζ is the coupling strength between the atom and the environment. This choice of spectrum allows us to define an approximate interaction picture transformation $\mathcal{U}_0(t) \approx \exp\left(-i\left(\delta\sigma^\dagger\sigma + \sum_k \omega_k a_k^\dagger a_k\right)t\right)$, as the electromagnetic environment (at zero temperature) does not now distinguish between eigenstates of the system. This choice of transformation simplifies the interaction picture Hamiltonian by removing terms oscillating with the laser frequency, such that,

$$\tilde{H}_I(t) = \sum_k \left(f_k^* \sigma^\dagger e^{i\omega_e t} a_k e^{-i\omega_k t} + f_k \sigma e^{-i\omega_e t} a_k^\dagger e^{i\omega_k t}\right), \tag{3.9}$$

and will automatically yield a master equation in Lindblad form. Notice that terms oscillating at the laser frequency have cancelled with the detuning terms in the interaction picture transformation. Partitioning the interaction Hamiltonian into system and envi-

ronment operators, we have $H_I(t) = \sum_\alpha A_\alpha(t) \otimes B_\alpha(t)$, where:

$$\begin{aligned} A_1(t) &= \sigma^\dagger e^{i\omega_e t} \qquad \text{and} \qquad B_1(t) = \sum_k f_k^* a_k e^{-i\omega_k t}, \\ A_2(t) &= \sigma e^{-i\omega_e t} \qquad \text{and} \qquad B_2(t) = \sum_k f_k a_k^\dagger e^{i\omega_k t}. \end{aligned} \tag{3.10}$$

We may now insert these terms into the definition of the interaction picture master equation given in Eq. 2.54:

$$\begin{aligned} \frac{\partial \tilde{\rho}_s(t)}{\partial t} &= -\sum_{\alpha\beta} \int_0^\infty d\tau \left([A_\alpha(t), A_\beta(t-\tau)\tilde{\rho}_s(t)]\, C_{\alpha\beta}(\tau) + h.c. \right), \\ &= -\int_0^\infty d\tau \left(e^{-i\omega_e \tau} \left[\sigma^\dagger, \sigma\tilde{\rho}_s(t)\right] C_{12}(\tau) + e^{i\omega_e \tau} \left[\sigma, \sigma^\dagger\tilde{\rho}_s(t)\right] C_{21}(\tau) + h.c. \right), \end{aligned} \tag{3.11}$$

where we have used $C_{11}(t) = C_{22}(t) = 0 \ \forall \ t$. As in Sec. 2.2.3, we may now define the one-sided Fourier transform of the bath correlation functions as $\Gamma_{ij}(\omega) = \int_0^\infty e^{i\omega t} C_{ij}(t) dt$, and write them in terms of the real and imaginary parts $\Gamma_{ij}(\omega) = \frac{\gamma_{ij}(\omega)}{2} + iS_{ij}(\omega)$, which yields:

$$\begin{aligned} \frac{\partial \tilde{\rho}_s(t)}{\partial t} &= -i \left(S_{21}(\omega_e) \left[\sigma^\dagger\sigma, \tilde{\rho}_s(t)\right] + S_{12}(-\omega_e) \left[\sigma\sigma^\dagger, \tilde{\rho}_s(t)\right] \right) \\ &\quad + \frac{\gamma_{21}(\omega_e)}{2} \left(2\sigma\tilde{\rho}_s(t)\sigma^\dagger - \left\{\sigma^\dagger\sigma, \tilde{\rho}_s(t)\right\} \right) + \frac{\gamma_{12}(-\omega_e)}{2} \left(2\sigma^\dagger\tilde{\rho}_s(t)\sigma - \left\{\sigma\sigma^\dagger, \tilde{\rho}_s(t)\right\} \right). \end{aligned}$$

The S_{jk} terms lead to environmentally induced shifts to the system energies, while γ_{jk} give the dissipation rates. Notice that the above master equation is automatically in Lindblad form, and thus generates trace-preserving, positive definite evolution of the system density operator. We can find analytic expressions for the rates in the above equation by evaluating the correlation functions in a similar fashion to the Redfield theory derived in Sec. 2.3.1:

$$\begin{aligned} C_{12}(t) &= \langle B_1(t) B_2 \rangle = \sum_k |f_k|^2 \langle a_k a_k^\dagger \rangle e^{-i\omega_k t} = \sum_k |f_k|^2 \left(\langle a_k^\dagger a_k \rangle + 1 \right) e^{-i\omega_k t}, \\ C_{21}(t) &= \langle B_2(t) B_1 \rangle = \sum_k |f_k|^2 \langle a_k^\dagger a_k \rangle e^{i\omega_k t}. \end{aligned} \tag{3.12}$$

In the continuum limit, the correlations take the form:

$$C_{12}(t) = \int_0^\infty J(\omega) \left(n(\omega) + 1 \right) e^{-i\omega t} d\omega \qquad \text{and} \qquad C_{21}(t) = \int_0^\infty J(\omega) n(\omega) e^{i\omega t} d\omega, \tag{3.13}$$

where $n(\omega) = (e^{\beta\omega} - 1)^{-1}$ is the occupation of the environment at frequency ω. The rates may be found using the formal relation given in Eq. 2.69, yielding the expressions:

$$\Gamma_{12}(\lambda) = \frac{\pi}{2}\zeta(n(\lambda)+1) - \frac{i\zeta}{2}\mathcal{P}\int_0^\infty \frac{n(\omega)+1}{\omega - \lambda} d\omega \quad \text{and} \quad \Gamma_{21}(\lambda) = \frac{\pi}{2}\zeta n(\lambda) + \frac{i\zeta}{2}\mathcal{P}\int_0^\infty \frac{n(\omega)}{\omega + \lambda} d\omega,$$

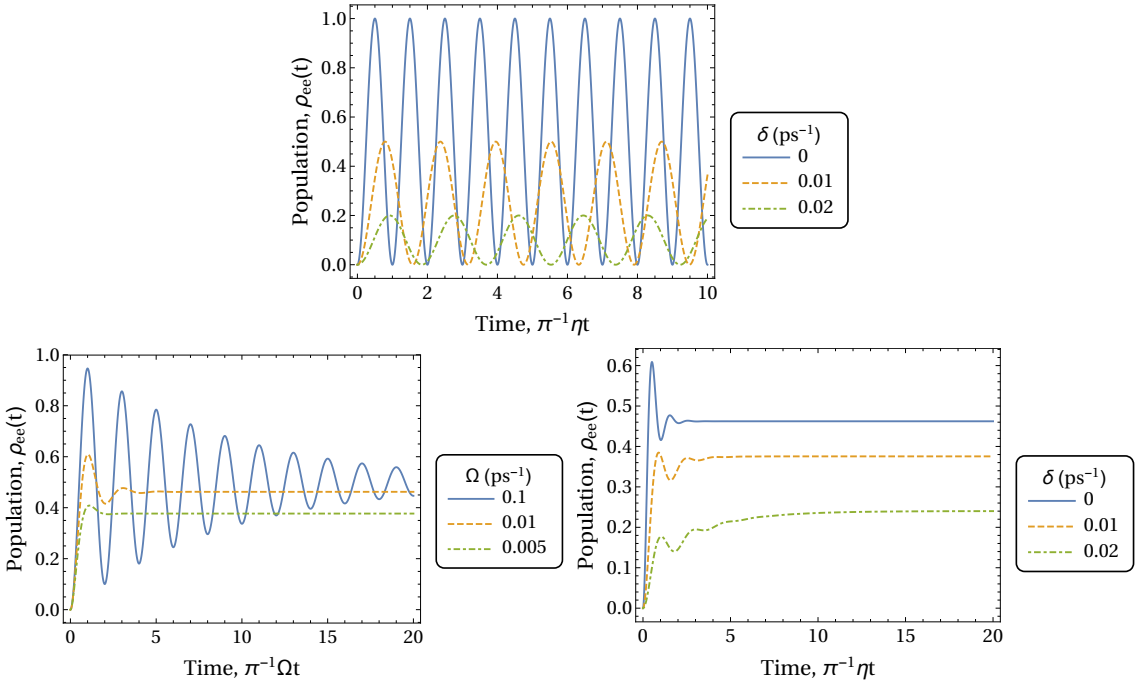


Figure 3.1: (Top) Unitary dynamics (i.e. $\gamma = \Gamma = 0$) for a two-level atom with $\Omega = 0.01$ ps^{-1} and various detunings plotted with scaled parameters. (Left) The dynamics of a resonantly driven two-level atom for various driving strengths, plotted in units of Rabi frequency. (Right) Plot showing the population dynamics for different detuning, with $\Omega = 0.01$ ps^{-1}. The time units are scaled using the generalised Rabi frequency $\eta = \sqrt{\delta^2 + \Omega^2}$. Other parameters for these plots are $\gamma^{-1} = 700$ ps and $\Gamma^{-1} = 400$ ps.

where we have used the flat spectral density $J(\omega) = \zeta$. For the case of atom in free space, we take a zero temperature limit of the field such that $n(\omega) = 0$. In this case the Lamb shift given by the complex part of the rate is negligible in comparison to the emission rate, thus in the Schrödinger picture the master equation takes the form:

$$\frac{\partial \rho_s(t)}{\partial t} = -i\left[H_s, \rho_s(t)\right] + \frac{\gamma}{2}\left(2\sigma\rho_s(t)\sigma^\dagger - \left\{\sigma^\dagger\sigma, \rho_s(t)\right\}\right), \tag{3.14}$$

which describes the spontaneous emission of a two-level atom with rate $\gamma = \pi\zeta/2$. A second phenomenological dissipator is often added to the RHS of Eq. 3.14 to describe dephasing processes, leading to additional decay of off-diagonal elements of the density operator while keeping the decay rate of diagonal terms unchanged[1]. We shall show later that, although commonly used in the literature, this pure dephasing master equation is insufficient to capture the effects of phonons processes in QDs. Incorporating this into the above equation, we have:

$$\frac{\partial \rho_s(t)}{\partial t} = -i\left[\delta\sigma^\dagger\sigma + \frac{\Omega}{2}, \rho_s(t)\right] + \frac{\gamma}{2}\left(2\sigma\rho_s(t)\sigma^\dagger - \left\{\sigma^\dagger\sigma, \rho_s(t)\right\}\right) + \Gamma\left(\sigma_z\rho_s(t)\sigma_z - \rho_s(t)\right), \tag{3.15}$$

[1]By simply summing Lindblad form dissipators on the RHS of the master equation, we are essentially assuming that the pure dephasing and spontaneous emission processes are entirely uncorrelated noise processes, and are associated to very different energy scales (in this case optical losses of an emitter compared to the fluctuations of the excited state energy level).

where Γ is the pure dephasing rate. Physically, one may think of the pure dephasing term as inducing random fluctuations in the excited state energy of the TLS. This leads to the accumulation of a random phase in the superposition between the excited and ground states of the TLS as the system undergoes Rabi oscillations. Upon taking an ensemble average of the system population dynamics one sees that this random phase leads to a damping of the Rabi oscillations, and thus coherence, of the TLS. This master equation is often referred to as the *quantum optical master equation*, and will be the starting point for our investigation of the emission characteristics of a classically driven atom.

Fig. 3.1 shows the population dynamics of the excited state of an atom initiated in its ground state. In all cases we see coherent oscillations induced by the driving field, as population is transferred between the ground and excited state. In the absence of dissipation [Fig. 3.1 (top)], the atom oscillates coherently with a period proportional to the generalised Rabi frequency $\eta = \sqrt{\delta^2 + \Omega^2}$; for resonant driving one sees complete population transfer between the ground and excited states. When the laser is detuned from the atomic splitting only partial Rabi oscillations occur, thus the atom remains mostly in its ground state.

When dissipation is included, the coherent oscillations are suppressed, vanishing altogether when $\gamma, \Gamma \gg \eta$. In this case the atom is not able to complete Rabi oscillations before spontaneous emission occurs, decreasing the population in the excited state as demonstrated in Fig. 3.1 (left). One also sees the steady state population decrease as a function of detuning in Fig. 3.1 (right), again because there are no longer full Rabi oscillations, thus the excited state is never fully populated.

3.2.2 Emission properties of a two-level atom

We saw in the previous section that the quantum optical master equation describes the evolution of the atomic degrees of freedom. However, in order to connect with experiments, we would like to relate the emission of the atom to the system properties. To do this we consider the electric field operator measured by a detector. Neglecting polarisation effects this may be written as:

$$\hat{\boldsymbol{E}}(t) = \hat{\boldsymbol{E}}^{(+)}(t) + \hat{\boldsymbol{E}}^{(-)}(t), \tag{3.16}$$

with the positive frequency component of the electric field defined as:

$$\hat{\boldsymbol{E}}^{(+)}(t) = \sum_k \mathcal{E}_k \hat{a}_k(t) \hat{\boldsymbol{e}}_k, \tag{3.17}$$

and the negative $\hat{\boldsymbol{E}}^{(-)}(t) = (\hat{\boldsymbol{E}}^{(+)}(t))^\dagger$. Here, $\mathcal{E}_k$ is the electric field strength, $\hat{\boldsymbol{e}}_k$ the unit vector for the electric field, and $\hat{a}_k$ is the annihilation operator of the k^{th}-mode of the environment. The intensity spectrum of the field may be found using the Wiener-Khinchin theorem [9, 42]:

$$I(\omega) = \int_0^\infty e^{-i\omega\tau} \left\langle \hat{\boldsymbol{E}}^{(-)}(t) \hat{\boldsymbol{E}}^{(+)}(t+\tau) \right\rangle d\tau. \tag{3.18}$$

We now wish to relate this intensity spectrum to atomic degrees of freedom tracked explicitly in the master equation. To do this, consider the Heisenberg equations of motion for the field operators:

$$\frac{\partial \hat{a}_k(t)}{\partial t} = -i\omega_k \hat{a}_k(t) - i f_k \tilde{\sigma}(t), \tag{3.19}$$

where for simplicity we have defined $\tilde{\sigma}(t) = e^{i\omega_l t}\sigma(t)$. We can integrate this formally using:

$$\frac{\partial}{\partial t}\left\{e^{i\omega_k t}\hat{a}_k(t)\right\} = \left\{i\omega_k \hat{a}_k(t) + \frac{\partial \hat{a}_k(t)}{\partial t}\right\} e^{i\omega_k t} = -i f_k \tilde{\sigma}(t) e^{i\omega_k t}, \tag{3.20}$$

such that,

$$a_k(t) = e^{-i\omega_k t} a_k(0) - i \int_0^t dt' f_k \tilde{\sigma}(t') e^{i\omega_k (t'-t)}, \tag{3.21}$$

where we have chosen an initial time $t_0 = 0$. Substituting this expression into the magnitude of the positive component of the electric field we have:

$$\hat{E}^{(+)}(t) = \sum_k \mathcal{E}_k \hat{a}_k(0) e^{-i\omega_k t} - i \sum_k \int_0^t dt' \mathcal{E}_k f_k \tilde{\sigma}(t') e^{i\omega_k (t'-t)}. \tag{3.22}$$

The first term in this expression is the free field contribution, i.e. the field in the absence of the atom. Since we assume the free field remains in the vacuum state, we may neglect this term when taking expectation values of the field operators. Now, taking the continuum limit we may write the electric field operator as:

$$\hat{E}^{(+)}(t) = -i \int_{-\infty}^{\infty} d\omega \int_0^t dt' \mathcal{E}(\omega) f(\omega) \tilde{\sigma}(t') e^{i\omega(t'-t)}, \tag{3.23}$$

where $\mathcal{E}(\omega)$ is the electric field strength over frequency ω, and $f(\omega)$ is the atom-field coupling strength. Notice that we have extended the limit of integration for frequency to $-\infty$, which is valid only when considering frequencies close to the atomic resonance. As in the previous section we may now assume that the coupling between the atom and field does not vary appreciably over the frequencies of the atom. This allows us to assume that both the coupling and electric field strengths are constant around the resonance of the atom, resulting in:

$$\begin{aligned} \hat{E}^{(+)}(t) &= -i\mathcal{E}\sqrt{\eta} \int_{-\infty}^{\infty} d\omega \int_0^t dt' \tilde{\sigma}(t') e^{i\omega(t'-t)} \\ &= -i\pi\mathcal{E}\sqrt{\eta} \int_0^t dt' \tilde{\sigma}(t')\delta(t'-t) = -i\mathcal{E}\sqrt{\frac{\pi\gamma}{2}}\tilde{\sigma}(t). \end{aligned} \tag{3.24}$$

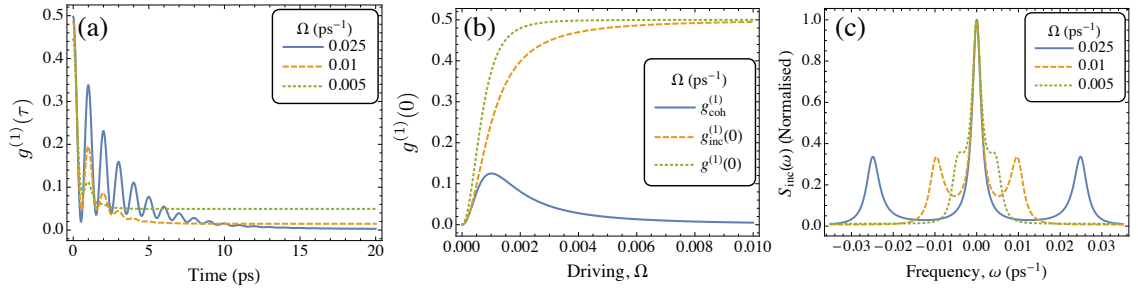


Figure 3.2: Figure showing (a) the dynamics of the first order correlation function for various driving strengths on resonance, (b) the balance of coherent and incoherent contributions as a function of driving strength at $\tau = 0$, and (c) the resonance fluorescence spectrum of the atomic system for various driving strengths normalised to the central peak, i.e. $S(\omega)/S(0)$. Other parameters are $\gamma^{-1} = 700$ ps and $\Gamma = 0$ ps^{-1}.

Thus the intensity spectrum in the long-time limit (steady-state) is given by $I(\omega) = I_s S(\omega)$, where I_s contains the normalisation factors, and

$$S(\omega) = \int_0^\infty g^{(1)}(\tau) e^{-i(\omega-\omega_l)\tau} d\tau, \tag{3.25}$$

gives the emission spectrum of the atom centred at the laser frequency in the long time limit, with the steady-state first order correlation function defined as $g^{(1)}(\tau) = \lim_{t\to\infty} \left\langle \sigma^\dagger(t)\sigma(t+\tau) \right\rangle$. To calculate this correlation function, we make use of the quantum regression theorem as outlined in Sec. 2.2.2. From Eq. 2.51, we have, $\left\langle \sigma^\dagger(t)\sigma(t+\tau) \right\rangle = \mathrm{tr}_s \left\{ \sigma^\dagger \Lambda(t,\tau) \right\}$,with the initial effective density matrix given as $\Lambda(t,\tau) = \sigma\rho_s(t)$.

Resonance Flourescence

The first-order correlation function has two significant spectral components corresponding to the transient oscillations and steady-state of the correlation function. The steady state contribution is associated with the *coherent emission* from the atom, or in other words, the elastic scattering of photons which have the same spectral properties as the incident light and are thus first order coherent[2] [42, 43]. Oscillations in the correlation function correspond to shifts in both the phase and frequency of the outgoing light from the driving field, and is often referred to as *inelastic* or *incoherent scattering*, as the scattered light is no longer first order coherent with the incident light.

We can thus split the correlation function into both coherent and incoherent contributions, such that $g^{(1)}(\tau) = g^{(1)}_{inc}(\tau) + g^{(1)}_{coh}$, where $g^{(1)}_{coh} = \lim_{\tau\to\infty} g^{(1)}(\tau) = |\langle\sigma_{ss}\rangle|^2$, and $\langle\sigma_{ss}\rangle$ is the steady state expectation value of σ. As $g^{(1)}_{coh}$ leads to a δ-function contribution at

[2]Interestingly, the elastically scattered photons are not coherent with the incident light to all orders; the interaction with the two level emitter (TLE) causes an anti-bunching effect, resulting in the light not being second-order coherent with the driving field.

the laser frequency in $S(\omega)$, we consider only the incoherent contribution to the spectrum:

$$S_{inc}(\omega) = \int_0^\infty \left(g^{(1)}(\tau) - g^{(1)}_{coh}\right) e^{-i(\omega-\omega_l)\tau} d\tau. \tag{3.26}$$

Analytic expressions for $g^{(1)}_{coh}$ and the initial condition for the quantum regression theorem can be obtained by solving the quantum optical master equation for its steady state, giving:

$$\begin{aligned}\rho_s(t\to\infty) =& \frac{1}{\gamma((\gamma+4\Gamma)^2+4\delta^2)+2\Omega^2(\gamma+4\Gamma)} \\ &\times \begin{pmatrix} \Omega^2(\gamma+4\Gamma) & -i\gamma\Omega(\gamma+4\Gamma)-2\gamma\delta\Omega \\ i\gamma\Omega(\gamma+4\Gamma)-2\gamma\delta\Omega & \gamma((\gamma+4\Gamma)^2+4\delta^2)+\Omega^2(\gamma+4\Gamma) \end{pmatrix}.\end{aligned} \tag{3.27}$$

For resonant driving, the coherent contribution to the spectrum is thus given by $g^{(1)}_{coh} = \gamma^2\Omega^2/(\gamma(\gamma+4\Gamma)+2\Omega^2)^2$, and the initial condition of the first-order correlation function is given by $\Lambda(0) = \sigma\rho_s(t\to\infty)$.

Fig. 3.2 (a) shows the first-order correlation function for increasing driving strength. Here we see that oscillations in the correlation function increase as a function of the driving strength, while the steady state value, and thus the coherent scattering contribution, decreases. This is shown explicitly in Fig. 3.2 (b) by the fraction of coherent and incoherent scattering at $\tau = 0$. The coherent contribution shows an increase at small driving strengths, reaching its maximum at $\sqrt{\gamma(\gamma+4\Gamma)/2}$, before being suppressed at large driving strengths, with the emission becoming dominated by incoherent scattering. At driving strengths smaller than the spontaneous emission rate, population is not raised to the excited state before being emitted, thus the light is elastically scattered, while for $\Omega > \sqrt{\gamma(\gamma+4\Gamma)/2}$ the system undergoes Rabi oscillations and thus scatters light incoherently. This is reflected in the dynamics of the correlation function shown in Fig. 3.2 (a), where at weak driving oscillations are heavily suppressed, and the dynamics are dominated by an exponential decay to the steady state.

The incoherent spectrum in Fig 3.2 (c) shows that at weak driving strengths there is a single peak centered about resonance. As the driving strength is increased one sees the emergence of a triple peak structure in the incoherent spectrum, often referred to as the *Mollow triplet* [28, 44], with the splitting of the peaks given by the driving strength Ω. On first sight, the underlying physical processes responsible for these peaks is not obvious, and would not be expected in the case of a driven classical dipole, where one would only ever observe a single Lorentzian peak at the dipole resonance, the height of which would change as a function of driving strength.

An intuitive explanation for the Mollow triplet can be found through the dressed state picture. Fig. 3.3 shows the eigenstates of a TLE coupled resonantly to a quantised electromagnetic field mode in the limit of large field occupations. Here we see that the degenerate eigenstates of the TLE and field mode are split by the driving strength Ω, which is synonymous with the coupling strength to the external field, forming the so-

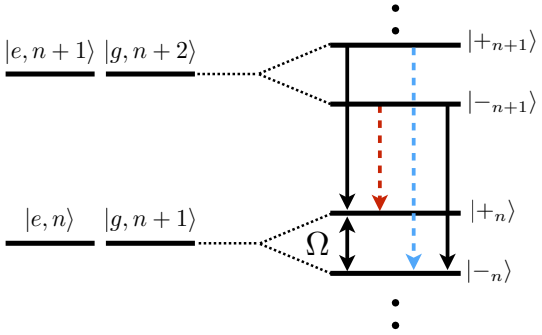


Figure 3.3: Figure demonstrating the mechanism leading to the emergence of the Mollow triplet. The solid black arrows correspond to emission at frequency ω_e, while the dashed lines represent emission at frequencies $\omega_e \pm \Omega$. On resonance, the light matter eigenstates are give by: $|\pm_n\rangle = (|g, n\rangle + |e, n-1\rangle)/\sqrt{2}$, which may be found by diagonalising the Jaynes-Cummings Hamiltonian.

called dressed states. This leads to four possible decay paths in which an optical photon may be emitted. The possible dipole transitions are $|\pm_{n+1}\rangle \to |\pm_n\rangle$ with frequency ω_e and $|\pm_{n+1}\rangle \to |\mp_n\rangle$ with frequency $\omega_e \pm \Omega$, which correspond to the locations of the peaks in the Mollow triplet.

3.3 Phonon effects in quantum dots

So far we have discussed the emission properties of atoms in the presence of a pure dephasing noise source. In this section we shall develop a formalism capable of capturing phonon effects in driven quantum dots and solid-state emitters in general. We subsequently investigate their role in the emission properties of these systems, demonstrating that phonons lead to significant deviations in the atomic behaviour discussed previously.

3.3.1 The variational polaron formalism

Consider a driven quantum dot coupled linearly to a bath of quantum harmonic oscillators, representing the vibrational lattice of the host material. As is well established in the literature, we shall model the QD as a two level system [13, 14, 21, 33, 45] with a ground state, $|0\rangle$, and excited state, $|X\rangle$, representing the absence and presence of an exciton respectively. For a QD driven by a CW laser with frequency ω_l, in the absence of spontaneous emission, we have the Hamiltonian:

$$H = \omega_x |X\rangle\langle X| + \Omega \cos(\omega_l t)\, \sigma_x + |X\rangle\langle X| \sum_k g_k (b_k^\dagger + b_k) + \sum_k \nu_k b_k^\dagger b_k. \tag{3.28}$$

Following a procedure identical to the one outlined in the previous section, we may simplify this Hamiltonian using the RWA and move to a frame rotating with respect to the laser frequency, ω_l, such that:

$$H = \delta \sigma^\dagger \sigma + \frac{\Omega}{2}\sigma_x + \sigma^\dagger \sigma \sum_k g_k (b_k^\dagger + b_k) + \sum_k \nu_k b_k^\dagger b_k, \tag{3.29}$$

where we have defined $\sigma = |0\rangle\langle X|$, and $\sigma_x = \sigma^\dagger + \sigma$. As in the atomic case $\delta = \omega_x - \omega_l$ is the detuning between the driving field and the QD splitting. The phonon environment is described by the creation and annihilation operators $b_k^\dagger$ and b_k respectively, with each mode of the environment coupling to the system with strength g_k, with corresponding frequency ν_k . For QDs, this coupling describes the displacement of the vibrational lattice of the host material as the charge configuration in the QD changes between its excited and ground states [20]. The coupling between the system and environment is fully characterised by the spectral density, for coupling between a QD and bulk LA-photons we take the phenomenological form [12–14]

$$J(\omega) = \alpha\omega^3 e^{-\omega^2/\omega_c^2}, \tag{3.30}$$

as was introduced in Sec. 2.3.2. Here ω_c is the cut-off frequency, and α is the coupling strength.

The solid-state nature of QDs often results in strong coupling between the excitonic degrees of freedom and the phonon environment. In this case the weak coupling master equation derived in Sec. 2.3.1 is insufficient to capture the interaction between the system and environment, often leading to inconsistent predictions or even unphysical system dynamics. We can, however, derive a master equation valid outside the weak coupling regime by applying a state dependent displacement operator, $\mathcal{U}_{pol} = \exp\left(\sigma^\dagger\sigma\sum_k \alpha_k(b_k^\dagger - b_k)\right) = |0\rangle\langle 0| + |X\rangle\langle X|\prod_k D(\alpha_k)$, to the Hamiltonian [8, 38–40, 46]. This unitary operator leads to a displacement of the environmental modes dependent on the state of the two level system, allowing one to derive a master equation which is *non-perturbative in the system environment coupling strength.* Applying this transformation to the system-environment Hamiltonian, we have:

$$H_p = \delta_r\sigma^\dagger\sigma + \frac{\Omega_r}{2}\sigma_x + \frac{\Omega}{2}\left(\sigma_x B_x + \sigma_y B_y\right) + \sigma^\dagger\sigma B_z + \sum_k \nu_k b_k^\dagger b_k, \tag{3.31}$$

where we have defined $\delta_r = \delta - \sum_k \alpha_k(2g_k - \nu_k\alpha_k)$, and $\Omega_r = \Omega B$, with the bath operators:

$$\begin{aligned} B_x &= \frac{1}{2}(B_+ + B_- - 2B), \\ B_y &= \frac{i}{2}(B_+ - B_-), \\ B_z &= \sum_k (g_k - \nu_k\alpha_k)(b_k^\dagger + b_k), \end{aligned} \tag{3.32}$$

where $B_\pm = \prod_k D(\pm\alpha_k)$, and the average displacement of the environment with respect to a thermal state is $B = \langle B_\pm\rangle = \exp\left(-\sum_k \alpha_k^2 \coth\left(\frac{\beta\nu_k}{2}\right)\right)$. In this transformed representation, the QD is dressed with vibrational modes of the environment. This leads to a shift in the QD energy eigenstates, and specifically results in a renormalisation of the Rabi frequency by the average displacement of the phonon environment.

We can eliminate the linear coupling to the phonon environment by choosing $\alpha_k =$

g_k/ν_k, reducing the Hamiltonian to what we shall refer to as *full polaron theory*. However, this approach is inappropriate when the dynamical timescales of the system approach the characteristic timescale of the environment (that is, the cut-off frequency). The master equation in the polaron representation is perturbative in the ratio of the driving strength and cut-off frequency of the environment (Ω/ω_c), relying on the vibrational modes of the environment to be instantaneously displaced as the QD is driven between its ground and excited states. Thus, in the strong driving limit, when Ω/ω_c is no longer peturbative, polaron theory can lead to inaccurate predictions for the properties of the system.

In contrast, we wish to develop the so-called *variational polaron theory*, where the magnitude of each displacement is kept as a variational parameter, chosen for each mode such that the free energy of the system is minimised. This will not only ensure that the system thermalises to an equilibrium state that minimises the free energy (and thus maximising the thermodynamic entropy), but also allows us to derive a master equation valid over a broad parameter regime [8, 40, 47]. However, finding an expression for the free energy F of a TLS governed by a spin-boson type Hamiltonian is extremely challenging. Instead, by treating the interaction Hamiltonian in the variational polaron frame as a perturbation, we shall minimise the Feynman-Bogoliubov upper bound A_B, which satisfies the condition $A_B \geq F$ [48], and takes the form [8, 38, 39]:

$$A_B = -\frac{1}{\beta}\ln\left\{\mathrm{tr}\left(e^{-\beta H_0}\right)\right\} + \langle H_I\rangle_{H_0} + \mathcal{O}(\langle H_I^2\rangle_{H_0}), \tag{3.33}$$

with,

$$\begin{aligned} H_0 &= \frac{\delta+R}{2}\sigma_z + \frac{R}{2}\mathbb{1} + \frac{\Omega_r}{2}\sigma_x + \sum_k \nu_k b_k^\dagger b_k, \\ H_I &= \frac{\Omega}{2}\left(\sigma_x B_x + \sigma_y B_y\right) + \sigma^\dagger \sigma B_z, \end{aligned} \tag{3.34}$$

and $R = \sum_k \alpha_k(2g_k - \nu_k\alpha_k)$. Here, the first term corresponds to the contribution of the free Hamiltonian H_0 to the free energy of the TLS. The second term $\langle H_I\rangle_{H_0}$ denotes the expectation value of H_I with respect to the canonical thermal state, and quantifies the effect of the system-environment interaction on the free energy to first order [48], which we have constructed to be zero. Now, choosing the displacement $\alpha_k = f_k/\nu_k$, where f_k minimises A_B, we obtain the expression:

$$\frac{\partial A_B}{\partial f_k} = \frac{1}{\mathrm{tr}\left(e^{-\beta H_0}\right)}\mathrm{tr}\left(\frac{\partial H_0}{\partial f_k}e^{-\beta H_0}\right) = 0, \tag{3.35}$$

which yields the variational functions $f_k = F(\nu_k)g_k$, with the form:

$$F(\nu_k) = \frac{\left(\eta_r - \delta_r \tanh\left(\frac{\beta\eta_r}{2}\right)\right)}{\eta_r - \tanh\left(\frac{\beta\eta_r}{2}\right)\left(\delta_r - \frac{\Omega_r^2}{2\nu_k}\coth\frac{\beta\nu_k}{2}\right)}. \tag{3.36}$$

Here $\eta_r = \sqrt{\delta_r^2 + \Omega_r^2}$ is the generalised Rabi frequency renormalised by the phonon environment. To carry-out the minimisation, we solve the equations for the renormalised Rabi

frequency and detunings self-consistently, which is most easily done in the continuum limit using the expressions:

$$\begin{aligned}\Omega_r &= \Omega \exp\left(-\frac{1}{2}\int_0^\infty \frac{J(\omega)F(\omega)}{\omega^2}\coth\left(\frac{\beta\omega}{2}\right)d\omega\right),\\ \delta_r &= \delta + \int_0^\infty \frac{J(\omega)F(\omega)}{\omega}(2-F(\omega))d\omega.\end{aligned} \tag{3.37}$$

This leads to a set of renormalised system parameters that minimise the free energy of the system. In the section that follows we shall give a detailed discussion of the advantages and limitations of this approach.

3.3.2 The variational polaron master equation and exciton dynamics

Phonon renormalisation of system energy scales

As mentioned in the previous section, in the polaron frame, the system energy scales become dependent on parameters of the environment. Both the resonance frequency of the QD and the Rabi frequency are renormalised by phonon terms, having a significant effect on the resultant exciton dynamics. For the rest of this chapter, we shall consider the resonance of the QD to be the polaron shifted resonance given by the full polaron theory, that is $\delta = -\int_0^\infty J(\omega)/\omega d\omega = -\sqrt{\pi}\alpha\omega_c^3/4$. This is consistent with an experimental procedure in which the resonance of the TLS is identified by sweeping a weak probe field across frequency, and taking the maximum absorption/flourescence to be resonance, which for a QD corresponds to the polaron shifted resonance.

In the variational frame, the Rabi frequency becomes renormalised by the average displacement of the environment, B, which in the continuum limit takes the form:

$$B = \langle B_\pm \rangle = \exp\left(-\frac{1}{2}\int_0^\infty \frac{J(\omega)F(\omega)^2}{\omega^2}\coth\left(\frac{\beta\omega}{2}\right)d\omega\right). \tag{3.38}$$

For the variational theory there are two important limits to be considered; at high temperatures and strong system-environment coupling strengths, the renormalised Rabi frequency Ω_r becomes exponentially suppressed. This results in a strong suppression of the coherent exciton dynamics, which become purely incoherent in the strong-coupling/high temperature regime [49]. In this case, the master equation will lead only to thermal relaxation. At small coupling and low temperature, the modes of the phonon environment are not strongly displaced, thus there is little renormalisation of the system energy scales. This results in the variational Hamiltonian reducing to the original spin-boson Hamiltonian, and is thus perturbative in the system-environment coupling strength.

Correlation functions

Before deriving an equation of motion to describe the reduced dynamics of the system, it is useful to consider the environmental correlation functions that will play a major role in the derivation. A detailed derivation of the variational correlation functions can be found in Appendix A, however, in the continuum limit we have:

$$\begin{aligned}
\Lambda_{xx}(t) &= \langle B_x(t)B_x\rangle = \frac{1}{2}\left(C(t)+G(t)-2B^2\right),\\
\Lambda_{yy}(t) &= \langle B_y(t)B_y\rangle = \frac{1}{2}\left(G(t)-C(t)\right),\\
\Lambda_{yz}(t) &= -2B\int_0^\infty \frac{J(\omega)(1-F(\omega))F(\omega)}{\omega}\left(\sin\omega t\coth\left(\frac{\beta\omega}{2}\right)+i\cos\omega t\right)d\omega,\\
\Lambda_{zz}(t) &= \int_0^\infty J(\omega)(1-F(\omega))^2\left(\cos\omega t\coth\left(\frac{\beta\omega}{2}\right)-i\sin\omega t\right)d\omega,
\end{aligned} \tag{3.39}$$

with the two remaining cross terms $\Lambda_{xy}(t)=\Lambda_{xz}(t)=0$. Here we have defined the terms:

$$\begin{aligned}
C(t) &= \langle B_\pm(t)B_\pm\rangle = B\exp\left(-\int_0^\infty \frac{J(\omega)F(\omega)^2}{\omega^2}\left(\coth\left(\frac{\beta\omega}{2}\right)\cos\omega t-i\sin\omega t\right)d\omega\right),\\
G(t) &= \langle B_\pm(t)B_\mp\rangle = B\exp\left(\int_0^\infty \frac{J(\omega)F(\omega)^2}{\omega^2}\left(\coth\left(\frac{\beta\omega}{2}\right)\cos\omega t+i\sin\omega t\right)d\omega\right),
\end{aligned} \tag{3.40}$$

and we have used the standard expression for the two-time correlation functions of the environment given in Sec. 2.2.3. Unfortunately, for the QD spectral density given in Eq. 3.30, finding an analytic form for these integrals is challenging, thus, we opt to solve these expression numerically.

The variational master equation

From the above correlation functions and Eq. 2.53, we obtain a master equation of the form:

$$\begin{aligned}
\frac{\partial\rho_s(t)}{\partial t} =& -i\left[\delta_r\sigma^\dagger\sigma+\frac{\Omega_r}{2}\sigma_x,\rho_s(t)\right]-\int_0^\infty d\tau\left(\left[\sigma_z,\sigma_z(-\tau)\rho_s(t)\right]\Lambda_{zz}(\tau)+h.c\right)\\
&-\frac{\Omega^2}{4}\int_0^\infty d\tau\left(\left[\sigma_x,\sigma_x(-\tau)\rho_s(t)\right]\Lambda_{xx}(\tau)+\left[\sigma_y,\sigma_y(-\tau)\rho_s(t)\right]\Lambda_{yy}(\tau)+h.c\right)\\
&+\frac{i\Omega}{2}\int_0^\infty d\tau\left(\left\{\left[\sigma_y,\sigma_z(-\tau)\rho_s(t)\right]-\left[\sigma_z,\sigma_y(-\tau)\rho_s(t)\right]\right\}\Lambda'_{yz}(\tau)+h.c\right),\\
=& -i\left[\delta_r\sigma^\dagger\sigma+\frac{\Omega_r}{2}\sigma_x,\rho_s(t)\right]-\left(\left[\sigma^\dagger\sigma,\Theta_z\rho_s(t)\right]+\left[\rho_s(t)\Theta_z^\dagger,\sigma^\dagger\sigma\right]\right)\\
&-\frac{\Omega^2}{4}\left(\left[\sigma_x,\chi_x\rho_s(t)\right]+\left[\rho_s(t)\chi_x^\dagger,\sigma_x\right]+\left[\sigma_y,\chi_y\rho_s(t)\right]+\left[\rho_s(t)\chi_y^\dagger,\sigma_y\right]\right)\\
&+\frac{i\Omega}{2}\left(\left[\sigma_y,\Xi_z\rho_s(t)\right]-\left[\sigma^\dagger\sigma,\Xi_y\rho_s(t)\right]+\left[\rho_s(t)\Xi_y^\dagger,\sigma^\dagger\sigma\right]-\left[\rho_s(t)\Xi_z^\dagger,\sigma_y\right]\right),
\end{aligned} \tag{3.41}$$

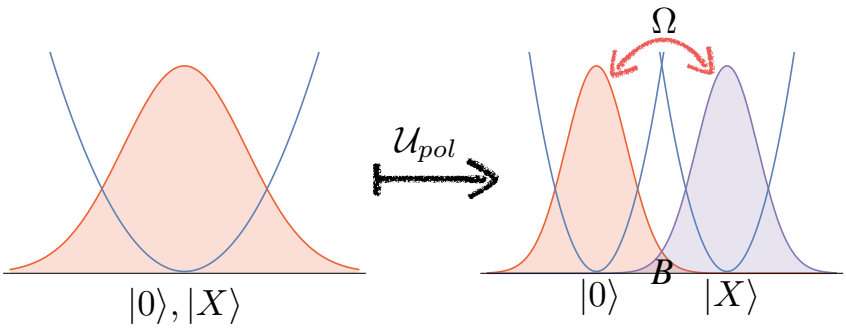


Figure 3.4: Schematic representation of the polaron transformation on a single mode of the environment. The transformation displaces the environment about an average B, with each potential well associated with a state of the QD. Reintroducing driving in the system Hamiltonian leads to tunnelling between these two wells.

where we have defined $\Lambda'_{yz}(\tau) = i\Lambda_{yz}(\tau)$ to satisfy the condition $\Lambda'_{yz}(-\tau) = (\Lambda'_{yz}(\tau))^*$. Unlike the electromagnetic environment describe in Sec. 3.2.1, the spectrum of the phonon environment varies appreciably over system energy scales, thus we must account for the full eigenstructure of the transformed system Hamiltonian when moving into the interaction picture, that is the Hamiltonian $H_s = \delta_r \sigma^\dagger \sigma + \frac{\Omega_r}{2}\sigma_x$, which has the eigenstates $|\psi_j\rangle$ and associated eigenvalues $\psi_\pm = \pm\eta_r/2$. Using the system eigenbasis, we can write the system rate operators such that

$$\begin{aligned}
\chi_\alpha &= \sum_{jk} \sigma_{jk} \int_0^\infty e^{-i\lambda_{jk}\tau} \Lambda_{xx}(\tau) d\tau |\psi_j\rangle\langle\psi_k|, \\
\Xi_\alpha &= \sum_{jk} \sigma_{jk} \int_0^\infty e^{-i\lambda_{jk}\tau} \Lambda'_{yz}(\tau) d\tau |\psi_j\rangle\langle\psi_k|, \\
\Theta_\alpha &= \sum_{jk} \sigma_{jk} \int_0^\infty e^{-i\lambda_{jk}\tau} \Lambda_{zz}(\tau) d\tau |\psi_j\rangle\langle\psi_k|,
\end{aligned} \tag{3.42}$$

where $\sigma_{jk} = \langle\psi_j|\sigma|\psi_k\rangle$, $\alpha \in \{\sigma_x, \sigma_y, \sigma^\dagger\sigma\}$, and $\lambda_{jk} = \psi_j - \psi_k$ is the difference in system eigenenergies.

Limitations of the variational polaron theory

Before proceeding any further, it is worth briefly describing the physics underlying the variational polaron formalism, and explore the various limits of the theory.

Consider first the limit in which the variational transformation gives no displacement to the modes of the environment, i.e. $F(\omega) \approx 0 \; \forall \; \omega$, which occurs when the cut-off frequency is comparable in magnitude to the system energy scale, and the system-environment coupling is weak. Here, the wave functions associated with each displacement have significant overlap with one another, meaning that it is not energetically favourable to displace modes of the environment [50, 51]. This leaves a single non-zero correlation function $\Lambda_{zz}(\tau)$, and no renormalisation of the system energy scales ($B = 1$), thus the variational

master equation reduces to the weak coupling case derived in Sec. 2.3.1 in which the system-environment coupling strength is treated perturbatively.

The opposite limit in which the environment is fully displaced (i.e. $F(\omega) = 1$) is often referred to as the full polaron theory. This limit is most easily understood in the context of the *independent boson model* [2, 11], that is, the QD Hamiltonian in the absence of driving ($\Omega = 0$). This is one of very few examples of exactly solvable open quantum systems models, and is diagonalised by the variational polaron transformation with displacement set to $\alpha_k = g_k/\nu_k$. The transformation displaces the modes of the environment contingent on the state of the QD, as demonstrated graphically in Fig 3.4, establishing two potential wells, distributed symmetrically about an average displacement B.

Upon reintroducing the driving field ($\Omega \neq 0$), the system-environment Hamiltonian may no longer be diagonalised by the polaron transformation, and the environment is displaced as the system coherently transitions between the ground and excited state. However, in the limit that the environment responds to the system dynamics instantaneously, specifically when the environmental cut-off is far greater than the driving strength ($\Omega/\omega_c \ll 1$), the polaron basis provides an ideal starting point for perturbation theory.

This naturally restricts the polaron master equation to regimes where the dominant modes of the environment are high frequency, that is, when the environmental response is fast in comparison to system time-scales. Outside of this regime, the bath no longer responds instantaneously to the tunnelling of the system, and the environmental wave function gets 'smeared out' between the two displaced wells, which in certain situations can generate non-classical states of the environment [50, 51]. Two important situations where this can occur are when the time-scales of the environment are of the same order as those of the system (e.g. excitonic energy transfer in molecular systems); and environments with sub-Ohmic and Ohmic[3] spectral densities, where the sluggish (low frequency) modes of the environmental are particularly important, leading to an infrared divergence in B. In both cases, terminating the polaron master equation at second order leads to an overestimation of the damping of coherent oscillations of the QD.

Including a variational parameter within the polaron transformation allows one to circumvent these issues somewhat. Instead of displacing the modes by the 'full-polaron amount', we fully displace the high-frequency modes of the environment, while leaving the low frequency modes un-displaced. This allows one to derive a 'hybridised' master equation, in which the low frequency modes are accounted for using a Redfield type treatment, while high frequency modes are treated using a polaron-like master equation. This greatly increases the regime of validity of the polaron master equation [8], allowing one to describe the dynamical behaviour of the system for Ohmic spectral densities, as well as when the environmental correlation time approaches that of system time-scales (i.e. when $\Omega \sim \omega_c$) due to the Redfield treatment of the low frequency modes. The variational master equation fails however, in regimes when sluggish modes of the environment are coupled strongly to the system, this is an extremely computationally challenging regime, due to the generation of significant system-environment correlations, and will be discussed

[3] A spectral density of the form $J(\omega) \propto \omega^s$ is referred to as super-Ohmic when $s > 1$, Ohmic when $s = 1$, and sub-Ohmic when $s < 1$.

in detail in Chapters 5 and 6.

Incorporating spontaneous emission

To investigate the emission properties of quantum dots, we must also consider the coupling to an electromagnetic environment in our theoretical description. To do so let us examine the light-matter interaction Hamiltonian in the polaron frame:

$$H_I^{EM}(t) = \sum_k \left(f_k^* \sigma^\dagger B_+ a_k e^{-i\omega_k t} + f_k \sigma B_- a_k^\dagger e^{i\omega_k t} \right), \tag{3.43}$$

where we now see the presence of phonon operators in the light-matter Hamiltonian. If we consider only spontaneous emission processes, i.e. when the photon field is at zero temperature, then the emission rate in the continuum limit is given by the Fourier transformed correlation function [37, 52]:

$$\gamma(\omega) = \mathrm{Re}\left[\int_0^\infty d\tau e^{-i\omega\tau} G(\tau) C_{12}(\tau) \right], \tag{3.44}$$

where $C_{12}(\tau) = \int_0^\infty d\omega J_{EM}(\omega) e^{i\omega\tau}$, is the correlation function for the EM field in the zero temperature limit, and $G(\tau)$ is the correlation function defined in Eq. 3.40.

Assuming once again that spectral density of the EM field does not vary appreciably over system energy scales, we may take the spectral density to be flat, $J_{EM}(\omega) \approx \zeta$. This allows us to resolve the frequency integral in the correlation function for the EM environment $C_{12}(\tau) \approx \pi\zeta\delta(\omega)/2 + i\mathcal{P}(\frac{1}{\tau})$, thus the spontaneous emission rate becomes:

$$\gamma(\omega) = \frac{\pi\zeta}{2} G(0) = \frac{\pi\zeta}{2}, \tag{3.45}$$

since $G(0) = 1$. Thus on timescales relevant to QDs, the spontaneous emission rate is not directly affected by phonon processes, and may be incorporated into the polaron master equation as a Lindblad-type dissipator [37, 52]. This is reliant on the electromagnetic environment have a flat spectral density, that is, for the spectral density to not vary appreciably over the over energy-scales of the QD. Thus the full master equation now takes the form:

$$\begin{aligned} \frac{\partial \rho_s(t)}{\partial t} =& -i\left[\delta_r \sigma^\dagger\sigma + \frac{\Omega_r}{2}\sigma_x, \rho_s(t)\right] - \left(\left[\sigma^\dagger\sigma, \Theta_z\rho_s(t)\right] + \left[\rho_s(t)\Theta_z^\dagger, \sigma^\dagger\sigma\right]\right) \\ &- \frac{\Omega^2}{4}\left([\sigma_x, \chi_x\rho_s(t)] + \left[\rho_s(t)\chi_x^\dagger, \sigma_x\right] + [\sigma_y, \chi_y\rho_s(t)] + \left[\rho_s(t)\chi_y^\dagger, \sigma_y\right]\right) \\ &+ \frac{i\Omega}{2}\left([\sigma_y, \Xi_z\rho_s(t)] - \left[\sigma^\dagger\sigma, \Xi_y\rho_s(t)\right] + \left[\rho_s(t)\Xi_y^\dagger, \sigma^\dagger\sigma\right] - \left[\rho_s(t)\Xi_z^\dagger, \sigma_y\right]\right) \\ &+ \frac{\gamma}{2}\left(2\sigma\rho_s(t)\sigma^\dagger - \left\{\sigma^\dagger\sigma, \rho_s(t)\right\}\right), \end{aligned} \tag{3.46}$$

where γ is the spontaneous emission rate.

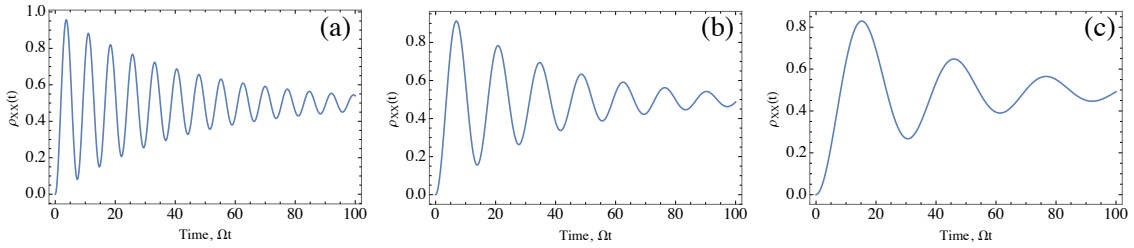


Figure 3.5: Plots showing the excited state dynamics for increasing system-environment coupling strength, highlighting the renormalisation of the Rabi frequency due to phonon renormalisation [33]. The system-environment coupling strengths are (a) $\alpha = 0.1$ ps^2, (b) $\alpha = 0.5$ ps^2, and (c) $\alpha = 1$ ps^2. Other parameters taken are representative of QD systems: $\Omega = 0.05$ ps^{-1}, $\gamma^{-1} = 700$ ps, and $\omega_c = 2.2$ ps^{-1}.

3.3.3 QD dynamics

Now that we have a form for the variational master equation we may model the effects of phonons on the QD dynamics. As mentioned previously, by considering the form of the Hamiltonian after the variational polaron transformation, one may gain some intuition as to the effect that phonons will have on the exciton dynamics. In Eq. 3.31 we see that the driving strength is renormalised by the average displacement of the phonon environment, such that $\Omega_r = \Omega B$. At either strong system-environment coupling strengths or high temperature, the average displacement of the environment, and thus the renormalised Rabi frequency, decreases [13]. This can be seen in Fig. 3.5, with the frequency of the coherent oscillations decreasing as a function of system-environment coupling strength, while the decay envelope of the population dynamics is set by the spontaneous emission rate and phonon-induced dissipation rates.

The effects of phonon processes may also be seen in the absorption spectrum of the QD, which for a two level system driven by a CW laser source is directly related to the steady-state population of the excited state [9, 42]. Fig. 3.6 (a) compares the absorption spectrum of both the phenomenological pure dephasing and variational polaron theories at low temperature ($T = 4$ K). The phenomenological theory predicts a sharp Lorentzian peak centred about atomic resonance, which may be found analytically as:

$$\langle \sigma^\dagger \sigma \rangle_{ss} = \frac{(\gamma + 4\Gamma)\Omega^2}{\gamma\left[4\delta^2 + (\gamma + 4\Gamma)^2\right] + 2\Omega^2(\gamma + 4\Gamma)}, \tag{3.47}$$

with a width proportional to the driving strength Ω as well as the spontaneous emission and dephasing rates. At resonance, driving above saturation ($\Omega \gg \gamma,\ \Gamma$), the steady state population of both the phonon and phenomenological theories is given by $\langle \sigma^\dagger \sigma \rangle|_{\delta=0} = \frac{1}{2}$, as can be seen in the phenomenological theory from Eq. 3.47. Here, the system undergoes damped Rabi oscillations, with no bias towards one particular state or the other in the long time limit.

Away from resonance the phonon theory no longer has a simple Lorentzian line-shape, showing additional sidebands, which are particularly clear for a blue detuned driving field ($\delta = \omega_X - \omega_l < 0$). These sidebands are caused by phonon assisted photon absorption,

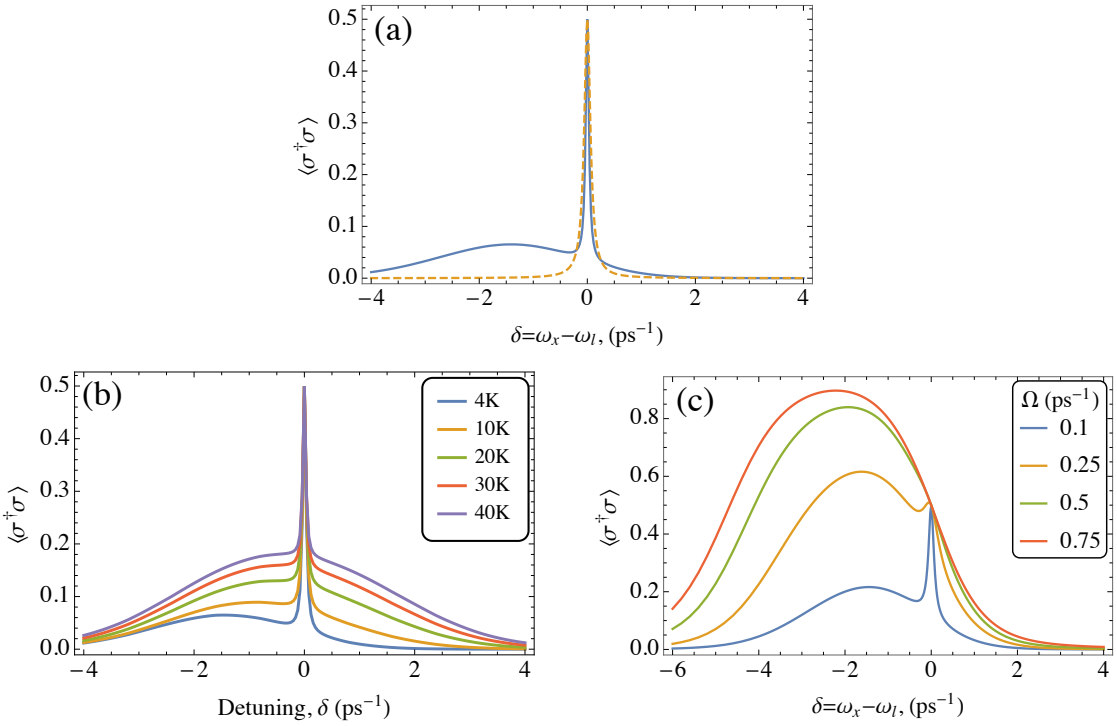


Figure 3.6: Plots comparing the steady state populations for (a) the phenomenological theory (dashed) and variational polaron master equation (solid) for $T = 4$ K, with the phenomenological dephasing rate $\Gamma = 1\times10^{-3}$ ps^{-1}; (b) variational theory with increasing temperature, notice how the line shape becomes more symmetric as phonon emission and absorption processes balance one another at high temperatures; and (c) shows a phonon induced population inversion at large driving strengths within the variational theory. Other parameters are: $\Omega = 0.05$ ps^{-1}, $\gamma^{-1} = 700$ ps, $\alpha = 0.027$ ps^2, and $\omega_c = 2.2$ ps^{-1}.

that is, when driven above resonance the QD may absorb a photon by simultaneously emitting a phonon into the environment with energy equal to the detuning of the photon, this is shown schematically in Fig. 3.7 (right). A similar process may also happen in reverse, whereby the excess energy required to absorb a red detuned photon ($\delta > 0$) may be gained by absorbing a phonon from the environment, as shown schematically in Fig. 3.7 (left). This inverse process is, however, suppressed at low temperature due to the low phonon occupation of the environment. Fig. 3.6 (b) demonstrates how these two processes balance one another at high temperatures leading to the emergence of a more symmetric line-shape, with broad phonon sidebands.

One interesting consequence of phonon assisted photon absorption is the potential to obtain a population inversion, i.e. more population in the excited state than the ground. In a traditional quantum optics set-up this is impossible for a TLS, the maximum excited state population occurs at resonant driving and can never exceed $\frac{1}{2}$ as the total emission processes (both spontaneous and stimulated) will always dominate over absorption, regardless of how strongly one drives the system.

When phonons are included in the description of the system we now have a new mechanism to populate the QD; phonon assisted absorption can produce significant exciton

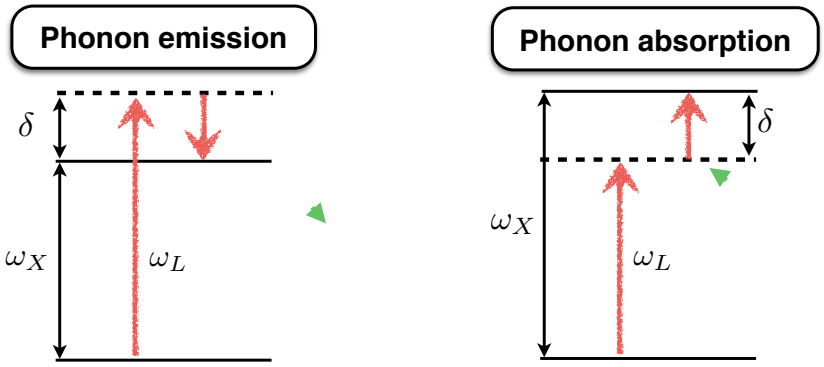


Figure 3.7: A schematic of phonon assisted photon absorption processes. (Left) A photon detuned above then exciton transition is absorbed by emitting a phonon into the environment. (Right) A photon at lower energy than the exciton transistion is absorbed by absorbing a phonon from the thermal environment

populations away from resonance, where spontaneous emission processes are suppressed. This reduces the total light emitted through spontaneous emission thus allowing a population inversion to occur at very strong driving strengths [36, 53], as shown in Fig. 3.6 (c).

3.4 Coherent and incoherent scattering from a QD

We shall now explore the effect that phonon interactions have on the emission properties of QDs, in particular focussing on the balance of coherent and incoherent emission. The balance of these two scattering processes plays a role in many of the proposed applications for QD devices; for example, single photon sources [15, 16]. Thus understanding the role that phonons have on the emission properties of QDs is essential in the development of photonic devices.

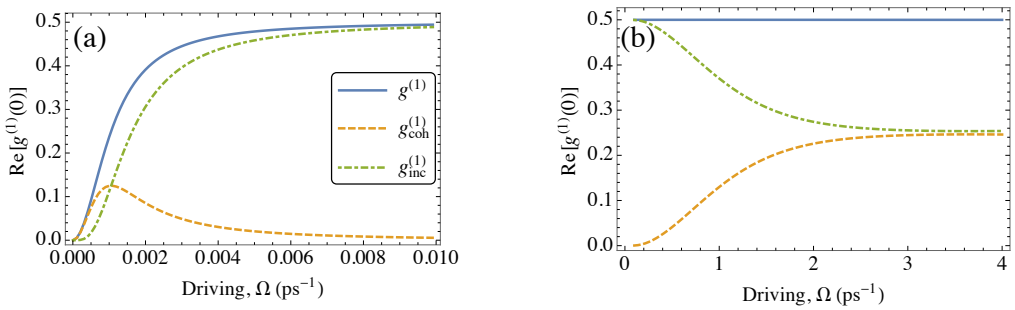


Figure 3.8: Driving dependence of the first-order correlation function in the presence of phonons for (a) weak and (b) strong driving [37]. At large driving strengths we see an enhancement of the coherent scattering, with incoherent and coherent emission processes balancing each other. Parameters used to generate these plots are $\gamma^{-1} = 700$ ps, $\alpha = 0.027$ ps^2, and $\omega_c = 2.2$ ps^{-1}.

3.4.1 Enhanced coherent scattering

In direct analogy to the pure dephasing model, to investigate the effect that phonon processes have on the balance of coherent and incoherent emission from a QD, we consider the driving dependence of the first-order correlation function at zero time delay. At weak driving the correlation function behaves similarly to the phenomenological case, as is shown in Fig. 3.8 – coherent scattering quickly tends to zero as the driving strength exceeds the QD spontaneous emission rate, with saturation occuring for $\Omega \sim 0.01$ ps^{-1}.

However, as was first shown in Ref. [37], for strong driving strengths we see a revival of the coherent scattering, contributing to approximately half of the light emitted from the QD for $\Omega \sim 3.5$ ps^{-1}. This is a significant departure from the atomic case, in which we expect the steady state coherence to remain zero above saturation, so what are the physical origins of this enhanced coherent scattering?

As for the Mollow triplet, we can answer this question by appealing to the physical intuition gained from the dressed state picture. In the presence of phonons we not only have transitions between the manifolds of the dressed states due to the EM environment, but also have phonon processes driving transitions between states within a single dressed state manifold. In other words, the phonons attempt to thermalise the system with respect to the dressed state basis, resulting in steady state coherence within the $\{|0\rangle, |X\rangle\}$ basis, and thus an increase in the coherent scattering (as $g^{(1)}_{coh} = |\langle\sigma\rangle_{ss}|^2$) [37]. This becomes particularly important when one drives the system strongly where the spectral density of the phonon environment is sampled closer to its peak, and thus the effective coupling to the phonons increases, such that phonon induced thermalisation occurs on a shorter timescale than optical processes.

3.4.2 The balance of coherent and incoherent scattering in QDs

Although heralding a departure from 'textbook' quantum optics, the driving strengths required to enter the enhanced coherent scattering regime are on the edge of what is currently experimentally attainable for CW excitation in QD systems. For example, the Rabi strengths typically used in resonance fluorescence are about $\Omega \sim 0.3$ ps^{-1} [29], which lies just at the onset of the enhance coherent scattering regime. We can, however, increase the effective Rabi frequency by detuning the driving field from the QD resonance, giving the generalised Rabi frequency $\eta_r = \sqrt{\delta_r^2 + \Omega_r^2}$. This allows one to reach large system energy scales simply by detuning from resonance, and hence sample the spectral density at larger values.

For the phenomenological theory ($\eta_r \to \eta = \sqrt{\delta^2 + \Omega^2}$), the fraction of coherently scattered light at zero time delay can be found analytically as:

$$\mathcal{F}_{coh} = \frac{g^{(1)}_{coh}}{g^{(1)}(0)} = \frac{\gamma^2}{\gamma + 4\Gamma} \frac{(\gamma + 4\Gamma)^2 + 4\delta^2}{\gamma((\gamma + 4\Gamma)^2 + 4\delta^2) + 2\Omega^2(\gamma + 4\Gamma)}, \tag{3.48}$$

with the incoherent fraction given by $\mathcal{F}_{inc} = 1 - \mathcal{F}_{coh}$.

In the limit of no pure dephasing, $\Gamma = 0$, this expression reduces to $\mathcal{F}_{coh} = \frac{\gamma^2 + 4\delta^2}{\gamma^2 + 4\delta^2 + 2\Omega^2}$.

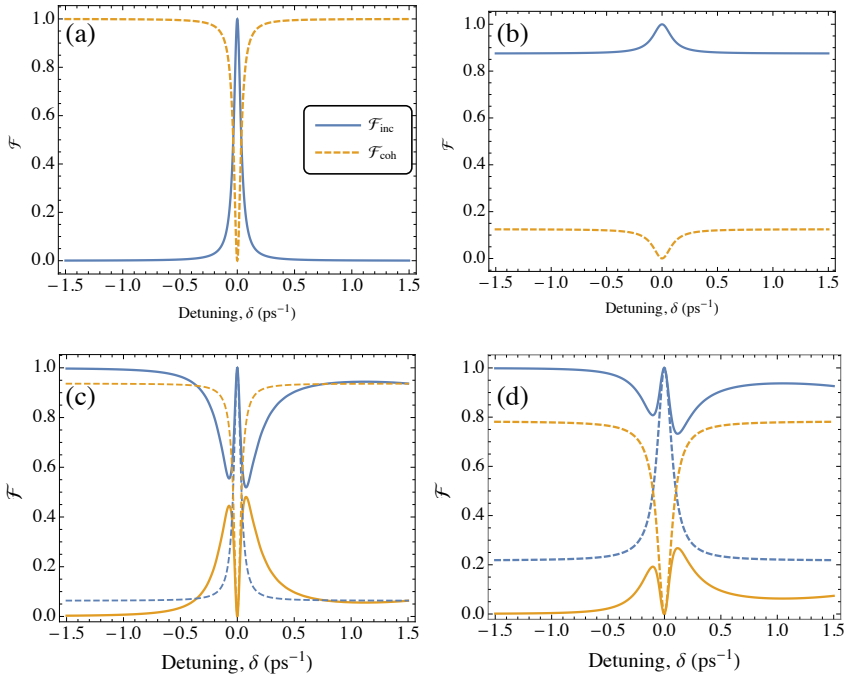


Figure 3.9: (a,b) Plots of the coherent and incoherent fraction within the pure dephasing model at $\Omega = 0.05$ ps^{-1}, with $\Gamma = 0$ (a) and 1/400 ps^{-1} (b). (c,d) Graphs showing the balance of coherent (yellow) to incoherent (blue) emission as a function of detuning for driving strengths $\Omega =$ 0.05 and 0.1 ps^{-1} respectively. The dashed curves show the fraction as predicted by the phenomenological theory, while the solid is the full (variational) phonon theory. Other parameters for these plots are $\gamma^{-1} = 700$ ps, $T = 4$ K, $\alpha = 0.027$ ps^2, and $\omega_c = 2.2$ ps^{-1}.

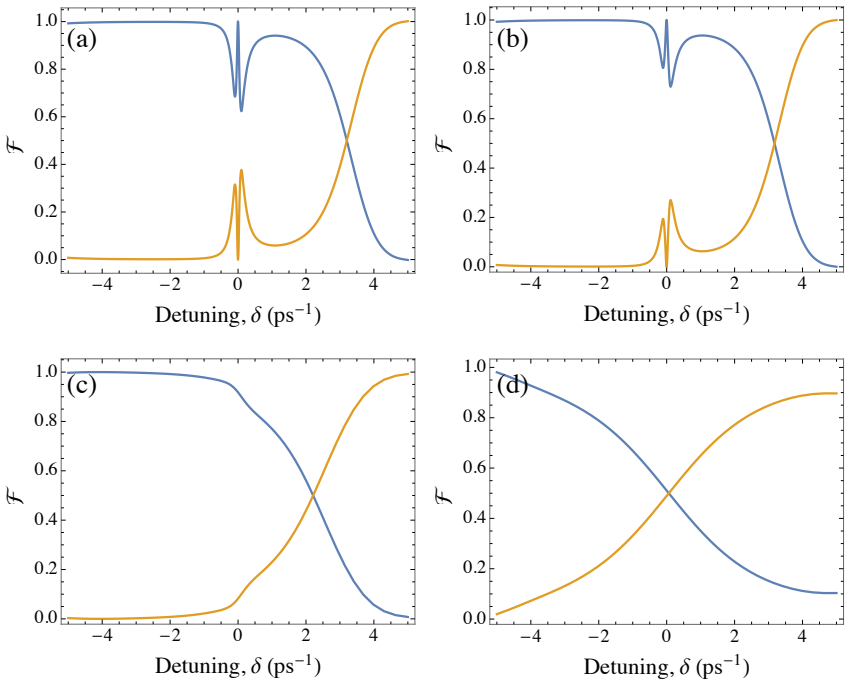


Figure 3.10: Graphs showing the fraction of coherent (yellow) to incoherently (blue) scattered light as a function of detuning within the variational polaron theory, for driving strength (a) $\Omega = 0.075$ ps^{-1}, (b) $\Omega = 0.1$ ps^{-1}, (c) $\Omega = 0.5$ ps^{-1}, and (d) $\Omega = 3$ ps^{-1}. Other parameters for these plots are $\gamma^{-1} = 700$ ps, $T = 4$ K, $\alpha = 0.027$ ps^2, and $\omega_c = 2.2$ ps^{-1}.

Above saturation ($\Omega \gg \gamma$), the incoherent fraction gives a symmetric Lorentzian peak about resonance, the width of which is proportional to the driving strength, with all light at resonance being incoherently scattered, as demonstrated in Fig 3.9 (a), which is consitent with Fig. 3.2 (b). Far off resonance ($\delta \gg \Omega, \gamma$), in the absence of pure dephasing, all scattered light is coherent $\mathcal{F}_{coh} \approx 1$ – in this regime the light simply scatters off the emitter without driving Rabi oscillations, thus keeping its phase coherence with the driving field.

For non-zero dephasing rates, the fraction of coherently scattered light is reduced. This is due to the dephasing suppressing the steady state coherence of the emitter, and thus the coherent contribution to the emission. This is demonstrated in Fig 3.9 (b), where we now see a significant reduction in coherently scattered light, even at modest dephasing rates. In fact, in the large dephasing limit ($\Gamma \gg \Omega, \gamma$), the steady state coherence is heavily suppressed and the coherent fraction of emitted radiation reduces to $\mathcal{F}_{coh} \approx 0$, leaving only incoherent emission.

When phonons are included, we see the emergence of significant structure in the coherent and incoherent fractions, even at weak driving. For resonant excitation and weak drivings, much like the atomic system, the emission of the QD is purely incoherent. In this regime, the phonon spectral density is sampled far from its peak, thus phonon processes are suppressed. As such, the QD undergoes full Rabi oscillations, and the emitted light is incoherent, as can be seen from Fig. 3.9 (c) and (d). However, away from resonance we observe an asymmetric feature not present in the atomic case; these striking differences can be attributed to a competition between energy scales of the system and environment. Just off resonance and at weak driving, phonon processes remain suppressed as the phonon spectral density is sampled far from its peak, hence the coherent emission increases following the pure dephasing model[4].

Unlike the pure dephasing model, however, the coherent emission is once again suppressed at larger detunings. Here the phonon spectral density is sampled closer to its peak, thus increasing the effective phonon coupling. This allows phonon processes to 'bridge' the energy difference between QD splitting and driving frequency, effectively tuning the QD back into resonance with the driving field, consequently allowing phonon assisted photon absorption, as is demonstrated schematically in Fig. 3.7. Furthermore, this process explains the asymmetry close to resonance – at low temperature the phonon absorption is suppressed due to low occupation numbers in the environment, this reduces phonon induced photon absorption for $\delta > 0$; when driving above resonance phonon assisted absorption comes into play (as shown in Fig. 3.6), thus leading to incoherent scattering processes.

Far from resonance, when the generalised Rabi frequency exceeds the environmental cut-off frequency (that is $\eta_r > \omega_c$), the phonon spectral density is sampled beyond its peak, reducing the effective phonon coupling and consequently phonon induced photon

[4]To compare like-for-like, the pure dephasing rate used in Fig. 3.9 (c) and (d) have been calculated using the expression $\Gamma = \frac{\Omega^2}{2}\mathrm{Re}\left[\int_0^\infty \mathrm{d}\tau \cos(\Omega\tau)\Lambda_{yy}(\tau)\right]$ which may be derived by taking the appropriate limits of the polaron master equation, as detailed in the supplementary information in Ref. [37].

absorption. From Fig. 3.10, this is particularly apparent at large positive detunings where there are virtually no phonon induced processes and therefore no photon absorption, leading to a revival of coherent scattering. For negative detuning, phonon emission is still possible (though suppressed) due to vacuum fluctuations in the phonon field, thus the majority of light remains incoherent – though at very large negative detunings (or strong driving strengths) there is an eventual suppression of the incoherent scattering as phonons become weakly coupled to then QD.

At very large driving strengths, phonon processes are suppressed at smaller detunings, resulting in the cross-over between coherent and incoherent scattering to occur at smaller detunings. This is highlighted when one enters the enhanced coherent scattering regime, where the effective coupling with the phonon environment is very strong, rapidly thermalising the QD with respect to the eigenstate basis, leading to a significant portion of the emission at resonance to be coherent.

3.5 Phonon effects in higher order correlation functions

3.5.1 Hong-Ou-Mandel, Hanbury-Brown Twiss, and $G^{(2)}$ measurements

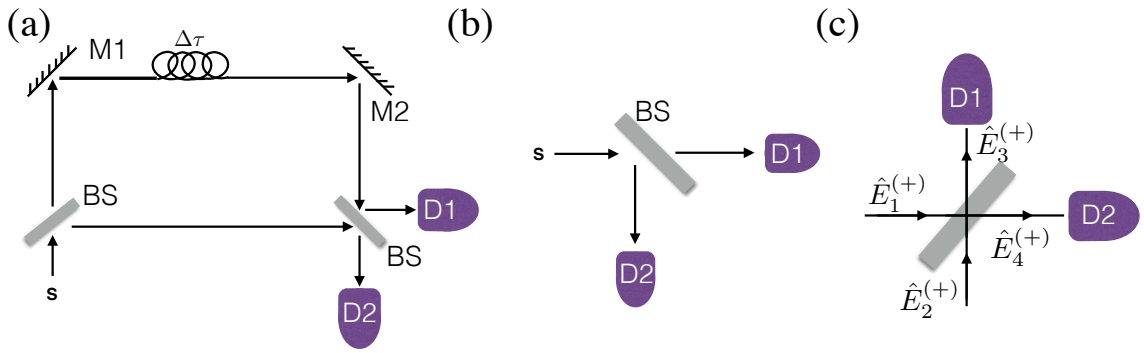


Figure 3.11: (a) Schematic picture of HOM apparatus for a continuously driven source. Photons from a source S enter the apparatus via a beam splitter (BS), one branch of the interferometer containing mirrors M1 and M2 is then delayed by $\Delta\tau$, before being incident on the final BS. Coincidence counts are then taken using the single photon detectors D1 and D2. (b) Shows HBT apparatus. Here a source S is incident on the BS, where detectors D1 and D2 measure multi-photon coincidences. (c) A beam splitter with incident modes $\hat{E}_1^{(+)}$, $\hat{E}_2^{(+)}$, producing output modes $\hat{E}_3^{(+)}$, $\hat{E}_4^{(+)}$ which are then measured using detectors D1 and D2.

In the previous section we saw that phonon processes lead to significant deviations in the first-order photon emission correlation function for a QD, when compared to an analogous atomic system. A natural question to ask is then how do phonons affect second-order correlations functions? The exact form of the second-order correlation function is context dependent. In this section we shall consider two cases which are particularly important for quantum information applications – Hong-Ou-Mandel [41] (HOM) and Hanbury-Brown Twiss [54–56] (HBT) experiments, as shown schematically in Fig. 3.11 (a) and (b) respec-

tively.

These experiments give insights into the measurement statistics of photons emitted from a source, information that is vital for many applications of photonic devices in quantum technologies. For example, the HBT experiment determines whether a source is bunched or anti-bunched, that is, whether or not it is a single photon source, a requirement for linear optical quantum computing [57, 58]. While, under certain conditions, the HOM experiment gives an indication of the indistinguishability of photons emitted from a source. This is particularly important in the generation of entangled states between photons and matter qubits [59].

3.5.2 Hong-Ou-Mandel experiments

Hong-Ou-Mandel experiments consider two photons incident on a 50:50 beam splitter; the photons are then measured using detectors placed at each of the output ports of the beam splitter, and the time-delay between detector clicks τ is recorded. As will be shown below, the measurements statistics of the HOM experiment show that there are no coincidence counts when the incident photons arrive simultaneously at the beam splitter [41]. In this section we consider the effect phonons have on the measurement statistics of the HOM experiment for a continuously driven QD, highlighting deviations from the behaviour predicted by the pure dephasing model and traditional quantum optics techniques.

Two-photon interference

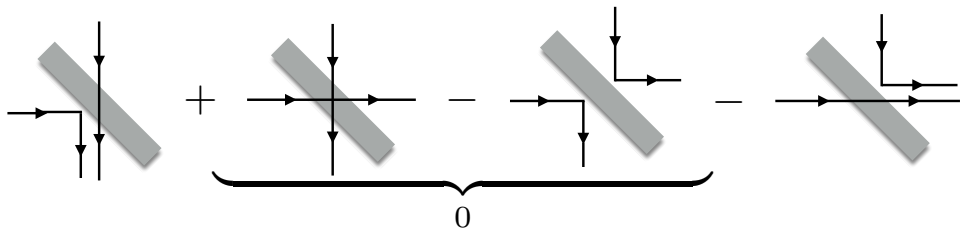
Consider the case of two photons that are simultaneously incident on a 50:50 beam splitter, with one photon at each input port. We can write this state in terms of creation and annihilation operators for the input field modes such that $|1_1, 1_2\rangle = \hat{a}_1^\dagger \hat{a}_2^\dagger |0\rangle$. We can relate the fields at the input ports to the output ports via the beam splitter transformation [42]:

$$\begin{pmatrix} \hat{E}_1^{(+)} \\ \hat{E}_2^{(+)} \end{pmatrix} = \frac{1}{\sqrt{2}} \begin{pmatrix} 1 & 1 \\ 1 & -1 \end{pmatrix} \begin{pmatrix} \hat{E}_3^{(+)} \\ \hat{E}_4^{(+)} \end{pmatrix}, \tag{3.49}$$

where for a single occupied field mode the electric field operator is given by $\hat{E}_j^{(+)} \propto a_j$. Thus, applying the beam splitter transformation to the field modes we get:

$$\hat{a}_1^\dagger \hat{a}_2^\dagger |0\rangle = \frac{1}{2}\left(b_1^\dagger b_1^\dagger + \cancel{\hat{b}_1^\dagger \hat{b}_2^\dagger} - \cancel{\hat{b}_2^\dagger \hat{b}_1^\dagger} - \hat{b}_2^\dagger \hat{b}_2^\dagger\right)|0\rangle = \frac{1}{\sqrt{2}}\left(|2,0\rangle - |0,2\rangle\right), \tag{3.50}$$

where $b_j^\dagger$ are the field operators for the output ports of the beam-splitter. Notice now that after the beam-splitter transformation the probability of measuring a single photon at each output port is zero. This is caused by incident photons accumulating a phase difference when they are reflected, resulting in the probability amplitude of detecting a single photon in each output port to cancel. This can be seen from the Feynman diagrams of the process:



where opposite phases cause the single-photon coincidence counts to cancel.

The presence of HOM interference is often considered to be a direct consequence of the indistinguishability of the incident photons, that is, contingent on the two incident photons having the same spatial and spectral properties. However, as pointed out by Legero et al. [60, 61], and subsequently Metz and Barrett [62], this is only true when one is operating in the bad detector limit, where the photon detectors have *no time resolution*. When the detectors are perfectly time resolved, then one will always measure zero coincidence counts at zero time-delay, regardless of whether the incident photons are indistinguishable (in the bad detector limit) or not.

In order to show this we follow the analysis of Legero et al. [60], and consider two photon wavepackets incident on the beam splitter shown in Fig 3.11 (c), with the electric field operators defined by:

$$E_1^{(+)}(t) = \phi_1(t)a_1 \qquad \text{and} \qquad E_2^{(+)}(t) = \phi_2(t)a_2, \tag{3.51}$$

where $\phi_i(t)$ describes both the envelope and phase evolution of the photon wavepacket incident at port i of the beam splitter. Consider the input state $|\Psi_{in}\rangle = |1_1, 1_2\rangle$, denoting a single photon incident at each input-port of the beam splitter. The probability of measuring a photon at detector 3 at time t, followed by a photon detected in mode 4 at $t + \tau$, is given by the correlation function:

$$\begin{aligned} G^{(2)}_{HOM}(t,\tau) =& \langle \Psi_{in}| E_3^{(-)}(t) E_4^{(-)}(t+\tau) E_4^{(+)}(t+\tau) E_3^{(+)}(t) |\Psi_{in}\rangle, \\ =& \langle 0| a_1 a_2 E_3^{(-)}(t) E_4^{(-)}(t+\tau) E_4^{(+)}(t+\tau) E_3^{(+)}(t) a_1^\dagger a_2^\dagger |0\rangle. \end{aligned} \tag{3.52}$$

Applying the beam splitter transformation we obtain an expression for the two time-correlation function:

$$G^{(2)}_{HOM}(t,\tau) = \frac{1}{4}|\phi_1(t+\tau)\phi_2(t) - \phi_2(t+\tau)\phi_1(t)|^2, \tag{3.53}$$

where we see that at zero time-delay between detector clicks, the coincidence probability vanishes regardless of the spatial or phase properties of the incident photons.

This means that for perfectly time-resolved measurements, the HOM dip will always be present and go to zero. Of course, for any situation of practical importance, we must account for finite detector response times, that is, the time taken for a detector to 'recover' after measuring the first photon. This consideration is particularly important for the case of a continuously driven emitter; in contrast to pulsed single photon sources, a driven emitter produces a train of photons, hence we must have time resolved measurements in order to distinguish between emission events.

The HOM two-time correlation function

To model a HOM experiment for a single continuously driven emitter, we consider a Mach-Zehnder interferometer, as shown schematically in Fig. 3.11 (a), one arm of which has a delay $\Delta\tau$ which is much greater than the photon coherence time to prevent single photon interference [31, 32, 63]. This allows us to consider the fields incident on the final beam splitter to be uncorrelated and mutually independent. Photon statistics are then collected using time resolved single photon detectors placed at the output ports of the final beam splitter.

As in the previous section, the probability of detecting a photon at both detectors 1 and 2 after some time delay τ is given by the two-time correlation function [60]:

$$G^{(2)}_{HOM}(t,\tau) = \langle \hat{E}_3^{(-)}(t)\hat{E}_4^{(-)}(t+\tau)\hat{E}_4^{(+)}(t+\tau)\hat{E}_3^{(+)}(t)\rangle, \tag{3.54}$$

where $\hat{E}_3^{(+)}(t)$ and $\hat{E}_4^{(+)}(t)$ are the positive frequency components on the fields incident on the detectors 1 and 2, as shown in Fig 3.11 (c). Relating the incident fields to the output fields using the beam splitter transformation, we have:

$$\begin{aligned} G^{(2)}_{HOM}(t,\tau) =& \left\langle \hat{E}_3^{(-)}(t)\hat{E}_4^{(-)}(t+\tau)\hat{E}_4^{(+)}(t+\tau)\hat{E}_3^{(+)}(t)\right\rangle, \\ =& \frac{1}{4}\left\langle (\hat{E}_1^{(-)}(t)+\hat{E}_2^{(-)}(t))(\hat{E}_1^{(-)}(t+\tau)-\hat{E}_2^{(-)}(t+\tau)) \right. \\ & \left. \times(\hat{E}_1^{(+)}(t+\tau)-\hat{E}_2^{(+)}(t+\tau))(\hat{E}_1^{(+)}(t)+\hat{E}_2^{(+)}(t))\right\rangle. \end{aligned} \tag{3.55}$$

Since the time-delay in one arm of interferometer allows us to treat the incident field modes as uncorrelated and independent, we can simplify the above expression by assuming that cross-terms in the correlation function factorises into the corresponding input fields, e.g. $\langle \hat{E}_1^{(+)}(t)\hat{E}_2^{(+)}(t+\tau)\hat{E}_2^{(-)}(t+\tau)\hat{E}_1^{(-)}(t)\rangle \rightarrow \langle \hat{E}_1^{(+)}(t)\hat{E}_1^{(-)}(t)\rangle\langle \hat{E}_2^{(+)}(t+\tau)\hat{E}_2^{(-)}(t+\tau)\rangle$. As outlined in Sec. 3.2.2, the electric field produced by a TLS can be directly related to the TLS operators, such that $\hat{E}^{(+)} \propto \sigma$, where σ is the lowering operator of the TLS. Thus, we can rewrite the HOM correlation function as:

$$\begin{aligned} G^{(2)}_{HOM}(\tau) \propto& \frac{1}{2}\lim_{t\rightarrow\infty}\left\{\langle\sigma^\dagger(t)\sigma^\dagger(t+\tau)\sigma(t+\tau)\sigma(t)\rangle \right. \\ & +2\,\mathrm{Re}\left[\langle\sigma_{ss}\rangle\left(\langle\sigma^\dagger(t)\sigma^\dagger(t+\tau)\sigma(t+\tau)\rangle - \langle\sigma^\dagger(t)\sigma(t+\tau)\sigma(t)\rangle\right)\right] \\ & \left. -|\langle\sigma^\dagger(t+\tau)\sigma(t)\rangle|^2 - |\langle\sigma(t+\tau)\sigma(t)\rangle|^2 + \langle\sigma^\dagger\sigma_{ss}\rangle^2\right\}, \end{aligned} \tag{3.56}$$

where we are considering only the steady-state emission from the QD by taking the limit $t\rightarrow\infty$. Normalising this correlation function to the long-time limit, we have:

$$g^{(2)}_{HOM}(\tau) = \frac{G^{(2)}_{HOM}}{\langle \hat{E}_1^{(-)}\hat{E}_1^{(+)}\rangle\langle \hat{E}_2^{(-)}\hat{E}_2^{(+)}\rangle}, \tag{3.57}$$

where,

$$\langle \hat{E}_1^{(-)}\hat{E}_1^{(+)}\rangle\langle \hat{E}_2^{(-)}\hat{E}_2^{(+)}\rangle \propto \langle\sigma^\dagger\sigma\rangle^2 - |\langle\sigma\rangle|^4. \tag{3.58}$$

As relevant to actual experiments [30, 32, 63], in order to capture the finite detector

time-resolution we model the detector by a Gaussian response function, such that:

$$R(\omega) = \sqrt{\frac{4\ln 2}{\pi\delta\tau}} \exp\left(-\frac{4\ln 2\ \omega^2}{\delta\tau^2}\right), \tag{3.59}$$

where $\delta\tau$ is the full width at half maximum, and the distribution is normalised such that it integrates to unity. This response function describes the interval of time required for the photon detector to reset after a detection event. The effect of finite detector resolution can then be accounted for by convolving the second-order correlation function with the response function:

$$\tilde{g}^{(2)}_{HOM}(\tau) = \int_{-\infty}^{\infty} g^{(2)}_{HOM}(x)R(x-\tau)dx = (g^{(2)}_{HOM} * R)(\tau). \tag{3.60}$$

Furthermore, we can recover the so-called 'bad detector limit' by letting the full width at half maximum (FWHM) $\delta\tau \to \infty$, leading to zero time-resolution.

HOM with a QD

To calculate the second-order correlation function we make use of the quantum regression theorem described in Sec. 2.2.2. For the above correlation function we require two separate initial conditions for the regression theorem, $\Lambda_1(t,0) = \sigma\rho(t)\sigma^\dagger$ and $\Lambda_2(t,0) = \sigma\rho(t)$. The evolution of the regression operator, $\Lambda_i(t,\tau)$, is given by:

$$\frac{\partial\Lambda_i(t,\tau)}{\partial\tau} = \mathcal{L}[\Lambda_i(t,\tau)], \tag{3.61}$$

where $\mathcal{L}[\bullet]$ is the same Liouvillian as the master equation of interest, that is, either the pure-dephasing or full variational master equations. As we are interested in the steady-state emission from the source, we replace the $\rho(t)$ with the physical reduced QD density operator in the steady state ρ_{ss}.

The phenomenological case. From the definition of the second-order correlation function in Eq. 3.56, at zero time delay one always sees a perfect interference pattern – as is consistent with Legero et al. [60]. This is demonstrated in Figs. 3.12 (a) and 3.13 (a) for various driving strengths and dephasing rates, respectively. At zero time-delay we see the expected dip indicating perfect HOM interference regardless of the driving strength or dephasing rate. This rises with the time delay, the rate of which depends on the spontaneous emission and dephasing rates of the emitter, which determine the spatial extent of the incident photons – when the second delayed photon enters the beam splitters it may still have finite overlap with the initial photon wavepacket. The oscillatory dynamics seen in the correlation function are a consequence of the Rabi oscillations of the emitter changing the probability of photon emission.

The interference pattern observed at zero time delay is reliant on an ideal photon detector; as discussed in the previous section, in reality all detectors have some finite response function. Fig. 3.12 (b) shows the second-order correlation function measured by

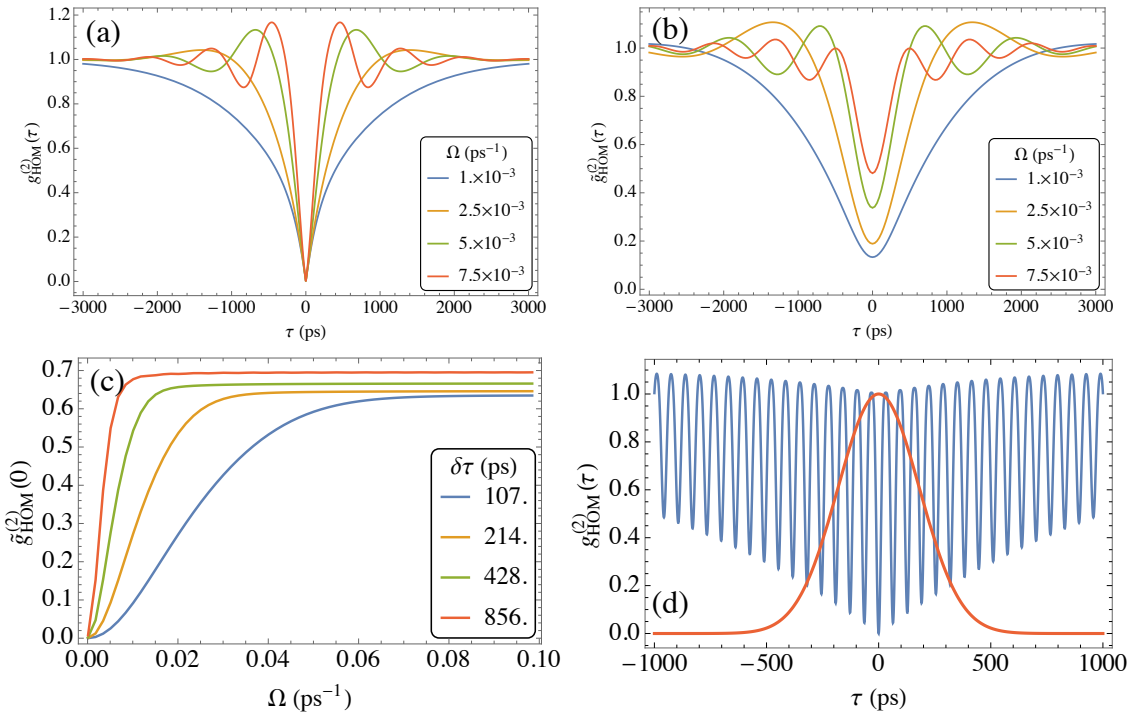


Figure 3.12: Behaviour of the normalised second-order correlation function, $g^{(2)}_{HOM}$, as a function of driving strength from the pure dephasing model. (a) Shows the unconvolved correlation function for increasing driving strength. (b) Shows the convolved correlation functions for a Gaussian detector response function with FWHM $\delta\tau = 428$ ps. (c) Shows the plateau in the visibility of the HOM interference when one reaches strong driving due to the detector response sampling many oscillations, the height of which changes with the detector FWHM $\delta\tau$. (d) Compares the time-scales of the detector response for $\delta\tau = 428$ ps (red) with the coherent oscillations of $g^{(2)}_{HOM}$ for a driving strength of $\Omega = 0.1$ ps^{-1} (blue). Other parameters for these plots are $\Gamma^{-1} = 1000$ ps, and $T_1 = \gamma^{-1} = 700$ ps.

a detector with a Gaussian response function, with full width at half maximum (FWHM) $\delta\tau = 428$ ps as is used in Ref. [31]. We see that for increasing driving strength, the interference dip is suppressed. This is due to the response function of the detector sampling multiple peaks and troughs of the correlation function. Physically, this amounts to the detector not being able to respond fast enough to the ever shorter dynamical timescales of the system with increasing driving strength. The height of the dip continues to increase as a function of driving strength until a plateau is reached, corresponding to the detector response function sampling over the many peaks and troughs of the correlation function, giving a non-zero average, as shown in Fig. 3.12 (c) and (d), respectively.

The visibility of the HOM dip is also reduced when the dephasing rate increases, as demonstrated in Fig. 3.13 (a) and (b). In addition to suppressing oscillatory dynamics in the correlation function, dephasing also narrows the two-photon interference dip. The dephasing reduces the coherence time of the photons emitted by the source, and consequently their spatial extent. The photon wavepacket therefore spends less time in the beam splitter, reducing the timescale over which two-photon interference can occur. Interestingly, from Fig. 3.13 (c), we see that at large dephasing the visibility of the interference

is recovered somewhat, with the HOM dip plateauing to a non-zero value dependent on the detector resolution and the spontaneous emission rate. This is due to the dynamics of the emitter becoming entirely incoherent for large dephasing rates, as is demonstrated by the population dynamics shown in Fig. 3.13 (e); in this regime, the correlation function is characterised by a purely exponential decay, the timescale of which is determined by the spontaneous emission rate of the emitter, thus the dip of the convolved correlation may be lower than when damped Rabi oscillations are present.

Phonon effects. When phonons are introduced, we see several important changes in the qualitative behaviour of the second-order correlation function. At weak to intermediate driving strengths we see similar behaviour to the pure dephasing case – the dynamical timescale in the correlation function decreases with increasing driving strength, thus, when convolved with the detector response function one sees that the visibility of HOM interference decreases, as shown in Fig. 3.14 (a, b). Unlike the pure dephasing case, however, at strong driving the detectors are unable to resolve any two-photon interference with $\tilde{g}^{(2)}_{HOM}(0)$ tending to unity, as demonstrated in Fig. 3.15 (a).

This behaviour is a consequence of the driving dependent dephasing rates in the variational master equation – as one increases the driving strength, the spectral density is sampled closer to its peak, thus at very strong driving strength the effective damping rate is very large. However, this does not significantly affect the timescale over which the coherent oscillations in the correlation function occurs, i.e. the oscillation period, but does decrease their lifetime. When convolved with the response function, the dynamics are too fast to be resolved by the detector, thus only the steady state value of the correlation function is observed, so that the integrals evaluate to unity.

Further differences between the pure dephasing and phonon models can be seen when one considers the variation in the behaviour of the correlation function with system-environment coupling strength or temperature. Naively one might expect that increasing the system-environment coupling strength will increase the dephasing on the QD, narrowing the HOM dip, and reducing its visibility. Strikingly, Fig. 3.14 (c, d) show the exact opposite behaviour, where increasing the coupling strength to the environment broadens the dip in the correlation function, increasing its visibility. This is due to phonon processes leading to a renormalisation of system energy scales; the Rabi frequency acting on the quantum dot gets renormalised by the average displacement of the phonon environment, which is exponentially dependent on the system-environment coupling strength. Thus, as the coupling strength increases, the effective system time-scales increase and the visibility of the HOM dip improves, as demonstrated also in Fig 3.15 (b).

Furthermore, we can obtain a similar improvement in the resolution of the HOM dip by increasing the temperature of the phonon environment, thus again renormalising the Rabi frequency, as shown in Fig. 3.14 (d, e). As can be seen from Fig. 3.15 (c) the visibility of the HOM interference dip increases until at a certain temperature it once again decreases reaching a plateau. The temperature at which this crossover occurs decreases as a function of the system-environment coupling strength. The cause of this behaviour is a transition from coherent to incoherent dynamics of the QD [49], which may be seen from the excited

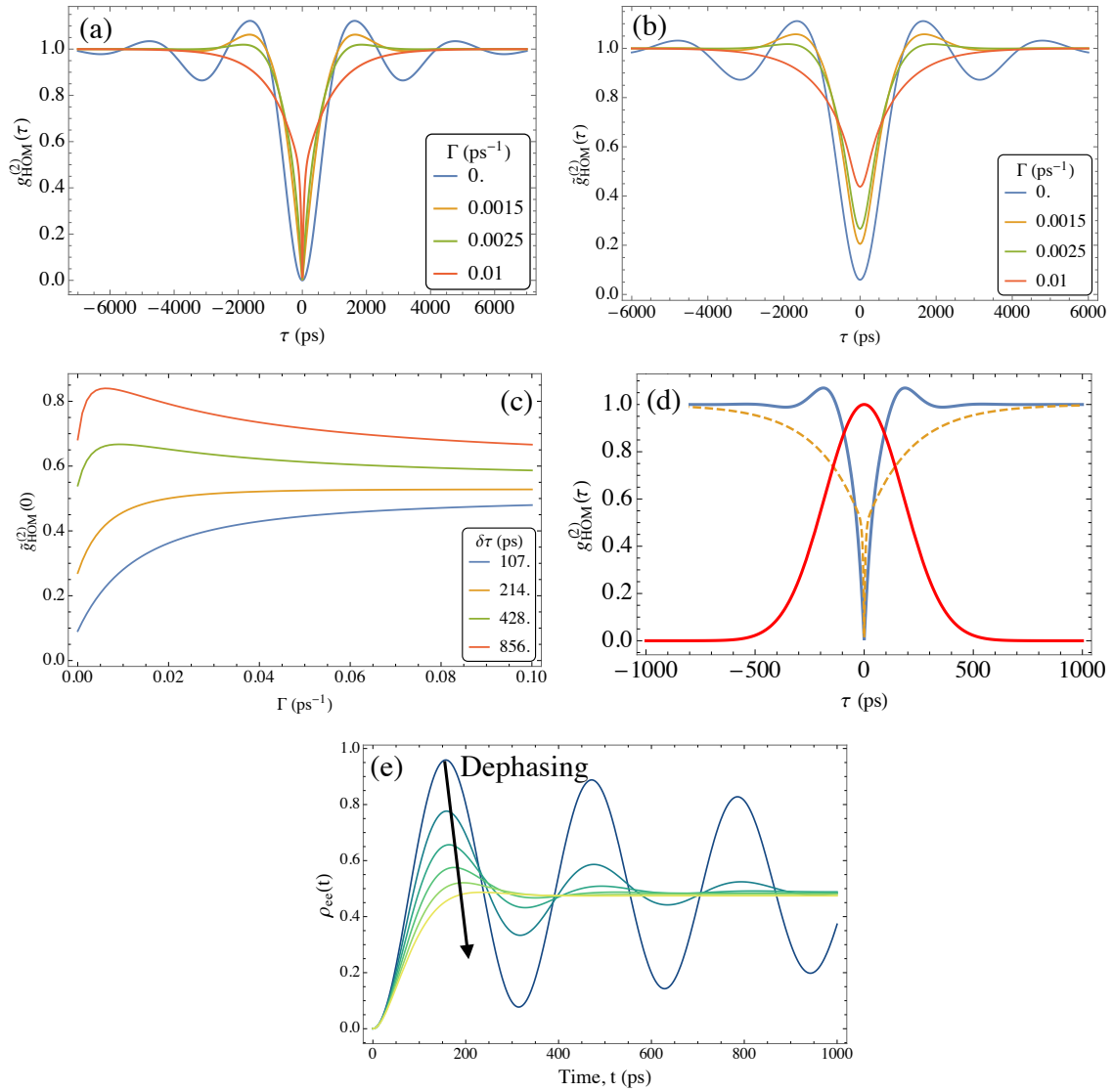


Figure 3.13: Behaviour of the normalised second-order correlation function, $g^{(2)}_{HOM}$, as a function of dephasing rate in the pure dephasing model. (a) Shows the unconvolved correlation function for increasing dephasing. (b) Shows the convolved correlation functions for a Gaussian detector response function with FWHM $\delta\tau = 428$ ps. (c) Shows the change in the visibility of HOM interference as a function of dephasing for several values of $\delta\tau$. (d) Shows the effect that strong (dashed, $\Gamma = 0.1$ ps^{-1}) and weak (solid, $\Gamma = 0.02$ ps^{-1}) dephasing has on the second-order correlation function, compared to the detector response (red). (e) Shows the effect of increasing dephasing on the TLS dynamics, demonstrating a transition from coherent to incoherent dynamics as indicated by the arrow. Other parameters for these plots are $\Omega = 0.02$ ps^{-1}, and $T_1 = \gamma^{-1} = 700$ ps.

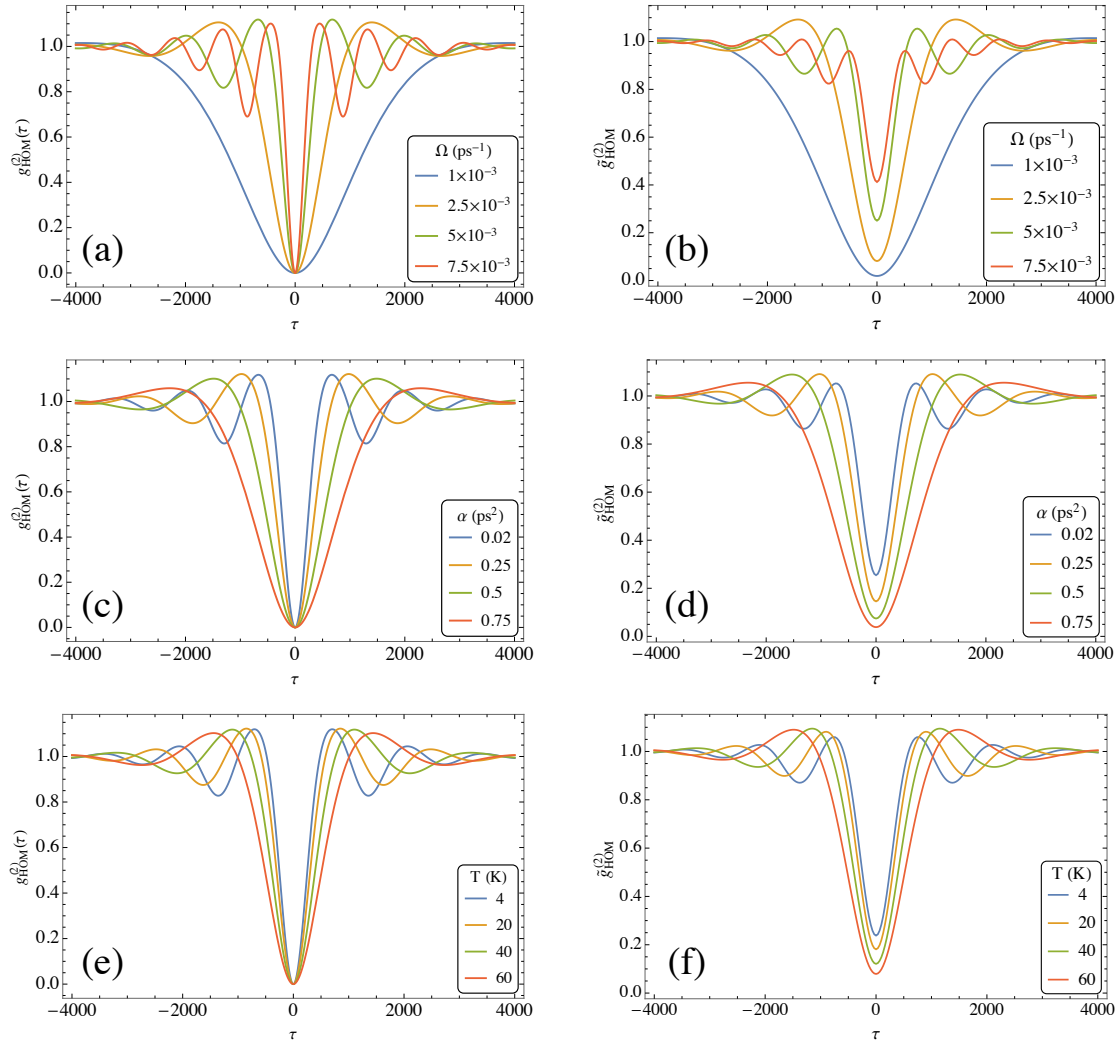


Figure 3.14: Behaviour of the unconvolved (left) and convolved (right) $g^{(2)}_{HOM}$ in the presence of phonons (calculated using the variational theory) for: (a,b) increasing driving strength with $\alpha = 0.027$ ps^2 and $T = 4$ K; (c,d) increasing system-environment coupling strength with $\Omega = 5 \times 10^{-3}$ ps^{-1} and $T = 4$ K; (e,f) increasing temperatures for $\alpha = 0.027$ ps^2 and $\Omega = 5 \times 10^{-3}$ ps^{-1}. Other parameters used for this plot are $\delta\tau = 428$ ps, $\omega_c = 2.2$ ps^{-1}, and $T_1 = \gamma^{-1} = 700$ ps.

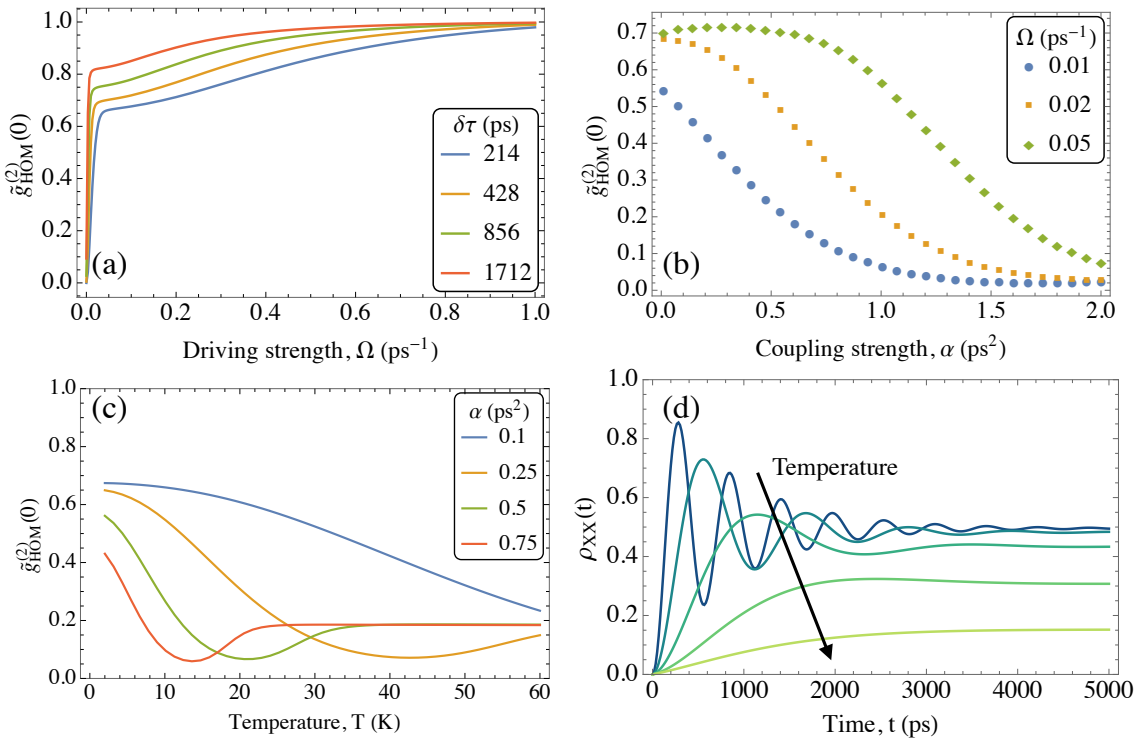


Figure 3.15: (a,b) The visibility of the HOM interference dip as a function of driving strength and system-environment coupling strength, respectively, with $T = 4$ K calculated from the variational theory. (c) Shows the visibility of the two photon interference pattern for increasing temperature and various system-environment coupling strengths, with (d) showing the transition from coherent to incoherent dynamics for $\alpha = 0.25$ ps^2 and increasing temperature. Other parameters for these plots are $\delta\tau = 428$ ps, $\omega_c = 2.2$ ps^{-1}, and $T_1 = \gamma^{-1} = 700$ ps.

state population dynamics in Fig. 3.15 (d). Thus at high temperatures, the only time-scale relevant to photon emission is the spontaneous emission rate of the QD, leading to an exponential decay of the correlation function. The time-scale of this exponential decay is set purely by the spontaneous emission rate, therefore the correlation function no longer has any temperature dependence, leading to the plateau observed in Fig. 3.15 (d).

3.5.3 Hanbury-Brown-Twiss experiments

In this section we shall discuss how the measurement statistics from a HBT experiment may be altered by phonon interactions. The HBT effect is an important tool in determining whether the light emitted from a system is bunched or anti-bunched; that is, are there multi- or single-photon states generated by the emitter. This measurement is performed by considering the light from a source incident at a single port, and measuring the coincidence counts from detectors placed at the output ports of the beam splitter, as shown schematically in Fig. 3.11 (b).

For a single photon source it is impossible to measure coincidence counts in a HBT set-up using perfectly time-resolved detectors. This can be see straightforwardly by considering a single photon incident on the beam splitter, that is the state $|\Psi_{in}\rangle = |1, 0\rangle$. By

applying the beam splitter transformation given in Eq. 3.49 to this state we obtain:

$$|\Psi_{in}\rangle = a_1^\dagger|0\rangle = \frac{1}{\sqrt{2}}(b_1^\dagger + b_2^\dagger)|0\rangle = \frac{1}{\sqrt{2}}\left(|1,0\rangle + |0,1\rangle\right), \tag{3.62}$$

where after the beam splitter, the photon is in an entangled state between output ports, therefore can only be detected at one detector or the other.

Consider now the measurement statistics of a multi-photon state incident on the beam splitter, $|\Psi_{in}\rangle = |N,0\rangle$, where $N \in \mathbb{Z}$. Applying the beam splitter transformation to this state we have:

$$|\Psi_{in}\rangle = (a_1^\dagger)^N|0\rangle = \frac{1}{2^{N/2}}(b_1^\dagger + b_2^\dagger)^N|0\rangle. \tag{3.63}$$

Using the binomial theorem we obtain:

$$\begin{aligned}\frac{1}{2^{N/2}}(b_1^\dagger + b_2^\dagger)^N|0\rangle =& \frac{1}{2^{N/2}}\sum_{k=0}^{N}\frac{N!}{k!(N-k)!}(b_1^\dagger)^{N-k}(b_2^\dagger)^k|0\rangle \\ &= \alpha_{N,0}|N,0\rangle + \alpha_{N-1,1}|N-1,1\rangle + \cdots + \alpha_{1,N-1}|1,N\rangle + \alpha_{0,N}|0,N\rangle,\end{aligned} \tag{3.64}$$

where $\alpha_{n,m}$ is the probability amplitude of state $|n,m\rangle$. As we can see from the above expression, the output state is a superposition of multiple photons in each arm of the beam splitter. Thus for large numbers of input photons, we see a large probability of coincidence counts. Therefore, the presence or absence of coincidence counts in the measurement statistics from a HBT set-up determines whether a source is bunched or anti-bunched, and hence whether it is a two level emitter.

HBT and time-resolved measurements

As in HOM-type experiments, we consider a CW source, therefore we must account for finite time resolution measurements. We can do this by considering the two-time photon emission correlation function given in Eq. 3.55. As we consider photons incident at only one of the input ports for HBT experiments we may set $E_2^{(+)} = 0$, such that the correlation function reduces to:

$$G^{(2)}_{HBT}(t,\tau) = \langle E_1^-(t)E_1^-(t+\tau)E_1^+(t+\tau)E_1^+(t)\rangle. \tag{3.65}$$

Writing the normalised HBT correlation function in terms of system operators we have:

$$g^{(2)}_{HBT}(\tau) = \lim_{t\to\infty}\frac{\langle\sigma^\dagger(t)\sigma^\dagger(t+\tau)\sigma(t+\tau)\sigma(t)\rangle}{|\langle\sigma^\dagger\sigma\rangle|^2}. \tag{3.66}$$

As in the HOM case, the correlation function measured by a detector with a finite time resolution can be found by convolving $g^{(2)}_{HBT}$ with the detector response function, $\tilde{g}^{(2)}_{HBT}(\tau) = \left(R * g^{(2)}_{HBT}\right)(\tau)$. Fig. 3.16 shows both the convolved and unconvolved HBT correlation functions calculated from they pure dephasing theory. For the unconvolved case we see that there is a dip at zero time-delay, demonstrating that the emitter is a perfect single photon source. This is a consequence of the two-level nature of the emitter we

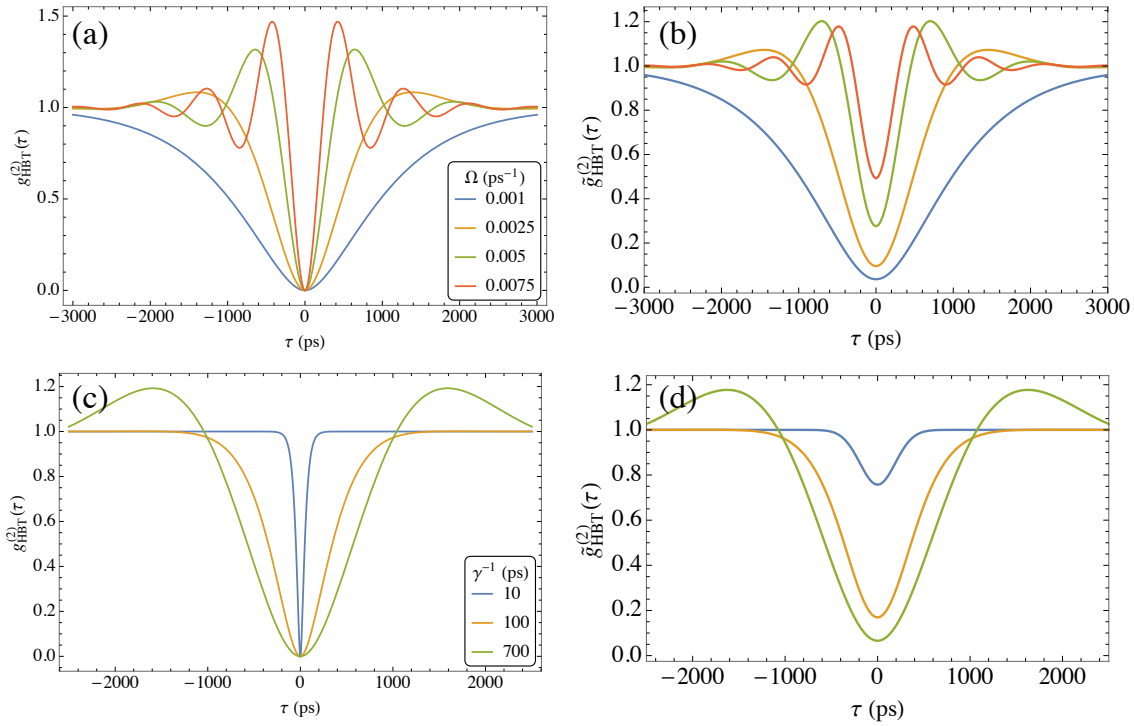


Figure 3.16: HBT second-order correlation function predicted by the pure dephasing model for (top) an ideal detector and (bottom) a detector with Gaussian response with FWHM of $\delta\tau = 428$ ps. (a,c) Show the driving dependence of the correlation function with $T_1 = 700$ ps. (b,d) Show the spontaneous emission rate dependence for $\Omega = 2\times10^{-3}$ ps^{-1}. The dephasing rate used for these plots is $\Gamma = 1\times10^{-3}$ ps^{-1}.

consider, which forbids multi-photon transitions, resulting in anti-bunched emission. The width of the dip around zero time-delay is dependent on both the driving strength and spontaneous emission rate, decreasing as a function of these parameters. Thus at strong driving or large spontaneous emission rates, the visibility of the HBT effect is suppressed when convolved with the finite detector response function.

Since the correlation function is a measure of the bunched or anti bunched nature of the photon source, at weak driving (or small spontaneous emission rate) the time delay between each emitted photon is large, and the correlation function increases slowly from zero time-delay – thus, independent photons can be distinguished. The delay between photon arrival time decreases as the driving and/or spontaneous emission rate is increased, decreasing the dynamical time-scales in the correlation function as demonstrated in Fig. 3.16 (a) and (b).

Unlike the HOM set-up, however, varying the pure-dephasing rate has little effect on the width of the peak in the HBT correlation function, instead leading to a suppression of Rabi oscillations. Physically, this is due to pure dephasing processes having little influence on the emission rate of the TLS, but rather it decreases the correlation time of the emitted photons, which is much more important for HOM type experiments (i.e. to show two photon interference).

When we rigorously include phonons in our theoretical description through the variational master equation the HBT correlation functions behave in a qualitatively similar

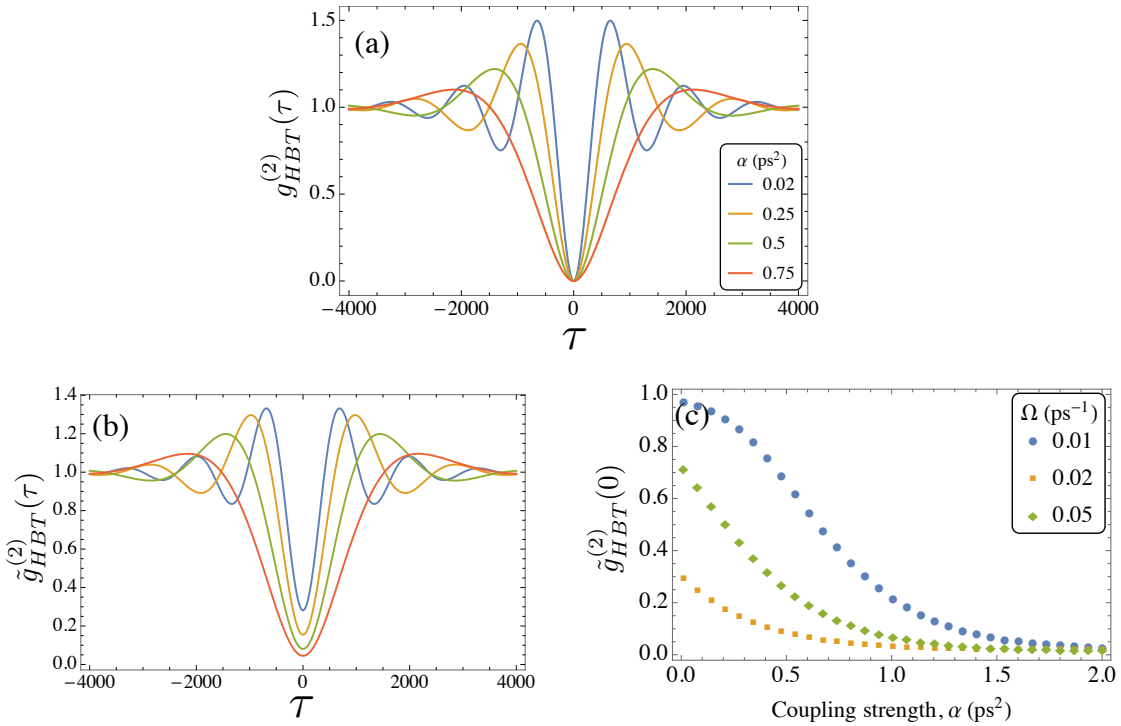


Figure 3.17: System-environment coupling strength dependence of the HBT second-order correlation function for (a) an ideal detector and (b) a detector with Gaussian response. (c) Shows $\tilde{g}^{(2)}_{HBT}(0)$ for various driving strengths, calculated from the variational theory. Other parameters for these plots are $\Omega = 5 \times 10^{-3}$ ps^{-1}, $\delta\tau = 428$ ps, $\omega_c = 2.2$ ps^{-1}, and $T_1 = \gamma^{-1} = 700$ ps.

way as the pure dephasing model when varying both the spontaneous emission rate and driving strength. In contrast to the phenomenological theory, however, when we increase the system-environment coupling strength or temperature (and thus the phonon induced dephasing rate) we see that the width of the dip at $\tau = 0$ increases. This is once again due to the renormalisation of the driving strength, thus increasing the time lag between subsequent photons, as shown explicitly in Fig. 3.17.

3.6 Summary

In this chapter we have developed a modified a theory of quantum optics capable of describing the emission characteristics of a driven QD in the presence of phonons. We have made use of the variational polaron formalism to capture the effect of phonons on both the system dynamics and optical properties, focusing in particular on deviations from a phenomenological pure dephasing model often employed in the quantum optics community. In doing so, we have demonstrated that phonons lead to a qualitative departure of the emitter photon correlation functions as predicted by 'textbook quantum optics' highlighting that in order to accurately capture and understand the behaviour of solid state photonic systems one must account for the microscopic origins of noise processes. Furthermore, we have shown that phonons can have some surprising and counter-intuitive

effects on the photon measurement statistics from a QD under CW driving; in particular demonstrating that the visibility of higher order correlation functions actually increases with the temperature and system-environment coupling strength.

CHAPTER 4

QUANTUM CORRELATIONS OF LIGHT AND MATTER THROUGH ENVIRONMENTAL TRANSITIONS

4.1 Introduction

The diversity of systems studied in cavity quantum electrodynamics (CQED) places the subject at the heart of many prospective quantum and classical technologies. Examples include single photon sources [15, 64], ultrafast optical switches [17, 18], and quantum gates [65–67], which require the development of robust, scalable, and potentially strongly coupled emitter-cavity systems. Though the quantum strong coupling (QSC) limit and beyond—in which the system eigenstates become light-matter entangled—have now been attained for single emitters in the microwave regime [68, 69], it remains technically demanding to manufacture optical cavities of sufficiently high quality (Q) factor to unambiguously demonstrate QSC phenomena. Example systems in which great strides have recently been made towards this goal include single self-assembled quantum dots (QDs) within optical nano- and microcavites [70–74]. Here, small mode volumes can readily be obtained, resulting in potentially large Q-factors and cavity coupling strengths that are substantial in comparison to the emitter decay rate. In conjunction with their solid state nature, this makes QD-cavity systems excellent candidates for future technological applications.

Nevertheless, it still remains a challenging endeavour to reach the QSC regime due to significant cavity losses [75, 76]. The broad cavity lineshape that results masks contributions from higher order dressed states, thus placing the system in an intermediate coupling regime that can be described using semiclassical techniques [77]. In addition to interactions with external electromagnetic fields, many CQED systems are also in contact with their host (e.g. thermal) environment; for example, as we have seen, in QDs this influence is often dominated by acoustic phonons [13, 14]. In order to explore the effect that such couplings have on the optical emission of the system, it is necessary to modify the standard quantum optics treatments [9], which as we saw in Chapter 3 lead to significant departures from atomic-like behaviour [29, 33, 36, 37, 78–83].

Here, we demonstrate that even for a lossy CQED system within an otherwise semiclassical regime, it is still possible to generate light-matter quantum correlations via transitions induced by the host environment. Specifically, we show that the presence of the host environment results in optical emission that is observably sensitive to the joint eigenstructure of the cavity and emitter, even if the optical transitions in its absence are not, and quantify the resulting deviations from the semiclassical description. This behaviour, which may be probed experimentally through asymmetries in both the cavity reflectivity and emission spectra, also challenges the notion that the addition of a thermal environment should simply decohere our system to a more classical effective description. The physics we describe is distinct from that captured by a semiclassical treatment of phonon-induced relaxation in cavity polariton systems [84], in which light-matter quantum correlations are inherent to the polaritonic state itself, rather than being generated by the host thermal environment as is the case here.

4.2 Cavity QD systems

We consider a driven cavity coupled to a single two level emitter (TLE), as shown schematically in Fig. 4.1(a). This is a model of wide importance, though later we shall also consider specific parameters relevant to QD-microcavity systems to provide experimental context. The cavity and TLE couple through a dipole interaction, and the cavity mode is driven by an incident CW laser with driving frequency ω_l – this is typical of QD-microcavity setups, as it is often challenging to optically address the QD directly. The resulting Hamiltonian takes the form:

$$H_s = \omega_X \sigma^\dagger \sigma + \omega_c a^\dagger a + g\sigma_x \left(a^\dagger + a\right) + 2\eta \cos\omega_l t \left(a^\dagger + a\right). \tag{4.1}$$

Here g is the emitter-cavity interaction strength, and η is now the cavity-laser coupling. $\sigma^\dagger = |X\rangle\langle 0|$ and $\sigma = |0\rangle\langle X|$ are raising and lowering operators for the TLE, while $a^\dagger$ and a are creation and annihilation operators for the cavity mode.

We may simplify this Hamiltonian using the rotating wave approximation (RWA) introduced in Chapter 3. Consider the transformation into the interaction picture with respect to the free Hamiltonian of the cavity and TLE $\mathcal{U}_0(t) = e^{-iH_0 t}$, with $H_0 = \omega_X \sigma^\dagger \sigma + \omega_c a^\dagger a$, with the interaction Hamiltonian defined as $H_I(t) = g\sigma_x \left(a^\dagger + a\right) + 2\eta \cos\omega_l t \left(a^\dagger + a\right)$. Thus, in the interaction picture we have:

$$\begin{aligned} H_I(t) &= g\left(\sigma^\dagger e^{i\omega_X t} + \sigma e^{-i\omega_X t}\right)\left(a^\dagger e^{i\omega_c t} + a e^{-i\omega_c t}\right) + 2\eta\cos\omega_l t\left(a^\dagger e^{i\omega_c t} + a e^{-i\omega_c t}\right), \\ &\approx g\left(\sigma a^\dagger e^{-i(\omega_X-\omega_c)t} + \sigma^\dagger a e^{i(\omega_X-\omega_c)t}\right) + \eta\left(a^\dagger e^{i(\omega_c-\omega_l)t} + a e^{-i(\omega_c-\omega_l)t}\right), \end{aligned} \tag{4.2}$$

where we have neglected terms oscillating with frequencies $\pm(\omega_X + \omega_C)$ and $\pm(\omega_L + \omega_C)$, which we assume average to zero over time-scales important to the emitter-cavity dynamics. This is a valid assumption when the respective TLS-cavity and cavity-driving frequencies are close to resonant, and results in the so-called driven Jaynes-Cummings

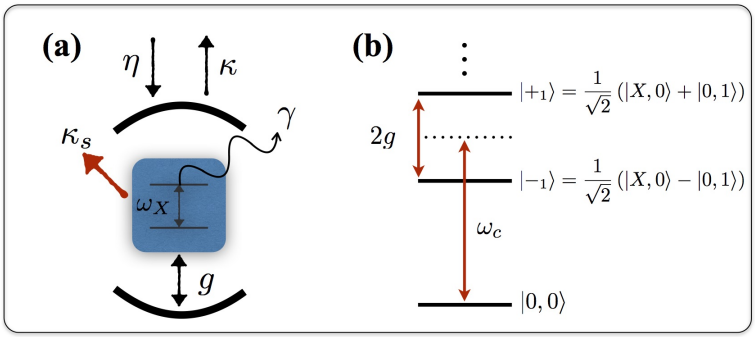


Figure 4.1: (a) Schematic of the emitter-cavity setup considered. The cavity is one sided, driven by a CW classical laser of frequency ω_L with strength η, and loses excitation through the top with rate κ, and the sides with rate κ_s. The TLE decay rate is γ, and the TLE-cavity coupling strength is g. (b) The first rung of the dressed state ladder, i.e. the lowest eigenstates of the coupled TLE-cavity system, in the absence of dissipation and driving.

Hamiltonian [42]. Transforming back to the Schrödinger picture, we have:

$$H_s = \omega_X \sigma^\dagger \sigma + g(\sigma^\dagger a + \sigma a^\dagger) + \omega_c a^\dagger a + \eta(a^\dagger e^{-i\omega_l t} + a e^{i\omega_l t}).$$

To remove the time dependence in the system Hamiltonian, we can move to a frame rotating at the laser driving frequency ω_L, using the unitary transformation $\mathcal{U}_{rot}(t) = \exp\left(-i\omega_l(\sigma^\dagger\sigma + a^\dagger a)t\right)$, yielding the Hamiltonian:

$$H_S = \delta\sigma^\dagger\sigma + g\left(\sigma^\dagger a + \sigma a^\dagger\right) + \eta\left(a^\dagger + a\right) + \nu a^\dagger a. \tag{4.3}$$

Here, $\nu = \omega_c - \omega_L$ and $\delta = \omega_X - \omega_L$ are the cavity and emitter detunings, respectively.

Eigenstates of the Jaynes-Cummings model

Before continuing, it is worth briefly discussing the eigenstructure of the Hamiltonian given in Eq. 4.3. In the absence of driving ($\eta = 0$ and $\omega_l = 0$), and for a resonant cavity-emitter system ($\omega_X = \omega_c = \omega_0$), we may find an analytic expression for the eigenvectors and eigenenergies of the Jaynes-Cummings Hamiltonian. We do so by decomposing the cavity operators into the Fock state basis, such that $a^\dagger = \sum_{n=0}^{\infty} \sqrt{n+1}|n+1\rangle\langle n|$. The cavity-emitter Hamiltonian then takes a block diagonal form in the basis $\{|X,n\rangle, |0,n+1\rangle\}$:

$$H_s = \bigoplus_{n=0}^{\infty} \begin{pmatrix} (n+1)\omega_0 & g\sqrt{n+1} \\ g\sqrt{n+1} & (n+1)\omega_0 \end{pmatrix}. \tag{4.4}$$

The eigenstates of this Hamiltonian are known as the light-matter dressed states,

$$|\pm_n\rangle = \frac{1}{\sqrt{2}}\left(|0,n+1\rangle \pm |X,n\rangle\right),$$

with associated energies $E_{\pm,n} = (n+1)\omega_0 \pm g\sqrt{n+1}$. These states form a ladder of light-matter entangled states, as shown schematically in Fig 4.1. Each rung of the ladder is split

by the emitter-cavity coupling strength, which is inhomogeneous in the cavity occupation, $2g\sqrt{n+1}$.

When the cavity mode is driven, the dressed states are no longer true eigenstates of the system. The driving term now couples rungs of the ladder together, thus driving populations between these states. In the weak driving limit, however, the eigenstates remain a good approximation for understanding the optical properties of the system.

4.3 Dissipation in Cavity QED systems

As shown schematically in Fig. 4.1(a), there are several potential dissipative processes that must be accounted for when describing the optical properties of solid state QED systems. These include: the field coupled directly to the emitter, leading to spontaneous emission via non-cavity field modes; emission (leakage) from the cavity either through the top mirror or the sides; and coupling between the TLE and the thermal environment. In this section we outline how these dissipative processes can be accounted for using the master equation formalism.

4.3.1 The phonon environment and polaron formalism

To highlight the qualitative changes in behaviour brought about by an explicit inclusion of the thermal environment, we model its impact on the system in two ways. The first simply assumes a phenomenological pure dephasing of the TLE coherences, which may be approximated by a semiclassical description in the appropriate limits. As in the previous chapter, we show that the pure dephasing approximation is generally inadequate. Instead, we once again follow a second, more rigorous approach, and retain a detailed, quantum mechanical description of the thermal environment to properly understand its influence on the system dynamics.

This will be achieved through a polaron representation master equation [33, 37, 79, 80, 83], which can then be related to the cavity optical emission through the input-output formalism [85, 86]. As in Chapter 3, we consider the environment to be described by a collection of harmonic oscillators, with a Hamiltonian of the form:

$$H = H_S + \sigma^\dagger\sigma \sum_k g_k(b_k^\dagger + b_k) + \sum_k \nu_k b_k^\dagger b_k, \tag{4.5}$$

where $b_k^\dagger$ (b_k) is the creation (annihilation) operator for mode k. The interaction between the system and phonon environment is given by the spectral density, which we once again take to have a super-Ohmic form appropriate to acoustic phonon processes, $J(\nu) = \alpha\nu^3 e^{-\nu^2/\nu_c^2}$, with α the coupling strength and ν_c now labelling the high frequency cut-off [13, 14].

As for the case of a classically driven QD, we apply a polaron transformation, $\mathcal{U}_{pol} = \exp\left(-\sigma^\dagger\sigma \sum_k \alpha_k(b_k^\dagger - b_k)\right)$ to the full system-environment Hamiltonian $H = H_S + H_B + H_I$ [33]. In this work we shall consider only cavity-emitter coupling strengths considerably smaller than the cut-off frequency of the phonon environment. This allows us to treat the

system dynamics adiabatically with respect to the environmental response, therefore the full polaron representation gives a good description of the environmental response. Thus the variational displacement function given in Eq. 3.36 reduces to $F(\nu) \approx 1 \ \forall \ \omega$, or equivalently the displacements take the form $\alpha_k = g_k/\nu_k$. This simplifies the analysis significantly, as the variational procedure in the presence of the optical cavity is no-longer a trivial step, due to cavity degrees of freedom entering the expression for the free energy bound.

Applying the polaron transformation, that is $\tilde{H} = \mathcal{U}_{pol}^{\dagger} H \mathcal{U}_{pol}$, we obtain the polaron frame Hamiltonian:

$$\tilde{H} = \delta\sigma^{\dagger}\sigma + gB\left(\sigma^{\dagger}a + \sigma a^{\dagger}\right) + \eta(a^{\dagger} + a) + \nu a^{\dagger}a + (XB_X + YB_Y) + \sum_k \nu_k b_k^{\dagger} b_k, \quad (4.6)$$

where we have absorbed the polaron shift to the emitter frequency, $\Delta_{\text{pol}} = \sum_k g_k^2/\nu_k$, into the definition of QD splitting, i.e. $\omega_X \to \omega_X - \Delta_{pol}$. Here, the TLE-cavity coupling strength has been renormalised by the average displacement of the oscillator environment, $g \to gB$, with $B = \text{tr}\left(B_{\pm}\rho_{\text{th}}\right) = \exp\left(-\frac{1}{2}\int_0^{\infty} \frac{J(\omega)}{\omega^2} \coth\frac{\beta\omega}{2} d\omega\right)$ denoting the expectation of the displacement operators $B_{\pm} = \exp\left(\pm\sum_k g_k(b_k^{\dagger} - b_k)/\nu_k\right)$ with respect to the thermal state $\rho_{\text{th}} = \exp\left(-\beta\sum_k \nu_k b_k^{\dagger} b_k\right)/\text{tr}\left(\exp\left(-\beta\sum_k \nu_k b_k^{\dagger} b_k\right)\right)$ at inverse temperature $\beta = 1/k_B T$. The transformed operators are $X = g(\sigma^{\dagger}a + \sigma a^{\dagger})$, $Y = ig(\sigma^{\dagger}a - \sigma a^{\dagger})$, $B_X = (1/2)(B_+ + B_- - 2B)$, and $B_Y = (i/2)(B_+ - B_-)$.

Moving into the interaction picture with respect to the coupled TLE-cavity Hamiltonian in the polaron frame, $\tilde{H}_s = \delta\sigma^{\dagger}\sigma + gB\left(\sigma^{\dagger}a + \sigma a^{\dagger}\right) + \eta(a^{\dagger} + a) + \nu a^{\dagger}a$, we derive a master equation for their reduced state, $\rho(t)$, by tracing out the environment within a second-order Born-Markov approximation. As in Chapter 3, this procedure may be thought of as a perturbative expansion about the system timescales, which for a cavity QED system is set by the ratio g/ν_c [37], and is thus non-perturbative in the TLE-environment coupling strength. Crucially, as the cut-off Λ is usually much larger than any other energy scale in the problem (not just g) and the renormalised coupling term $gB\left(\sigma^{\dagger}a + \sigma a^{\dagger}\right)$ appears explicitly in the system Hamiltonian $\tilde{H}_S$, this expansion does not preclude the exploration of TLE-cavity dressed states. It simply enables us to move beyond weak TLE-environment couplings by retaining multi-boson processes [87].

Using this Hamiltonian in conjunction with Eq. 2.49, we may derive a second-order master equation of the form

$$\frac{\partial\rho(t)}{\partial t} = -i\left[\tilde{H}_s, \rho(t)\right] + \mathcal{K}_{th}\left[\rho(t)\right]. \quad (4.7)$$

With the help of the expression given in Eq. 2.54, the phonon dissipator may be written in terms of the system operators:

$$\mathcal{K}_{th}\left[\rho(t)\right] = -\int_0^{\infty} d\tau \left(\left[X, X(-\tau)\rho(t)\right]\tilde{\Lambda}_{XX}(\tau) + \left[Y, Y(-\tau)\rho(t)\right]\tilde{\Lambda}_{YY}(\tau)\right) + h.c. \quad (4.8)$$

The environmental correlation functions $\tilde{\Lambda}_{XX}(t)$ and $\tilde{\Lambda}_{YY}(t)$ are then found by taking the *full polaron limit* in Eq. 3.39, that is, by setting the variational function $F(\omega) = 1 \; \forall \; \omega$. The resulting correlation functions then take the form

$$\tilde{\Lambda}_{XX}(\tau) = B^2(e^{\varphi(\tau)} + e^{-\varphi(\tau)} - 1) \quad \text{and} \quad \tilde{\Lambda}_{YY}(\tau) = B^2(e^{\varphi(\tau)} - e^{-\varphi(\tau)}), \tag{4.9}$$

where $\varphi(\tau) = \int_0^\infty \omega^{-2} J(\omega)(\coth(\beta\omega/2)\cos\omega\tau - i\sin\omega\tau)d\omega$. As with the variational master equation given in Eq. 3.41, we may simplify the phonon dissipator by expanding the system operators in the eigenbasis such that the dissipator takes the form:

$$\mathcal{K}_{th}\left[\rho(t)\right] = -([X, \Phi_X\rho(t)] + [\rho(t)\Phi_X^\dagger, X] + [Y, \Phi_Y\rho(t)] + [\rho(t)\Phi_Y^\dagger, Y]), \tag{4.10}$$

with the rate operators defined as

$$\begin{aligned}
\Phi_X &= \int_0^\infty \tilde{\Lambda}_{XX}(\tau)e^{-i\tilde{H}_s\tau}Xe^{i\tilde{H}_s\tau}d\tau = \sum_{jk} X_{j,k}\int_0^\infty \tilde{\Lambda}_{XX}(\tau)e^{-i\lambda_{jk}\tau}|\psi_j\rangle\langle\psi_k|d\tau, \\
\Phi_Y &= \int_0^\infty \tilde{\Lambda}_{YY}(\tau)e^{-i\tilde{H}_s\tau}Ye^{i\tilde{H}_s\tau}d\tau = \sum_{jk} Y_{j,k}\int_0^\infty \tilde{\Lambda}_{YY}(\tau)e^{-i\lambda_{jk}\tau}|\psi_j\rangle\langle\psi_k|d\tau,
\end{aligned} \tag{4.11}$$

where the states $|\psi_j\rangle$ satisfy the relation $\tilde{H}_s|\psi_j\rangle = \psi_j|\psi_j\rangle$. We have also defined $X_{j,k} = \langle\psi_j|X|\psi_k\rangle$, $Y_{j,k} = \langle\psi_j|Y|\psi_k\rangle$, and $\lambda_{jk} = \psi_j - \psi_k$. Notice that in the limit that the cavity is taken to be a classical field, that is, the cavity operators are replaced with complex numbers, we recover the polaron limit of the variational master equation for a classically driven QD derived in Chapter 3.

When referring to the phenomenological treatment in which the bath is assumed to lead only to pure dephasing of the TLE coherences, the Hamiltonian in Eq. 4.7 reduces to that given in Eq. 4.3, i.e. $\tilde{H}_s \to H_s$, while the polaron dissipator becomes:

$$\mathcal{K}_{\text{th}}[\rho(t)] \to \mathcal{K}_{\text{pd}}[\rho(t)] = \frac{\Gamma}{2}\mathcal{L}_{\sigma_z}[\rho(t)] = \Gamma\left(\sigma_z\rho(t)\sigma_z - \rho(t)\right),$$

where Γ defines the pure dephasing rate.

4.3.2 Cavity loss and spontaneous emission

As mentioned, in addition to phonon emission and absorption, there are several other loss processes to consider in cavity QED. Specifically, one must account for photon losses from both the top and sides of the cavity, as well as emission from the TLE directly into the electromagnetic field.

Consider the Hamiltonian of the electromagnetic environments in a rotating frame with respect to the driving frequency, $H = H_s + H_I^{TLS} + H_I^{Cav} + H_B^{TLS} + H_B^{Cav}$, where:

$$\begin{aligned}
H_I^{TLS} &= \sum_k \left(h_k^*\sigma a_k^\dagger e^{i\omega_l t} + h_k\sigma^\dagger a_k e^{-i\omega_l t}\right), \\
H_I^{Cav} &= \sum_{j=1,2}\sum_k \left(g_{j,k}^* a_{j,k}^\dagger a \; e^{i\omega_l t} + g_{j,k}a_{j,k}a^\dagger e^{-i\omega_l t}\right),
\end{aligned} \tag{4.12}$$

and H_B^{Cav} and H_B^{QD} are the free Hamiltonians of the associated fields. Here h_k is the coupling strength between the TLS and and the k^{th}-mode EM field, and $g_{j,k}$ is the coupling between the cavity and k^{th}-mode field associated to lost through the top mirror ($j = 1$) and the side of the cavity ($j = 2$).

From this Hamiltonian we may derive a 2^{nd}-order master equation for each electromagnetic environment independently as there is no coupling directly between the fields and, by assuming these environments have flat spectral densities, we may move into the interaction picture with respect to the free Hamiltonian as in Sec. 3.2.1. In the limit that each electromagnetic environment is in its ground state (zero temperature), this leads to a master equation of the form:

$$\begin{aligned}\frac{\partial \rho}{\partial t} =& - i\left[H_s, \rho(t)\right] + \mathcal{K}_{\text{th}}[\rho(t)] + \frac{\kappa + \kappa_s}{2}\left(2a\rho(t)a^\dagger - \left\{a^\dagger a, \rho(t)\right\}\right) \\ &+ \frac{\gamma}{2}\left(2\sigma\rho(t)\sigma^\dagger - \left\{\sigma^\dagger\sigma, \rho(t)\right\}\right),\end{aligned} \tag{4.13}$$

where γ is the TLE spontaneous emission, κ is the loss rate through the top of the cavity, and κ_s is the loss through the sides.

4.3.3 Input-Output formalism

In many CQED systems it is often not possible to directly probe properties of the system, but rather one measures the radiation emitted by the cavity. In order to relate the optical properties of the system to the expectation values extracted from the master equation we make use of the input-output formalism [85, 86]; this allows us to draw a formal connection between the reduced state of the cavity-TLE system and the state of the field outside the cavity, from which we may obtain an expression for the cavity reflectivity.

In this section we shall derive the input-output relations for the radiation emitted through the mirrors of an optical cavity. The approximations used to obtain the input-output relations allow one to consider each environment independently, thus we can simplify the derivation significantly by considering only the field emitted through the cavity mirrors. The phonon interactions, side leakage, and spontaneous emission of the TLE are then accounted for at the master equation level when calculating system expectation values. The light-matter coupling Hamiltonian for a driven CQED system in the lab-frame is $H = H_s + H_I + H_E$, where we have defined:

$$\begin{aligned}H_s =& \omega_X\sigma^\dagger\sigma + g\left(\sigma^\dagger a + \sigma a^\dagger\right) + \eta\left(a^\dagger e^{-i\omega_l t} + a e^{i\omega_l t}\right) + \omega_c a^\dagger a, \\ H_I =& \int_0^\infty d\omega f(\omega)\left(b(\omega)a^\dagger + b^\dagger(\omega)a\right), \\ H_E =& \int_0^\infty d\omega\ \omega b^\dagger(\omega)b(\omega),\end{aligned} \tag{4.14}$$

where for convenience we have already taken the continuum limit of the field modes, with $f(\omega)$ defining the coupling strength between the modes and the electromagnetic environment. From the above Hamiltonian we can derive the following Heisenberg equations of

motion:

$$\begin{aligned}\frac{\partial a(t)}{\partial t} &= i\left[H,a\right] = -ig\sigma(t) - i\omega_c a(t) - i\int_{-\infty}^{\infty} d\omega f(\omega) b(t,\omega) - i\eta e^{-i\omega_l t},\\ \frac{\partial b(t,\omega)}{\partial t} &= -if(\omega)a(t) - i\omega b(t,\omega).\end{aligned} \tag{4.15}$$

Note that we have made our first approximation here; by assuming that the modes of the external environment important to the evolution of the cavity are those close to resonance, we are able to extend the frequency integral to $-\infty$. We can eliminate the external field operators from the cavity equation of motion by finding the formal solution for the environmental degrees of freedom, which can be done by recognising:

$$\frac{\partial}{\partial t}\left\{e^{i\omega t}b(t,\omega)\right\} = e^{i\omega t}\left(i\omega b(t,\omega) + \frac{\partial b(t,\omega)}{\partial t}\right) = -if(\omega)a(t). \tag{4.16}$$

Integrating this expression formally, the limits that we take will specify whether we get the input (state of the field modes at times earlier than t) or the output fields (state of the field modes at times later than t). Consider first the case of the input field, where we have:

$$e^{i\omega t}b(t,\omega) - e^{i\omega t_0}b_0(\omega) = -if(\omega)\int_{t_0}^{t} dt' a(t')e^{i\omega t'}, \tag{4.17}$$

where $t_0 < t$ and the initial condition of the environment is denoted $b_0(\omega) = b(t_0,\omega)$. Rearranging this expression to obtain a formal solution for the external field mode we have:

$$b(t,\omega) = e^{-i\omega(t-t_0)}b_0(\omega) - if(\omega)\int_{t_0}^{t} dt' a(t')e^{i\omega(t'-t)}. \tag{4.18}$$

Substituting this into the expression for the cavity field, we have:

$$\begin{aligned}\frac{\partial a(t)}{\partial t} =& -ig\sigma(t) - i\omega_c a(t) - i\int_{-\infty}^{\infty} d\omega f(\omega) b_0(\omega) e^{-i\omega(t-t_0)}\\ &- \int_{t_0}^{t} dt' \int_{-\infty}^{\infty} d\omega f^2(\omega) a(t') e^{i\omega(t'-t)} - i\eta e^{-i\omega_l t}.\end{aligned} \tag{4.19}$$

As is consistent with the master equation derivation, we can greatly simplify this expression by assuming the spectrum of the external environment is flat, that is, $f(\omega) \approx \sqrt{\kappa/2\pi} =$ const. This is effectively a Markov approximation as it implicitly assumes that the two-time correlation function of the environment is a δ-function, that is, the time-scale over which the environment relaxes to equilibrium is significantly faster than any relevant system timescale. Using this approximation we can simplify the above equation using the definition of the δ-function:

$$\int_0^{\infty} d\tau y(\tau) \int_{-\infty}^{\infty} d\omega e^{-i\omega\tau} = 2\pi \int_0^{\infty} d\tau y(\tau)\delta(\tau), \tag{4.20}$$

where $y(\tau)$ is a function of τ. This gives the equation:

$$\frac{\partial a(t)}{\partial t} = -ig\sigma(t) - i\omega_c a(t) - \frac{\kappa}{2}a(t)e^{-i\omega_l t} - \sqrt{\kappa}a_{in}(t) - i\eta e^{-i\omega_l t}, \tag{4.21}$$

where we have defined the *input field* as:

$$a_{in}(t) = \frac{i}{\sqrt{2\pi}}\int_{-\infty}^{\infty} d\omega e^{-i\omega(t-t_0)}b_0(\omega). \tag{4.22}$$

This field describes a collective degree of freedom of the external field incident on the cavity at times less than t. We can now follow the same procedure to gain an expression in terms of the output field, this time we integrate Eq. 4.16 from t to t_1 (i.e. $t_1 > t$):

$$e^{i\omega t_1}b_1(\omega) - e^{i\omega t}b(t,\omega) = -if(\omega)\int_t^{t_1} dt' a(t')e^{i\omega t'}, \tag{4.23}$$

with $b_1(t,\omega) = b(t_1,\omega)$. Rearranging this gives:

$$b(t,\omega) = b_1(\omega)e^{-i\omega(t-t_1)} + if(\omega)\int_t^{t_1} dt' a(t')e^{-i\omega_l t'}e^{-i\omega(t-t')}. \tag{4.24}$$

Substituting this expression into the Heisenberg equation for the cavity field, we have:

$$\begin{aligned}\frac{\partial a(t)}{\partial t} =& -ig\sigma(t) - i\omega_c a(t) - i\int_{-\infty}^{\infty} d\omega f(\omega)b_1(\omega)e^{-i\omega(t-t_1)} \\ &+ \int_t^{t_1} dt' \int_{-\infty}^{\infty} d\omega f^2(\omega)a(t')e^{i\omega(t'-t)} - i\eta e^{-i\omega_l t}.\end{aligned} \tag{4.25}$$

We can now define the output field as:

$$a_{out}(t) = \frac{i}{\sqrt{2\pi}}\int_{-\infty}^{\infty} d\omega b_1(\omega)e^{-i\omega(t-t_1)}, \tag{4.26}$$

leading to the equation:

$$\frac{\partial a(t)}{\partial t} = -ig\sigma(t) - i\omega_c a(t) - \sqrt{\kappa}a_{out}(t) + \frac{\kappa}{2}a(t) - i\eta e^{-i\omega_l t}. \tag{4.27}$$

By subtracting Eq. 4.21 and 4.27 we can obtain the input-output relations:

$$a_{out}(t) - a_{in}(t) = \sqrt{\kappa}a(t). \tag{4.28}$$

Studying Eq. 4.21, it is clear that rather than defining a driving term with the Hamiltonian, we may incorporate our classical driving field into the input field. This corresponds to having a coherent state of the electromagnetic environment incident on the cavity, such

that:

$$a_{in}(t) \longrightarrow i\frac{\eta}{\sqrt{\kappa}}e^{-i\omega_l t} + \tilde{a}_{in}(t), \tag{4.29}$$

where $\tilde{a}_{in}(t)$ now represents the vacuum contribution. Using the input-output relation we may now define the complex reflection coefficient of the cavity [42, 77]:

$$a_{out}(t) = ra_{in}(t), \tag{4.30}$$

where $r \in \mathbb{C}$ is the reflectivity of the cavity. To gain numerical values for the cavity reflectivity we shall find steady state expectation values of the cavity operator from the master equation given in Eq. 4.13. However, the input-output relations in Eq. 4.28 are defined in the lab frame, while Eq. 4.13 is written in a frame rotating with respect to the driving frequency ω_l. Thus, transforming to a frame rotating with respect to the driving frequency, we have:

$$\begin{aligned}\langle a(t)\rangle_{lab} &= \mathrm{tr}\left(a\varrho(t)\right) = \mathrm{tr}\left(\mathcal{U}_{rot}(t)a\mathcal{U}^{\dagger}_{rot}(t)\mathcal{U}_{rot}(t)\varrho(t)\mathcal{U}^{\dagger}_{rot}(t)\right), \\ &= \mathrm{tr}\left(a\rho(t)\right)e^{-i\omega_l t} = \langle a(t)\rangle e^{-i\omega_l t},\end{aligned} \tag{4.31}$$

where $\varrho(t)$ and $\rho(t)$ are the lab and rotating frame density operators respectively, and $\langle a(t)\rangle$ is the expectation value in the rotating frame, which can be calculated directly from the master equation given in Eq. 4.13. Taking expectation values in Eq. 4.30 we obtain the expression:

$$r = \frac{\langle a_{out}\rangle}{\langle a_{in}\rangle} = 1 + \sqrt{\kappa}\frac{\langle a\rangle_{lab}}{\langle a_{in}\rangle} = 1 + \sqrt{\kappa}\frac{\langle a\rangle e^{-i\omega_l t}}{i\eta e^{-i\omega_l t}/\sqrt{\kappa}} = 1 - i\kappa\frac{\langle a\rangle}{\eta}. \tag{4.32}$$

From this expression we can extract both the magnitude of the reflected light, $|r|$, and also the phase shift imparted on the reflected light, φ, using $r = |r|e^{i\varphi}$, where $\varphi = \arg(r)$.

4.4 Phonon Induced Asymmetries

4.4.1 The semi-classical regime of cavity QED

Having outlined our theoretical approach, let us focus our analysis on what we shall term the intermediate coupling regime, as it has particular experimental relevance to optical microcavities [75, 76]. Here, $\kappa + \kappa_s \gtrsim g > \gamma$, such that cavity leakage is significant. For an atomic system, this regime is characterised by a symmetric double peak structure in both the steady state TLE population and cavity occupation on scanning a weak driving field through resonance. In the cavity case, this can be seen by the dashed curve in Fig. 4.2 (left) which treats the TLE-cavity coupling fully quantum mechanically (through H_s), but includes the host environment only through a phenomenological pure dephasing process. The peaks lie at resonances of the first two eigenstates of the TLE-cavity system, that is, the first rung of the dressed state ladder [see Fig. 4.1(b)]. However, unlike the true QSC regime (in which $g > \kappa + \kappa_s, \gamma$), the broad cavity transition obscures contributions from higher order dressed states, allowing an effective semiclassical description to be derived [76,

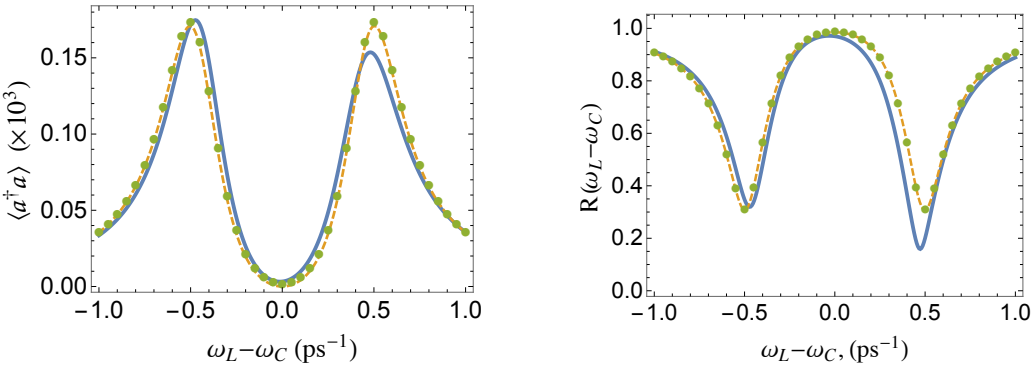


Figure 4.2: Steady-state cavity occupation (left) and reflectivity (right) in the intermediate coupling regime for the semiclassical (points), pure dephasing (dashed) and full polaron (solid) master equations. Here, the driving strength is weak, $\eta = 0.01\kappa$, with other parameters chosen to be relevant to QD-microcavity setups [76]: $\kappa = g = 0.5$ ps^{-1}, $\kappa_s = 0.5\kappa$, $\gamma = 0.01\kappa$, $\Gamma = 0.005\kappa$, $\alpha = 0.05$ ps^2, $\Lambda = 2$ ps^{-1}, and $T = 4$ K.

77]. The double peak structure may then be interpreted simply as a normal mode splitting between two classical oscillators. This can be shown by considering the relevant optical Bloch equations, obtained from the pure dephasing master equation in the rotating frame:

$$\frac{\partial\langle\sigma\rangle}{\partial t} = -\left(i\nu + \frac{\gamma}{2} + 2\Gamma\right)\langle\sigma\rangle + ig\langle\sigma_z a\rangle, \tag{4.33}$$

$$\frac{\partial\langle a\rangle}{\partial t} = -\left(i\nu + \frac{\kappa+\kappa_s}{2}\right)\langle a\rangle - ig\langle\sigma\rangle - i\eta, \tag{4.34}$$

with $\langle\hat{O}\rangle = \mathrm{tr}(\hat{O}\rho)$. By applying a mean-field approximation between the cavity and TLE, such that $\langle\sigma_z a\rangle \approx \langle\sigma_z\rangle\langle a\rangle$, we neglect any quantum light-matter correlations and is equivalent to assuming that the density operator of the cavity and emitter is separable. From these equations we may extract expressions for the steady state of the form:

$$\langle\sigma\rangle = \frac{g\eta\langle\sigma_z\rangle}{\left(i\nu + \frac{\gamma+2\Gamma}{2}\right)\left(i\nu + \frac{\kappa+\kappa_s}{2}\right) - g^2\langle\sigma_z\rangle} \quad \text{and} \quad \langle a\rangle = \frac{i\eta\left(i\nu + \frac{\gamma+2\Gamma}{2}\right)}{\left(i\nu + \frac{\gamma+2\Gamma}{2}\right)\left(i\nu + \frac{\kappa+\kappa_s}{2}\right) - g^2\langle\sigma_z\rangle}.$$

In the weak driving limit, we may further assume that on average the TLE remains close to its ground state, such that $\langle\sigma_z\rangle \approx -1$ [77, 88]. For a sufficiently lossy cavity and weak driving, the resulting semiclassical theory agrees perfectly with the pure dephasing approach, as demonstrated in Fig. 4.2.

4.4.2 Phonon induced asymmetries

Discrepancies in the reflectivity spectra become apparent, however, when comparing to the full (polaron) master equation which treats *both* the TLE-cavity coupling and the thermal environment quantum mechanically. We now see a shift in the peak positions due to bath renormalisation of the TLE-cavity coupling, and an asymmetry in the cavity population that was entirely absent in either the pure dephasing or semiclassical calculations. Clearly, such simplified approaches are unable to properly capture the physics of our system in the presence of the host environment. Importantly, this implies that the semiclassical

description breaks down here even within the lossy cavity regime, as we shall quantify below, and thus the addition of a thermal environment generates quantum correlations within our system.

Fig. 4.2 (right) compares the cavity reflectivity spectra for the same intermediate coupling parameters as the cavity population just described. We see that while the semi-classical theory once again agrees with the pure dephasing master equation, capturing the characteristic normal mode splitting as expected, in the polaron treatment the suppression of the cavity population for $\omega_L - \omega_c > 0$ is exhibited also in asymmetries within the cavity reflectivity.

We can attribute these asymmetric features to the quantum mechanical nature of the host environment, which plays a vital role in determining the system dynamics. In Fig. 4.2, where we have chosen parameters relevant to the acoustic phonon environment common in QD-microcavity systems, bath-induced transitions occur on a faster timescale than other dissipative processes, i.e. cavity leakage and spontaneous emission. The phonon bath is thus sensitive to coherence shared between the cavity and QD emitter, with the result that it mediates transitions directly between the emitter-cavity dressed states. Specifically, when we tune the driving field to the upper dressed state resonance ($\omega_L - \omega_c \approx 1$ ps^{-1}), phonon emission allows population to transfer from the upper to the lower dressed state, with an associated loss of energy to the environment. This leads to a suppression of the upper dressed state population and also of the reflected light. Provided that the temperature is not too high, the inverse process, which raises population from the lower to the upper dressed state by phonon absorption, is comparatively weaker. Thus, in Fig. 4.2, we see that for negative detunings between the cavity and driving field ($\omega_L - \omega_c < 0$), the lineshapes of the polaron and semiclassical theories are very similar. The resulting asymmetries herald a failure of the semiclassical theory, which by definition cannot be sensitive to the coherence shared between the TLE and cavity. This is a somewhat counterintuitive point. Naively one might think of phonons purely as a source of decoherence, that is, as giving rise to processes that should push the system towards a more classical description. However, here we see that the sensitivity of the host environment to quantum correlations in fact results in the breakdown of the semiclassical description of our system, and we must instead reinstate a quantum mechanical explanation.

4.4.3 Phonon induced light-matter correlations

Further quantitative insight into departures from the semiclassical theory can be gained by considering the correlation error (CE), defined in Ref. [89] as:

$$\mathrm{CE} = \frac{|\langle \sigma^\dagger a \rangle - \langle \sigma^\dagger \rangle \langle a \rangle|}{|\langle \sigma^\dagger a \rangle|}. \tag{4.35}$$

This measure quantifies deviations of the cavity-TLE expectation to the mean field values, providing an indication of how accurate the semi-classical approximation is, and in our case, giving insight into the correlations generated by phonon processes.

Fig. 4.3 (left) shows the CE for both the phenomenological pure dephasing (dashed)

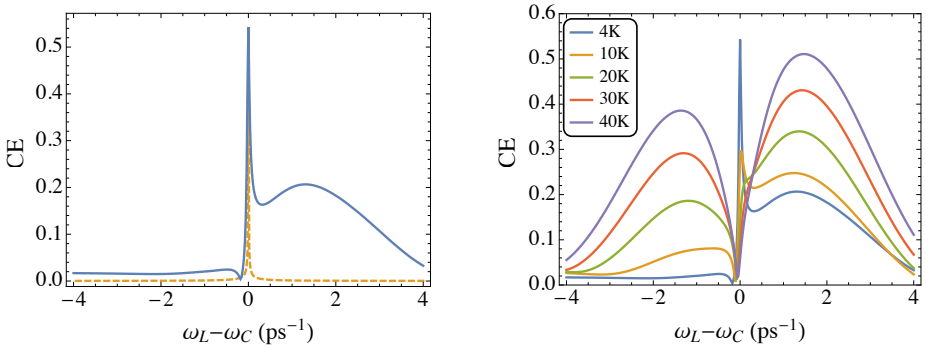


Figure 4.3: Left: Correlation error as a function of detuning comparing the phenomenological (dashed) and full polaron (solid) master equations at $T = 4$ K. Right: Correlation error at increasing temperature (lower to upper curves) for the full polaron master equation. All other parameters are as in Fig 4.2.

and full polaron (solid) master equations at $T = 4$ K. The phenomenological theory shows deviations from semiclassicality only when driving at the cavity resonance, and most importantly not at all around the TLE-cavity dressed state resonances. In contrast, within the full theory significant correlations are apparent across a much broader range of driving frequencies, induced by the action of the thermal environment. Due to the low temperature considered, this behaviour is asymmetric about the cavity resonance. Hence, when driving around the lower dressed state, the host environment has little effect, which leads only to a small CE and the semiclassical theory giving an accurate account of the TLE-cavity behaviour. However, at positive detuning significant correlations are apparent, unambiguously demonstrating the breakdown of the semiclassical description of the TLE-cavity system due to the presence of the thermal environment.

4.4.4 Cavity florescence spectra

It is natural to ask whether the effects we predict are robust against variations in temperature. The asymmetries in the cavity lineshapes presented in Fig. 4.2 do indeed decrease as a function of increasing temperature due to environmental absorption processes balancing emission. However, from Fig. 4.3 (right) we see that the off-resonant CE is enhanced substantially as a function of temperature for both positive and negative detuning, in the latter case due to absorption processes generating correlations between the emitter and cavity. Thus the semiclassical description of the light-matter degrees of freedom remains insufficient to characterise the TLE-cavity system even as temperature is increased. Despite the fact that lineshape asymmetries decrease at high temperatures, deviations from the semiclassical theory can still be observed experimentally by looking at the spectra of photons emitted from the cavity when driving either the lower or upper dressed state resonantly (confirming also that environmental transitions do indeed drive population between the dressed states). In the former case, only at low temperatures should we expect emission centred solely around the lower dressed state, while in the latter, bath-mediated transitions should lead to emission from both the lower and upper dressed states at all temperatures, in stark contrast to the conventional expectation.

In Fig. 4.4 we plot the cavity incoherent emission spectrum, which is defined in direct

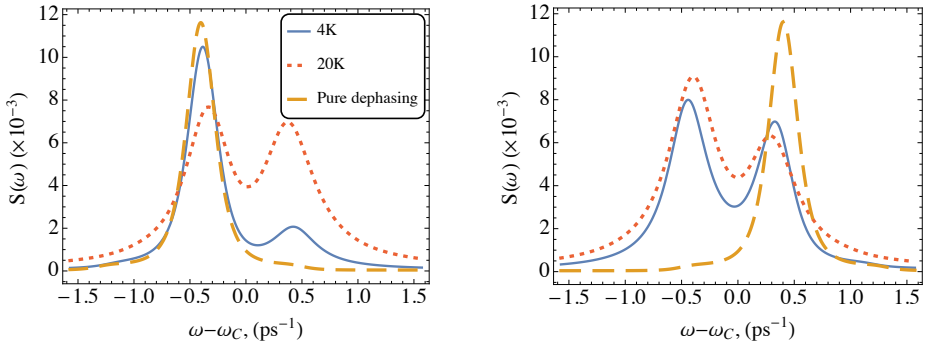


Figure 4.4: Comparison of the cavity emission spectra using the phenomenological (dashed curve) and full polaron (solid curve) master equations, under resonant excitation of the lower dressed state (left) and the upper dressed state (right) transitions. Parameters are as in Fig. 4.2, except $\eta = 0.1$ ps^{-1}.

analogy to the classically driven QD:

$$S(\omega) \propto \mathrm{Re}\left[\int_0^\infty g^{(1)}_{inc}(\tau) e^{i(\omega_L-\omega)\tau} d\tau\right],$$

with $g^{(1)}_{inc}(\tau) = \lim_{t\to\infty}\langle a^\dagger(t+\tau)a(t)\rangle - |\langle a^\dagger\rangle_{ss}|^2$ obtained from our master equation using the quantum regression theorem, as described in Sec. 2.2.2 and used in Chapter 3 [9]. Here $\langle a^\dagger\rangle_{ss}$ is the steady state expectation value of the cavity operator, which describes coherent emission. At low temperatures (solid curve) Fig. 4.4 (left) shows the expected resonant response from a normal mode, with a dominant peak around the driven lower dressed state transition. The spectra calculated either with the phenomenological (pure dephasing) or polaron master equations remain similar, with only a small noticeable effect of including the thermal environment in a rigorous manner. However, the low temperature spectra become markedly different when we drive the upper dressed state, as shown in Fig. 4.4 (right). While the phenomenological theory again shows a single dominant peak – now at the upper dressed state resonance and symmetric to the previous case – in the polaron theory we see the emergence of an additional feature. In fact, bath-mediated dressed state transitions lead here to a strong suppression of the peak around the upper dressed state, and correspondingly to substantial emission at the (undriven) lower dressed state frequency. For larger temperatures (dotted curves) significant population is also promoted from the lower to the upper dressed state, leading to dramatic changes in the emission spectra also when driving the lower dressed state. Hence, by measuring the spectra of light emitted from the cavity, we can unambiguously demonstrate the presence of bath-mediated transitions between the joint eigenstates of the emitter-cavity system at both low and high temperatures, evidencing also the quantum mechanical nature of the host environment.

4.4.5 Beyond the Intermediate coupling regime

Finally, it is worth mentioning that the sensitivity of the environment to the underlying TLE-cavity eigenstructure is not restricted to the intermediate coupling regime, but is in fact present over wider regions of parameter space. Here we shall demonstrate that similar

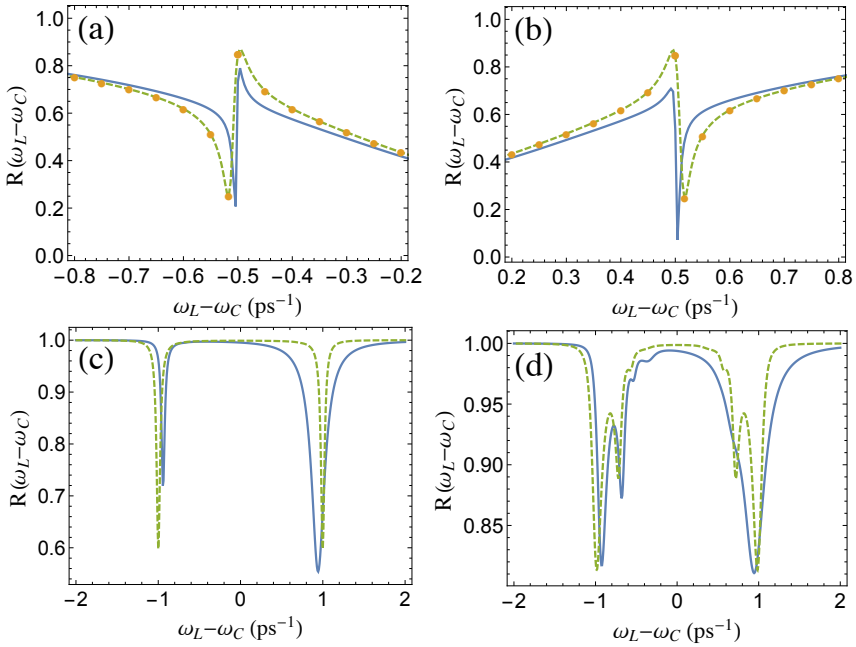


Figure 4.5: Upper: Asymmetry in Fano resonance profiles between emitter-cavity detuning $\omega_c - \omega_x = -0.5$ ps^{-1} (a), and $\omega_c - \omega_x = 0.5$ ps^{-1} (b). Parameters are $\eta = 0.003$ps^{-1}, $\kappa = 1$ ps^{-1}, $g = 0.1$ ps^{-1}, $\Gamma = 0.001$ ps^{-1}, $\kappa_s = 0.5$ ps^{-1}, $\gamma = 1/700$ ps^{-1}, $\Lambda = 2.8$ ps^{-1}, $\alpha = 0.3$ ps^{-1}, and $T = 2$ K. Lower: Thermal effects in the QSC regime at weak driving $\eta = 0.005$ ps^{-1} (c), and strong driving $\eta = 0.08$ ps^{-1} (d). Parameters are $\kappa = 0.1$ ps^{-1}, $g = 1$ ps^{-1}, $\Gamma = 0.01$ ps^{-1}, $\kappa_s = 0$, $\gamma = 1/700$ ps^{-1}, $\Lambda = 2.8$ ps^{-1}, $\alpha = 0.025$ ps^{-1}, and $T = 4$ K.

effects emerge in the both the Fano and the quantum strong coupling (QSC) regimes.

The Fano regime of cavity QED occurs when $\kappa + \kappa_s \gg g \gg \gamma$. This regime is characterised by a sharp peak in the cavity reflectivity at the emitter resonance, while the rest of the cavity line-shape remains unchanged, which is the result of classical interference between two competing decay pathways [90]. This behaviour can be seen in line-shapes given in Fig. 4.5(a) and (b). Here we see excellent agreement between the semiclassical theory and the pure dephasing master equation, showing a sharp peak in the reflectivity spectra at the emitter resonance $\Delta = \pm 0.5$ ps^{-1}, which is symmetric for both the positively and negatively detuned case. Though less pronounced than in the intermediate coupling regime, environmental induced asymmetries become apparent when comparing the cavity line-shape obtained from the full polaron master equation for an emitter tuned above the cavity resonance ($\omega_c - \omega_X = 0.5$ ps^{-1}) and below ($\omega_c - \omega_X = -0.5$ ps^{-1}).

In the QSC limit [Fig. 4.5 (c) and (d)], the coupling strength g becomes the dominant energy scale, $g \gg \kappa + \kappa_s, \gamma$, which allows contributions from higher order dressed states to be resolved. Additionally, the long cavity lifetime results in host environmental influences becoming particularly significant. This is especially true at strong driving, shown in Fig. 4.5(d), where in the polaron theory the asymmetric broadening is so pronounced that it prevents us from resolving any higher order contributions to the upper dressed state resonance.

4.5 Summary and Discussion

In summary, we have shown that the presence of a thermal environment allows one to generate light-matter quantum correlations in CQED systems within otherwise semiclassical regimes. Importantly, despite its regular use in the literature, the pure dephasing model is simply insufficient to describe the emission characteristics of cavity-QD systems in a broad range of parameter regimes. Sensitivity of the environment to the coherence shared between the TLE and cavity leads to direct transitions between their joint eigenstates, and consequently a breakdown of the semiclassical approach. Thus, the microscopic behaviour of the phonon environment must be accounted for in theoretical descriptions of the system to accurately describe the cavity emission.

A key requirement for phonon asymmetries to be present in the reflectivity and emission spectra of solid-state cavity QED systems is for the time-scale associated to photon losses are longer than those associated to phonon processes, thus allowing phonon transitions to take place. For typical optical micropillar systems operating in the intermediate regime phonon processes occur on the sub-picosecond time-scale [13, 14] while cavity loss rates vary widely from tens to hundreds of picoseconds [70, 76, 91], depending primarily on differing fabrication techniques. This satisfies the requirement for phonon asymmetries to be present, however, in order for these effects to be unambigiously observed experimentally, the fluorescence spectra of the cavity must also be resolved over energy scale associated to the light-matter coupling strength. For example, in micropillar systems the light-matter coupling strength varies significantly depending on the the placement of the QD within the cavity. To be explicit, the light-matter coupling can range from $g = 0.022$ ps^{-1} (15 μeV) [76] to $g = 0.068$ ps^{-1} (45 μeV) [70] and in some cases even as high as $g = 0.17$ ps^{-1} (107 μeV) [92]. This energy scale is sufficiently large to be resolved by modern interferometer set-ups using cross-polarisation schemes to isolate the cavity emission.

Since the effects also persists over a broad range of parameters regimes of cavity QED it is possible to observe phonon induced asymmetries in a number of other solid-state photonic devices, e.g. photonic crystal cavities [18, 71–74], diamond colour centres [73, 93, 94], and superconducting circuits [68, 69, 95].

CHAPTER 5

THE REACTION COORDINATE FORMALISM

5.1 Introduction

A quantum system coupled to its macroscopic environment constitutes a challenging theoretical problem in which the large number of environmental degrees of freedom can lead to both conceptual and practical difficulties [2, 4, 11, 96, 97]. The master equation formalism has been developed to offer a simple and intuitive approach for describing such systems; the complex dynamical evolution of the many-body environment is not tracked explicitly, but instead only its effect on the reduced state of the system of interest is considered, eliminating all information on the environmental state. In most cases one must also rely on a series of assumptions in deriving a tractable master equation[1]. These customarily neglect the formation of system-bath correlations and lead to the eventual thermalisation of the system with respect solely to its internal Hamiltonian, resulting in canonical equilibrium states.

However, as discussed in Chapters 3 and 4 there are numerous situations of practical relevance where system-environment coupling can be strong and/or non-Markovian memory effects important, rendering traditional master equation treatments insufficient to describe the system dynamics. In the context of QDs, we overcame these restrictions by way of the polaron formalism; this enabled us to derive a master equation valid in the strong system-environment coupling regime. However, the variational master equation still relies on important environmental energy scales being much larger than those of the system, thus defining a perturbative treatment in terms of system parameters instead of the usual system-bath coupling [87]. An obvious question then arises: how do we describe an open quantum system in regimes where no clear perturbative parameter exists?

Here, by incorporating a collective coordinate of the environment into an effective system Hamiltonian, we develop a master equation formalism valid in such a regime. This enables us to straightforwardly determine key environmental properties as well as track the dynamic generation of correlations between the system and bath. Specifically, we characterise the departure of the environment from its initial Gaussian thermal state due to interactions with the quantum system, and show that the resulting correlations — both

[1] As discussed in previous chapters, the most common are the Born-Markov approximations, wherein the bath is assumed to be static, memoryless, and uncorrelated with the system, remaining in thermal equilibrium throughout the dynamical evolution [2].

quantum and classical, measured in terms of the mutual information — can have a profound effect on the system dynamics too, even persisting into the steady-state. We demonstrate that system-bath correlations are in fact generated on two distinct timescales, with long-lived correlations leading to a departure of the system steady-state from canonical equilibrium, as would otherwise be expected from a perturbative (Born-Markov) treatment, thus heralding the failure of the accepted statistical mechanics view of thermalisation [2]. Correctly capturing system-environment correlations is hence shown to be crucial in order to properly describe both the system transient and equilibrium behaviour. As a further, and unique, aspect of our approach we illustrate how noncanonical equilibrium states can still be characterised in terms of thermal states, but now with respect to the *effective* system-collective coordinate Hamiltonian. This also reveals simple experimental signatures by which deviations from canonical thermodynamics can be observed in real physical systems, for example through measurements of system populations.

5.2 Reaction coordinate mapping and master equation

Our method relies on keeping track of a collective environmental degree of freedom, and to do so we make use of the reaction coordinate mapping [98–107]; we take a quantum system coupled to a bosonic environment and map to a model in which a collective mode of the environment, known as the reaction coordinate (RC), is incorporated within an effective system Hamiltonian. We then treat the residual environment within a full second-order Born-Markov master equation formalism. By comparing the RC master equation to the numerically exact hierarchical equations of motion (HEOM) [108, 109] we demonstrate essentially perfect agreement in the dynamics across all timescales (see below). Thus, all important system-bath, and indeed intra-bath [50, 51], correlations are incorporated into the system-RC Hamiltonian in the regimes we study.

Though our approach may be applied quite generally, we shall focus in this work on a two-level system (TLS) described by the spin-boson Hamiltonian [2, 4, 8, 11, 39, 49, 96, 97, 110–116]:

$$H = \frac{\epsilon}{2}\sigma_z + \frac{\Delta}{2}\sigma_x + \sigma_z \sum_k f_k(c_k^\dagger + c_k) + \sum_k \nu_k c_k^\dagger c_k. \tag{5.1}$$

Here, $c_k^\dagger$ (c_k) are creation (annihilation) operators for bosonic modes of frequency ν_k, which couple to the TLS with strength f_k, and σ_i ($i = x, y, z$) are TLS Pauli operators defined such that $\sigma_z = |1\rangle\langle 1| - |2\rangle\langle 2|$, with the orthonormal basis of the TLS defined as $\{|1\rangle, |2\rangle\}$. In the absence of the bath, the TLS splitting is determined by the bias ϵ and tunneling Δ.

5.2.1 The Reaction Coordinate Mapping

We now apply a normal mode transformation to Eq. 5.1 to incorporate the most important environmental degrees of freedom into a new effective system Hamiltonian. We carry out this procedure by first defining a collective coordinate of the environment [98], the RC, which couples directly to the TLS, and is in turn coupled to a residual harmonic environment, as shown schematically in the left panel of Fig 5.1. This leads to a mapped

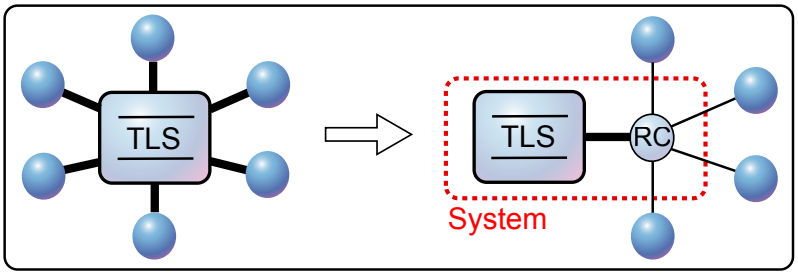


Figure 5.1: A TLS interacting with a bosonic environment (left) is mapped to a TLS coupled only to a collective mode, which is in turn damped by a residual bath (right).

Hamiltonian of the form:

$$H_{\mathrm{RC}} = \frac{\epsilon}{2}\sigma_z + \frac{\Delta}{2}\sigma_x + \lambda\sigma_z(a^\dagger + a) + \Omega a^\dagger a + \sum_k \omega_k b_k^\dagger b_k + (a^\dagger + a)\sum_k g_k(b_k^\dagger + b_k) + (a^\dagger + a)^2 \sum_k \frac{g_k^2}{\omega_k}, \tag{5.2}$$

where the collective coordinate is defined such that:

$$\lambda(\hat{a}^\dagger + \hat{a}) = \sum_k f_k(c_k^\dagger + c_k). \tag{5.3}$$

The TLS-RC coupling strength is given by $\lambda^2 = \sum_k f_k^2$, such that the RC creation and annihilation operators satisfy the canonical commutation relation $[a, a^\dagger] = 1$. This choice of coupling also fixes the RC frequency to be $\Omega^2 = \lambda^{-2}\sum_k \nu_k f_k^2$. The RC is now coupled linearly to a residual harmonic environment characterised by the spectral density $J_{\mathrm{RC}}(\omega) = \sum_k g_k^2\delta(\omega - \omega_k)$. There is also a term quadratic in the system operators in Eq. 5.2, known as the counter term, which is used to renormalise the mode frequency and avoid divergences due to friction [102, 117].

In order to give a concrete example we consider two specific spin-boson ohmic spectral densities commonly used in the chemical physics literature, specifically the under- and overdamped spectral densities. In this chapter our attention will be focused on the overdamped spectral density [118]:

$$J_{\mathrm{SB}}(\omega) = \frac{\alpha\omega_c\omega}{\omega^2 + \omega_c^2}, \tag{5.4}$$

with bath cut-off frequency ω_c and system-bath coupling strength α, giving a reorganisation energy of $\int_0^\infty J_{\mathrm{SB}}(\omega)/\omega = \pi\alpha/2$.

In Chapter 6 we shall also consider the underdamped spectral density [119, 120]

$$J_{SB}(\omega) = \frac{\alpha\Gamma\omega_0^2\omega}{(\omega^2 - \omega_0^2)^2 + \Gamma^2\omega^2}, \tag{5.5}$$

where the reorganisation energy is given by $\pi\alpha$ and the characteristic frequency of this spectral density are set by the parameters ω_0 and Γ. As we shall show, this spectral density is important in the description of excitonic energy transfer in molecular systems

in the presence of a structured environment. By choosing spectral densities above allows us to benchmark our results against data attained from the numerically exact HEOM.

In order to fully specify the mapping described above, we must relate the RC and spin-boson (SB) spectral densities. We do this by following the procedure first outlined by Garg et al. [98, 101] and derive the spectral density, both before and after the mapping, from the classical equations of motion [121]. Since the spectral density doesn't contain any information about the system itself, but rather just the coupling strength between the system and environment, it then follows that in Eq. 5.1 we can swap the TLS for a continuous classical coordinate q moving in a potential $V(q)$. This yields a Hamiltonian of the form

$$H_q = \frac{P_q^2}{2} + U(q) + q\sum_k \tilde{f}_k \hat{x}_k + q^2 \sum_k \frac{\tilde{f}_k^2}{2\nu_k^2} + \frac{1}{2}\sum_k \left(\hat{p}_k^2 + \nu_k^2 \hat{x}_k^2\right), \tag{5.6}$$

where, for simplicity, we have written Eq. 5.6 in the position representation, with coordinate and momentum operators of the environment defined as

$$\hat{x}_k = \sqrt{\frac{1}{2\nu_k}}(c_k^\dagger + c_k) \quad \text{and} \quad \hat{p}_k = i\sqrt{\frac{\nu_k}{2}}(c_k^\dagger - c_k), \tag{5.7}$$

and the coupling between the TLS and the k^{th} mode of the environment is given by $\tilde{f}_k = \sqrt{2\nu_k} f_k$. From this Hamiltonian, we attain a set of classical equations of motion:

$$\begin{aligned} \ddot{q}(t) &= -U'(q) - \sum_k \tilde{f}_k x_k(t) - q(t)\sum_k \frac{\tilde{f}_k^2}{\nu_k^2}, \\ \ddot{x}_k(t) &= -\tilde{f}_k q(t) - \nu_k^2 x_k(t). \end{aligned} \tag{5.8}$$

We can eliminate the bath variables from the equation of motion for the classical coordinate by making use of the Fourier transform, $\tilde{h}(z) = \int_{-\infty}^{\infty} h(t) e^{-izt} dt$. This leads to an equation of the form $\tilde{K}(z)\tilde{q}(z) = -\tilde{U}'(q)$, where the Fourier space operator is defined as

$$\tilde{K}(z) = -z^2\left(1 + \sum_k \frac{\tilde{f}_k^2}{\nu_k^2(\nu_k^2 - z^2)}\right) = -z^2\left(1 + \int_0^\infty d\nu \frac{J_{\mathrm{SB}}(\nu)}{\nu\,(\nu^2 - z^2)}\right). \tag{5.9}$$

For an Ohmic (odd) spectral density, we can evaluate this integral using the residue theorem, making use of the poles at $\nu = \pm z$, giving $\tilde{K}(z) = -z^2 + i\pi J_{\mathrm{SB}}(z)$. By writing $z = \omega - i\epsilon$, it follows that [121]

$$J_{\mathrm{SB}}(\omega) = \frac{1}{\pi}\lim_{\epsilon \to 0+} \mathrm{Im}\left[K(\omega - i\epsilon)\right]. \tag{5.10}$$

We now use the same procedure to write $\tilde{K}(z)$ in terms of the RC spectral density. Since the mapping at this stage is exact, then the Fourier transformed operator, $\tilde{K}(z)$, will be identical before and after the normal mode transformation. If we once again swap the TLS for a continuous coordinate, and write the RC Hamiltonian given in Eq. 5.2 in

position space, we then have

$$H_q = \frac{P_q^2}{2} + U(q) + \kappa q\hat{x} + \frac{\kappa^2}{2\Omega^2}q^2 + \frac{1}{2}\left(\hat{p}^2 + \Omega^2\hat{x}^2\right) + \hat{x}\sum_k \tilde{g}_k\hat{X}_k + \hat{x}^2\sum_k \frac{\tilde{g}_k^2}{2\omega_k^2} + \frac{1}{2}\sum_k\left(\hat{P}_k^2 + \omega_k^2\hat{X}_k^2\right), \tag{5.11}$$

where we have scaled the coupling strengths such that $\kappa = \sqrt{2\Omega}\lambda$ and $\tilde{g}_k = \sqrt{2\Omega}\sqrt{2\omega_k}g_k$, and the position and momentum operators are defined as

$$\begin{aligned} \hat{x} &= \sqrt{\tfrac{1}{2\Omega}}\left(a^\dagger + a\right) \qquad \text{and} \qquad \hat{p} = i\sqrt{\tfrac{\Omega}{2}}\left(a^\dagger - a\right), \\ \hat{X}_k &= \sqrt{\tfrac{1}{2\omega_k}}\left(b_k^\dagger + b_k\right) \qquad \text{and} \qquad \hat{P}_k = i\sqrt{\tfrac{\omega_k}{2}}\left(b_k^\dagger - b_k\right), \end{aligned} \tag{5.12}$$

This Hamiltonian leads to classical equations of motion of the form

$$\begin{aligned} &\ddot{q} + \kappa\hat{x} + \frac{\kappa^2}{\Omega^2}q = -U'(q), \\ &\ddot{\hat{x}} + \left(\Omega^2 + \sum_k \frac{\tilde{g}_k^2}{\omega_k^2}\right)\hat{x} + \kappa q + \sum_k \tilde{g}_k\hat{X}_k = 0, \\ &\ddot{\hat{X}}_\alpha + \tilde{g}_\alpha\hat{x} + \omega_\alpha^2\hat{X}_\alpha = 0. \end{aligned} \tag{5.13}$$

By moving to Fourier space and eliminating both the RC and environment from the equation of motion for the classical coordinate, we get the expression for the Fourier space operator

$$\tilde{K}(z) = -z^2 + \frac{\kappa^2}{\Omega^2}\frac{\mathcal{L}(z)}{\Omega^2 + \mathcal{L}(z)},$$

where, by using the definition of the RC spectral density, we have

$$\mathcal{L}(z) = -z^2\left(1 + \sum_k \frac{\tilde{g}_k^2}{\omega_k^2(\omega_k^2 - z^2)}\right) = -z^2\left(1 + 4\Omega\int_0^\infty \frac{J_{\mathrm{RC}}(\omega)}{\omega\left(\omega^2 - z^2\right)}d\omega\right). \tag{5.14}$$

Considering the RC to have an Ohmic spectral density of the form $J_{\mathrm{RC}}(\omega) = \gamma\omega\exp\left(-\omega/\Lambda\right)$, the integral reduces to $\mathcal{L}(z) = -z^2 + 2i\pi\Omega\gamma z$, in the limit $\Lambda \to \infty$. By plugging this into Eq. 5.10, we get the condition

$$J_{\mathrm{SB}}(\omega) = \frac{1}{\pi}\lim_{\epsilon\to 0+}\mathrm{Im}\left[\tilde{K}(\omega - i\epsilon)\right] = \frac{1}{\pi}\frac{2\pi\Omega\gamma\kappa^2\omega}{(\Omega^2 - \omega^2)^2 + (2\pi\Omega\gamma)^2\omega^2}. \tag{5.15}$$

Notice that this expression is of the same form as the spectral density given in Eq. 5.5, thus the RC mapping is exact for an underdamped environment. We shall explore this spectral density, and its effects on the dynamical evolution of the TLS, in the following chapter. In order for Eq. 5.15 to be consistent with the original overdamped spin-boson

spectral density, we identify the relations:

$$\omega_c = \frac{\Omega}{2\pi\gamma}, \qquad \text{and} \qquad \alpha = \frac{2\lambda^2}{\pi\Omega}, \tag{5.16}$$

which give us,

$$J_{\mathrm{SB}}(\omega) = \frac{\alpha\omega_c\omega}{\omega_c^2 - \frac{2\omega^2\omega_c^2}{\Omega^2} + \frac{\omega^4\omega_c^2}{\Omega^4} + \omega^2}. \tag{5.17}$$

Finally, by choosing γ such that $\omega_c \ll \Omega$ [99], we recover the spin-boson spectral density in (Lorentz-Drude) overdamped form,

$$J_{\mathrm{SB}}(\omega) = \frac{\alpha\omega_c\omega}{\omega^2 + \omega_c^2}. \tag{5.18}$$

The RC mapping presented in this work has many similarities with the chain mapping techniques for open quantum systems [105, 111, 122, 123]; here orthogonal polynomials are used to unitarily map a bosonic environment with a continuous spectral density to a semi-infinite 1D chain of Harmonic oscillators. In this mapped representation, the dynamics of the system may then be calculated using a variety of numerical techniques, for example variational matrix product states [124], or those based on density matrix renormalisation groups (DMRG) in the so-called Time Evolving Density with Orthogonal Polynomial Algorithm (TEDOPA) [111, 125, 126]. However, though the chain mappings may be applied to environments described by a broad set of spectral densities, there are a number of practical difficulties to consider when implementing these techniques. For example, at high temperatures the dimension of the composite Hilbert space becomes large due to high occupations numbers of each oscillator in the chain. Furthermore, in order to simulate the system dynamics the bosonic chain in the mapped Hamiltonian is terminated at some site, this leads to the reflection of excitation by the final site in the chain [124]. As a result large chain lengths, and therefore system dimensions, are often required in order to prevent numerical artefacts in the system dynamics. Thus, in order to accurately describe the system dynamics using the chain mapping approach, both sophisticated numerical techniques and significant computational resources are required.

In contrast, the relative simplicity of the RC model allows one to make use of the master equation formalism, thus greatly simplifying the dynamical description of the system. Furthermore, by terminating the RC with a Markovian environment, we prevent the possibility of reflection by the final site of the chain, therefore eliminating any unphysical recurrences in the dynamical evolution of the system.

5.2.2 Reaction coordinate master equation

We now wish to use Eq. 5.2 to derive a master equation treating the TLS-RC coupling exactly (up to some number of basis states in the RC) while the coupling to the residual environment is treated to second order within a Born-Markov approximation. To this end, we define the interaction Hamiltonian as:

$$H_I = \hat{A} \otimes \hat{B} + \tilde{\lambda}\ \hat{A}^2, \tag{5.19}$$

where $\hat{A} = a^\dagger + a$, $\hat{B} = \sum_k g_k(b_k^\dagger + b_k)$, and $\tilde{\lambda} = \sum_k g_k^2/\omega_k$. To derive the RC master equation we first move into the interaction picture using the transformation $\tilde{H}_I(t) = \exp\left(i(H_0 + H_B)t\right) H_I \exp\left(-i(H_0 + H_B)t\right) = \hat{A}(t) \otimes \hat{B}(t) + \tilde{\lambda}\ \hat{A}^2(t)$, where $H_0 = \frac{\epsilon}{2}\sigma_z + \frac{\Delta}{2}\sigma_x + \lambda\sigma_z(a^\dagger + a) + \Omega a^\dagger a$, is the TLS-RC Hamiltonian, and $H_B = \sum_k \omega_k b_k^\dagger b_k$. Using the expression derived in Sec. 2.2.1, we obtain the interaction picture master equation for the reduced TLS-RC density operator $\rho(t)$

$$\begin{aligned}\frac{\partial\tilde{\rho}(t)}{\partial t} &= -i\ \mathrm{tr}_B\left[\tilde{H}_I(t), \rho(0)\otimes\rho_B\right] - \int_0^t d\tau\ \mathrm{tr}_B\left[\tilde{H}_I(t), \left[\tilde{H}_I(t-\tau), \tilde{\rho}(\tau)\otimes\rho_B\right]\right], \\ &= -i\ \tilde{\lambda}\left[\hat{A}^2(t), \rho(0)\right] - \tilde{\lambda}^2\int_0^t d\tau\left[\hat{A}^2(t), \left[\hat{A}^2(t-\tau), \tilde{\rho}(\tau)\right]\right] \\ &\quad - \int_0^t d\tau\Big(\left[\hat{A}(t), \left[\hat{A}(t-\tau), \tilde{\rho}(t)\right]\right]\Gamma^+(\tau) + \left[\hat{A}(t), \left\{\hat{A}(t-\tau), \tilde{\rho}(\tau)\right\}\right]\Gamma^-(\tau)\Big). \quad (5.20)\end{aligned}$$

Here, we have made use of the Born approximation, that is, we have assumed that the mapped system (i.e. TLS-RC) and environment remain in the product state $\rho(t)\otimes\rho_B$ for all time, where $\rho_B = \exp(-\beta\sum_k \omega_k b_k^\dagger b_k)/\mathrm{tr}\left(\exp(-\beta\sum_k \omega_k b_k^\dagger b_k)\right)$. The correlation functions are defined as $\Gamma^\pm = \mathrm{tr}\left((\hat{B}(\tau)\hat{B} \pm \hat{B}(-\tau)\hat{B})\rho_B\right)/2$. In the continuum limit we may write them as

$$\Gamma^+(\tau) = \int_0^\infty d\omega J_{\mathrm{RC}}(\omega)\coth\left(\frac{\beta\omega}{2}\right)\cos\omega\tau \quad \text{and} \quad \Gamma^-(\tau) = i\int_0^\infty d\omega J_{\mathrm{RC}}(\omega)\sin\omega\tau, \quad (5.21)$$

above, as outlined in the previous section, the RC spectral density takes the form $J_{\mathrm{RC}}(\omega) = \gamma\omega\exp(-\omega/\Lambda)$ in the limit that that the cut-off frequency $\Lambda \longrightarrow \infty$. We can simplify Eq. 5.20 further by noticing that

$$-i\tilde{\lambda}\left[\hat{A}^2(t), \tilde{\rho}(t)\right] = -i\tilde{\lambda}\left[\hat{A}^2(t), \tilde{\rho}(0)\right] - \tilde{\lambda}^2\int_0^t d\tau\left[\hat{A}^2(t), \left[\hat{A}^2(t-\tau), \tilde{\rho}(\tau)\right]\right]. \quad (5.22)$$

By substituting this into the above master equation and taking the full Markovian limit, that is, we take the time integrals to infinity, we acquire the RC master equation

$$\begin{aligned}\frac{\partial\tilde{\rho}(t)}{\partial t} &= -i\tilde{\lambda}\left[\hat{A}^2(t), \tilde{\rho}(t)\right] - \int_0^\infty\int_0^\infty d\tau d\omega J_{\mathrm{RC}}(\omega)\coth\left(\frac{\beta\omega}{2}\right)\cos\omega\tau\left[\hat{A}(t), \left[\hat{A}(t-\tau), \tilde{\rho}(t)\right]\right] \\ &\quad - i\int_0^\infty\int_0^\infty d\tau d\omega J_{\mathrm{RC}}(\omega)\sin\omega\tau\left[\hat{A}(t), \left\{\hat{A}(t-\tau), \tilde{\rho}(t)\right\}\right]. \quad (5.23)\end{aligned}$$

The definition of $J_{\mathrm{RC}}(\omega)$ assumes an infinite cut-off frequency, hence the first and last terms of Eq. 5.23 are divergent. However, we can eliminate the divergent contributions by

integrating the last term by parts, such that

$$\int_0^\infty d\tau \sin\omega\tau \hat{A}(t-\tau) = -\mathcal{P}\left(\frac{\hat{A}(t)}{\omega}\right) + \int_0^\infty d\tau \frac{\cos\omega\tau}{\omega}\frac{\partial\hat{A}(t-\tau)}{\partial\tau}. \tag{5.24}$$

Using the principal value part of this integral we can cancel the counter term, which, after moving back into the Schrödinger picture, gives the master equation

$$\begin{aligned}\frac{\partial\rho(t)}{\partial t} =& -i\left[H_0,\rho(t)\right] - \int_0^\infty\int_0^\infty d\tau d\omega J_{\mathrm{RC}}(\omega)\cos\omega\tau\coth\left(\frac{\beta\omega}{2}\right)\left[\hat{A},\left[\hat{A}(-\tau),\rho(t)\right]\right] \\ &- \int_0^\infty\int_0^\infty d\tau d\omega J_{\mathrm{RC}}(\omega)\frac{\cos\omega\tau}{\omega}\left[\hat{A},\left\{\left[\hat{A}(-\tau),H_0\right],\rho(t)\right\}\right].\end{aligned} \tag{5.25}$$

In order to derive the interaction picture system operators we shall diagonalise the TLS-RC system Hamiltonian, H_0, numerically. Let $|\varphi_n\rangle$ be an eigenstate of the system Hamiltonian, such that $H_0|\varphi_n\rangle = \varphi_n|\varphi_n\rangle$. We can now write the position operators in this eigenbasis:

$$\hat{A} = \sum_{jk} A_{j,k}|\varphi_j\rangle\langle\varphi_k|, \tag{5.26}$$

where $A_{j,k} = \langle\varphi_j|\hat{A}|\varphi_k\rangle$. In the interaction picture this becomes

$$\hat{A}(t) = \sum_{jk} A_{j,k}e^{i\xi_{jk}t}|\varphi_j\rangle\langle\varphi_k|, \tag{5.27}$$

where $\xi_{nm} = \varphi_n - \varphi_m$ is the difference between the n^{th} and m^{th} eigenvalues. Using this definition we can include the rates from Eq. 5.25 into the operators, such that

$$\hat{\chi} = \int_0^\infty\int_0^\infty d\omega d\tau\ J_{\mathrm{RC}}(\omega)\cos\omega\tau\coth\left(\frac{\beta\omega}{2}\right)\hat{A}(-\tau), \tag{5.28}$$

$$\approx \frac{\pi}{2}\sum_{jk} J_{\mathrm{RC}}(\xi_{jk})\coth\frac{\beta\xi_{jk}}{2}A_{jk}|\varphi_j\rangle\langle\varphi_k|, \tag{5.29}$$

$$\hat{\Xi} = \int_0^\infty\int_0^\infty d\omega d\tau\frac{J_{\mathrm{RC}}(\omega)\cos\omega\tau}{\omega}\left[H_0,\hat{A}(-\tau)\right], \tag{5.30}$$

$$\approx \frac{\pi}{2}\sum_{jk} J_{\mathrm{RC}}(\xi_{jk})A_{jk}|\varphi_j\rangle\langle\varphi_k|, \tag{5.31}$$

where we have neglected the imaginary Lamb shift terms which we expect to small (this will be justified through benchmarking). We can now write the master equation as

$$\frac{\partial\rho(t)}{\partial t} = -i\left[H_0,\rho(t)\right] - \left[\hat{A},\left[\hat{\chi},\rho(t)\right]\right] + \left[\hat{A},\left\{\hat{\Xi},\rho(t)\right\}\right]. \tag{5.32}$$

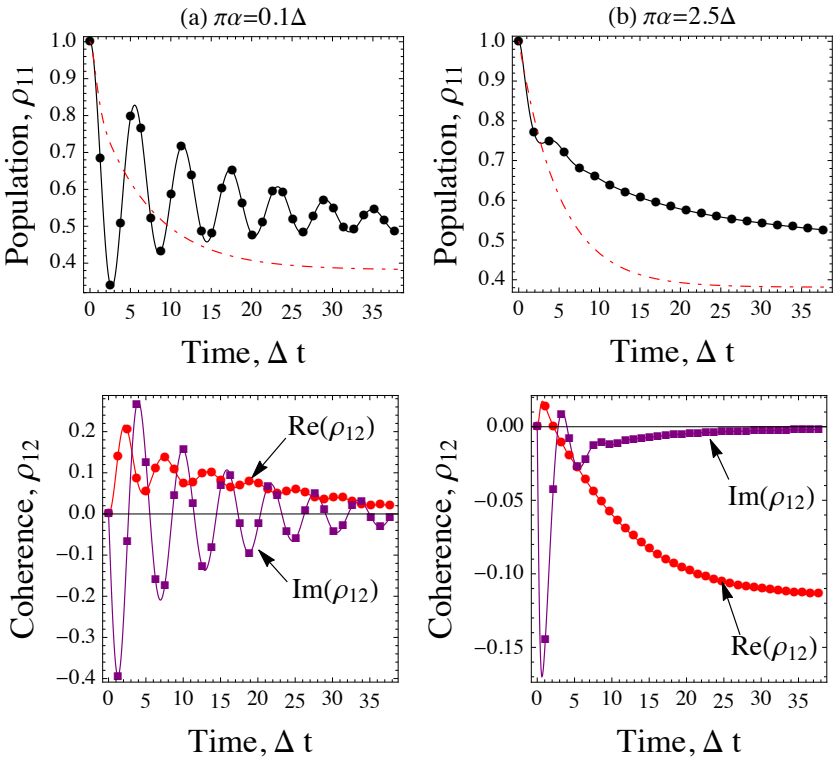


Figure 5.2: TLS (Top) population and (Bottom) coherence dynamics from the RCME (solid curves), weak coupling theory (red, dash-dot curves), and converged HEOM data (points). Parameters: $\epsilon = 0.5\Delta$, $\omega_c = 0.05\Delta$, $\beta\Delta = 0.95$, and (a) $\pi\alpha = 0.1\Delta$, (b) $\pi\alpha = 2.5\Delta$. HEOM data was provided by Neill Lambert.

5.3 Time evolution of the RC model

5.3.1 Benchmarking

In order to demonstrate the validity of the reaction coordinate master equation (RCME), we benchmark its predictions for the TLS population dynamics ($\rho_{11} = \langle 1|\rho|1\rangle$) against converged data generated using the numerically exact HEOM technique.

The HEOM are a set of time-local equations for the reduced system dynamics, governed by the spin-boson Hamiltonian (Eq. 5.1), which capture the bath dynamics and system-bath correlations through a set of auxiliary density matrices [108, 109, 120, 127]. These equations are exact under the assumption of a under- or overdamped spectral density, as given in Eq. 5.4 and 5.5, and an initially separable system-bath state at t = 0. Furthermore, the exact nature of the HEOM allow one to capture the effect of both non-Markovian dynamics and system-environment correlations on the reduced state of the system.

To give an illustrative example, in Fig. 5.2 we have taken parameters that are typical for excitonic energy transfer in molecular systems [47, 111, 127, 128], with a representative value of $\Delta = 200$ cm^{-1} (given in spectroscopic units[2]) setting the other energy scales (i.e. $t \sim 1$ ps at $\Delta t = 35$). The TLS is initialised in state $|1\rangle$, uncorrelated with both

[2]Though not an SI unit, wavenumbers (cm^{-1}) are used for convenience in spectroscopic measurements as a unit of frequency. Physically, wavenumbers correspond to the number of cycles of the measured radiation travelling at the speed of light in vacuum per cm.

the RC and residual bath, which are taken to be in their respective thermal equilibrium states at a temperature $T = 1/\beta$ (≈ 300 K for $\Delta = 200$ cm^{-1}). We observe essentially perfect agreement between the RCME and the HEOM for a slow environment and for spin-boson coupling strengths [(a) $\pi\alpha = 20$ cm^{-1}, (b) $\pi\alpha = 500$ cm^{-1}] encompassing the transition from the coherent to the incoherent regime[3]. In contrast, a standard weak coupling approach, treating the interaction term in Eq. 5.1 to second order, fails even qualitatively to capture the correct system behaviour for any parameters shown. It is thus clear that environmental memory and the generation of correlations with the system—both of which are ignored in the weak coupling calculation—are crucial in order to capture the correct dynamical behaviour in this regime. Moreover, although we invoke a Born-Markov approximation between the TLS-RC and residual environment, the impact of these correlations on the TLS can be accurately described simply through the TLS-RC coupling. This is somewhat remarkable, given that any non-thermal state effects of the original bath have been reduced solely to the action of a single mode on the TLS.

5.3.2 Environmental dynamics and correlations

The most important aspect of our formalism is that the inclusion of environmental degrees of freedom into the system Hamiltonian allows us to gain additional insight into the dynamics of both the environmental state and system-environment correlations. We do this by calculating two complementary measures; the RC non-Gaussianity [129, 130], which probes the environmental evolution:

$$\delta_G[\rho_{\mathrm{RC}}(t)] = S(\varrho) - S\left(\rho_{\mathrm{RC}}(t)\right), \tag{5.33}$$

and the TLS-RC quantum mutual information (QMI) [131], characterising the correlations:

$$\mathcal{I}(\rho_S : \rho_{\mathrm{RC}}) = S(\rho_s) + S(\rho_{\mathrm{RC}}) - S(\rho). \tag{5.34}$$

Here, ρ_{RC} (ρ_s) is the reduced state of the RC (TLS) and $S(\chi) = -\mathrm{tr}\left(\chi \ln \chi\right)$ is the von-Neumann entropy. The non-Gaussianity determines the distance from ρ_{RC} to the nearest Gaussian reference state ϱ, and is defined such that $\delta_G = 0$ iff ρ_{RC} is Gaussian. The QMI quantifies the total classical and quantum correlations shared between the TLS and RC [131]. Both measures act as rigorous lower bounds for the original spin-boson environment, which enables us to explore properties of the multi-mode bath and its correlations with the system simply through the single mode RC.

To show this let χ be the density matrix describing the state of both the system and environment in the original spin-boson representation, with the reduced states of the system, $\rho_s = \mathrm{tr}_E\chi$, and the environment, $\rho_E = \mathrm{tr}_s\chi$. Let $\mathcal{U} = \mathbb{1}_S \otimes \mathcal{R}$ be the unitary transformation that maps the spin-boson model to the RC model. Applying this unitary to the reduced state of the system has no effect due to the trace over the environment. However, on the reduced state of the environment this unitary transforms the spin-boson basis to that of the RC and residual bath, that is, $\mathcal{R}^\dagger\rho_E\mathcal{R} = \rho_{RC+B}$.

[3] We see similarly excellent agreement for larger cut-off frequencies, as will be shown in Chapter 6.

The quantum mutual information for the system and the spin-boson environment is given by:

$$\mathcal{I}(\rho_s : \rho_E) = S(\rho_s) + S(\rho_E) - S(\chi) = S(\rho_s) + S(\rho_{RC+B}) - S(\tilde{\chi}), \tag{5.35}$$

where $\tilde{\chi} = \mathcal{U}^\dagger \chi \mathcal{U}$ is the total state in the RC basis. Here we have used the unitary equivalence of the von-Neumann entropy to write the quantum mutual information in terms of the RC basis.

To proceed we shall make use of the strong subadditivity of the von-Neumann entropy, that is:

$$S(\tilde{\chi}) + S(\rho_{RC}) \leq S(\rho_{S+RC}) + S(\rho_{RC+B}), \tag{5.36}$$

where $\rho_{S+RC} = \mathrm{tr}_B \tilde{\chi}$, with the trace taken over the residual environment. Using this property in conjunction with Eq. 5.35 gives:

$$\begin{aligned} \mathcal{I}(\rho_s : \rho_E) &\geq S(\rho_S) + S(\rho_{RC+B}) + S(\rho_{RC}) - S(\rho_{s+RC}) - S(\rho_{RC+B}), \\ &\geq S(\rho_s) + S(\rho_{RC}) - S(\rho_{S+RC}). \end{aligned} \tag{5.37}$$

Therefore, we have the condition

$$\mathcal{I}(\rho_s : \rho_E) \geq \mathcal{I}(\rho_s : \rho_{RC}). \tag{5.38}$$

Hence, the mutual information between the system and RC acts as a lower bound to the mutual information between the system and spin-boson environment. Furthermore, in the limit that the Born approximation holds between the composite system (TLS and RC) and the residual environment, that is $\tilde{\chi} \approx \rho_{s+RC} \otimes \rho_B$, then the inequality in Eq. 5.38 becomes an equality due to the additive nature of the von-Neumann entropy.

Similarly, the non-Gaussianity can be shown to be invariant under symplectic transformation (i.e. operators that are quadratic in field operators) and monotonically decreases under partial trace [129]. This means that the non-Gaussianity of the RC acts as a rigorous lower bound for the non-Gaussianity of the original spin-boson environment, that is:

$$\delta_G[\rho_E] \geq \delta_G[\rho_{RC}]. \tag{5.39}$$

As with the quantum mutual information, in the limit that the Born approximation holds between the mapped system and residual environment, then the additive nature of the von-Neumann entropy implies that this measure also becomes *exact* for the original spin-boson environment.

Fig. 5.3 shows the dynamics of the non-Gaussianity and the QMI at both strong and weak system-environment coupling α. One of the most striking features of these plots is the presence of two distinct timescales, which is most obvious for weak couplings, but is also present at stronger coupling strengths. At short times, the QMI is oscillatory, an indication of the memory effects implied by system-environment correlations, which also push the RC away from its initial Gaussian state. At longer times, we see that system-

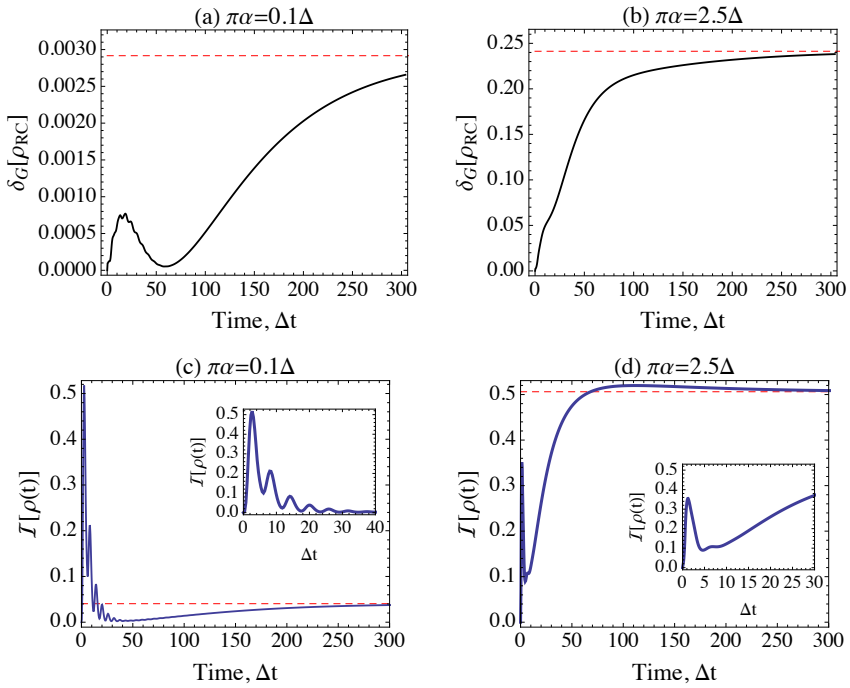


Figure 5.3: Dynamics of the RC non-Gaussianity (a,b) and TLS-RC mutual information (c,d) for weak and strong system-bath coupling strengths, with steady state values indicated (dash-dot lines). Parameters: $\epsilon = 0.5\Delta$, $\omega_c = 0.05\Delta$ and $\beta\Delta = 0.95$, e.g. for $\Delta = 200$ cm^{-1}, $T \approx 300$ K, and $t \sim 10$ ps at $\Delta t = 300$.

environment correlations—and consequently non-Gaussian environmental states—are also generated on a second timescale, and in fact persist into the steady state, with values of both the non-Gaussianity and QMI dependent on the coupling strength as demonstrated in Fig. 5.4. We therefore find a situation in which the Born-Markov approximation breaks down on all timescales. It describes neither the short time transient dynamics, due to the absence of bath memory effects in the Markov approximation, nor the long time behaviour, due to the generation of significant TLS-bath correlations. This leads to non-Gaussian (and hence non-thermal) environmental states upon tracing out the TLS, neglected in the Born approximation. Our line of enquiry also raises an intriguing question: if correlations can so dramatically affect the Gaussian nature of the environment, how do they impact upon the state of the TLS?

5.4 Noncanonical equilibrium states

A clue can already be taken from Fig. 5.4, where we find that the steady-state properties of both the RC and TLS-RC correlations may be described by a thermal state with respect to H_0, i.e.

$$\rho_{\rm th} = \frac{e^{-\beta H_0}}{Z} = \frac{1}{Z} e^{-\beta\left(\frac{\epsilon}{2}\sigma_z + \frac{\Delta}{2}\sigma_x + \lambda\sigma_z(a^\dagger + a) + \Omega a^\dagger a\right)}, \tag{5.40}$$

where $Z = \mathrm{tr}(e^{-\beta H_0})$. Likewise, in Fig. 5.5 we show that the equilibrium behaviour of the TLS (after tracing out the mode) clearly departs from the canonical statistics

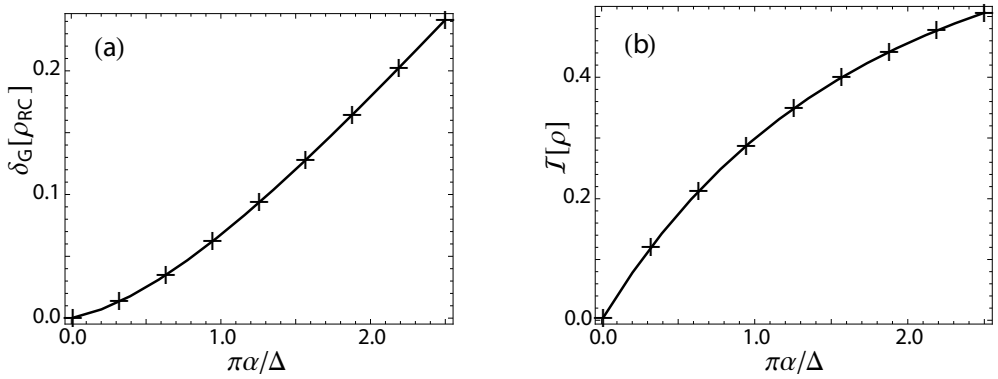


Figure 5.4: Steady-state non-Gaussianity (a) and quantum mutual information (b) as a function of coupling strength, derived from the RCME (solid curve) and a thermal state with respect to the TLS-RC Hamiltonian H_0 (crosses), see Eq. 5.40. Parameters: $\epsilon = 0.5\Delta$, $\omega_c = 0.05\Delta$ and $\beta\Delta = 0.95$ (≈ 300 K for $\Delta = 200$ cm^{-1}).

expected from a perturbative, weak coupling treatment of the environmental influence, which would be given instead by a thermal state with respect only to the TLS Hamiltonian, $H_S = \frac{\epsilon}{2}\sigma_z + \frac{\Delta}{2}\sigma_x$.

Fig. 5.5(a) explores the temperature dependence of the TLS equilibrium state in the energy eigenbasis. To emphasise the departure from canonical statistics we have plotted the population ratio on a logarithmic scale. For a canonical distribution we expect a linear dependence on the inverse temperature, shown by the dash-dot line, and given by $\ln(\rho_{gg}/\rho_{ee}) = -\beta\eta$, where $\eta = \sqrt{\epsilon^2 + \Delta^2}$ is the TLS splitting. Crucially, however, the RCME steady state shows a clear deviation from this linear behaviour with decreasing temperature. To provide context, taking our estimate again of $\Delta = 200$ cm^{-1} relevant to molecular systems, we see that deviations from canonical statistics begin to become apparent around $\beta\Delta = 0.95 \approx 300$ K, and should thus be observable *even at room temperature* in such systems. Note, from the inset, that a non-zero level of coherence is also apparent around such temperatures (and lower), again pointing to the noncanonical nature of the TLS equilibrium state. These departures demonstrate that we cannot represent the TLS steady state as a Gibbs distribution over the system eigenstates. They also quantify relatively simple experimental signatures of the breakdown of canonical statistics in open quantum systems. For example, by measuring only the TLS populations over a reasonable temperature range, we may infer the emergence of noncanonical equilibrium states simply by observing a nonlinear temperature dependence as shown.

Finally, in Fig. 5.5 (b) we examine the TLS steady state as a function of system-bath coupling strength at constant temperature. We again see significant deviations from the (unchanging) canonical thermal state, such as the development of steady state coherences within the TLS eigenstate basis, which are apparent for any non-vanishing coupling strength. Nevertheless, it is evident from all plots in Fig. 5.5, by the agreement between Eq. 5.40 and the HEOM, that the noncanonical steady state is still extremely well described by a thermal state across a wide range of parameters, though now in the mapped TLS-RC representation. This behaviour is a clear result of the TLS-environment correla-

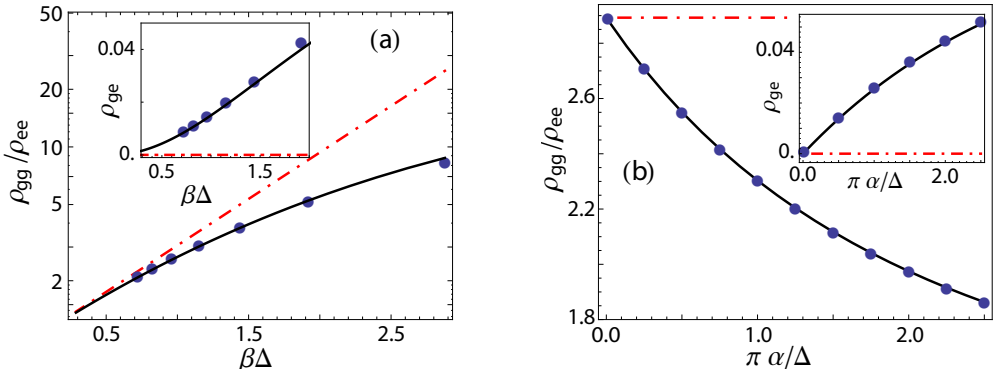


Figure 5.5: Steady state population ratio (ρ_{gg}/ρ_{ee}) and coherence (ρ_{ge}) in the *eigenstate* basis of the TLS Hamiltonian H_S, with $|g\rangle$ ($|e\rangle$) being the ground (excited) eigenstate: (a) against temperature (at $\pi\alpha = 0.5\Delta$) and (b) against coupling strength (at $\beta\Delta = 0.95$). Shown are predictions from the HEOM (points), a thermal state with respect to the TLS-RC Hamiltonian H_0 (solid), and a thermal state with respect to H_S (dash-dot). Parameters: $\epsilon = 0.5\Delta$ and $\omega_c = 0.05\Delta$. Considering $\Delta = 200$ cm^{-1} gives $T = 575$ K for $\beta\Delta = 0.5$, $T = 288$ K for $\beta\Delta = 1$, and $T = 115$ K for $\beta\Delta = 2.5$. HEOM data was provided by Neill Lambert.

tions; the TLS cannot be considered merely as being in a product state with a (thermal) environment. The non-separability of the steady state thus implies that the equilibrium behaviour of the TLS cannot be described as a thermal distribution over its eigenstates either, but rather, one should also consider states of the environment within the description. This is markedly different to standard master equation techniques and statistical mechanics approaches, where the system equilibrates to the canonical thermal state which may be characterised by the bath temperature and system Hamiltonian alone, an artefact of applying the Born approximation.

5.5 Summary

To summarise, by exploiting a collective coordinate mapping, we have derived a master equation valid in the non-adiabatic regime of the spin-boson model. Notably, besides an accurate description of the system dynamics, our approach also allows us to quantify the accumulation of system-environment correlations with time, as well as probe the dynamic evolution of states of the environment. We have shown that properly accounting for the generation of system-environment correlations is essential for describing both the transient dynamics and equilibrium distributions of open systems in this regime. In particular, we have demonstrated that long-lived correlations lead to the emergence of noncanonical system equilibrium states that can be characterised in a simple and intuitive way within our formalism, as thermal states of the system-collective coordinate Hamiltonian. Our approach can be applied to a number of systems of practical relevance. For example, in molecular and solid-state (e.g. superconducting) devices [2, 4, 11, 87, 96–98, 118, 132–138], system-environment coupling can be strong and memory effects important. Taking parameters relevant for energy transfer processes in molecular dimers, we have shown

that deviations from canonical statistics could be observable even at room temperature, which raises the intriguing question of the role of noncanonical equilibrium states in larger molecular aggregates [135–137]. Finally, a proper understanding of equilibrium states is a vital component in the growing field exploring the thermodynamics of quantum systems; the full implications of noncanonical steady-states in open quantum systems [139, 140] thus constitutes a fascinating topic for future exploration.

CHAPTER 6

ENERGY TRANSFER IN NON-ADIABATIC REGIMES

6.1 Introduction

Since quantum coherence was first observed in photosynthetic systems [135], determining its precise functional role in producing efficient and robust excitonic energy transfer (EET) across pigment protein complexes has been a driving force for the field of quantum biology [141]. Theoretical work on the subject quickly identified that purely coherent energy transport is insufficient to explain the high efficiencies and rates observed. For resonant systems, this is due to the inherent reversibility of coherent dynamics, while biased systems become localised in the site basis when the inter-site energy difference is greater than the tunnelling energy, thus reducing exciton transport. These difficulties may be circumvented when noise processes induced by an external environment are also present, providing mechanisms for rapid and efficient EET [142–146].

However, accounting for the effects of the external environment in photosynthetic systems is a daunting theoretical prospect [2, 4, 11, 96, 97]. Strong coupling between the system and its low frequency environment lead to significant system-environment correlations that, as was shown in Chapter 5, are present even in the steady state [147, 148]. In addition to the low frequency environment, the spectral density of the pigment protein complex is often structured, that is, there are specific underdamped vibrational modes of the environment that couple strongly to the electronic degrees of freedom. There is now increasing evidence suggesting that these underdamped modes are a contributing factor to the long-lived electronic coherences observed in photosynthetic complexes [119, 149, 150], as well as qualitative links between the quantum mechanical nature of these vibrational modes and enhanced transfer rates [151].

A multitude of powerful computational methods have been developed to model these systems – e.g. hierarchical equations of motion (HEOM) [108, 120, 152–154], density matrix renormalisation group [111, 114], and those based on the path integral formalism [110] – all of which can converge to numerically exact results in specific regimes. However, these techniques are computationally challenging, and often give very little intuitive insight into

the underlying physical mechanisms.

As demonstrated in Chapter 5, the reaction coordinate model provides an intuitive method for accurately describing the dynamical behaviour of a system coupled to a low frequency environment. Here, we shall apply the reaction coordinate master equation (RCME) [98–102, 147] to describe EET in a molecular dimer system. We show that the RC model captures all important correlations between the system and environment for EET in the presence of an under- and overdamped enviroment, agreeing perfectly with numerically exact data generated using the HEOM [120, 152–154]. Furthermore, we demonstrate that the RC model greatly out performs the closely related Zusman equations [99, 102, 155], a set of drift diffusion equations often used to describe tunnelling processes in molecular systems, which we derive from the RC master equation as the semiclassical limit.

Finally we discuss the influence that a structured environment has on the energy transfer dynamics in a molecular dimer system [149, 156]. This is done formally by incorporating an underdamped mode into the system Hamiltonian using the RC formalism, while the broad background environment is described using a second overdamped RC. We show that the presence of structure in the spectral density can enhance the EET rate, particularly when the underdamped environment is tuned to the resonance of the molecular dimer.

6.2 System Hamiltonian and the reaction coordinate mapping

6.2.1 Energy transport Hamiltonian

To investigate the effect a low frequency environment has on EET, we consider a simple model of excitation in a molecule with two sites. Each site has an excited state $|e_j\rangle$, corresponding to a single excitation at site j with energy ϵ_j, and ground state $|g_j\rangle$ in the absence of the excitation. Each site is coupled to individual, but identical, thermal environments, modelled as a continuum of harmonic oscillators [2].

The Hamiltonian for the system and environment may then be written as:

$$\begin{aligned} H = {} & (\varepsilon_1+\varepsilon_2)|e_1e_2\rangle\langle e_1e_2| + \varepsilon_1|e_1g_2\rangle\langle e_1g_2| + \varepsilon_2|g_1e_2\rangle\langle g_1e_2| + \frac{\Delta}{2}(|e_1g_2\rangle\langle g_1e_2| + |g_1e_2\rangle\langle e_1g_2|) \\ & + |e_1\rangle\langle e_1|\otimes\mathbb{1}_2\sum_k c_{1,k}(a^\dagger_{1,k}+a_{1,k}) + \mathbb{1}_1\otimes|e_2\rangle\langle e_2|\sum_k c_{2,k}(a^\dagger_{2,k}+a_{2,k}) + \sum_{j=1}^{2}\sum_k \nu_k a^\dagger_{j,k}a_{j,k}, \end{aligned} \tag{6.1}$$

where the identity operator is given by $\mathbb{1}_j = |e_j\rangle\langle e_j| + |g_j\rangle\langle g_j|$, and Δ is the inter-site tunnelling strength. We have also defined the creation and annihilation operators, $a_{j,k}$ and $a^\dagger_{j,k}$, at site j, which satisfy the commutation relation $\left[a_{i,k}, a^\dagger_{j,k'}\right] = \delta_{i,j}\delta_{k,k'}$. To discuss the energy transfer dynamics between the two sites, we shall only consider the dynamics of a single excitation in the system. Hence, by applying the projector, $\mathbb{1}_{sub} =$

$|e_1g_2\rangle\langle e_1g_2| + |g_1e_2\rangle\langle g_1e_2|$, we obtain the Hamiltonian for the single excitation subspace:

$$\begin{aligned} H_{sub} =& \sum_{j=1}^{2} \varepsilon_j |j\rangle\langle j| + \frac{\Delta}{2}(|1\rangle\langle 2| + |2\rangle\langle 1|) + \sum_{j=1}^{2} |j\rangle\langle j| \sum_k c_{j,k}\sqrt{2\nu_k}\hat{x}_{j,k} \\ &+ \frac{1}{2}\sum_{j=1}^{2}\sum_k \left(\hat{p}_{j,k}^2 + \nu_k^2 \hat{x}_{j,k}^2\right), \end{aligned} \tag{6.2}$$

where we have defined the basis $\{|1\rangle = |e_1g_2\rangle, |2\rangle = |g_1e_2\rangle\}$, and also the bath coordinates such that:

$$\hat{x}_{j,k} = \sqrt{\frac{1}{2\nu_k}}\left(a_{j,k}^\dagger + a_{j,k}\right) \qquad \text{and} \qquad \hat{p}_{j,k} = i\sqrt{\frac{\nu_k}{2}}\left(a_{j,k}^\dagger - a_{j,k}\right). \tag{6.3}$$

We can simplify this expression by rewriting the Hamiltonian in terms of an effective single phonon environment. We do so by rotating the coordinate system of the environmental modes such that:

$$\hat{x}_{1,k} = \hat{q}_k \cos\alpha_k + \hat{q}'_k \sin\alpha_k \qquad \text{and} \qquad \hat{x}_{2,k} = -\hat{q}_k \sin\alpha_k + \hat{q}'_k \cos\alpha_k. \tag{6.4}$$

Substituting this into equation 6.2, gives:

$$\begin{aligned} H =& \sum_{j=1}^{2} \varepsilon_j |j\rangle\langle j| + \frac{\Delta}{2}(|1\rangle\langle 2| + |2\rangle\langle 1|) + \sum_k \sqrt{2\nu_k}\left(c_{1,k}\cos\alpha_k |1\rangle\langle 1| - c_{2,k}\sin\alpha_k |2\rangle\langle 2|\right)\hat{q}_k \\ &+ \sum_k \sqrt{2\nu_k}\left(c_{1,k}\sin\alpha_k |1\rangle\langle 1| + c_{2,k}\cos\alpha_k |2\rangle\langle 2|\right)\hat{q}'_k \\ &+ \frac{1}{2}\sum_k \dot{\hat{q}}_k^2 + \left(\dot{\hat{q}}'_k\right)^2 + \nu_k^2\left(\hat{q}_k^2 + \left(\hat{q}'_k\right)^2\right). \end{aligned} \tag{6.5}$$

Now, by choosing $c_{1,k}\cos\alpha_k = c_{2,k}\sin\alpha_k$, such that $\alpha_k = \arctan\left(c_{1,k}/c_{2,k}\right)$, a set of environmental modes decouple entirely from the system, leading only to a global phase. Thus, we may now write the energy transport Hamiltonian in spin-boson form:

$$H = \frac{\epsilon}{2}\sigma_z + \frac{\Delta}{2}\sigma_x + \sigma_z \sum_k \sqrt{2\nu_k} c_{1,k}\cos\alpha_k \hat{q}_k + \frac{1}{2}\sum_k \dot{\hat{q}}_k^2 + \nu_k^2 \hat{q}_k^2, \tag{6.6}$$

where $\epsilon = \varepsilon_1 - \varepsilon_2$, and we have defined the Pauli operators as $\sigma_z = |1\rangle\langle 1| - |2\rangle\langle 2|$ and $\sigma_x = |1\rangle\langle 2| + |2\rangle\langle 1|$. For simplicity, we now assume that the system-bath coupling is the same at each site, i.e. $c_{1,k} = c_{2,k}$ for all k, hence $\cos\alpha_k = 1/\sqrt{2}$. Finally, by defining the bath operators in term of creation and annihilation operators:

$$\hat{q}_k = \sqrt{\frac{1}{2\nu_k}}\left(\tilde{b}_k^\dagger + \tilde{b}_k\right) \qquad \text{and} \qquad \dot{\hat{q}}_k = i\sqrt{\frac{\nu_k}{2}}\left(\tilde{b}_k^\dagger - \tilde{b}_k\right), \tag{6.7}$$

we have the Hamiltonian:

$$H_{SB} = \frac{\epsilon}{2}\sigma_z + \frac{\Delta}{2}\sigma_x + \sigma_z \sum_k c_k \left(\tilde{b}_k^\dagger + \tilde{b}_k\right) + \sum_k \nu_k \tilde{b}_k^\dagger \tilde{b}_k, \tag{6.8}$$

where the bath coupling constants are now $c_k = c_{1,k}/\sqrt{2}$.

As was introduced in the previous chapter, we shall characterise the phonon environment using two spectral densities relevant to excitonic energy transfer systems, the under- and over-damped forms:

$$J_{UD}(\omega) = \frac{\alpha_{UD}\Gamma\omega_0^2\omega}{(\omega_0^2-\omega^2)^2+\Gamma^2\omega^2} \qquad \text{and} \qquad J_{OD}(\omega) = \alpha_{OD}\omega_c\frac{\omega}{\omega^2+\omega_c^2}, \tag{6.9}$$

both of which are a special case of the general spin-boson spectral density $J_{SB}(\omega) = \sum_k |c_k|^2\delta(\omega-\omega_k)$.

6.2.2 Reaction coordinate mapping

Now that our Hamiltonian is in spin-boson form, it is straightforward to apply the RC mapping introduced in Chapter 5, resulting in a mapped system Hamiltonian of the form:

$$\begin{aligned}
H_{RC} &= H_S + H_I + H_B + H_C,\\
H_S &= \frac{\epsilon}{2}\sigma_z + \frac{\Delta}{2}\sigma_x + \lambda\sigma_z\left(a^\dagger + a\right) + \Omega\ a^\dagger a,\\
H_I &= \left(a^\dagger + a\right)\sum_k g_k\left(b_k^\dagger + b_k\right),\\
H_B &= \sum_k \omega_k b_k^\dagger b_k,\\
H_C &= \left(a^\dagger + a\right)^2 \sum_k \frac{g_k^2}{\omega_k},
\end{aligned} \tag{6.10}$$

As before, the collective coordinate is defined as $\lambda(a^\dagger+a) = \sum_k g_k(\tilde{b}_k^\dagger+\tilde{b}_k)$, where $\lambda = \sum_k c_k^2$, and the RC frequency is $\Omega = \lambda^{-1}\sqrt{\sum_k \omega_k f_k^2}$. However, as in the previous chapter, both the under- and over-damped spectral densities lead to divergences in the RC coupling strength (λ) and frequency (Ω) calculated by the formal expressions defined above [98, 99]. Following the mapping as before, by choosing the reaction coordinate spectral density to have the form $J_{RC}(\omega) = \gamma\omega\exp(-\omega/\Lambda)$, and using Eq. 5.10 in the limit that $\Lambda\to\infty$, we find the relation:

$$J_{SB}(\omega) = \frac{4\gamma\omega\Omega^2\lambda^2}{(\Omega^2-\omega^2)^2+(2\pi\gamma\Omega\omega)^2}. \tag{6.11}$$

Thus the mapping described above is exact for the underdamped spectral density when $\Omega=\omega_0$, $\lambda=\sqrt{\pi\alpha_{UD}\omega_0/2}$, and $\gamma = \Gamma/2\pi\omega_0$. Once more, can also recover the over damped spectral density by choosing γ such that $\omega_c \ll \Omega$, such that the RC coupling strength and

splitting satisfy:

$$\omega_c = \frac{\Omega}{2\pi\gamma} \qquad \text{and} \qquad \alpha_{OD} = \frac{2\lambda^2}{\pi\Omega}. \tag{6.12}$$

6.3 Time evolution in the RC model

To describe the time evolution of the RC model we shall take two approaches. The first uses the reaction coordinate master equation derived in Sec. 5.2.2. The second is to apply further approximations to the RC master equation in order to derive a set of partial differential equations (PDE) known as the Zusman equations. In the chemical physics literature the Zusman equations are often the 'end-goal' of the RC mapping, however, as we shall show in subsequent sections, the RC master equation gives accurate population dynamics over a much larger area of parameter space than the Zusman equations.

6.3.1 Reaction coordinate master equation

As in the previous section, we shall model the time evolution of the RC model using the master equation formalism, where the coupling to the residual environment is treated to second order. In the Schrödinger picture, the RC master equation is given by:

$$\frac{\partial\rho(t)}{\partial t} = -i\left[H_S, \rho(t)\right] - \left[\hat{A}, [\hat{\chi}, \rho(t)]\right] + \left[\hat{A}, \left\{\hat{\Xi}, \rho(t)\right\}\right], \tag{6.13}$$

where $A = a^\dagger + a$, and the rate operators are defined as:

$$\hat{\Xi} = \frac{\pi}{2}\sum_{j,k=1}^{2n} \gamma\omega_{jk} A_{jk} |\varphi_j\rangle\langle\varphi_k| \quad \text{and} \quad \hat{\chi} = \frac{\pi}{2}\sum_{j,k=1}^{2n} \gamma\omega_{jk} \coth\frac{\beta\omega_{jk}}{2} A_{jk} |\varphi_j\rangle\langle\varphi_k|. \tag{6.14}$$

Here $|\varphi_j\rangle$ is a system eigenstate associated with the RC system Hamiltonian, i.e. $H_S|\varphi_j\rangle = \varphi_j|\varphi_j\rangle$, and n is the number of Fock states taken in the RC. Eq. 6.13 captures the interaction between the two level system and reaction coordinate non-perturbatively, while the residual bath is assumed to be weakly coupled to the composite system, and is thus treated in a purely Markovian fashion.

6.3.2 Zusman equations

To derive the Zusman equations (a detailed account of this derivation is given in Appendix B), our starting point will be the RC master equation before the environmental correlation functions have been evaluated, as given by Eq. 5.25

$$\begin{aligned}\frac{\partial\rho(t)}{\partial t} = &-i\left[H_S, \rho(t)\right] - \gamma\int_0^\infty d\tau \int_0^\infty d\omega\ \omega\cos\omega\tau\coth\left(\frac{\beta\omega}{2}\right)\left[\hat{A}, \left[\hat{A}(-\tau), \rho_S(t)\right]\right] \\ &- \gamma\int_0^\infty d\tau \int_0^\infty d\omega\cos\omega\tau\left[\hat{A}, \left\{\left[\hat{A}(-\tau), H_S\right], \rho(t)\right\}\right].\end{aligned} \tag{6.15}$$

We can simplify the time-dependent RC operators using the Caldeira-Leggett (CL) prescription [2, 98, 99, 157], in which the time scale of the system evolution is assumed to be much longer than that of the environment. This allows one to expand the time-dependent operators as $\hat{A}(t) = e^{-iH_s t}\hat{A}e^{iH_s t} \approx \hat{A} + it\left[H_s, \hat{A}\right]$. Inserting this approximate form for the interaction picture operators into Eq. 6.15 and taking a high temperature approximation, we can evaluate the frequency and time integrals. We then move to a phase-space representation for the master equation by way of the Wigner transformation, leading to the generalised Fokker-Planck equation in Klein-Kramers form [158]:

$$\frac{\partial \hat{W}}{\partial t} + \mathcal{H}\hat{W} + (i\mathcal{Z} - \Omega^2 x)\frac{\partial \hat{W}}{\partial p} + p\frac{\partial \hat{W}}{\partial x} = \pi\gamma\Omega\frac{\partial}{\partial t}\left(p\hat{W} + \frac{1}{\beta}\frac{\partial \hat{W}}{\partial p}\right), \tag{6.16}$$

where $\hat{W} = \sum_{ij} W_{ij}(x,p,t)|i\rangle\langle j|$, with $|i\rangle \in \{|1\rangle, |2\rangle\}$ the site basis of the TLS, and the Wigner function is defined as

$$W_{ij}(x,p,t) = \frac{1}{2\pi}\int_{-\infty}^{\infty} dx' e^{-ipx'}\left\langle i, x + \frac{x'}{2}\right|\rho(t)\left|x - \frac{x'}{2}, j\right\rangle.$$

Here x and p are the phase space coordinates of the reaction coordinate. For brevity, we have defined the super-operators in Eq. 6.16 as:

$$\mathcal{H}\hat{W} = i\left[(\frac{\epsilon}{2} + \sqrt{2\Omega}\lambda x)\sigma_z + \Delta\sigma_x, \hat{W}\right] \quad \text{and} \quad \mathcal{Z}\frac{\partial \hat{W}}{\partial p} = \frac{i\sqrt{2\Omega}\lambda}{2}\left\{\sigma_z, \frac{\partial \hat{W}}{\partial p}\right\}. \tag{6.17}$$

In its current form Eq. 6.16 remains a challenging equation to solve. We may simplify it, however, by eliminating the momentum coordinate in the differential equation. We do this by assuming that the RC momentum remains in thermal equilibrium for all time, which is valid in the high friction limit. This enables us to expand the Wigner function in terms of Hermite polynomials, resulting in a hierarchy of equations. By taking terms that are first order in the inverse friction (γ^{-1}), we acquire a set of drift diffusion equations, commonly referred to as the Zusman equations:

$$\begin{aligned}
\frac{\partial \mu_{11}(t,x)}{\partial t} &= \frac{1}{2\pi\gamma\Omega}\frac{\partial}{\partial x}\left((\Omega^2 x + \sqrt{2\Omega}\lambda)\mu_{11}(t,x) + \frac{1}{\beta}\frac{\partial \mu_{11}(t,x)}{\partial x}\right) + i\frac{\Delta}{2}(\mu_{12}(t,x) - \mu_{21}(t,x)),\\
\frac{\partial \mu_{22}(t,x)}{\partial t} &= \frac{1}{2\pi\gamma\Omega}\frac{\partial}{\partial x}\left((\Omega^2 x + \sqrt{2\Omega}\lambda)\mu_{22}(t,x) + \frac{1}{\beta}\frac{\partial \mu_{22}(t,x)}{\partial x}\right) - i\frac{\Delta}{2}(\mu_{12}(t,x) - \mu_{21}(t,x)),\\
\frac{\partial \mu_{12}(t,x)}{\partial t} &= \frac{1}{2\pi\gamma\Omega}\frac{\partial}{\partial x}\left(\frac{1}{\beta}\frac{\partial \mu_{12}(t,x)}{\partial x} + \Omega^2 x\mu_{12}(t,x)\right) + i(\epsilon + 2\sqrt{2\Omega}\lambda x)\mu_{12}(t,x)\\
&\quad + i\frac{\Delta}{2}(\mu_{11}(t,x) - \mu_{22}(t,x)),\\
\frac{\partial \mu_{21}(t,x)}{\partial t} &= \frac{1}{2\pi\gamma\Omega}\frac{\partial}{\partial x}\left(\frac{1}{\beta}\frac{\partial \mu_{21}(t,x)}{\partial x} + \Omega^2 x\mu_{21}(t,x)\right) + i(\epsilon + 2\sqrt{2\Omega}\lambda x)\mu_{21}(t,x)\\
&\quad - i\frac{\Delta}{2}(\mu_{11}(t,x) - \mu_{22}(t,x)),
\end{aligned} \tag{6.18}$$

where $\mu_{ij}(t,x)$ is a phase-space variable describing the time evolution of both the dimer

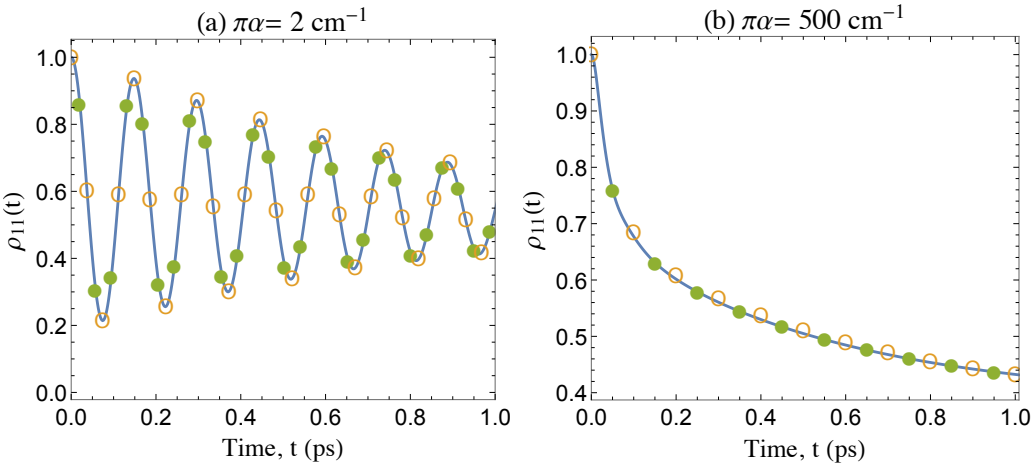


Figure 6.1: Comparison of the dimer site population dynamics $\rho_{11}(t)$ calculated from the RCME (solid), Zusman equations (open-points) and the HEOM (solid-points) for various coupling strengths. The cut-off frequency taken is $\omega_c = 53.08$ cm^{-1}. The other parameters are $\Delta = 200$ cm^{-1}, $\epsilon = 100$ cm^{-1}, and the temperature is $T = 300$ K.

and RC with respect to the phase space parameter x. We can then obtain the time evolution of the TLS population ($\rho_{11}(t)$) and coherence ($\rho_{12}(t)$) using:

$$\rho_{11}(t) = \int_{-\infty}^{\infty} \mu_{11}(t,x)dx \quad \text{and} \quad \rho_{12}(t) = \int_{-\infty}^{\infty} \mu_{12}(t,x)dx.$$

In deriving the Zusman equation we have used a semi-classical treatment of the RC in which quantum correlations between the RC and dimer are neglected – a consequence of assuming the momentum is in thermal equilibrium and the high temperature approximation. This allows one to capture system dynamics in the high friction limit, but quickly fails in situations where correlations between the RC and TLS become important, as will be discussed in the sections that follow. One may extend the validity of the Zusman equations by considering higher order terms in the friction expansion, however, these equations quickly become unwieldy and computationally impractical.

6.4 System dynamics

To calculate the population dynamics using Eq. 6.13, we assume the system and reaction coordinate are uncorrelated at time $t = 0$, with the RC in a thermal state and an excitation localised at site 1, that is, $\rho(0) = \mathcal{Z}^{-1}|1\rangle\langle 1| \otimes \exp\left(-\beta\Omega a^\dagger a\right)$, where $\mathcal{Z} = \mathrm{tr}\left(\exp\left(-\beta\Omega a^\dagger a\right)\right)$. For the Zusman equations, this gives the boundary condition:

$$\mu_{11}(0,x) = 2\sqrt{\frac{\tanh\left(\frac{\beta\Omega}{2}\right)}{\pi}} e^{-\Omega\tanh\left(\frac{\beta\Omega}{2}\right)x^2}, \tag{6.19}$$

while $\mu_{22}(0,x) = \mu_{21}(0,x) = \mu_{12}(0,x) = 0$. We shall now compare the dynamical behaviour as predicted by the RC master equation and Zusman equations solved numeri-

cally [159, 160], benchmarked against the HEOM, for both the under- and over-damped spectral densities.

6.4.1 Overdamped spectral density

In Fig. 6.1 we compare the time evolution of the population at site 1 as predicted by the RCME (solid curves), Zusman equations (open points) and the HEOM (solid points) for an overdamped environment. Here we take parameters representative of a subset of the Fenna-Matthews-Olson complex [127] for an overdamped spectral density with cut-off frequency $\omega_c = 53.08$ cm^{-1}. We see that, in this regime, the agreement between the RCME and the HEOM is excellent at both weak and strong coupling to the environment, capturing the transition from coherent to incoherent energy transfer [49]. It is clear, therefore, that by including the RC into the system Hamiltonian, we are able to faithfully represent all relevant system-environment correlations in the dimer evolution.

Furthermore, for an overdamped environment, the damping from the residual environment suppresses any significant oscillations in the RC degrees of freedom — to put it another way, the RC dynamics are in a high friction regime. Thus the Zusman equations remain an adequate description of the dimer system, producing excellent agreement with the HEOM for the system population dynamics, as is demonstrated in Fig. 6.1.

Non-Canonical thermal states and the dynamical generation of correlations

The system-environment correlations captured through the RC mapping have interesting implications for both the dynamical and steady state properties of the system. For example, in Chapter 5 we saw that the coupling between the system and environment generates significant short and long-time correlation [148], in addition to non-Gaussian states of the environment [147].

These correlations also have consequences for probing the dynamics in excitonic energy transfer systems. For example, consider a system that is initially in equilibrium with its external environment, before being perturbed by a driving field. Naïvely one might assume that the initial state of the system in this situation may be the canonical thermal state with respect to the internal system Hamiltonian. Fig. 6.2, however, demonstrates that this assumption may be misleading in the context of our molecular dimer system, in particular when probing the population and coherence dynamics. Here, we consider the dynamical evolution of the dimer in the excitonic (eigenstate) basis, when the system is initiated in the canonical thermal state:

$$\rho_s(0) = \frac{e^{-\beta(\frac{\epsilon}{2}\sigma_z + \frac{\Delta}{2}\sigma_x)}}{\mathcal{Z}_C}, \tag{6.20}$$

with $\mathcal{Z}_C = \mathrm{tr}_s\left(e^{-\beta(\frac{\epsilon}{2}\sigma_z + \frac{\Delta}{2}\sigma_x)}\right)$, and the RC is once again taken to be initially in a canonical thermal state. The energy transfer dynamics shown in Fig. 6.2 display coherent oscillations in the dimer excitonic basis, and even the dynamical generation of coherences. This comes as quite a surprise when compared to less sophisticated master equation techniques in which the system-environment coupling is treated perturbatively. Often in such

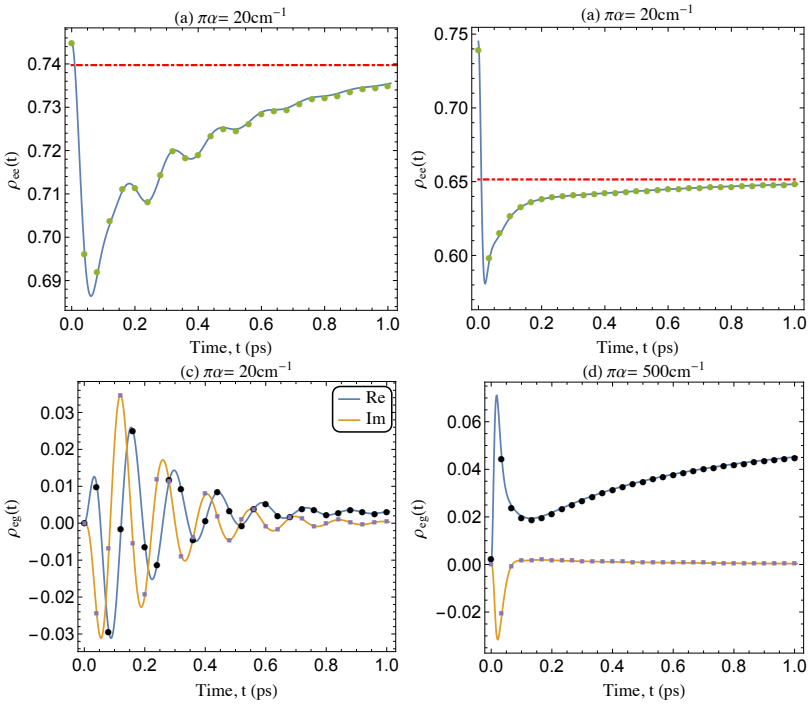


Figure 6.2: Top: Plots showing the population dynamics when system is initiated in the canonical thermal state given in Eq. 6.20. The solid curve is RC and the dot-dashed line is the non-canonical steady state given in Eq. 6.21 and the points are the HEOM. Bottom: The corresponding real and imaginary part of the dimer coherence in the excitonic (eigenstate) basis calculated using the RCME (solid) and the HEOM (points). Other parameters for this plot are the same as Fig. 6.1(c) - left and (d) - right. Overdamped HEOM data provided by Neill Lambert.

approaches one would expect there to be no dynamical evolution at all in the dimer eigenbasis as the state given in Eq. 6.20 is the expected equilibrium steady-state.

However, in regimes in which the environmental correlation time is long, significant correlations are accumulated between the system and environment. As was shown in Chapter 5, this results in the canonical thermal state no-longer describing the true equilibrium state of the system. Instead the steady-state may be expressed as a canonical thermal state with respect to the full reaction coordinate Hamiltonian:

$$\rho(t \to \infty) = \frac{e^{-\beta(\frac{\epsilon}{2}\sigma_z + \frac{\Delta}{2}\sigma_x + \lambda\sigma_z(a^\dagger + a) + \Omega\ a^\dagger a)}}{\mathcal{Z}_{NC}}, \tag{6.21}$$

where $\mathcal{Z}_{NC} = \mathrm{tr}\left(e^{-\beta H_S}\right)$. Thus, upon initiating the dimer in the canonical thermal state, cohererent oscillations occur before the system equilibrates to the non-canonical thermal state.

6.4.2 Underdamped spectral density

In this section we shall discuss the role of an underdamped spectral density on the EET dynamics of the molecular dimer system. The resultant complex system dynamics have particular relevance to EET in the presence of structured environments, where the system

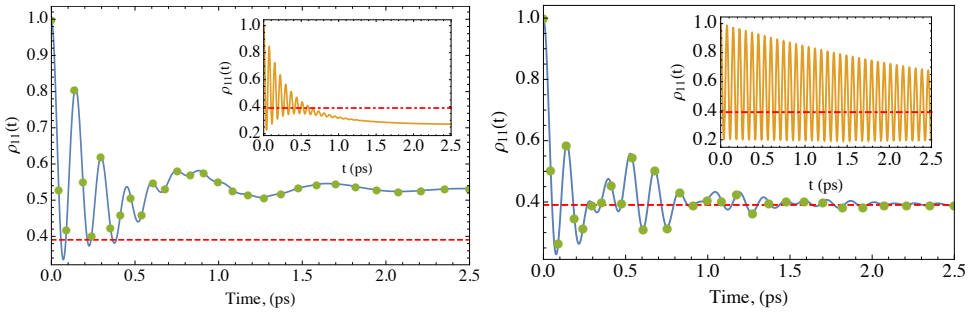


Figure 6.3: (a) Population dynamics for an underdamped spectral density with $\omega_0 = 40$ cm^{-1}, $\pi\alpha_{UD} = 20$ cm^{-1}, (b) Population dynamics for an underdamped spectral density with $\omega_0 = 220$ cm^{-1}, $\pi\alpha_{UD} = 10$ cm^{-1}. Here RC (solid), HEOM (points), and Zusman equations (inset) for the underdamped spectral density. Other parameters used for these plots are: $\Delta = 200$ cm^{-1}, $\epsilon = 100$ cm^{-1}, $\Gamma = 10$ cm^{-1}, and $T = 300$ K. Underdamped HEOM data provided by Arend Djikstra.

may be strongly coupled to lossy vibrational modes dominant in the vibrational spectrum of pigment protein complexes.

Fig. 6.3 compares the population and coherence dynamics for the RC master equation (solid), HEOM (points), Zusman equations (inset), along with the non-canonical steady state (dashed-red) for both a low ($\omega_0 = 40$ cm^{-1}) and high ($\omega_0 = 220$ cm^{-1}) frequency underdamped spectral density.

In both cases we see that the Zusman equations fail to capture the correct dynamical behaviour of the molecular dimer. This failure may be attributed to the dynamical response of the RC itself; for the low frequency spectral density, when one compares the RC frequency ($\Omega = 40$ cm^{-1}) to the friction acting on the mode ($\gamma = 1.5 \times 10^{-3}$), we see that the reaction coordinate is weakly damped, thus the high frequency limit taken to derive the Zusman equation is invalid, i.e. the momentum of the RC does not remain in thermal equilibrium in this regime. This can be seen explicitly in Fig 6.4 where we have shown the time evolution of the expectation values of the RC position $\langle\hat{x}(t)\rangle = \mathrm{tr}(\hat{x}\rho(t))$, and momentum $\langle\hat{p}(t)\rangle = \mathrm{tr}(\hat{p}\rho(t))$, where:

$$\hat{x} = \sqrt{\frac{1}{2\Omega}}(a^\dagger + a) \quad \text{and} \quad \hat{p} = i\sqrt{\frac{\Omega}{2}}(a^\dagger - a). \tag{6.22}$$

The plot shows significant oscillations at multiple frequencies in both the RC position and momentum, which is gradually damped at long times, equilibrating to non-zero values consistent with the non-canonical thermal state given in Eq. 6.21.

The disagreement between the Zusman equations and the RC model is exacerbated further when the underdamped spectrum is tuned close to the resonance of the dimer $\omega_0 = 220$ cm^{-1}, with the dimer resonance $\eta = \sqrt{\epsilon^2 + \Delta^2} \approx 223$ cm^{-1}. Here the RC is further out of the overdamped regime, thus, as can be seen in Fig. 6.4 (b), it undergoes even more significant oscillations. In this regime the Zusman equations are completely unable to capture the dynamical behaviour of the system, predicting only rapid oscillations in the dimer population (Fig. 6.4 inset). The RC model, on the other hand, shows excellent agreement with the HEOM for both short and long times, capturing perfectly the

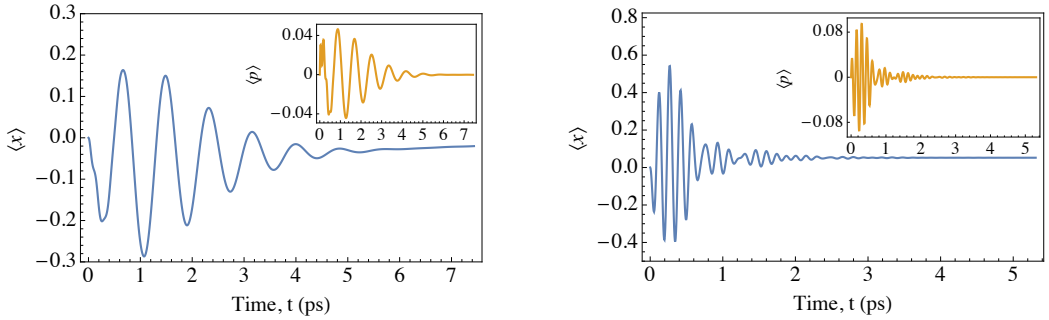


Figure 6.4: The reaction coordinate position (main) and momentum (inset) for (Left) $\omega_0 = 40$ cm^{-1}, $\pi\alpha_{UD} = 20$ cm^{-1}, and (Right) $\omega_0 = 220$ cm^{-1}, $\pi\alpha_{UD} = 10$ cm^{-1}. Other parameters used for these plots are the same as Fig 6.3.

population dynamics of the dimer. In both the low and high frequency cases, the population dynamics show complex beating behaviour, with oscillations at multiple frequencies. Using the RC formalism we have a clear interpretation for this behaviour. As shown by the right hand plot of Fig. 6.4, in this regime the collective coordinate of the environment is able to oscillate strongly, leading to the TLS population and coherence dynamics being modulated by the RC frequency.

This can be seen explicitly from Fig 6.5, where we have taken the Fourier transform of the population dynamics given in Fig. 6.3, that is:

$$S(\omega) = \mathrm{Re}\left[\int_0^\infty dt e^{i\omega t}\left(\rho_{11}(t) - \rho_{11}(t\to\infty)\right)\right], \tag{6.23}$$

where we have subtracted the steady state population, $\rho_{11}(t \to \infty)$, to remove the δ-function contribution from the steady-state population. For a low frequency underdamped spectrum, we see the presence of two specific frequencies, one at the RC mode frequency ($\omega_0 = 40$ cm^{-1}), and the other at the dimer splitting ($\eta = \sqrt{\epsilon^2 + \Delta^2} \approx 223$ cm^{-1}).

When the peak of the spectral density approaches the dimer splitting we not only see an increase in the lifetime of coherent oscillations, but also significantly more structure in the oscillation spectrum, as reflected in the right hand plot of Fig 6.5, where numerous peaks emerge. This comes as somewhat of a surprise given that the reorganisation energy,

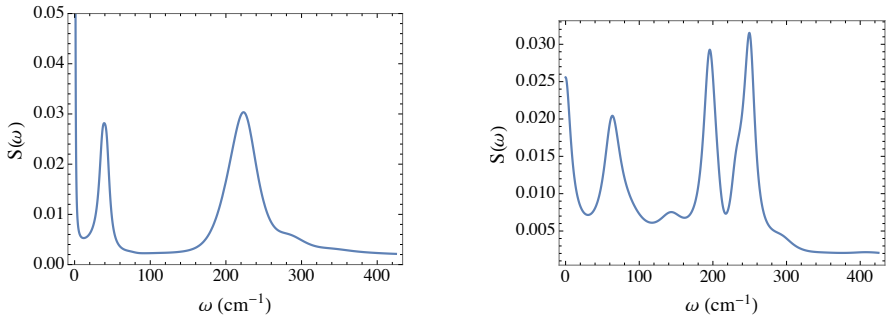


Figure 6.5: Plot showing the Fourier transform of populations for the RC dynamics in Fig. 6.3, demonstrating the presence of multiple oscillation frequencies. (Left) $\omega_0 = 40$ cm^{-1}, and (Right) $\omega_0 = 220$ cm^{-1}.

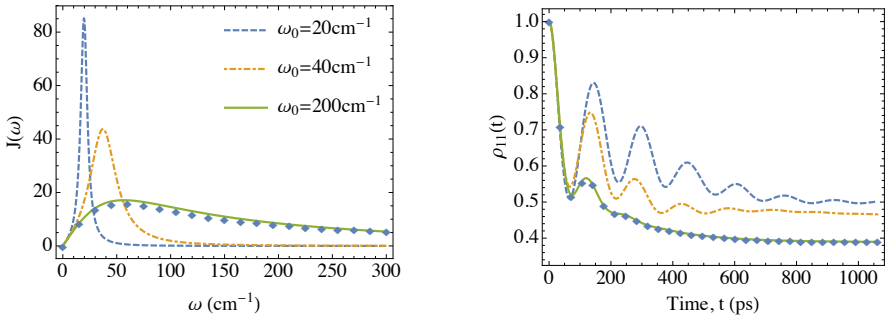


Figure 6.6: (Left) Underdamped (curves) and overdamped (points) spectral densities for several environmental frequencies. (Right) The dynamics associated to these spectral densities. Here we see a smooth transition from underdamped to overdamped regime for large environmental frequencies. The parameters are the same as Fig. 6.3, with $\Gamma = \omega_0^2 \omega_c^{-1}$, and $\pi\alpha = 100$ cm^{-1}.

which is often interpreted as the effective system-environment coupling strength, is the same in both low and high frequency cases. Again, we may explain this by appealing to the physical intuition gained from the RC model; the environmental response, and thus RC splitting, lies close to the resonant frequency of the dimer, leading to an enhancement of the interaction between the dimer and RC, thus suppressing dissipation from the residual environment. As a result of this enhanced coupling, the spectrum of the system cannot be associated to the bare frequencies of the dimer and RC, but rather the eigenstates of the composite system. Here we see a double peak structure about $\omega \sim 220$ cm^{-1}, which are split by the RC-dimer coupling strength $2\lambda = 66$ cm^{-1}, such that the dimer population oscillates at the joint eigenfrequency $\omega \sim \omega_0 \pm \lambda$. This is reminiscent of the vacuum Rabi splitting observed in cavity QED systems, in which the eigenstates of the system are the light-matter entangled dressed states discussed in Sec. 4.2.

The presence of multiple oscillation frequencies in the population dynamics has important implications to a number of ongoing experiments on excitonic energy transfer systems – it is common practice to assign electronic and vibrational frequencies from the power spectrum obtained using the 2D spectroscopy [161]. However, the results given above demonstrate that this is not so straightforward in situations where underdamped oscillations are present, as one must also account for the coupling between the molecular dimer and any underdamped modes present which lead to the formation of vibronic states.

As a final remark, we can show that the RC model for an underdamped spectrum convergences to the overdamped case in regimes where $\Gamma, \omega_0 \gg 1$. We demonstrate this by defining a cut-off frequency in the underdamped spectrum as $\omega_c = \omega_0^2/\Gamma$, this sets the energy scale of the overdamped spectrum in the appropriate limit. Using this definition we fix $\Gamma = \omega_0^2/\omega_c$ and consider the underdamped spectrum for increasing ω_0 as is demonstrated in Fig. 6.6. Here we see a smooth transition between the under- and over-damped spectral densities, with the two theories agreeing well at large ω_0.

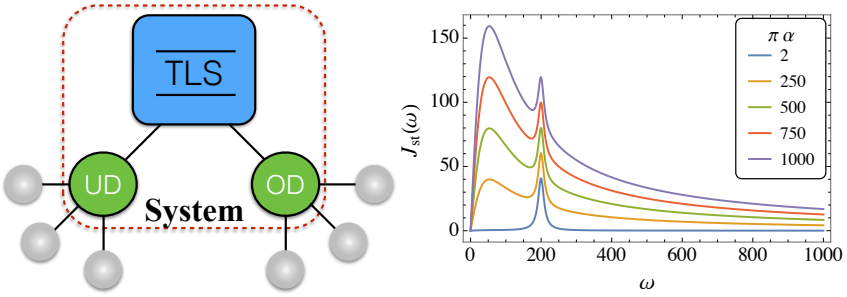


Figure 6.7: (Left) A schematic of the RC model for a structured environment with one underdamped (UD) and overdamped (OD) environment, each coupled to their own residual environment. (Right) The structured spectral density with the overdamped environment considered at various reorganisation energies. The underdamped vibrational mode is at $\omega_0 = 200$ cm^{-1}, with $\Gamma = 20$ cm^{-1} and $\pi\alpha = 2$ cm^{-1}.

6.5 Structured environments

In this section we shall explore how a structured environment alters the energy transfer rate in a molecular dimer system. To do this we shall consider the dynamics of a dimer coupled to a broad background environment described by an overdamped spectral density, with structure accounted for using a second underdamped environment. We shall model both environments using the RC mapping outlined previously, extracting an independent RC for each environment, allowing us to rigorously account for dissipation on the underdamped mode. This is distinct from the typical phenomenological approach often used in the literature [151, 156], in which structure is accounted for by incorporating discrete vibrational modes into the system Hamiltonian in an ad-hoc fashion.

To proceed we shall consider a TLS coupled to an environment with a broad overdamped Lorentz-Drude spectral density, with a second underdamped environment with peak centered around ω_0. The Hamiltonian describing the system and environments may be written as:

$$H_{ST} = H_{Dim} + \sigma_z \sum_{j=1}^{2} \sum_k f_k^{(j)} (c_{j,k} + c_{j,k}^\dagger) + H_B, \tag{6.24}$$

with $H_B = \sum_k \omega_k^{(j)} c_{j,k}^\dagger c_{j,k}$, and $H_{Dim} = \frac{\epsilon}{2}\sigma_z + \frac{\Delta}{2}\sigma_x$ is the Hamiltonian for the molecular dimer system. The two independent environments are characterised by the spectral densities:

$$J_j(\omega) = \sum_k |f_k^{(j)}|^2 \delta(\omega - \omega_k^{(j)}), \tag{6.25}$$

with $J_1(\omega) = J_{OD}(\omega)$ and $J_2(\omega) = J_{UD}(\omega)$. The combination of these terms leads to an effective spectral density with a broad background, given by the overdamped spectral density, and a sharp peak associated to the underdamped spectral density. An illustrative example of the effective spectral density is given by the right hand plot of Fig. 6.7.

We shall assume that these environments are initially uncorrelated with one another, but are able to generate correlations through interactions mediated by the dimer. This allows each environment to be mapped to the RC model independently, as is shown schemat-

ically in Fig. 6.7 (Left). Applying the mapping we obtain the Hamiltonian:

$$H_s = \frac{\epsilon}{2}\sigma_z + \frac{\Delta}{2}\sigma_x + \sigma_z \sum_i \eta_i \left(a_i^\dagger + a_i\right) + \sum_i \Omega_i a_i^\dagger a_i, \tag{6.26}$$

with a_1 (a_2) the annihilation operator of the reaction coordinate associated with the under- (over-) damped environment. Each RC then couples to an independent residual environment, which has a Hamiltonian of the form:

$$H_I = \sum_i \left(a_i^\dagger + a_i\right) \sum_k g_k^{(i)} \left(b_{i,k}^\dagger + b_{k,i}\right), \tag{6.27}$$

where b_i and $b_i^\dagger$ are the ladder operators for each environment, which are characterised by the residual spectral density $\tilde{J}_i(\omega) = \sum_k |g_k^{(i)}|^2 \delta(\omega - \omega_k) = \gamma_i \omega$. The parameters describing the RC can then be found in terms of the original spectral density using the relations given in Section 6.2.

6.5.1 Reaction coordinate model for structured environments

By following the derivation for the RC master for each independent environment we obtain the equation of motion describing the dynamics for the TLS and *both* reaction coordinates:

$$\frac{\partial \rho(t)}{\partial t} = -i\left[H_s, \rho(t)\right] - \sum_i \left[\hat{A}_i, \left[\hat{\chi}_i, \rho(t)\right]\right] + \left[\hat{A}_i, \left\{\hat{\Xi}_i, \rho(t)\right\}\right], \tag{6.28}$$

with $\hat{A}_i = (a_i^\dagger + a_i)$, and the rate operators $\hat{\chi}_i$ and $\hat{\Xi}_i$ defined in analogy to the single RC method.

6.5.2 Transition from coherent to incoherent energy transport

We now wish to quantitatively analyse the energy transfer rate for both structured and unstructured environments. In regimes where the dimer splitting is greater than the tunnelling rate (in this case $\epsilon = 100$ cm^{-1} and $\Delta = 40$ cm^{-1}), we can do so by defining a rate using the the classical rate equations [127]:

$$\frac{dP_1(t)}{dt} = -k_{1\to 2}P_1 + k_{2\to 1}P_2 \qquad \text{and} \qquad \frac{dP_2(t)}{dt} = k_{1\to 2}P_1 - k_{2\to 1}P_2, \tag{6.29}$$

where P_i is the population at site i and $k_{i\to j}$ is the transfer rate between sites i and j. This leads to a purely exponential decay of the dimer populations, thus neglecting all coherent contributions in the energy transfer dynamics. Though a coarse approximation this procedure gives insight into the overall transfer rate, and is accurate in regimes where the tunnelling between sites is weak and coherent dynamics are suppressed.

In Fig. 6.8 (Left) we plot the inter-site transfer rate as a function of the reorganisation energy for the RC master equation (solid curve), HEOM (points), and the Redfield theory as derived in Sec. 2.3.1, for a system coupled to a single over damped environment. Here we see that both the RC master equation and HEOM captures the smooth transition

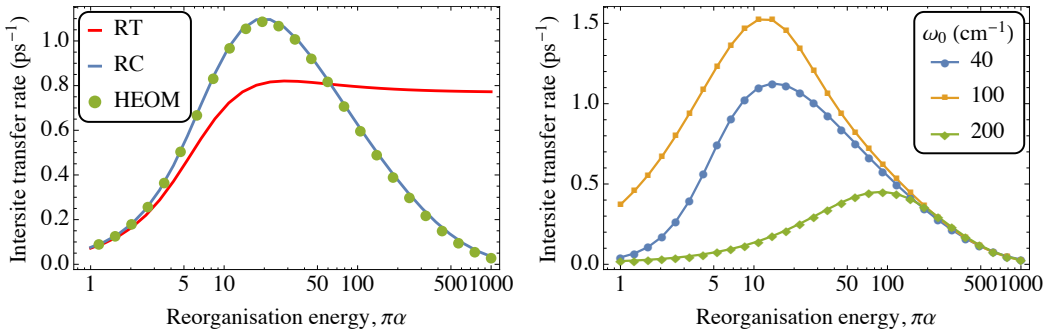


Figure 6.8: Change in the intersite energy transfer rate $k_{2\to1}$ for increasing reorganisation energy for (Left) Redfield (RT), RC, and HEOM theories. The RC master equation (solid blue) and HEOM (points) predict a smooth transition between coherent and incoherent energy transfer, while a weak coupling Redfield master equation (Red) fails to capture the correct behaviour for all but the weakest coupling strength. (Right) Energy transfer rate for a single underdamped environment for various characteristic frequencies ω_0 with $\Gamma = 20$ cm^{-1}; notice that the maximal transfer rate occurs close to the resonance of the TLS. Other parameters are $\epsilon = 100$ cm^{-1}, $\Delta = 40$ cm^{-1}, $\omega_c = 53$ cm^{-1}, and $T = 300$ K. Overdamped HEOM data provided by Neill Lambert.

between coherent and incoherent dynamics [49], while the Redfield theory fails to capture the correct transfer rate for all but the smallest coupling strengths, plateauing at large reorganisation energies [8, 127].

We may also explore the EET rate in the presence of an underdamped environment using the RC master equation. As shown by Fig. 6.8 (Right), much like the overdamped example, the energy transfer rate for the underdamped spectral density shows a peak at some intermediate coupling strength, the position and height of which is highly dependent on the characteristic frequency of the underdamped environment. Specifically, the transfer rate reaches its maximum when the peak of the underdamped spectrum approaches the resonance of the dimer ($\omega_0 \sim \eta \approx 107$ cm^{-1}). As was discussed in Sec. 6.4.2, when the dimer and the RC are close to resonant, the vibronic states of the composite system play a significant role in the dynamics; in this case they increase the number of pathways available for energy to be transferred between the two sites of the dimer [156], thus increasing the EET rate.

In Fig. 6.9 we repeat the rate equation analysis in the presence of a structured environment, with the underdamped contribution set to a constant reorganisation energy, while the coupling to the overdamped environment is varied. Here we see that the when the overdamped environment is weakly coupled to the dimer, the presence of the underdamped environment enhances the energy transfer rate. This enhancement is particularly apparent when the underdamped environment is close to the resonance of the dimer, decreasing when the underdamped oscillator is tuned away from resonance.

As in Fig. 6.8, this enhancement is due to the underdamped environment increasing the number of transfer pathways generated by the manifold of vibronic states. When the underdamped environment is tuned away from resonance, the effective coupling between the dimer and underdamped RC is reduced, thus the number of vibronic states that can be explored by the composite system decrease, consequently reducing the rate of EET.

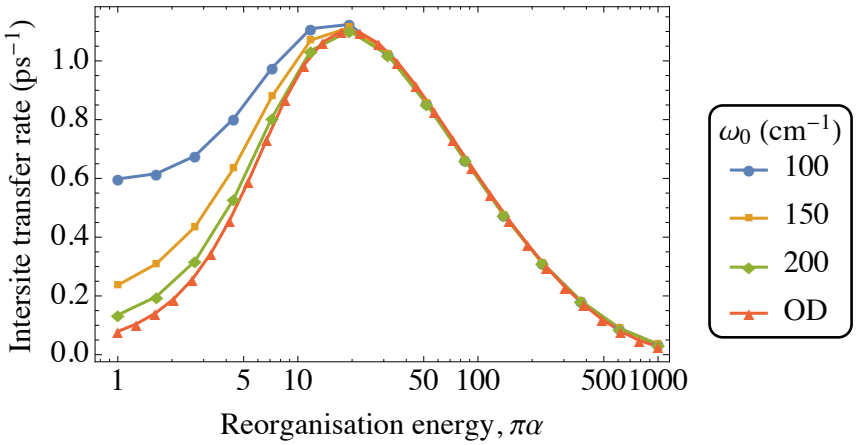


Figure 6.9: Enhancement of transfer rate when structure in the environment is considered. The reorganisation energy of the underdamped environment is kept constant at $\pi\alpha_{UD} = 2$ cm^{-1} and several frequencies ω_0 are considered, while the reorganisation energy of the overdamped environment is increased. For comparison, we have also included the transfer rate for a overdamped unstructured environment. The dimer and overdamped parameters are the same as Fig. 6.8, while the underdamped environments have $\Gamma = 20$ cm^{-1} and $T = 300$ K.

At large overdamped reorganisation energies, however, the enhancement is suppressed, regardless of the underdamped frequency, and the transfer rate follows that of a single overdamped environment. This is a consequence of the overdamped environment becoming the dominant influence on the energy transfer dynamics, such that the vibronic states provided by the underdamped environment have little effect on the EET dynamics.

6.6 Summary

In summary, we have shown that the RC master equation provides a powerful and intuitive method for describing excitonic energy transfer – and more generally open quantum systems – for regimes in which the environmental correlation time is large. Furthermore, we have demonstrated that the RC master equation greatly outperforms the closely related semi-classical Zusman equations, demonstrating that not only is the mapping important to capture the correct system dynamics, but one must also account for correlations between the molecular dimer and the RC. These correlations lead to complex system dynamics, demonstrating multiple oscillation frequencies in the system population dynamics which we interpret as feedback from a collective mode of the environment.

Furthermore, we have applied the RC model to describe the behaviour of structured phonon environments, demonstrating that the presence of structure in the environment is capable of greatly increasing the rate of energy transport within in the molecular dimer system. In doing so we have highlighted that this enhancement is dependent on the energy scale of the underdamped vibrations within the environment, reaching its peak when the vibrations lie close to the resonance of the molecular dimer.

CHAPTER 7

CONCLUSIONS AND FURTHER WORK

The work presented in this thesis tackles a number of important problems related to the theory of open quantum systems, focussing on regimes in which a system is strongly coupled to its many-body environment. In doing so, we have highlighted several examples where the system-environment coupling can have counter-intuitive and often surprising implications for the properties of the system.

Specifically, in Chapter 3 we found that the balance of coherently and incoherently scattered light from a classically driven QD is significantly altered by phonon interactions when compared to an analogous atomic system. Furthermore, we also showed that phonon processes directly affect the second-order correlation functions of a driven QD, which has surprising consequences for the measurement statistics of the emitted photons.

The effect of phonons on the emission properties of QDs discussed in Chapter 3 naturally poses the question: can we exploit phonon interactions to develop schemes for quantum technologies? For example, it may be possible to employ the enhanced coherent scattering regime to develop a bright sources of indistinguishable photons, or even use phonon induced processes to enhance the visibility of two photon interference experiments discussed towards the end of the chapter.

In Chapter 4 we explored the emission properties of cavity QD systems; in doing so, we showed that dissipative processes in the form of phonon interactions induce quantum light-matter correlations in otherwise semi-classical regimes of cavity QED. In other words, the dissipative system is more quantum mechanical than the non-dissipative one, challenging the notion that environmental interactions decohere a system to a more classical description.

A natural extension of this work would be to develop and apply the variational polaron formalism introduced in Chapter 3 to cavity QED systems. This would extend the polaron theory to a broad range of cavity QED regimes, for example when the cavity-emitter coupling strength exceeds the cut-off frequency of the environment. This would provide a powerful formalism applicable not only to quantum dot photonic devices, but also to many other architectures for quantum technologies, e.g. superconducting circuits.

In Chapter 5 we developed the reaction coordinate formalism; this provided us with a powerful and intuitive technique for describing the dynamics of a system coupled to an environment with a long correlation time. We demonstrated that this technique not only captured the correct system dynamics in computationally challenging regimes, but also

gave direct insight into the correlations shared between the system and environment, as well as the dynamical evolution of the environment itself. In doing so, we identified that system-environment correlations persist into the steady state, generating non-canonical system equilibrium states.

One possible extension of the RC technique would be to combine it with the variational polaron formalism. In the variational theory, high frequency modes are displaced and treated in a polaron type formalism, while the low frequency modes are treated within the weak coupling framework. This limits the variational theory to regimes in which the low frequency modes of the environment are coupled peturbatively to the system. In contrast, the RC formalism has been shown to be a powerful tool for describing the interaction between a system and environment in which the low frequency modes are dominant, even in strong coupling regimes. Thus its seems natural to ask whether we can combine the two theories into a polaron-reaction coordinate hybrid theory. Here the spectral density of the environment would be partitioned into a high and low frequency contribution. The RC mapping would then be applied to the low frequency modes, while the high frequency portion is accounted for using the polaron formalism. The resultant *polaron-reaction coordinate master equation* (PoRC-ME) has the potential to be applicable over a large regime of parameter space, while maintaining the computational simplicity that makes the master equation formalism so appealing.

In Chapter 6 the RC master equation was applied to describe the excitonic energy transfer dynamics in a molecular dimer system. Here we discussed the influence that under- and overdamped environments have on the excitonic dynamics, using insight gained through the RC formalism to describe the subsequent complex systems dynamics. Furthermore, we showed that the presence of structure in the environmental spectral density can, under certain conditions, enhance the excitonic energy transfer rate.

An extension of this work would be to apply the RC formalism to more complex energy transport systems, either with more structured environments, or multiple sites, for example in the Fenna-Matthew-Olsen (FMO) complex. However, each site (and therefore RC) introduced has a hefty computational cost, with the state space scaling exponentially. Thus in order to describe such systems using the RC formalism one would need to develop schemes to restrict the size of the state space when one increases the number of RCs considered, for example by discarding elements of the density operator that do not play a significant role on the EET dynamics.

APPENDIX A

CORRELATION FUNCTION FOR THE VARIATIONAL THEORY

In this appendix we derive the environmental correlation functions for the variational polaron Hamiltonian given in Eq. 3.31. The expression derived below will then be used to derive the variational master equation. Furthermore, we show that both the weak coupling and polaron correlation functions may be recovered from the variational theory in the appropriate limits.

A.1 Variational correlation functions

For the variational theory we have four bath operators to consider:

$$\begin{aligned} B_x &= \frac{1}{2}(B_+ + B_- - 2B), \\ B_y &= \frac{i}{2}(B_+ - B_-), \\ B_z &= \sum_k \tilde{g}_k \left(b_k^\dagger + b_k\right), \\ B &= \langle B_\pm \rangle = \mathrm{tr}_B \left(B_\pm \rho_B\right), \end{aligned} \tag{A.1}$$

where $B_\pm = \prod_k D(\pm\alpha_k)$, $D(\alpha_k) = \exp(\alpha_k(a_k^\dagger - a_k))$, and $\tilde{g}_k = g_k - \nu_k\alpha_k$. In the variational theory, the displacements take the form $\alpha_k = c_k F(\nu_k)/\nu_k$, where $F(\nu_k)$ is the variational function defined in Eq. 3.36. To find the two time correlation functions of the form $\langle B_i(t)B_j(s)\rangle$, for the associated operators, we shall work in the coherent state representation. The thermal state of the environment written in the coherent state representation is given by:

$$\rho_{therm} = \bigotimes_k \int d^2\alpha_k P(\alpha_k)|\alpha_k\rangle\langle\alpha_k|, \tag{A.2}$$

where $P(\alpha_k) = \exp\left(-\alpha_k^2/\bar{n}_k\right)/\pi\bar{n}_k$ and $\bar{n}_k = \left(\exp\left(-\beta\nu_k\right) - 1\right)^{-1}$ is the average occupation number of mode k.

Since each mode is defined in it's own Hilbert space, we can evaluate the correlation functions for a single mode and then generalise to the many mode case. Starting with the

average displacement for the thermal state, we have:

$$\begin{aligned}
B = \langle B_{\pm}\rangle &= \prod_k \int d^2\beta_k P(\beta_k)\,\langle\beta_k|D(\pm\alpha_k)|\beta_k\rangle\,,\\
&= \prod_k \int d^2\beta_k P(\beta_k)\,\Big\langle 0|D^{\dagger}(\beta_k)D(\pm\alpha_k)D(\beta_k)|0\Big\rangle\\
&= \prod_k \int d^2\beta_k P(\beta_k) e^{\pm\alpha_k(\beta_k^{\star}-\beta_k)}\,\langle 0|D(\pm\alpha_k)|0\rangle\,,\\
&= \prod_k \int d^2\beta_k \frac{1}{\pi\bar{n}_k} e^{-\frac{\beta_k^2}{\bar{n}_k}} e^{\pm(\alpha_k\beta_k^{\star}-\alpha_k^{*}\beta_k)} e^{-\alpha_k} = e^{-\sum\limits_k |\alpha_k|^2(\bar{n}_k+1/2)}\\
&= e^{-\sum\limits_k \frac{g_k^2}{\nu_k^2}(\bar{n}_k+1/2)} = e^{-\frac{1}{2}\sum\limits_k \frac{g_k^2}{\nu_k^2}\coth\frac{\beta\nu_k}{2}}.
\end{aligned} \tag{A.3}$$

To deal with the other correlation functions we use the following properties of the displacement operators:

$$D(a)D(b) = e^{iIm(ab^{\star})}D(a+b) \qquad \text{and} \qquad e^{-i\nu a^{\dagger}at}D(a)e^{i\nu a^{\dagger}at} = D(ae^{i\nu t}), \tag{A.4}$$

where,

$$\begin{aligned}
\langle B_{\pm}(t)B_{\pm}(s)\rangle &= \prod_k e^{iIm(|\alpha_k|^2 e^{i\nu_k(t-s)})}\langle D(\pm\alpha_k(e^{i\nu_k t}+e^{i\nu_k s}))\rangle,\\
&= \prod_k e^{iIm(|\alpha_k|^2 e^{i\nu_k(t-s)})} e^{-|\alpha_k|^2(e^{i\nu_k t}+e^{i\nu_k s})(e^{-i\nu_k t}+e^{-i\nu_k s})(\bar{n}_k+1/2)},\\
&= \prod_k e^{i|\alpha_k|^2\sin(\nu_k(t-s))} e^{-|\alpha_k|^2(1+\cos(\nu_k(t-s)))\coth(\frac{\beta\nu_k}{2})},\\
&= e^{-\sum\limits_k |\alpha_k|^2(1+\cos(\nu_k(t-s))\coth(\frac{\beta\nu_k}{2})-i\sin(\nu_k(t-s))},\\
&= C(t-s).
\end{aligned} \tag{A.5}$$

Similarly, for the other combination of B's:

$$\begin{aligned}
\langle B_{\pm}(t)B_{\mp}(s)\rangle &= \langle\prod_k e^{iIm(-|\alpha_k|^2 e^{i\nu_k(t-s)})}D(\pm 2\alpha_k(e^{i\nu_k t}-e^{i\nu_k s}))\rangle,\\
&= \prod_k e^{-i|\alpha_k|^2\sin(\nu_k(t-s)))} e^{-|\alpha_k|^2(1-\cos(\nu_k(t-s)))\coth(\frac{\beta\nu_k}{2})},\\
&= e^{-\sum\limits_k |\alpha_k|^2\Big((1-\cos(\nu_k(t-s))\coth(\frac{\beta\nu_k}{2})+i\sin(\nu_k(t-s))\Big)},\\
&= G(t-s).
\end{aligned} \tag{A.6}$$

So the the x and y correlation functions may then be written as:

$$\begin{aligned}
\Lambda_{xx}(t-s) = \langle B_x(t)B_x(s)\rangle &= \frac{1}{2}(C(t-s)+G(t-s)-2B^2),\\
\Lambda_{yy}(t-s) = \langle B_y(t)B_y(s)\rangle &= \frac{1}{2}(C(t-s)-G(t-s)),\\
\langle B_x(t)B_y(s)\rangle = \langle B_y(t)B_x(s)\rangle &= 0,
\end{aligned} \tag{A.7}$$

Now for the z correlation functions, consider the case of a displacement on a single mode:

$$\begin{aligned}
\langle D(\delta_k)B_z(s)\rangle =&\tilde{g}_k \left\langle D(\delta_k)\left(b_k^\dagger e^{i\nu_k s}+b_k e^{-i\nu_k s}\right)\right\rangle,\\
=&\tilde{g}_k\int d^2\gamma_k P(\gamma_k)\left(\left\langle\gamma_k|D(\delta_k)b_k^\dagger|\gamma_k\right\rangle e^{i\nu_k s}+e^{-i\nu_k s}\left\langle\gamma_k|D(\delta_k)|\gamma_k\right\rangle\right),\\
=&\tilde{g}_k\int d^2\gamma_k P(\gamma_k)\left((\gamma_k-\delta_k)^* e^{i\nu_k s}+\gamma_k e^{-i\nu_k s}\right)\left\langle\gamma_k|D(\delta_k)|\gamma_k\right\rangle, \qquad \text{(A.8)}\\
=&\tilde{g}_k\int d^2\gamma_k P(\gamma_k)e^{-|\delta_k|^2/2}e^{\gamma_k^*\delta_k-\gamma_k\delta_k^*}\left(e^{i\nu_k s}(\gamma_k-\delta_k)^*+\gamma_k e^{-i\nu_k s}\right),\\
=&\tilde{g}_k e^{-|\delta_k|^2(\bar{n}_k+1/2)}\left(\delta_k\bar{n}_k e^{-i\nu_k s}-\delta_k^*(1+\bar{n}_k)e^{i\nu_k s}\right).
\end{aligned}$$

Applying this to the many modes case, and substituting in the variational displacement, $\delta_k=\pm 2\alpha_k e^{i\nu_k t}$:

$$\begin{aligned}
\langle B_\pm(t)B_z(s)\rangle =&e^{-4\sum_k \alpha_k^2(\bar{n}_k+1/2)}\sum_k\left(\frac{\pm 2g_kF(\nu_k)}{\nu_k}(g_k-g_kF(\nu_k))\bar{n}_k e^{i\nu_k t}e^{-i\nu_k s}\right.\\
&\left.-\frac{\pm 2g_kF(\nu_k)}{\nu_k}(g_k-g_kF(\nu_k))^*(1+\bar{n}_k)e^{i\nu_k}\right)\\
=&\pm B\sum_k\frac{g_k^2(1-F(\nu_k))F(\nu_k)}{\nu_k}\left(\bar{n}_k e^{-i\nu_k s}-(1+\bar{n}_k)e^{i\nu_k s}\right)\\
=&\pm B\sum_k\frac{g_k^2(1-F(\nu_k))F(\nu_k)}{\nu_k}\left(2i\sin\nu_k(t-s)(\bar{n}_k-\frac{1}{2})-\cos\nu_k(t-s)\right)\\
=&\pm B\sum_k\frac{g_k^2(1-F(\nu_k))F(\nu_k)}{\nu_k}\left(i\sin\nu_k(t-s)\coth\frac{\beta\nu_k}{2}-\cos\nu_k(t-s)\right)
\end{aligned}$$

which leads to the correlation functions $\langle B_x(t)B_z(s)\rangle=0$ and:

$$\begin{aligned}
&\Lambda_{yz}(t-s)=\langle B_y(t)B_z(s)\rangle\\
&=-B\sum_k\frac{g_k^2(1-F(\nu_k))F(\nu_k)}{\nu_k}\left(\sin\nu_k(t-s)\coth\frac{\beta\nu_k}{2}+i\cos\nu_k(t-s)\right).
\end{aligned}\qquad \text{(A.9)}$$

Similarly, we find that:

$$\begin{aligned}
\langle B_z(t)B_x(s)\rangle&=0,\\
\Lambda_{zy}(t-s)=\langle B_z(t)B_y(s)\rangle&=-\Lambda_{yz}(t-s),
\end{aligned}\qquad \text{(A.10)}$$

and,

$$\Lambda_{zz}(t-s)=\langle B_z(t)B_z(s)\rangle=\sum_k(g_k-\nu_k\alpha_k)^2\left(\cos\nu_k(t-s)\coth\frac{\beta\nu_k}{2}-i\sin\nu_k(t-s)\right).$$

It is useful for our correlation functions to have the property, $\Lambda_{ij}^*(t)=\Lambda_{ij}(-t)$, however $\Lambda_{yz}^*(t)=-\Lambda_{yz}(-t)$, so we define a correlation function $\Lambda'_{yz}(t)$ such that $\Lambda'_{yz}(t)=i\Lambda_{yz}(t)$.

Thus, in the continuum limit we have:

$$\begin{aligned}
\Lambda_{xx}(\tau) =& \frac{B^2}{2}\left(e^{\phi(\tau)} + e^{-\phi(\tau)} - 2\right) \\
\Lambda_{yy}(\tau) =& \frac{B^2}{2}\left(e^{\phi(\tau)} - e^{-\phi(\tau)}\right) \\
\Lambda_{zz}(\tau) =& \int_0^\infty J(\omega)(1-F(\omega))^2\left(\cos\omega\tau\coth\frac{\beta\omega}{2} - i\sin\omega\tau\right)d\omega \\
\Lambda'_{yz}(\tau) =& B\int_0^\infty \frac{J(\omega)F(\omega)(1-F(\omega))}{\omega}\left(\cos\omega\tau - i\sin\omega\tau\coth\frac{\beta\omega}{2}\right)d\omega
\end{aligned} \tag{A.11}$$

where $B = \exp\left\{-\frac{1}{2}\int_0^\infty \frac{J(\omega)F(\omega)^2}{\omega^2}\coth\frac{\beta\omega}{2}d\omega\right\}$, and $\phi(\tau) = \int_0^\infty \frac{J(\omega)F(\omega)^2}{\omega^2}\left(\cos\omega\tau\coth\frac{\beta\omega}{2} - i\sin\omega\tau\right)d\omega$.

Recovering the polaron theory

The polaron limit can be recovered by fixing the variational displacement to $\alpha_k = g_k/\nu_k$, or equivalently, setting the variational function to $F(\omega) = 1\ \forall\ \omega$. Immediately, from the definitions given in A.11, the average displacement becomes:

$$B = e^{-\frac{1}{2}\int_0^\infty \frac{J(\omega)}{\omega^2}\coth\left(\frac{\beta\omega}{2}\right)d\omega}, \tag{A.12}$$

and the correlation functions reduce to $\Lambda_{yz}(\tau) = \Lambda_{zz}(\tau) = \Lambda_{zy}(\tau) = 0\ \forall\ \tau$, and:

$$\begin{aligned}
\Lambda_{xx}(\tau) =& \frac{B^2}{2}\left(e^{\int_0^\infty \frac{J(\omega)}{\omega^2}\left(\cos\omega\tau\coth\frac{\beta\omega}{2} - i\sin\omega\tau\right)d\omega} + e^{-\int_0^\infty \frac{J(\omega)}{\omega^2}\left(\cos\omega\tau\coth\frac{\beta\omega}{2} - i\sin\omega\tau\right)d\omega} - 2\right) \\
\Lambda_{yy}(\tau) =& \frac{B^2}{2}\left(e^{\int_0^\infty \frac{J(\omega)}{\omega^2}\left(\cos\omega\tau\coth\frac{\beta\omega}{2} - i\sin\omega\tau\right)d\omega} - e^{-\int_0^\infty \frac{J(\omega)}{\omega^2}\left(\cos\omega\tau\coth\frac{\beta\omega}{2} - i\sin\omega\tau\right)d\omega}\right)
\end{aligned}$$

The weak coupling limit

The weak coupling correlation function can be recovered by setting the displacement of the environment to zero, that is $\alpha_k = 0$ and consequently $F(\omega) = 0$. In this case, the average displacement, and thus the renormalisation of phonon parameters becomes $B = 0$, and the correlation functions reduce to $\Lambda_{yz}(\tau) = \Lambda_{zy}(\tau) = \Lambda_{xx}(\tau) = \Lambda_{yy}(\tau) = 0\ \forall\ \tau$, leaving:

$$\Lambda_{zz}(\tau) = \int_0^\infty J(\omega)\left(\cos\omega\tau\coth\frac{\beta\omega}{2} - i\sin\omega\tau\right)d\omega \tag{A.13}$$

APPENDIX B

THE ZUSMAN EQUATIONS

In this appendix we will derive the Zusman equations from the reaction coordinate master equation defined in Eq. 6.15, given by:

$$\begin{aligned}\frac{\partial\rho(t)}{\partial t} =& -i\left[H_S,\rho(t)\right] - \gamma\int_0^\infty d\tau\int_0^\infty d\omega\ \omega\cos\omega\tau\coth\frac{\beta\omega}{2}\left[\hat{A},\left[\hat{A}(-\tau),\rho_S(t)\right]\right]\\ &-\gamma\int_0^\infty d\tau\int_0^\infty d\omega\cos\omega\tau\left[\hat{A},\left\{\left[\hat{A}(-\tau),H_S\right],\rho(t)\right\}\right],\end{aligned} \tag{B.1}$$

where $A = a^\dagger + a$ is the RC operator, and the RC Hamiltonian is defined as:

$$H_S = \frac{\epsilon}{2}\sigma_z + \frac{\Delta}{2}\sigma_x + \lambda\sigma_z\left(a^\dagger + a\right) + \Omega a^\dagger a \tag{B.2}$$

B.1 The Caldeira-Leggett limit

To begin the derivation, we shall use the Caldeira-Leggett approximation [2] to simplify the time dependence of the system operators. In the limit that the system is evolving slowly in comparison to the environment, one can expand the time dependence of the system operators such that:

$$\hat{a}(t) = e^{iH_St}\hat{a}e^{-iH_St} \approx \hat{a} + it\left[H_S,\hat{a}\right] = (1 - i\Omega t)\hat{a}. \tag{B.3}$$

Implicit in this expansion is a high temperature approximation, this can be understood by noticing that the most important energy-scale of the environment is the temperature, hence for the Caldeira-Leggett approximation to valid typical system frequencies ω_0 must satisfy the condition $\omega_0 \ll \beta^{-1}$. This leads to a master equation of the form:

$$\begin{aligned}\frac{\partial\rho_S(t)}{\partial t} =& -i\left[H_S,\rho_S(t)\right] - \Gamma_1\left[\hat{a}^\dagger+\hat{a},\left[\hat{a}^\dagger+\hat{a},\rho_S(t)\right]\right] - \Gamma_2\left[\hat{a}^\dagger+\hat{a},\left[\hat{a}^\dagger-\hat{a},\rho_S(t)\right]\right]\\ &-\Gamma_3\left[\hat{a}^\dagger+\hat{a},\left\{\hat{a}^\dagger+\hat{a},\rho_S(t)\right\}\right] - \Gamma_4\left[\hat{a}^\dagger+\hat{a},\left\{\hat{a}^\dagger-\hat{a},\rho_S(t)\right\}\right].\end{aligned} \tag{B.4}$$

We can calculate the rates in the above master equation using the relation $\int_0^\infty d\tau\cos\omega\tau = \pi\delta(\omega)$, such that

$$\begin{aligned}
\Gamma_1 &= \lim_{\omega\to 0} \pi J_{RC}(\omega) \coth\frac{\beta\omega}{2} = \frac{2\pi\gamma}{\beta},\\
\Gamma_2 &= i\Omega \int_0^\infty \int_0^\infty d\tau d\omega J_{RC}(\omega) \coth\frac{\beta\omega}{2}\tau\cos\omega\tau \approx -\frac{2\pi\gamma\Omega}{\beta}\int_0^\infty d\tau\tau\delta(\tau) = 0,\\
\Gamma_3 &= i\Omega \int_0^\infty \int_0^\infty d\tau d\omega \frac{J_{RC}(\omega)\cos\omega\tau}{\omega}\tau = i2\pi\gamma\Omega\int_0^\infty d\tau\ \tau\delta(\tau) = 0,\\
\Gamma_4 &= -\ \Omega \int_0^\infty \int_0^\infty d\tau d\omega \frac{J_{RC}(\omega)\cos\omega\tau}{\omega} = -\pi\gamma\Omega,
\end{aligned} \tag{B.5}$$

where we have taken the high temperature limit for Γ_2, such that $\coth\frac{\beta\omega}{2} \approx \frac{2}{\beta\omega}$. This yields the Caldeira-Leggett master equation:

$$\frac{\partial\rho_S(t)}{\partial t} = -i\left[H_S, \rho_S(t)\right] - \frac{\pi\gamma}{\beta}\left[\hat{a}^\dagger + \hat{a}, \left[\hat{a}^\dagger + \hat{a}, \rho_S(t)\right]\right] + \frac{\pi\gamma\Omega}{2}\left[\hat{a}^\dagger + \hat{a}, \left\{\hat{a}^\dagger - \hat{a}, \rho_S(t)\right\}\right]. \tag{B.6}$$

B.2 Phase space master equation

In this section, we shall derive a Wigner phase space representation of the Caldeira-Leggett master equation B.6 [102], before applying a series of approximations in order to derive the Zusman equations. First we define the Wigner function as:

$$\hat{W} = \frac{1}{2\pi}\int_{-\infty}^{\infty} dx' e^{-ipx'}\left\langle x + \frac{x'}{2}|\rho_S(t)|x - \frac{x'}{2}\right\rangle, \tag{B.7}$$

where $\hat{W}$ is a 2 by 2 matrix due to the spin degrees of freedom. In the coordinate representation, the RC coordinate Hamiltonian takes the form:

$$H_S = \frac{\epsilon}{2}\sigma_z + \frac{\Delta}{2}\sigma_x + \kappa\sigma_z\hat{x} + \frac{1}{2}\left(\hat{p}^2 + \Omega^2\hat{x}^2\right), \tag{B.8}$$

with $\kappa = \sqrt{2\omega}\lambda$, and the position and momentum operators are defined as:

$$\hat{x} = \sqrt{\frac{1}{2\Omega}}(a^\dagger + a) \qquad \text{and} \qquad \hat{p} = i\sqrt{\frac{1}{2\Omega}}(a^\dagger - a). \tag{B.9}$$

In order to determine our master equation in the Wigner representation, we need to know the phase space representations of the mode operators, i.e. the value of

$$\left\langle x + x'/2|\hat{O}\rho_S(t)|x - x'/2\right\rangle \quad \text{and} \quad \left\langle x + x'/2|\rho_S(t)\hat{O}|x - x'/2\right\rangle,$$

where $\hat{O}$ is an operator on the mode space. Starting with position:

$$\begin{aligned}\int_{-\infty}^{\infty} dx' e^{-ipx'} \langle x + x'/2|\hat{x}\rho_S(t)|x - x'/2\rangle &= \int_{-\infty}^{\infty} dx' e^{-ipx'} (x + x'/2) \langle x + x'/2|\rho_S(t)|x - x'/2\rangle, \\ &= \left(x + \frac{i}{2}\frac{\partial}{\partial p}\right) \hat{W},\end{aligned} \tag{B.10}$$

and for $\rho_S(t)\hat{x}$ just take the complex conjugate. Similarly, for the momentum operator we have:

$$\int_{-\infty}^{\infty} dx' e^{-ipx'} \langle x + x'/2|\hat{p}\rho_S(t)|x - x'/2\rangle = \left(p - \frac{i}{2}\frac{\partial}{\partial x}\right) \hat{W}. \tag{B.11}$$

So using these relations, the unitary part of equation B.6 becomes:

$$[H_s, \rho_S(t)] \leftrightarrow \left[\frac{\epsilon}{2}\sigma_z + \frac{\Delta}{2}\sigma_x, \hat{W}\right] + \kappa\left(x\left[\sigma_z, \hat{W}\right] + \frac{i}{2}\left\{\sigma_z, \frac{\partial \hat{W}}{\partial p}\right\}\right) - ip\frac{\partial \hat{W}}{\partial x} + i\Omega^2 x\frac{\partial \hat{W}}{\partial x}. \tag{B.12}$$

In phase-space the Caldeira-Leggett dissipators correspond to:

$$\begin{aligned}[\hat{x}, [\hat{x}, \rho_S(t)]] &\leftrightarrow -\frac{\partial^2 \hat{W}}{\partial p^2}, \\ [\hat{x}, \{\hat{p}, \rho_S(t)\}] &\leftrightarrow 2i\frac{\partial}{\partial p}\left(p\hat{W}\right).\end{aligned} \tag{B.13}$$

Plugging this into the master equation B.6, leads to the generalised Fokker-Planck equation in Klein-Kramers form [162]:

$$\frac{\partial \hat{W}}{\partial t} + \mathcal{H}\hat{W} + i\mathcal{Z}\frac{\partial \hat{W}}{\partial p} + p\frac{\partial \hat{W}}{\partial x} - \Omega^2 x\frac{\partial \hat{W}}{\partial p} = \Omega\pi\gamma\frac{\partial}{\partial p}\left(p\hat{W} + \frac{1}{\beta}\frac{\partial \hat{W}}{\partial p}\right), \tag{B.14}$$

where we have defined the super-operators:

$$\mathcal{H}\hat{W} = i\left[\left(\frac{\epsilon}{2} + \kappa x\right)\sigma_z + \frac{\Delta}{2}\sigma_x, \hat{W}\right] \qquad \text{and} \qquad \mathcal{Z}\frac{\partial \hat{W}}{\partial p} = \frac{i\kappa}{2}\left\{\sigma_z, \frac{\partial \hat{W}}{\partial p}\right\}. \tag{B.15}$$

B.2.1 Smoluchowski equation

To eliminate the momentum coordinate from equation B.14 we will use the procedure outlined by Coffey [162], and originally formulated by Brinkman for the case of Brownian oscillator [163]. To do this, we expand the the Wigner function in terms of Hermite polynomials:

$$\hat{W} = e^{-\mu^2/4} \sum_{n=0}^{\infty} D_n(\mu)\hat{\phi}_n(x, t), \tag{B.16}$$

where we have rescaled the momentum coordinate such that $\mu = \sqrt{\beta}p$, the function $\hat{\phi}(x, t)$ is a two by two matrix describing the electronic dependence of the Wigner function and

$D_n(\mu)$ is the set of orthogonal Weber functions which are given by:

$$D_n(y) = 2^{-n/2} e^{-y^2/4} H_n(\frac{y}{\sqrt{2}}), \tag{B.17}$$

where $H_n(z)$ are the Hermite polynomials. The Weber functions satisfy the following relations:

$$\begin{aligned}
&D_{n+1}(y) - yD_n(y) + nD_{n-1}(y) = 0,\\
&\partial_y D_n(y) + \frac{y}{2} D_n(y) - nD_{n-1}(y) = 0,\\
&\partial_y D_n(y) - \frac{y}{2} D_n(y) + D_{n+1}(y) = 0,\\
&\partial_y^2 D_n(y) + \left(n + \frac{1}{2} - \frac{y^2}{4}\right) D_n(y) = 0,\\
&\int_{-\infty}^{\infty} D_n(y) D_m(y) dy = n!\sqrt{2\pi}\delta_{m,n}.
\end{aligned} \tag{B.18}$$

Using these relations and substituting B.16 into B.14, we can acquire a Brinkmann hierarchy. Starting with the right hand side of equation B.14:

$$\begin{aligned}
\frac{\partial}{\partial\mu}\left(\mu\hat{W} + \frac{\partial\hat{W}}{\partial\mu}\right) =& e^{-\mu^2/4} \sum_n \left(\frac{1}{2} D_n(\mu) - \frac{\mu^2}{4} D_n + \partial_\mu^2 D_n(\mu)\right) \hat{\phi}(x,t),\\
=& - e^{\mu^2/4} \sum_n n D_n(\mu) \hat{\phi}_n(x,t).
\end{aligned} \tag{B.19}$$

The left hand side of B.14 can be found using a similar procedure, the first two terms are trivial, the third term is given by:

$$\begin{aligned}
\mathcal{Z}\partial_p \hat{W} =& \sqrt{\beta}\mathcal{Z}\partial_\mu \hat{W}\\
=& \sqrt{\beta}\mathcal{Z} \sum_{n=0}^{\infty} e^{-\mu^2/4} \hat{\phi}_n(x,t) \left(\partial_\mu D_n(\mu) - \frac{\mu}{2} D_n(\mu)\right),\\
=& - \sqrt{\beta}\mathcal{Z} \sum_{n=0}^{\infty} e^{-\mu^2/4} D_{n+1}(\mu) \hat{\phi}_n(x,t),
\end{aligned} \tag{B.20}$$

similarly for the fifth term. For the fourth term:

$$\begin{aligned}
p\partial_x \hat{W} =& \frac{1}{\sqrt{\beta}} e^{-\mu^2/4} \sum_{n=0}^{\infty} \mu D_n(\mu) \partial_x \hat{\phi}_n(x,t),\\
=& \frac{1}{\sqrt{\beta}} e^{-\mu^2/4} \sum_{n=0}^{\infty} \left(D_{n+1}(\mu) + nD_{n+1}(\mu)\right) \partial_x \hat{\phi}_n(x,t).
\end{aligned} \tag{B.21}$$

Finally, multiplying by $\left(n!\sqrt{2\pi}\right)^{-1} \exp\left(\mu^2/4\right) D_m(\mu)$, and integrating over the rescaled

momentum, μ, gives the Brinkmann hierarchy:

$$\frac{\partial\hat{\phi}_m}{\partial t} + \mathcal{H}\hat{\phi}_m - \sqrt{\beta}\mathcal{Z}\hat{\phi}_{m-1} + \frac{1}{\sqrt{\beta}}\left(\frac{\partial\hat{\phi}_{m-1}}{\partial x} + (m+1)\frac{\partial\hat{\phi}_{m+1}}{\partial x}\right) + \sqrt{\beta}\Omega^2 x\hat{\phi}_{m-1} + \pi\gamma\Omega m\hat{\phi}_m = 0. \tag{B.22}$$

We now define the differential operators:

$$\begin{aligned}\mathcal{J} &= -\frac{\sqrt{\beta}}{\eta}\left(\frac{1}{\beta}\frac{\partial}{\partial x} + \Omega^2 x - i\mathcal{Z}\right),\\ \mathcal{J}_D &= -\frac{1}{\eta\sqrt{\beta}}\frac{\partial}{\partial x},\end{aligned} \tag{B.23}$$

which allows us to write:

$$\frac{1}{\eta}\left(\dot{\hat{\phi}}_m + \mathcal{H}\hat{\phi}_m\right) + m\hat{\phi}_m = \mathcal{J}\hat{\phi}_{m-1} + (m+1)\mathcal{J}_D\hat{\phi}_{m+1}, \tag{B.24}$$

where $\eta = \pi\gamma\Omega$ quantifies the friction acting on the mode. We now move to Laplace space with respect to the time coordinate, using the transformation:

$$\tilde{\varphi}_n = \tilde{\varphi}_n(x,s) = \int_{-\infty}^{\infty}\hat{\phi}_n(x,t)e^{-st}dt, \tag{B.25}$$

which leads to the relation:

$$\frac{\partial\hat{\phi}_n}{\partial t} \overset{\text{LT}}{\Longrightarrow} s\tilde{\varphi}_n - \hat{\phi}_n(x,0). \tag{B.26}$$

For a mode initially in a thermal state, the initial conditions of the system is entirely determined by $\hat{\phi}_0(x,0)$, such that $\hat{\phi}_n(x,0) = 0$ for $n > 0$, leading to the following hierarchy of equations in Laplace space:

$$\frac{1}{\eta}\left(s\tilde{\varphi}_0 + \hat{\phi}_0(x,0) + \mathcal{H}\tilde{\varphi}_0\right) = \mathcal{J}_D\tilde{\varphi}_1, \tag{B.27}$$

$$\frac{1}{\eta}\left(s\tilde{\varphi}_1 + \mathcal{H}\tilde{\varphi}_1\right) + \tilde{\varphi}_1 = \mathcal{J}\tilde{\varphi}_0 + 2\mathcal{J}_D\tilde{\varphi}_2, \tag{B.28}$$

$$\frac{1}{\eta}\left(s\tilde{\varphi}_2 + \mathcal{H}\tilde{\varphi}_2\right) + 2\tilde{\varphi}_2 = \mathcal{J}\tilde{\varphi}_1 + 4\mathcal{J}_D\tilde{\varphi}_3. \tag{B.29}$$

$$\vdots \tag{B.30}$$

We can close these equations by assuming $\tilde{\varphi}_3 = 0$ (which is consistent with keeping terms to leading order in η^{-2}) and hence solve for $\tilde{\varphi}_0$. So, inverting the equation for $\tilde{\varphi}_2$:

$$\tilde{\varphi}_2 = \frac{\mathcal{J}\tilde{\varphi}_1}{\frac{1}{\eta}(s+\mathcal{H}) + 2}, \tag{B.31}$$

and subbing this into the equation $\tilde{\varphi}_1$, gives:

$$\tilde{\varphi}_1 = \frac{\mathcal{J}\tilde{\varphi}_0}{\frac{1}{\eta}(s+\mathcal{H}) + 1 + \frac{2\mathcal{J}_D\mathcal{J}}{\frac{1}{\eta}(s+\mathcal{H})+2}}, \tag{B.32}$$

which leads to the equation:

$$\frac{1}{\eta}\left(s\tilde{\varphi}_0+\hat{\phi}_0(x,0)+\mathcal{H}\tilde{\varphi}_0\right)=\frac{\mathcal{J}_D\mathcal{J}\tilde{\varphi}_0}{1+\frac{1}{\eta}(s+\mathcal{H})+\frac{2\mathcal{J}_D\mathcal{J}}{\frac{1}{\eta}(s+\mathcal{H})+2}}. \tag{B.33}$$

In the very large damping limit, the friction coefficient η is much larger than any other time scale. Hence, we can keep terms only to leading order in the inverse friction η^{-1}, giving:

$$s\tilde{\varphi}_0+\hat{\phi}_0(x,0)+\mathcal{H}\tilde{\varphi}_0=\eta\mathcal{J}_D\mathcal{J}\tilde{\varphi}_0. \tag{B.34}$$

Inverting the Laplace transform therefore gives:

$$\frac{\partial\hat{\phi}_0}{\partial t}=-i\left[\left(\frac{\epsilon}{2}+\kappa x\right)\sigma_z+\frac{\Delta}{2}\sigma_x,\hat{\phi}_0\right]+\eta\mathcal{J}_D\mathcal{J}\hat{\phi}_0. \tag{B.35}$$

Finally, writing $\hat{\phi}_0=\sum_{i,j}^{2}\mu_{ij}(x,t)|i\rangle\langle j|$ gives the Zusman equations:

$$\begin{aligned}
\frac{\partial\mu_{11}(t,x)}{\partial t}&=\frac{1}{2\pi\gamma\Omega}\frac{\partial}{\partial x}\left((\Omega^2x+\kappa)\mu_{11}(t,x)+\frac{1}{\beta}\frac{\partial\mu_{11}(t,x)}{\partial x}\right)+i\frac{\Delta}{2}(\mu_{12}(t,x)-\mu_{21}(t,x)),\\
\frac{\partial\mu_{22}(t,x)}{\partial t}&=\frac{1}{2\pi\gamma\Omega}\frac{\partial}{\partial x}\left((\Omega^2x+\kappa)\mu_{22}(t,x)+\frac{1}{\beta}\frac{\partial\mu_{22}(t,x)}{\partial x}\right)-i\frac{\Delta}{2}(\mu_{12}(t,x)-\mu_{21}(t,x)),\\
\frac{\partial\mu_{12}(t,x)}{\partial t}&=\frac{1}{2\pi\gamma\Omega}\frac{\partial}{\partial x}\left(\frac{1}{\beta}\frac{\partial\mu_{12}(t,x)}{\partial x}+\Omega^2x\mu_{12}(t,x)\right)+i(\epsilon+2\kappa x)\mu_{12}(t,x)\\
&\quad+i\frac{\Delta}{2}(\mu_{11}(t,x)-\mu_{22}(t,x)),\\
\frac{\partial\mu_{21}(t,x)}{\partial t}&=\frac{1}{2\pi\gamma\Omega}\frac{\partial}{\partial x}\left(\frac{1}{\beta}\frac{\partial\mu_{21}(t,x)}{\partial x}+\Omega^2x\mu_{21}(t,x)\right)+i(\epsilon+2\kappa x)\mu_{21}(t,x)\\
&\quad-i\frac{\Delta}{2}(\mu_{11}(t,x)-\mu_{22}(t,x)),
\end{aligned} \tag{B.36}$$

To solve the Zusman equations we first need an initial conditions. If we assume that the system starts in the excited state and the mode in a thermal state $\rho_m=Z^{-1}\exp\{-\beta\Omega a^\dagger a\}$, then the only non-zero variable will be $n_{11}(x,0)$. Hence, the thermal state in Wigner space may be written as:

$$W_{th}=\frac{2\tanh\left(\frac{\beta\Omega}{2}\right)}{\pi}e^{-\tanh\left(\frac{\beta\Omega}{2}\right)\left(\Omega x^2+\frac{1}{\Omega}p^2\right)}. \tag{B.37}$$

We then integrate over the momentum coordinate to attain the initial condition:

$$\mu_{11}(x,0)=\int_{-\infty}^{\infty}dpW_{th}(0,x,p)=2\sqrt{\frac{\tanh\left(\frac{\beta\Omega}{2}\right)}{\pi}}e^{-\Omega\tanh\left(\frac{\beta\Omega}{2}\right)x^2}, \tag{B.38}$$

while $\mu_{12}(x,0)=\mu_{21}(x,0)=\mu_{22}(x,0)=0$ for all x.

BIBLIOGRAPHY

[1] M. Nielsen and I. Chuang, *Quantum Computation and Quantum Information* (Cambridge University Press, 2000).

[2] H. P. Breuer and F. Petruccione, *The Theory of Open Quantum Systems* (Oxford University Press, Oxford, 2002).

[3] R. Horodecki, P. Horodecki, M. Horodecki, and K. Horodecki, Rev. Mod. Phys. **81**, 865 (2009).

[4] A. J. Leggett, S. Chakravarty, A. T. Dorsey, M. Fisher, A. Garg, and W. Zwerger, Rev. Mod. Phys. **59**, 1 (1987).

[5] S. Nakajima, Progress of Theoretical Physics **20**, 948 (1958).

[6] R. Zwanzig, The Journal of Chemical Physics **33**, 1338 (1960).

[7] D. P. McCutcheon, arXiv:1504.05970 (2015).

[8] D. P. S. McCutcheon and A. Nazir, The Journal of Chemical Physics **135**, 114501 (2011).

[9] H. Carmichael, *Statistical Methods in Quantum Optics 1: Master Equations and Fokker-Planck Equations* (Springer, 1998).

[10] G. Lindblad, Communications in Mathematical Physics **48**, 119 (1976).

[11] U. Weiss, *Quantum Dissipative Systems* (World Scientific, Singapore, 2008).

[12] A. Nazir, Physical Review B **78**, 153309 (2008).

[13] A. J. Ramsay, T. M. Godden, S. J. Boyle, E. M. Gauger, A. Nazir, B. W. Lovett, A. M. Fox, and M. S. Skolnick, Phys. Rev. Lett. **105**, 177402 (2010).

[14] A. J. Ramsay, A. V. Gopal, E. M. Gauger, A. Nazir, B. W. Lovett, A. M. Fox, and M. S. Skolnick, Phys. Rev. Lett. **104**, 017402 (2010).

[15] D. Press, S. Götzinger, S. Reitzenstein, C. Hofmann, A. Löffler, M. Kamp, A. Forchel, and Y. Yamamoto, Phys. Rev. Lett. **98**, 117402 (2007).

[16] O. Fedorych, C. Kruse, A. Ruban, D. Hommel, G. Bacher, and T. KÃŒmmell, Applied Physics Letters **100**, 061114 (2012).

[17] V. Loo, C. Arnold, O. Gazzano, A. Lemaître, I. Sagnes, O. Krebs, P. Voisin, P. Senellart, and L. Lanco, Phys. Rev. Lett. **109**, 166806 (2012).

[18] R. Bose, D. Sridharan, H. Kim, G. S. Solomon, and E. Waks, Phys. Rev. Lett. **108**, 227402 (2012).

[19] A. Imamoğlu, D. D. Awschalom, G. Burkard, D. P. DiVincenzo, D. Loss, M. Sherwin, and A. Small, Phys. Rev. Lett. **83**, 4204 (1999).

[20] P. Kok and B. W. Lovett, *Introduction to optical quantum information processing* (Cambridge University Press, 2010).

[21] D. Bimberg, M. Grundmann, and N. N. Ledentsov, *Quantum dot heterostructures* (John Wiley & Sons, 1999).

[22] D. Bimberg, *Semiconductor nanostructures* (Springer Science & Business Media, 2008).

[23] M. Bayer, O. Stern, P. Hawrylak, S. Fafard, and A. Forchel, Nature **405**, 923 (2000).

[24] K. Brunner, U. Bockelmann, G. Abstreiter, M. Walther, G. Böhm, G. Tränkle, and G. Weimann, Phys. Rev. Lett. **69**, 3216 (1992).

[25] T. H. Stievater, X. Li, D. G. Steel, D. Gammon, D. S. Katzer, D. Park, C. Piermarocchi, and L. J. Sham, Phys. Rev. Lett. **87**, 133603 (2001).

[26] H. Kamada, H. Gotoh, J. Temmyo, T. Takagahara, and H. Ando, Phys. Rev. Lett. **87**, 246401 (2001).

[27] H. Htoon, T. Takagahara, D. Kulik, O. Baklenov, A. L. Holmes, and C. K. Shih, Phys. Rev. Lett. **88**, 087401 (2002).

[28] A. Nick Vamivakas, Y. Zhao, C.-Y. Lu, and M. Atature, Nat Phys **5**, 198 (2009).

[29] Y.-J. Wei, Y. He, Y.-M. He, C.-Y. Lu, J.-W. Pan, C. Schneider, M. Kamp, S. Höfling, D. P. S. McCutcheon, and A. Nazir, Phys. Rev. Lett. **113**, 097401 (2014).

[30] Y. He, Y.-M. He, Y.-J. Wei, X. Jiang, M.-C. Chen, F.-L. Xiong, Y. Zhao, C. Schneider, M. Kamp, S. Höfling, et al., Phys. Rev. Lett. **111**, 237403 (2013).

[31] R. B. Patel, A. J. Bennett, K. Cooper, P. Atkinson, C. A. Nicoll, D. A. Ritchie, and A. J. Shields, Phys. Rev. Lett. **100**, 207405 (2008).

[32] R. Proux, M. Maragkou, E. Baudin, C. Voisin, P. Roussignol, and C. Diederichs, Phys. Rev. Lett. **114**, 067401 (2015).

[33] D. P. S. McCutcheon and A. Nazir, New J. Phys. **12**, 113042 (2010).

[34] S. Weiler, A. Ulhaq, S. M. Ulrich, D. Richter, M. Jetter, P. Michler, C. Roy, and S. Hughes, Phys. Rev. B **86**, 241304 (2012).

[35] J. H. Quilter, A. J. Brash, F. Liu, M. Glässl, A. M. Barth, V. M. Axt, A. J. Ramsay, M. S. Skolnick, and A. M. Fox, Phys. Rev. Lett. **114**, 137401 (2015).

[36] S. Hughes and H. J. Carmichael, New Journal of Physics **15**, 053039 (2013).

[37] D. P. S. McCutcheon and A. Nazir, Phys. Rev. Lett. **110**, 217401 (2013).

[38] R. A. Harris and R. Silbey, The Journal of Chemical Physics **83**, 1069 (1985).

[39] R. Silbey and R. A. Harris, The Journal of Chemical Physics **80**, 2615 (1984).

[40] D. P. S. McCutcheon, N. S. Dattani, E. M. Gauger, B. W. Lovett, and A. Nazir, Phys. Rev. B **84**, 081305 (2011).

[41] C. K. Hong, Z. Y. Ou, and L. Mandel, Phys. Rev. Lett. **59**, 2044 (1987).

[42] D. A. Steck, *Quantum and atom optics* (available online at http://steck.us/teaching, 2006).

[43] B. Stiller, U. Seyfarth, and G. Leuchs, arXiv:1411.3765 (2014).

[44] B. R. Mollow, Phys. Rev. **188**, 1969 (1969).

[45] A. Zrenner, E. Beham, S. Stufler, F. Findeis, M. Bichler, and G. Abstreiter, Nature **418**, 612 (2002).

[46] R. Silbey and R. W. Munn, The Journal of Chemical Physics **72**, 2763 (1980).

[47] F. A. Pollock, D. P. S. McCutcheon, B. W. Lovett, E. M. Gauger, and A. Nazir, New J. Phys. **15**, 075018 (2013).

[48] R. P. Feynman, *Statistical Mechanics: A set of lectures* (Westview Press, 1972).

[49] A. Nazir, Phys. Rev. Lett. **103**, 146404 (2009).

[50] S. Bera, S. Florens, H. U. Baranger, N. Roch, A. Nazir, and A. W. Chin, Phys. Rev. B **89**, 121108 (2014).

[51] S. Bera, A. Nazir, A. W. Chin, H. U. Baranger, and S. Florens, Phys. Rev. B **90**, 075110 (2014).

[52] K. Roy-Choudhury and S. Hughes, Opt. Lett. **40**, 1838 (2015).

[53] S. Hughes and H. J. Carmichael, Phys. Rev. Lett. **107**, 193601 (2011).

[54] R. Hanbury Brown and R. Q. Twiss, Nature **178**, 1046 (1956).

[55] R. H. Brown and R. Q. Twiss, Proceedings of the Royal Society of London A: Mathematical, Physical and Engineering Sciences **242**, 300 (1957).

[56] R. H. Brown and R. Q. Twiss, Proceedings of the Royal Society of London A: Mathematical, Physical and Engineering Sciences **243**, 291 (1958).

[57] P. Kok, W. J. Munro, K. Nemoto, T. C. Ralph, J. P. Dowling, and G. J. Milburn, Rev. Mod. Phys. **79**, 135 (2007).

[58] S. Buckley, K. Rivoire, and J. Vučković, Reports on Progress in Physics **75**, 126503 (2012).

[59] D. Walls and G. Milburn, *Quantum Optics* (Springer, 2008).

[60] T. Legero, T. Wilk, A. Kuhn, and G. Rempe, Applied Physics B **77**, 797 (2003).

[61] T. Legero, T. Wilk, M. Hennrich, G. Rempe, and A. Kuhn, Phys. Rev. Lett. **93**, 070503 (2004).

[62] J. Metz and S. D. Barrett, Phys. Rev. A **77**, 042323 (2008).

[63] R. B. Patel, A. J. Bennett, I. Farrer, C. A. Nicoll, D. A. Ritchie, and A. J. Shields, Nat Photon **4**, 632 (2010).

[64] P. Michler, A. Kiraz, C. Becher, W. V. Schoenfeld, P. M. Petroff, L. Zhang, E. Hu, and A. Imamoğlu, Science **290**, 2282 (2000).

[65] T. Pellizzari, S. Gardiner, J. Cirac, and P. Zoller, Phys. Rev. Lett. **75**, 3788 (1995).

[66] L. M. Duan, M. D. Lukin, J. I. Cirac, and P. Zoller, Nature **414**, 413 (2001).

[67] C.-H. Su, A. Greentree, W. Munro, K. Nemoto, and L. Hollenberg, Phys. Rev. A **78**, 062336 (2008).

[68] A. Wallraff, D. I. Schuster, A. Blais, L. Frunzio, R. S. Huang, J. Majer, S. Kumar, S. M. Girvin, and R. J. Schoelkopf, Nature **431**, 162 (2004).

[69] T. Niemczyk, F. Deppe, H. Huebl, E. P. Menzel, F. Hocke, M. J. Schwarz, J. J. Garcia-Ripoll, D. Zueco, T. Hummer, E. Solano, et al., Nat Phys **6**, 772 (2010).

[70] J. P. Reithmaier, G. Sek, A. Loffler, C. Hofmann, S. Kuhn, S. Reitzenstein, L. V. Keldysh, V. D. Kulakovskii, T. L. Reinecke, and A. Forchel, Nature **432**, 197 (2004).

[71] T. Yoshie, A. Scherer, J. Hendrickson, G. Khitrova, H. M. Gibbs, G. Rupper, C. Ell, O. B. Shchekin, and D. G. Deppe, Nature **432**, 200 (2004).

[72] K. Hennessy, A. Badolato, M. Winger, D. Gerace, M. Atature, S. Gulde, S. Falt, E. L. Hu, and A. Imamoğlu, Nature **445**, 896 (2007).

[73] A. Faraon, I. Fushman, D. Englund, N. Stoltz, P. Petroff, and J. Vuckovic, Nat Phys **4**, 859 (2008).

[74] J. Kasprzak, S. Reitzenstein, E. A. Muljarov, C. Kistner, C. Schneider, M. Strauss, S. Hofling, A. Forchel, and W. Langbein, Nat Mater **9**, 304 (2010).

[75] C. Hu, A. Young, J. O'Brien, W. Munro, and J. Rarity, Phys. Rev. B **78**, 085307 (2008).

[76] A. B. Young, R. Oulton, C. Y. Hu, A. C. T. Thijssen, C. Schneider, S. Reitzenstein, M. Kamp, S. Höfling, L. Worschech, A. Forchel, et al., Phys. Rev. A **84**, 011803 (2011).

[77] C. Y. Hu and J. G. Rarity, Phys. Rev. B **91**, 075304 (2015).

[78] D. P. S. McCutcheon and A. Nazir, Phys. Rev. B **83**, 165101 (2011).

[79] C. Roy and S. Hughes, Phys. Rev. X **1**, 021009 (2011).

[80] C. Roy and S. Hughes, Phys. Rev. Lett. **106**, 247403 (2011).

[81] P. Kaer, P. Lodahl, A.-P. Jauho, and J. Mørk, Phys. Rev. B **87**, 081308 (2013).

[82] P. Kaer and J. Mørk, Phys. Rev. B **90**, 035312 (2014).

[83] I. Wilson-Rae and A. Imamoğlu, Phys. Rev. B **65**, 235311 (2002).

[84] A. Kavokin and G. Malpuech, *Cavity Polaritons* (Elsevier, 2003).

[85] M. J. Collett and C. W. Gardiner, Phys. Rev. A **30**, 1386 (1984).

[86] C. W. Gardiner and M. J. Collett, Phys. Rev. A **31**, 3761 (1985).

[87] A. Würger, Phys. Rev. B. **57**, 347 (1998).

[88] E. Waks and D. Sridharan, Phys. Rev. A **82**, 043845 (2010).

[89] S. Hughes and C. Roy, Phys. Rev. B **85**, 035315 (2012).

[90] A. E. Miroshnichenko, S. Flach, and Y. S. Kivshar, Rev. Mod. Phys. **82**, 2257 (2010).

[91] E. Peter, P. Senellart, D. Martrou, A. Lemaître, J. Hours, J. M. Gérard, and J. Bloch, Phys. Rev. Lett. **95**, 067401 (2005).

[92] S. Reitzenstein, S. Münch, P. Franeck, A. Rahimi-Iman, A. Löffler, S. Höfling, L. Worschech, and A. Forchel, Phys. Rev. Lett. **103**, 127401 (2009).

[93] J. Riedrich-Moller, L. Kipfstuhl, C. Hepp, E. Neu, C. Pauly, F. Mucklich, A. Baur, M. Wandt, S. Wolff, M. Fischer, et al., Nat Nano **7**, 69 (2012).

[94] R. Albrecht, A. Bommer, C. Deutsch, J. Reichel, and C. Becher, Phys. Rev. Lett. **110**, 243602 (2013).

[95] L. S. Bishop, J. M. Chow, J. Koch, A. A. Houck, M. H. Devoret, E. Thuneberg, S. M. Girvin, and R. J. Schoelkopf, Nat Phys **5**, 105 (2009).

[96] A. Nitzan, *Chemical Dynamics in Condensed Phases: Relaxation, Transfer and Reactions in Condensed Molecular Systems* (Oxford University Press, Oxford, 2006).

[97] V. May and O. Kühn, *Charge and Energy Transfer Dynamics in Molecular Systems* (Wiley, Berlin, 2011), 3rd ed.

[98] A. Garg, J. N. Onuchic, and V. Ambegaokar, J. Chem. Phys. **83**, 4491 (1985).

[99] M. Thoss, H. Wang, and W. H. Miller, J. Chem. Phys. **115**, 2991 (2001).

[100] J. Cao and G. A. Voth, J. Chem. Phys. **106**, 1769 (1997).

[101] K. H. Hughes, C. D. Christ, and I. Burghardt, J. Chem. Phys. **131**, 124108 (pages 15) (2009).

[102] L. Hartmann, I. Goychuk, and P. Hänggi, J. Chem. Phys. **113**, 11159 (2000).

[103] J. Roden, W. T. Strunz, K. B. Whaley, and A. Eisfeld, The Journal of Chemical Physics **137**, 204110 (2012).

[104] R. Martinazzo, B. Vacchini, K. H. Hughes, and I. Burghardt, J. Chem. Phys. **134**, 011101 (2011).

[105] M. P. Woods, R. Groux, A. W. Chin, S. F. Huelga, and M. B. Plenio, Journal of Mathematical Physics **55**, 032101 (2014).

[106] A. Imamoğlu, Phys. Rev. A **50**, 3650 (1994).

[107] B. M. Garraway, Phys. Rev. A **55**, 2290 (1997).

[108] Y. Tanimura, Phys. Rev. A. **41**, 6676 (1990).

[109] Y. Tanimura and R. Kubo, J. Phys. Soc. Jpn. **58**, 101 (1989).

[110] N. Makri and D. E. Makarov, J. Chem. Phys. **102**, 4600 (1995).

[111] J. Prior, A. W. Chin, S. F. Huelga, and M. B. Plenio, Phys. Rev. Lett. **105**, 050404 (2010).

[112] A. Alvermann and H. Fehske, Phys. Rev. Lett. **102**, 150601 (2009).

[113] H. Wang and M. Thoss, New J. Phys. **10**, 115005 (2008).

[114] F. B. Anders, R. Bulla, and M. Vojta, Phys. Rev. Lett. **98**, 210402 (2007).

[115] A. Winter, H. Rieger, M. Vojta, and R. Bulla, Phys. Rev. Lett. **102**, 030601 (2009).

[116] S. Jang, Y.-C. Cheng, D. R. Reichman, and J. D. Eaves, J. Chem. Phys. **129**, 101104 (2008).

[117] C. Fleming, A. Roura, and B. Hu, Annals of Physics **326**, 1207 (2011).

[118] J. Gilmore and R. H. McKenzie, J. Phys.: Condens. Matter **17**, 1735 (2005).

[119] Y. Fujihashi, G. R. Fleming, and A. Ishizaki, The Journal of Chemical Physics **142**, 212403 (2015).

[120] A. G. Dijkstra, C. Wang, J. Cao, and G. R. Fleming, The Journal of Physical Chemistry Letters **6**, 627 (2015).

[121] A. J. Leggett, Phys. Rev. B **30**, 1208 (1984).

[122] A. W. Chin, Ã. Rivas, S. F. Huelga, and M. B. Plenio, Journal of Mathematical Physics **51**, 092109 (2010).

[123] M. P. Woods, M. Cramer, and M. B. Plenio, Phys. Rev. Lett. **115**, 130401 (2015).

[124] F. A. Schröder, A. W. Chin, and R. H. Friend, arXiv:1507.02202 (2015).

[125] A. W. Chin, J. Prior, R. Rosenbach, F. Caycedo-Soler, S. F. Huelga, and M. B. Plenio, Nat Phys **9**, 113 (2013).

[126] R. Rosenbach, J. Cerrillo, S. F. Huelga, J. Cao, and M. Bodo Plenio, arXiv:1510.03100 (2015).

[127] A. Ishizaki and G. R. Fleming, J. Chem. Phys. **130**, 234111 (pages 10) (2009).

[128] M. Thorwart, J. Eckel, J. Reina, P. Nalbach, and S. Weiss, Chem. Phys. Lett. **478**, 234 (2009).

[129] M. G. Genoni, M. G. A. Paris, and K. Banaszek, Phys. Rev. A **78**, 060303 (2008).

[130] M. G. Genoni and M. G. A. Paris, Phys. Rev. A **82**, 052341 (2010).

[131] B. Groisman, S. Popescu, and A. Winter, Phys. Rev. A **72**, 032317 (2005).

[132] K. Le Hur, P. Doucet-Beaupre, and W. Hofstetter, Phys. Rev. Lett. **99**, 126801 (2007).

[133] G. D. Mahan, *Many-Particle Physics* (Plenum, New York, 1990).

[134] M. Goldstein, M. H. Devoret, M. Houzet, and L. I. Glazman, Phys. Rev. Lett. **110**, 017002 (2013).

[135] G. Engel, T. Calhoun, E. Read, T. Ahn, T. Mančal, Y. Cheng, R. Blankenship, and G. Fleming, Nature **446**, 782 (2007).

[136] H. Lee, Y.-C. Cheng, and G. R. Fleming, Science **316**, 1462 (2007).

[137] E. Collini and G. D. Scholes, Science **323**, 369 (2009).

[138] D. H. Santamore, N. Lambert, and F. Nori, Phys. Rev. B **87**, 075422 (2013).

[139] C. K. Lee, J. Cao, and J. Gong, Phys. Rev. E **86**, 021109 (2012).

[140] E. A. Martinez and J. P. Paz, Phys. Rev. Lett. **110**, 130406 (2013).

[141] N. Lambert, Y.-N. Chen, Y.-C. Cheng, C.-M. Li, G.-Y. Chen, and F. Nori, Nat Phys **9**, 10 (2013).

[142] F. Caruso, A. W. Chin, A. Datta, S. F. Huelga, and M. B. Plenio, J. Chem. Phys. **131**, 105106 (2009).

[143] A. Kolli, A. Nazir, and A. Olaya-Castro, The Journal of Chemical Physics **135**, 154112 (2011).

[144] J. Wu, F. Liu, Y. Shen, J. Cao, and R. J. Silbey, New Journal of Physics **12**, 105012 (2010).

[145] P. Rebentrost, M. Mohseni, I. Kassal, S. Lloyd, and A. Aspuru-Guzik, New Journal of Physics **11**, 033003 (2009).

[146] F. Levi, S. Mostarda, F. Rao, and F. Mintert, Reports on Progress in Physics **78**, 082001 (2015).

[147] J. Iles-Smith, N. Lambert, and A. Nazir, Phys. Rev. A **90**, 032114 (2014).

[148] J. Strümpfer and K. Schulten, The Journal of Chemical Physics **131**, 225101 (2009).

[149] E. K. Irish, R. Gómez-Bombarelli, and B. W. Lovett, Phys. Rev. A **90**, 012510 (2014).

[150] F. Novelli, G. H. Richards, A. Roozbeh, K. E. Wilk, P. M. Curmi, and J. A. Davis, arXiv:1503.00251 (2015).

[151] E. J. O'Reilly and A. Olaya-Castro, Nat Commun **5** (2014).

[152] Y. Tanimura, The Journal of Chemical Physics **137**, (2012).

[153] M. Tanaka and Y. Tanimura, The Journal of Chemical Physics **132**, 214502 (2010).

[154] M. Tanaka and Y. Tanimura, Journal of the Physical Society of Japan **78**, 073802 (2009).

[155] Q. Shi, L. Chen, G. Nan, R. Xu, and Y. Yan, The Journal of Chemical Physics **130**, 164518 (2009).

[156] N. Killoran, S. F. Huelga, and M. B. Plenio, arXiv:1412.4136 (2014).

[157] A. Caldeira and A. Leggett, Physica A: Statistical Mechanics and its Applications **121**, 587 (1983).

[158] H. Risken, in *The Fokker-Planck Equation* (Springer Berlin Heidelberg, 1984), vol. 18 of *Springer Series in Synergetics*, pp. 63–95.

[159] J. Johansson, P. Nation, and F. Nori, Computer Physics Communications **183**, 1760 (2012).

[160] J. Johansson, P. Nation, and F. Nori, Computer Physics Communications **184**, 1234 (2013).

[161] D. Hayes, G. B. Griffin, and G. S. Engel, Science **340**, 1431 (2013).

[162] W. T.Coffey, Y. P. Kalmykov, S. V. Titov, and B. P. Mulligan, Phys. Chem. Chem. Phys. **9**, 3361 (2007).

[163] H. Brinkman, Physica **22**, 29 (1956).